Structure-activity relationships of novel anti-diabetic ruthenium compounds: synthesis, characterization, mechanistic and *in vitro* studies

Submitted in fulfilment of the requirements for the degree of

Doctor of Philosophy

in the School of Chemistry and Physics

at the University of KwaZulu-Natal

by

Madikoloha Daniel Makanyane

February 2024

Supervisor: Professor Irvin N. Booysen

Co-supervisor: Dr Allen Mambanda

As the candidate's supervisors, we have approved this thesis for submission:

Signed: _ [redacted] Date: 08/02/2024

Signed: __ [redacted] Date: 08/02/2024

Table of Contents

Chapter 3

Bovine serum albumin uptake and polypeptide disaggregation studies of hypoglycaemic ruthenium(II) uracil Schiff-base complexes

Chapter 4

Anti-amyloid aggregation and anti-hyperglyceamic activities of novel ruthenium(II) Schiff base chelates containing uracil moieties

Chapter 5

Encapsulation of anti-diabetic ruthenium(II) uracil compounds into chitosan (CS)-polyvinyl alcohol (PVA) electrospun nanofibers: Nanofabrication, characterization and desorption kinetics

Chapter 6

Conclusion and recommendation for further studies

Declaration 1 - Plagiarism

I, Madikoloha Daniel Makanyane, declare that:

i. The research reported in this dissertation, except where otherwise indicated, is my original research.
ii. This thesis has not been submitted for any degree or examination at any other university.
iii. This thesis does not contain other persons' data, pictures, graphs, or other information unless specifically acknowledged as being sourced from other persons.
iv. This thesis does not contain other persons' writing unless specifically acknowledged as being sourced from other researchers. Where other written sources have been quoted, then:
    a) Their words have been re-written but the general information attributed to them has been referenced.
    b) Where their exact words have been used, then their writing has been placed in italics and inside quotation marks, and referenced.
v. This thesis does not contain text, graphics or tables copied and pasted from the internet, unless specifically acknowledged, and the source being detailed in the thesis and in the References sections.

Signed:…  …(Daniel M. Makanyane) Date: 08/02/2024

Signed:……  ……(Prof. Irvin N. Booysen) Date: 08/02/2024

Signed:……  ……(Dr. Allan Mambanda) Date: 08/02/2024

Declaration 2 - Publications

Thus far, one manuscript has been published:

- S. Maikoo, M.D. Makanyane, I.N. Booysen, P. Ngubane, A. Khathi ''**Ruthenium compounds as potential therapeutic agents for type 2 diabetes mellitus'',** *European Journal of Medicinal Chemistry*, 2021, **231**, 11. https://doi.org/10.1016/j.ejmech.2020.113064

The manuscript below is currently under review:

- M.D. Makanyane, S. Maikoo, F.R. Van Heerden, L. Rhyman, P. Ramasami, L.P. Mabuza, P. Ngubane, A. Khathi, A. Mambanda, I.N. Booysen ,'' **Bovine serum albumin uptake and polypeptide disaggregation studies of hypoglycaemic ruthenium(II) uracil Schiff-base complexes**''.

The following manuscripts are currently in preparation:

- M.D. Makanyane, L. Rhyman, P. Ramasami, L.P. Mabuza, P. Ngubane, A. Khathi, A. Mambanda, I.N. Booysen ,''**Anti-amyloid aggregation and anti-hyperglyceamic activities of novel ruthenium(II) uracil Schiff base compounds''.**
- M.D. Makanyane, L.P. Mabuza, P. Ngubane, A. Khathi, A. Mambanda, I.N. Booysen,'' **Encapsulation of anti-diabetic ruthenium(II) uracil compounds into chitosan (CS)-polyvinyl alcohol (PVA) electrospun nanofibers: Nanofabrication, characterization, desorption kinetics and *in vitro* glucose metabolism activities''**.

Signed:… […]…(Daniel M. Makanyane) Date: 08/02/2024

Signed:…… […]……(Prof. Irvin N. Booysen) Date: 08/02/2024

Signed:… […]…(Dr. Allan Mambanda) Date: 08/02/2024

Acknowledgments

I would like to thank my supervisor, Prof Irvin Noel Booysen and co-supervisor, Dr Allen Mambanda for imparting their technical and theoretical knowledge on me. In addition, for their patience and encouragement when I suffered a prolonged case of appendicitis which was originally misdiagnosed at a government hospital. Furthermore, I am also grateful to them for giving me the opportunities to mentor masters and honours students within our research group.

I would also like to express my gratitude to the following people:

- Mr. Leigh Andre Hunter for crystallographic data collection and processing.
- Mr. Craig Douglas Grimmer for his assistance with NMR spectroscopy.
- Mrs. Caryl Janse van Rensburg for collecting mass spectroscopy and elemental analysis data.

The continuous support from my peers including: Ms D. Moodley, Mr K. Kantize, Mr P. Mangundu, Mr S. Shoba, Dr S. Maikoo, Ms T. Mapapiro, Ms V. Ngwenya and Dr Robert Kumah were of utmost importance for me. I am thankful to the National Research Foundation (NRF) for subsistence and research funding. My experiences within the well-equipped research laboratories of the University of KwaZulu-Natal were very enriching.

Moreover, I am eternally blessed by the unlimited support and love from my wife, Mrs Makanyane-Mokoena Octavia Nthabeleng. I want to acknowledge my younger brother, Lehlohonolo Alexander Makanyane for his continued support, encouragement, the periods of fasting and praying throughout the years of my studies and post-recovery of my surgical operation.

Data-availability

Supporting information related to the experimental chapters 3 – 5 can be found in the listed google-drive links:

- **Chapter 3:** https://drive.google.com/file/d/1qvp5A2DenVHJwtycBQNnis0BdOfX8hvu/view?usp=drive_link
- **Chapter 4:** https://drive.google.com/drive/folders/1ID8rngNLxGpQ2XqcmOFWgXUy6sobcy1R?usp=drive_link
- **Chapter 5:** https://drive.google.com/file/d/1Ik9ucefwC5FhTzuoc7x9hrdZpWIlczSS/view?usp=drive_link

List of Figures

List of tables

list of schemes

Common abbreviations and acronyms

bpy	Bipyridine
BSA	Bovine Serum Albumin
CS	Chitosan
DFT	Density Functional Theory
DMF	Dimethylformamide
DMSO	Dimethylsulfoxide
H_2dpa	5,6-diaminouracil
H_4ucp	2,6-bis-((6-amino-3,4-dimethyluracilimino)methylene)pyridine)
DPPH	2,2-di(4-tert-octylphenyl)-1-picrylhydrazyl
FTIR	Fourier Transform Infrared Spectroscopy
HOMO	Highest Occupied Molecular Orbital
hIAPP	human islet amyloid polypeptide
HSA	Human Serum Albumin
LMCT	Ligand-to-metal Charge Transfer
LUMO	Lowest unoccupied Molecular Orbital
MeOH	Methanol
MLCT	Metal-to-Ligand Charge Transfer
MTT	3-[4,5-dimethylthiazol-2-yl]-2,5 diphenyl tetrazolium bromide
NMR	Nuclear Magnetic Resonance
NO	Nitric Oxide
ORTEP	Oak Ridge Thermal Ellipsoid Plot
PBS	Phosphate Buffered Saline
PVA	Polyvinyl alcohol
UPW	Ultra-pure water
urdpa	5-((pyridin-2-yl)methyleneamino)-6-aminouracil)
urqda	5-((quinolin-2-yl)methyleneamino)-6-aminouracil)
urpy	5-((pyridin-2-yl)methyleneamino)uracil)
urdp	5-((quinolin-2-yl)methyleneamino)-6-aminouracil))
urdy	6-amino-1,3-dimethyl-5-((pyridin-2-ylmethylene)amino)uracil)
PXRD	Powder X-ray diffraction
RMSD	Root-Mean-Square-Deviation
SEM	Scanning Electron Microscopy
ThT	Thioflavin T
UV-Vis	Ultraviolet-Visible
XRD	X-Ray Diffraction

Abstract

Type 2 Diabetes Mellitus (T2DM) is a chronic metabolic disorder which is globally responsible for millions of fatalities per year. Management of T2DM typically involves orally administered anti-hyperglycaemic drugs in conjunction with dietary interventions. However, the current conventional therapy seems to be largely ineffective as patients continue to develop complications such as cardiovascular diseases, blindness and kidney failure. Existing alternative treatment entails the administration of organic therapeutic pharmaceuticals, but these drugs have various side effects such as nausea, headaches, weight gain, and respiratory and liver damage. Transition metal complexes have shown promise as anti-diabetic agents owing to their diverse mechanisms of activity. In particular, selected ruthenium compounds have exhibited intriguing biological behaviours as Protein Tyrosine Phosphatase (PTP) 1B and Glycogen Synthase Kinase 3 (GSK-3) inhibitors, as well as aggregation suppressants for the human islet amyloid polypeptide (hIAPP).

The introduction chapter served as a survey on studies pertaining to ruthenium compounds as metallo-drugs for T2DM. Herein, we also provide perspectives on directions to fully elucidate *in vivo* functions of this class of potential metallopharmaceuticals. More specifically, there is still a need to investigate the pharmacokinetics of ruthenium drugs in order to establish their biodistribution patterns which will affirm whether these metal complexes are substitutionally inert or serve as pro-drugs. In addition, embedding oral-administered ruthenium complexes into bio-compatible polymers can be a prospective means of enhancing stability during drug delivery. This chapter was concluded with a descriptive rationale of the research study as well as specifying the specific research aims and objectives.

Our prior studies have illustrated that the uracil ruthenium(II) diimino complex, [Ru(H_3ucp)Cl(PPh_3)] (**1**) (H_4ucp = 2,6-*bis*-((6-amino-1,3-dimethyluracilimino)methylene)pyridine) displayed high hypoglycaemic effects in diet-induced diabetic rats. To rationalize the anti-diabetic effects of **1** in the first

experimental chapter, three new derivatives have been prepared, *cis*-[Ru(bpy)$_2$(urdp)]Cl$_2$ (**2**) (urdp = 2,6-*bis*-((uracilimino)methylene)pyridine), *trans*-[RuCl$_2$(PPh$_3$)(urdp)] (**3**), and *cis*-[Ru(bpy)$_2$(H$_4$ucp)](PF$_6$)$_2$ (**4**). Various physicochemical techniques were utilized to characterize the structures of the novel ruthenium compounds. Prior to biomolecular interactions or *in vitro* studies, the stabilities of **1 – 4** were monitored in anhydrous DMSO, aqueous phosphate buffer containing 2% DMSO, and dichloromethane (DCM) *via* UV-Vis spectrophotometry. Time-dependent stability studies showed ligand exchange between DMSO nucleophiles and chloride co-ligands of **1** and **3,** which was suppressed in the presence of an excess amount of chloride ions.

In addition, the metal complexes **1** and **3** are stable in both DCM and an aqueous phosphate buffer containing 2% DMSO. In the case of compounds **2** and **4** with no chloride co-ligands within their coordination spheres, high stability in aqueous phosphate buffer containing 2% DMSO was observed. Fluorescence emission titrations of the individual ruthenium compounds with bovine serum albumin (BSA) showed that the metal compounds interact non-discriminately within the protein's hydrophobic cavities as moderate to strong binders. The metal complexes were capable of disintegrating mature amylin amyloid fibrils. *In vivo,* glucose metabolism studies in the liver (Chang) cell lines confirmed enhanced glucose metabolism as evidenced by the increased glucose utilization and glycogen synthesis in liver cell lines in the presence of complexes **2 – 4**.

The second experimental chapter, reports on the formation and characterization of new diamagnetic ruthenium uracil *mono*-imine compounds: [(η^6-*p*-cymene)Ru^{II}(L)Cl] (L = urpda = 5-((pyridin-2-yl)methyleneamino)-6-aminouracil) for **1**, urdpy = 6-amino-1,3-dimethyl-5-((pyridin-2-ylmethylene)amino)uracil) for **2** or urqd = 5-((quinolin-2-yl)methyleneamino)-6-aminouracil) for **3**); *cis*-[Ru^{II}(L)(bipy)$_2$] (L = urpy = 5-((pyridin-2-yl)methyleneamino)uracil) for **4** and H$_2$dadp = 5,6-diaminouracil for **5**); *trans*-[Ru^{II}(L)(PPh$_3$)Cl$_2$] (L = urpda for **6**) are described. Various physicochemical

techniques were utilized to characterize the structures of the novel ruthenium compounds.

Furthermore, the DPPH and NO radical scavenging capabilities of metal complexes (**2 – 10**) were investigated. UV-Vis spectrophotometry data of the time-dependent (for 24 h) studies show that 4 and 5 are stable in aqueous phosphate buffer containing 2% DMSO. Similarly, the stabilities of **1 - 3** and **6** monitored in chloro-containing and non-coordinating solvent dichloromethane show that they are kinetically inert, whereas, in a high nucleophilic environment, the chloride co-ligands of **1 - 3** and **6** were rapidly substituted by DMSO. In contrast, the substitution of the labile ligand of the complexes by DMSO molecules from its solution with a high chloride content was suppressed. Solution chemical reactivities of the different metal complexes were rationalized by density functional theory computations. Furthermore, the binding affinities and strengths between BSA and the respective metal complexes were monitored using fluorescence spectroscopy. Mutually, these metal complexes showed comparable capabilities of denaturing mature BSA aggregates which was established by fluorescence spectroscopy and Transmission Electron Microscopy (TEM).

The final experimental chapter entails the encapsulation of the ruthenium complexes **1 - 10** into separate organic chitosan (CS)-polyvinyl alcohol (PVA) blends and the subsequent nanofabrication of their electrospun nanofiber (ENF) conjugates, Ru-CS-PVA ENFs. Intravenous injections of insulin can be regarded as a primitive method for Diabetes Mellitus management which characteristically leads to patients developing insulin resistance while oral-administered anti-diabetic organodrugs such as Metformin have exhibited low bio-availability and typically induce gastrointestinal (GI) side-effects. Although the intravenous injections of selected metal compounds in Streptozocin (STZ)-diabetic results have delivered promising results, limited work has been done to evaluate their efficiencies during oral administration. Herein, the fabricated chitosan (CS)-polyvinyl alcohol (PVA) electrospun nanofibers (CS-PVA ENFs) of the leading insulin-enhancing ruthenium complex 1, cis-$[Ru(bipy)_2(H_4ucp)](PF_6)_2$ and its analogs: **2 – 10**. The Ru-CS-PVA ENFs

nanocomposites were characterized by using (SEM-EDX), powder X-ray diffraction, and FTIR spectroscopy. The Ru-CS-PVA ENF nanohybrids exhibited randomly oriented fiber mat morphology with mean diameters in the range of 118 - 280 nm. Metal-based drug release kinetics of **1 - 10** from the ENF polymer matrix were measured spectrophotometrically at pH 1.5 and 7.4, respectively. Electronic spectral trends and data analysis over a 24-hour data collection period reveals variable dissolution rates with first-order rate (kobs) constants ranging from 0.0146 to 2.74 μM h-1 with accompanying hyperchromism effects between 5.69 to 37.6% at a pH of 1.5 while at a pH of 7.4, kobs value limits were 0.0104 and 3.89 μM h^{-1} rendering corresponding 19.14 and 87.32% hypochromic shifts. The release kinetics data of **1 - 10** were spontaneously released into the aqueous media from the Ru-CS-PVA ENFs, with the highest and releasing rates recorded for complexes 8 and 4, espectively.

Keywords: Organoruthenium; diabetes; inhibitors; suppressants; coordination; imino, uracil, BSA uptake, amylin disaggregation, electrospun nanofibers; dissolution kinetics; glucose metabolism

Chapter 1

1.1 General background:

Type 2 diabetes mellitus (T2DM) is a condition associated with reduced sensitivity to insulin by peripheral tissues such as skeletal muscle and fat leading to poor regulation of blood sugar levels.[1] This chronic metabolic disorder is primarily caused by dietary habits involving large amounts of carbohydrates and saturated fats accompanied with limited physical activity.[2] It is also known that reactive oxygen species (ROS) can play a key role in the progression of TD2M.[3] Physiologically, T2DM can potentially culminate in a host of secondary ailments including cardiovascular diseases, kidney failure, blindness, and peripheral artery disease (PAD).[4, 5] Moreover, T2DM remains a global challenge with annual diagnosed patients in 2014 being fourfold to that of 1980.[6] Consequently, the rapid upsurge in the occurrence of this disease placed a significant burden on public health systems. In fact, empirical studies in selected developing countries have shown that diabetes is a common occurrence in low-income households but, contrastingly, survey statistics of the Republic of South Africa portrayed that T2DM is more prevalent in affluent communities.[7]

Hyperglycaemia associated with T2DM is typically managed with oral administration of anti-hyperglycaemic drugs but overdependence and unhealthy lifestyle choices, such as chronic consumption of unbalanced diets accompanied by physical inactivity, render the drugs ineffective.[8] The latter is the main reason why T2DM remains such a lethal disease with the global mortalities rapidly increasing among various age groups.[9] Oral-administered anti-diabetic drugs have also been shown to exhibit side effects and limited pharmacological profiles; therefore, their use is patient-dependent.[10] Among these is the established pharmaceutical, Metformin which is administered at relatively high concentration due to slow absorption through the gastrointestinal (GI) tract leading to limited bio-availability.[11]

Metal-based compounds have shown appreciable promise as new insulin sensitivity-enhancing compounds in the treatment of T2DM.[12] Metal compounds of vanadium, ruthenium, chromium, zinc and manganese have been widely investigated and have shown diverse mechanisms of activities.[12, 13] In particular, ruthenium coordination compounds have been investigated for their protein tyrosine phosphatase (PTP) 1B and Glycogen Synthase Kinase (GSK)-3β inhibitory activities as well as suppressants for aggregation of the human islet amyloid polypeptide (HIAPP).[14-16] Selected ruthenium complexes have also been reported to be antagonists of ryanodine receptors and dipeptidyl peptidase-4 (DPPIV) while the nitric oxide radical neutralizer AMD6221, [Ru(H_3dtpa)(Cl)] (H_3dtpa = diethylenetriaminepentaacetic acid) illustrated distinctive cardioprotective activities at the *in vitro* level.[17-19] Furthermore, the favourable attributes of the metal centre are described as a preferred synthon in metal-based drug discovery. As limited data has been acquired on the pharmacokinetics of ruthenium-based insulin-enhancing agents, the reactivity of ruthenium complexes toward biomolecules is briefly discussed in the introduction chapter. Leading candidates that show high activity, and target specificity with limited or no side effects during credible diabetic animal model studies may be incorporated into polymer matrixes to facilitate drug delivery through oral administration or transdermal patches.

1.1.2. Significance of ruthenium:

Ruthenium possesses several attractive features for novel diabetic drug discovery.[20] Firstly, ruthenium shares similar chemical reactivity to its group congener and essential metal, iron. Indicative of iron, ruthenium compounds mimics a high affinity to transferrin which is one of the core reasons for the low *in vivo* toxicity.[21] Hence, it is plausible to perceive organoruthenium compounds with labile co-ligands as pro-drugs that convert to active drugs under physiological conditions.[22] In fact, ruthenium has shown optimal coordination affinities towards various biomolecules. Furthermore, characteristic conducive uptake of ruthenium complexes by human serum albumin (HSA) elaborates their facile distribution through the bloodstream.[23] This transition metal has well developed coordination chemistry where robust metal

cores, as well as co-ligands, can be tailored to promote aqueous stability and cell permeability.[24] Tailoring of the coordination spheres can be done by use of various ligand systems that can render four coordinate tetrahedral species, five coordinate half-sandwich or six-coordinate octahedral ruthenium species. The steric factors and electronic properties of the resultant metal complexes dictate the nature of the interaction with the physiological target.[25] Ruthenium is a redox-active *d*-block element, and its coordination compounds have illustrated good interconversion for the Ru(II)/Ru(III) redox couple which often has been integral in the scavenging of Reactive Oxygen Species (ROS) as well as for *in vivo* reductions to physiologically stable and active species.[22, 26]

1.1.3 Ruthenium-based anti-diabetic drugs

Literature trends reveal that anti-diabetic ruthenium complexes induce upregulation of insulin expression by various modes. Experimental data demonstrate that anti-diabetic ruthenium-based drugs can target selected proteins or enzymes that are associated with glucose homeostasis. It is apparent that structural features, redox, and electronic properties of drug candidates have profound influences on the drug-biological target interactions.[12-26]

1.1.3.1 Human islet amyloid polypeptide (hIAPP) aggregation suppressants:

Ruthenium polypyridyl nitrogen-donor complexes have been widely explored for their fibril inhibitory capabilities of the human islet amyloid polypeptide (hIAPP), a macromolecule that is co-secreted with insulin.[27-29] Aggregation of the hIAPP is associated with the development of T2DM as this phenomenon leads to pancreatic beta-cell apoptosis which causes impaired insulin production.[30] This distinctive inhibitory action of these ruthenium complexes is initiated by their covalent attachment to intracellular bodies of the pancreatic *ß*-cells, which in turns modulates insulin production, therefore maintaining blood sugar levels. Direct binding of a ruthenium active species to distorted oligomers of hIAPP, have also encouraged disaggregation.[28]

High resolution mass spectra of hIAPP with the ruthenium chemotherapeutic drug, [ImH][$RuCl_4$(DMSO)(Im)] (NAMI A) (Im = imidazole) as well as diamagnetic ruthenium compounds: *cis*-[Ru(bipy)Cl_4] (bipy = 2, 2′-bipyridine) and *cis*-[Ru(bipy)$_2Cl_2$] illustrated that the respective metal compounds undergo hydrolysis prior to coordination towards the biomolecule, see **Figure 1.1**.[28] These monomeric compounds could attenuate the self-aggregation of the polypeptide by up to 80% when monitored *via* Thioflavin T (THT) fluorescence binding measurements. Transmission electron and atomic force micrographs concurred that the N-heterocyclic ruthenium(II) and –(III) compound could impede fibrillation. However, further clinical advancement of the aforementioned metal compounds is limited by their poor water solubility.

Isostructural *meridional* trichlororuthenium(III) compounds, *mer*-[$RuCl_3$(DMSO)(Z)] (DMSO = dimethyl sulphoxide, Z = 2, 2′-bipyridine (bipy), 1, 10-phenanthroline (phen) or dipyrido [*3,2-f:2′,3′-h*] quinoxaline (dpq)) could dissociate aggregates of hIAPP into nano-scaled particles.[31] The main driver towards the disaggregation activities was accounted to the *pi*-conjugation of the N-donor bidentate chelates which played an instrumental role in eliminating the disordering of the hIAPP polymers through π-π stacking between electron delocalized aromatic groups of the hIAPP residues and the chelates of the individual ruthenium complexes. A 3-(4,5)-dimethyl-2-thiazolyl-2,5-diphenyl-tetrazolium bromide (MTT) bio-assay deduced that these monomeric complexes increased the viability of INS-1 cells (hIAPP-induced insulinoma cell line) which advocates for their low toxicity.[28]

Amyloidosis of the hIAPP has been correlated with damaging reactive oxygen species (ROS) which are established carcinogenic inducers that can escalate cellular mutations.[32] Ruthenium(II) compounds with multidentate pyridyl nitrogen-donor chelates: *cis*-[Ru(Y)$_3$](ClO_4)$_2$, (Y = bipy or pip) (pip = 2-phenylimidazo[4,5-*f*][1,10]phenanthroline) and [Ru(phtpy)(phen)Cl]ClO_4 (phtpy = 2,6-*bis*(2-pyridyl)-4-phenylpyridine, phen = 1,10-phenanthroline) have shown to optimally scavenge ROS while interrupting β-sheet self-stacking of hIAPP, see **Figure 1.2**.[29] Indicatively, the

most lipophilic metal complex, [Ru(phtpy)(phen)Cl]ClO_4 could gradually disperse oligomers into spherical nanoparticles. Administration of this metallo-drug candidate also led to good insulinoma (INS-1) cellular preservation, exceeding the threshold cell viability (> 100%) suggesting cellular growth. Another indicator of its therapeutic activity was its converse effects on the triggering of caspase-8 and -9 enzymes which normally triggers the malicious caspase-3 enzyme, which is a promotor DNA denaturation and proteolysis.

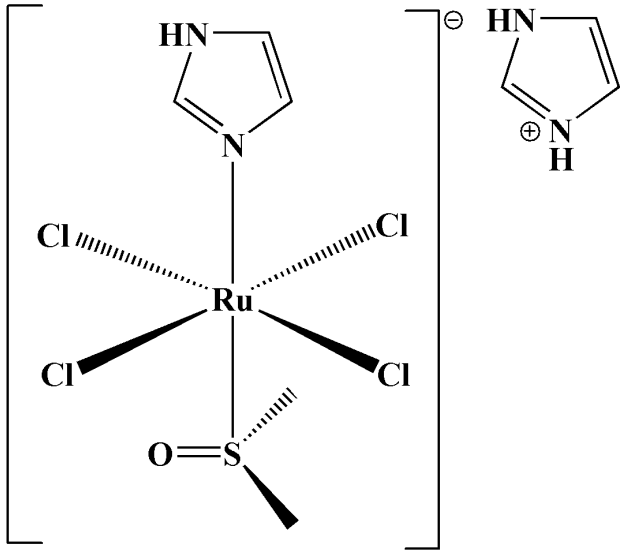

NAMI-A

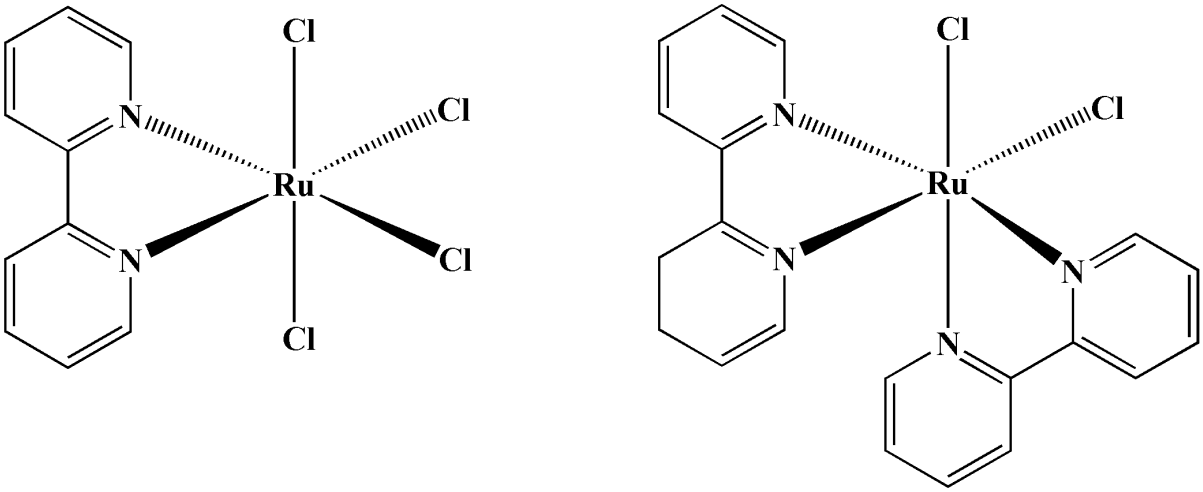

Figure 1.1: *Structures of the mononuclear N-donor ruthenium(II) and –(III) compounds.*

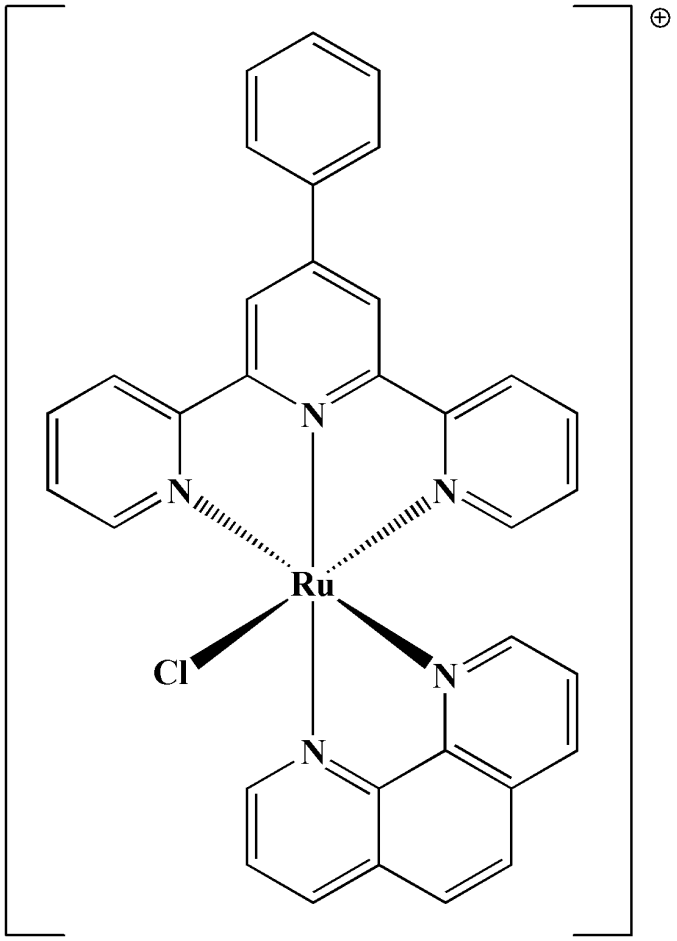

Figure 1.2: *Structure of the '3+2' ruthenium(II) complex salt, [Ru(phtpy)(phen)Cl]⁺ with bi- or tridentate polypyridyl chelators.*

To address aqueous permissibility, the design strategy evolved to incorporate binuclear ruthenium(III) complex salts: $Na_2[\{trans\text{-}RuCl_4(DMSO)\}_2(\mu\text{-}X)]$ {X = pyrazole (pyz), pymeridine (pym), 2, 2′-bipyridine (bipy)} which afforded high disintegration activities of the bio-polymers into nanoscale-sized particles and higher hIAPP inhibitory activities than their corresponding monomeric metal compounds: $Na[\{trans\text{-}RuCl_4(DMSO)\}(X)]$ see **Figure 1.3**.[27] Polypeptide binding interactions of the dinuclear metal complex salts renders redox-inactive conjugates dissipated the peak currents of their metal-based redox couples within the respective cyclic voltammograms. Moreover, co-administration of the dimeric species and hIAPP to the insulinoma cells (INS-1) resulted in concentration-dependent trends in cell viability where lower metal compounds concentrations afforded cell viabilities between 72.1%∓5.9% to 89.8%±2.1%. Interestingly, a structure-activity relationship between

the dimeric and monomeric species could be drawn, which tentatively accounted for the higher metal coordination affinities of the former to the polypeptide.

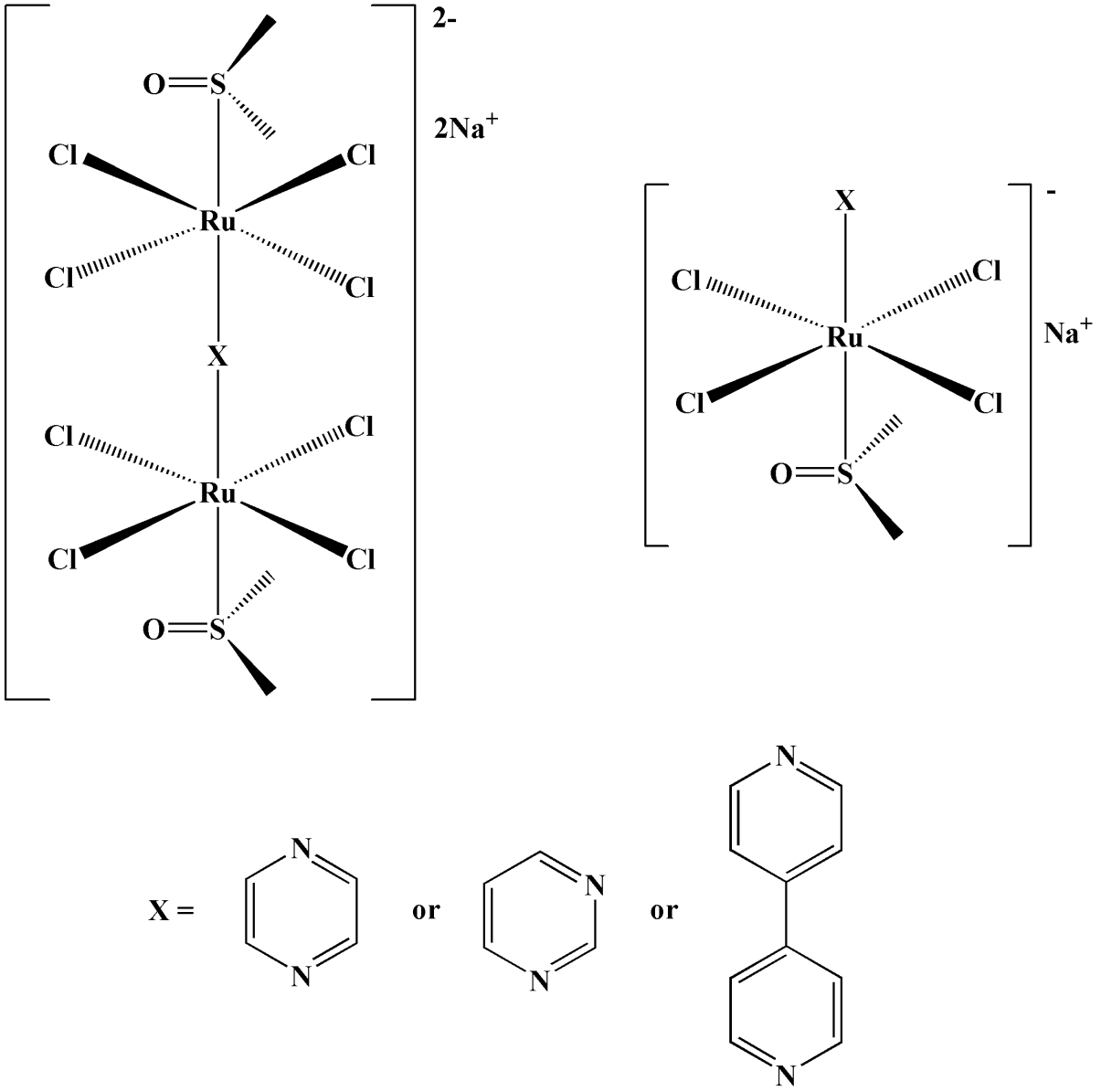

Figure 1.3: Structures of the NAMI-A prototype dinuclear organoruthenium compounds and the corresponding mononuclear metal compounds

A recent advancement includes the tagging of the *cis*-$[Ru(bipy)]^{2+}$ core with two bio-relevant methionine (Hmet) moieties to induce more physiological compatibility to the resultant metal complex, *cis*-$[Ru(bipy)(met)_2 \cdot 3H_2O]$ see **Figure 1.4**.[15] This metal complex could reduce aggregated hIAPP fibrils between 10 to 100 nm when administered in a ratio of 5:1 with respect to the polypeptide. After 3 days, the aggregates diminished totally. A concentration-dependent quenching of the THT

fluorescence was observed upon exposing the metal complex to the distorted polypeptide growths which serves as affirmation of direct covalent coordination and non-direct interactions such as hydrophobic bonding. The optimal inhibitory activity of the metal complex was attributed to its low steric strain, possible lability of deprotonated met amino acids upon coordination to the oligomers and the biological relevance of the met group which presumably culminated into INS-1 high cell viability.

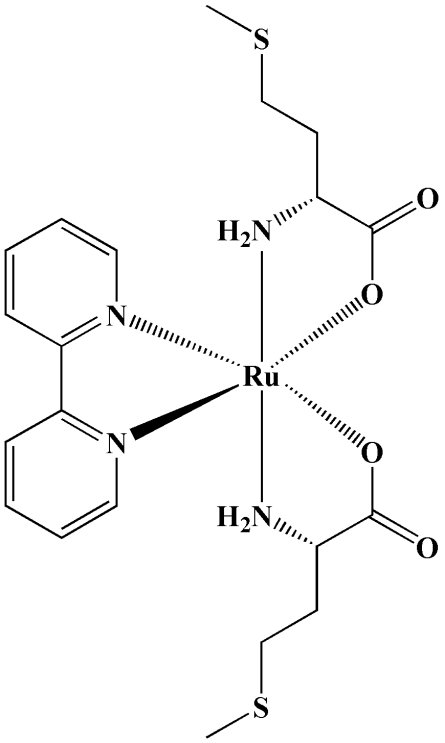

Figure 1.4: *Structure of the biologically relevant mononuclear metal complex, cis-[Ru(bipy)(met)$_2$].*

1.1.3.2 Protein Tyrosine Phosphatase (PTP) inhibitory activities

Extensive work has been conducted on the PTP inhibitory activities of vanadium compound and their pharmacokinetic traces concur with the corresponding *in vivo* studies.[33] It is well established that vanadium(IV) compounds act as glucose-lowering drugs by undergoing physiological transformation to the active drug, vanadate.[33] Vanadate shares the same charge and geometry as phosphate, which is able to inhibit the autophosphorylation of PTP 1B enzyme. Although ruthenium also possesses an analogous species, ruthenium tetraoxide, [RuO_4], this compound is highly volatile and

is formed in the presence of strong oxidants. Hence, ruthenium complexes should convey an insulin-enhancing mechanism different from that of vanadium complexes. At the onset of T2DM, the PTP-1B enzyme acts as a key negative regulator of insulin and therefore, PTP-1B is a logical target for rational drug design strategies. Ong *et al.*[34] have highlighted that designing metal chelates that can inhibit PTP-1B enzyme is notoriously challenging. In particular, PTP enzymes are structurally similar to and hence share comparable binding sites that are partially concealed. However, these researchers could design selective organometallic complexes that could selectively and sensitively target the PTP-1B enzyme. Fascinatingly, as per their drug design approach, the 2-pyridyl(benzimidazole/ imidazole) linkers could interact with the enzyme's peripheral positions, while concurrently the respective appending phenyl-difluoromethylphosphonic analogues acid (PFP) moieties could bind within the confined binding sites. Experimental studies also hint at the possibility of '*activation*' for the metal complexes *via* reactions with amino acids or displacement of a chloro co-ligand with an aqua co-ligand.[34]

Han *et al* have designed an arene ruthenium(II) complex, [(η^6-*p*-cymene)Ru(en)Cl]PF_6 (en = ethylenediamine) which has shown high coordinative affinities towards sulphur donors, see **Figure 1.5**.[16] Attesting to the distinctive chemical reactivity of this model diamagnetic ruthenium compound, its reactions with 2-mercaptobenzanilide (Hmb) afforded thiolate mono and binuclear ruthenium compounds: [(η^6-cym)Ru(en)(mb)](PF_6) and [(μ-S){(η^6-cym)Ru}$(mb)_3$](PF_6) under physiological pH of 7.4 and in an acidic media of 5.3, respectively. The use of Hmb ligand is rationalized based on the fact that its well-recognized prototypical system for investigated PTP-1B inhibitory activities in hydrogen peroxide and glutathione which catalyses the oxidation of Hmb to sulfenyl-amide derivative, 2-phenyl-1,2-benzisothiazol-3(2*H*)-one and the reverse process, respectively. The thiolate ruthenium compounds could promote slower redox interconversions between Hmb and the sulfenyl-amide analogue. The basis of the supressed redox kinetics is on the preferential coordination ability of the metal centre to the sulphur atoms of Hmb and its oxidized form. Hence, the lower PTP 1B inhibitory activity of 19 μM (IC_{50}) of [(η^6-*p*-cymene)Ru(en)Cl]PF_6

could be ascribed to the direct coordination of metal centre to the enzymatic active site, cysteine 215.

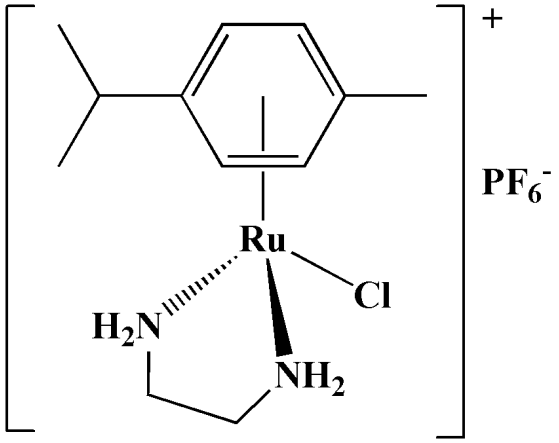

Figure1.5: *Structure of the PTP 1B organometallic inhibitor, [(η^6-p-cymene)Ru(en)Cl]PF_6.*

1.1.3.3 Ruthenium-based Glycogen Synthase Kinase 3 (GSK-3) inhibitors

A physiological target for a different class of N-heterocyclic ruthenium anti-diabetic drugs is the glycogen synthase kinase 3 (GSK-3) which is a proven initiator of T2DM.[35] GSK-3 has two different isoforms: *a* and *β* which largely differ based on the nature of their catalytic domains.[36] GSK-3 is a multifunctional protein kinase but its adverse role in T2DM has been associated with the autophosphorylation of serine or threonine moieties of Glycogen Synthase (GS) which is an important enzyme utilized for the conversion of glucose to glycogen.[37] Hence, deactivation of GSK-3 is thought to be the core mechanism of therapeutic activity of many ruthenium compounds and as such, inorganic molecules have been designed to bind within the ATP binding site of GSK-3*β*.[38]

Meggers *et al.*[39] reported the first *N*-heterocyclic ruthenium complexes which acted as protein kinase inhibitors. More specifically, these metal complexes were designed similarly with respect to steric considerations of the natural-occurring alkaloid, Staurosporine, see **Figure 1.6**. Slight alterations in the stereo-electronic properties of the bidentate *bis*-benzimidazole ligands and the metal cores rendered non-specificity in the inhibitory activities compared to the corresponding IC_{50} values of Staurosporine.

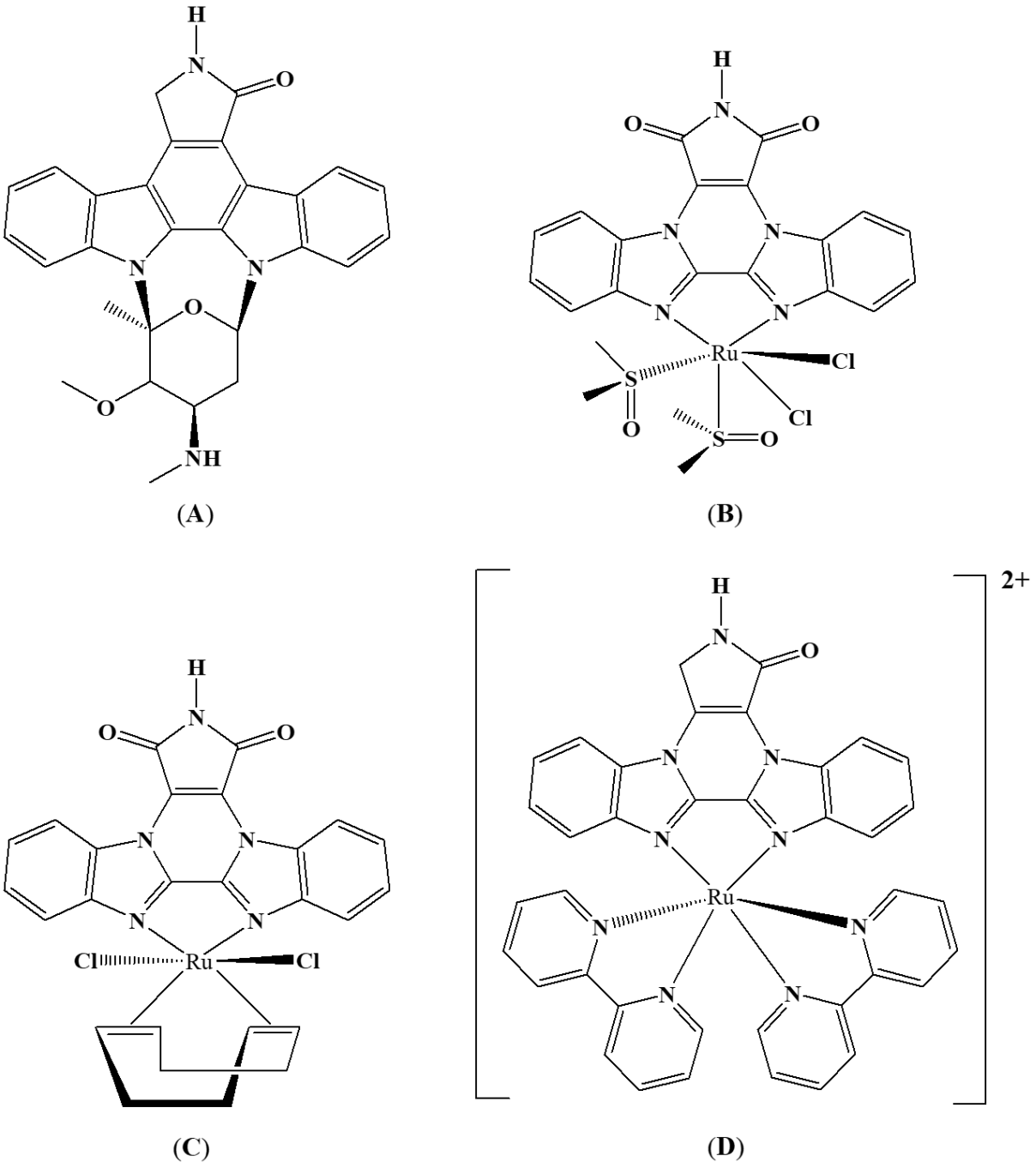

Figure 1.6: *Structures of (**A**) Staurosporine and (**B - D**) derivatives of ruthenium(II) heterocyclic compounds.*

In subsequent research studies, correlations between the structural features and enzymatic inhibitory activities were done for new organometallic compounds.[40] These metal complexes are comprised of a cyclopentadienyl ruthenium(II) core accompanied by the replacement of the *bis*-benzimidazole moiety with a pyridocarbazole ring system, or the latter substituted with different electron-donating

and withdrawing functional groups. In addition, the resultant 4-coordinate metal complexes had monodentate ligands which could be carbon monoxide, cyanide or trifluorophosphate. The inhibitory effects could be lowered to the nanomolar range compared to those of the earlier ruthenium heterocyclic derivatives shown in **Figure 1.6** with a protein kinase inhibitory activity at the micromolar level.

Evolution of the Staurosporine-mimicking design strategy led to other organometallic ruthenium salts of hexafluorophosphate with diverse protein kinase inhibitory profiles.[41] Among these metalloinhibitors is the diamagnetic ruthenium complex cation, $[(\eta^6\text{-}p\text{-cymene})RuCO(pyam)Cl]^+$ (pyam = (pyridin-2-yl)methanamine) which affords 8 nM GSK-3α inhibitory activity. In addition, the space- filling of the cationic metal complex illustrated that the combined electron densities shielding the metal centre rendering it kinetically inert.

In fact, co-crystals of the most active arene ruthenium complex with GSK-3β has been isolated.[42] This is illustrated by the organometallic compound, (R_{Ru})-NP549 occupied the ATP-binding site of GSK-3β where the inorganic-biomolecule adducts are stabilized by a combination of electrostatic, hydrophobic and hydrogen-bonding interactions, see **Figure 1.7**. These favourable intramolecular contacts induce a low IC_{50} value of $\leq$ 0.04 nM where stereoelectronic features of the metal complex facilitated the conducive binding site. Moreover, the metal complex is generally highly selective to GSK-3β and has shown distinctive changes in the anatomy of Zebrafish embryos which were synonymous with the dysregulation of GSK-3 cellular activities.[42]

Of particular interest is that the selectivity could be manipulated by increasing steric bulk around the diamagnetic ruthenium(II) centre where the Schiff base metal complexes: Λ-**FL172** and Λ-**FL411** had higher affinities towards the more spatially-available ATP-binding site of *p*21-activated kinase (PAK-1), see **Figure 1.8**.[43] The six-coordinate ruthenium species with the neutral *N*-((pyridin-2-yl)methylene)benzenamine (for Λ-**FL172**) and 2-((phenylimino)methyl)pyridin-4-

amine (for Λ-**FL411**) bidentate chelators afforded notable improved PAK-1 inhibitory activities than the racemic mixtures of DW12 and NP309. Solid-state structural analysis supported the improved inhibitory profiles towards Λ-**FL172** where the pyridylimino resides in close proximity to the glycine-rich loop. Succeeding experiments show that altering the stereoelectronic properties of the functional groups adjoined to the pyridocarbazole ring and the remaining co-ligands of octasporines led to modulation of binding susceptibilities towards other protein kinases such as PIM-1, DAPK-1 and MLCK.[44]

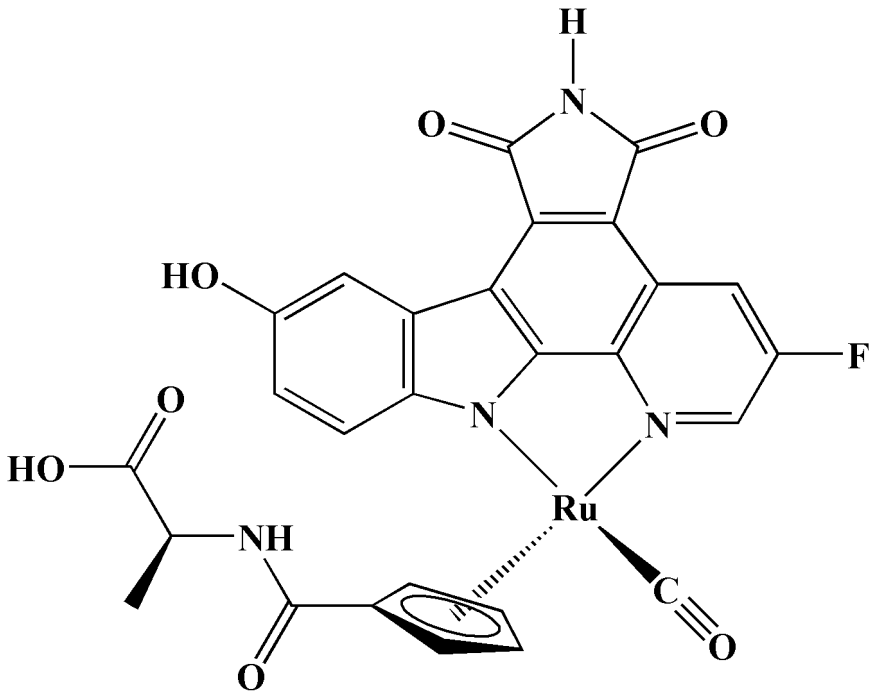

Figure 1.7: *Molecular structure of (R_{Ru})-NP549.*

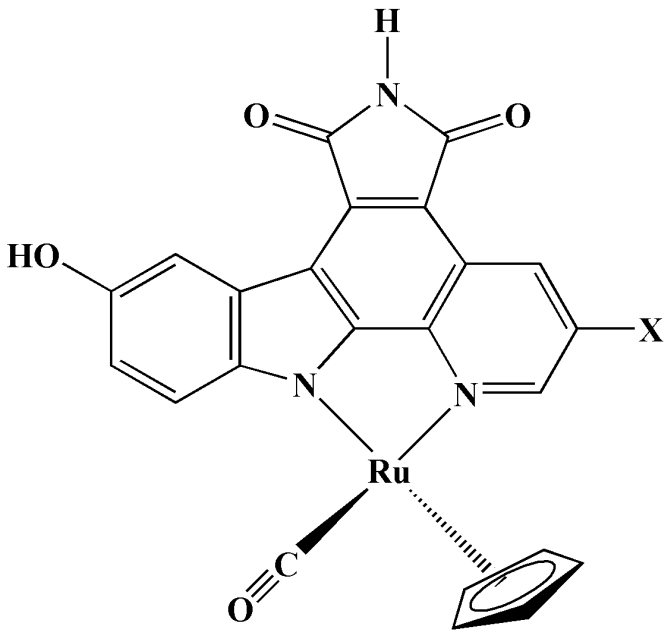

(**A**)

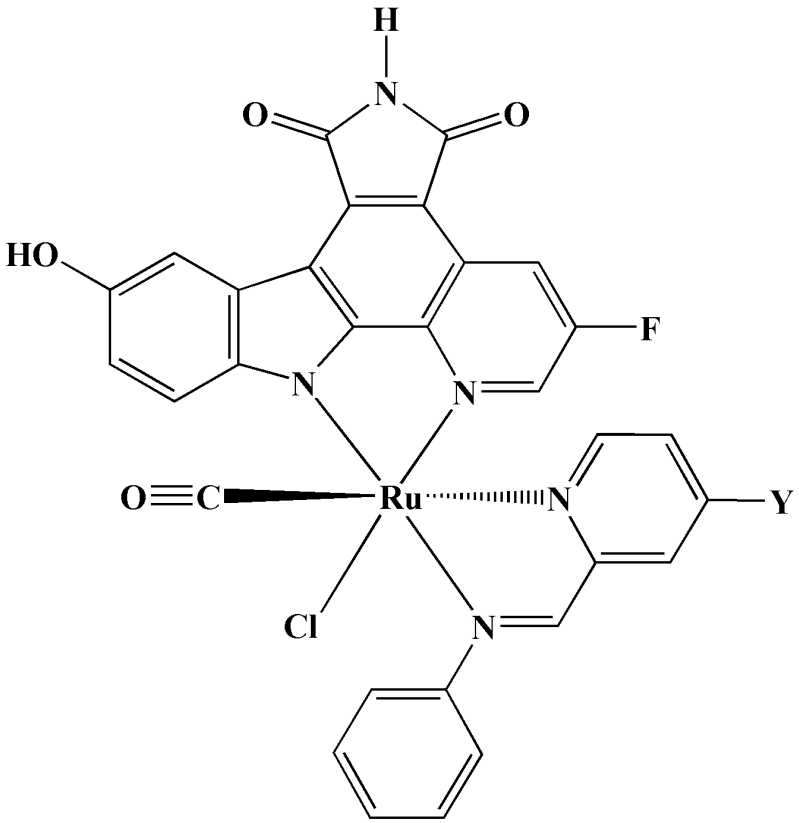

(**B**)

Figure 1.8: (**A**) *Structural analogs of 4-coordinate ruthenium complexes where X can be H (for DW12) or F (for NP309) and* (***B***) *octahedral ruthenium species where Y can be H (for Λ-**FL172**) or NH_2 (for Λ-**FL411**).*

1.1.3.4 Ruthenium compounds as cardioprotective agents in T2DM

Most recently, a ruthenium(II) complex containing an uracil-derived Schiff base, [RuCl(PPh_3)(H_3ucp)] (H_4ucp = 2,6-*bis*-((6-amino-1,3-dimethyluracilimino)methylene) pyridine) displayed no toxicity in skeletal muscle and was able to encourage glucose-lowering effects in diet-induced pre-diabetic animals, see **Figure 1.9**.[45] The hypoglycaemic activities of the ruthenium diimine complex was accompanied with reduced caloric intake and plasma ghrelin concentrations compared to the corresponding parameters measured of untreated diet-induced pre-diabetic rats. This implied that the metal complex revitalized the biological function of insulin in glucose homeostasis. Administration of the metal-based drug in conjunction with special dietary conditions resulted in improved blood circulation based on deflated mean arterial blood pressure which corresponded to the decreased heart-to-body ratio.

The mode of therapeutic activity was believed to be governed by the metal complex's potential anti-inflammatory and proven antioxidant activities.[45, 46] Also, depreciated concentrations of malondialdehyde and elevated concentrations in superoxide dismutase and glutathione peroxidase supports the ruthenium compound's radical scavenging capabilities.[47] Liver-protective effects were also observed where the histopathological micrographs of the livers for animals treated with the metallo-drug showed significantly lower lipid congestion than that of the untreated animals.[48] At this stage, the mechanism of this potential metallopharmaceutical is not clearly understood, and hence more work must be done to deduce the pharmacokinetics, aqueous stability and affinity towards key enzymes, peptides and low molecular weight biological nucleophiles.

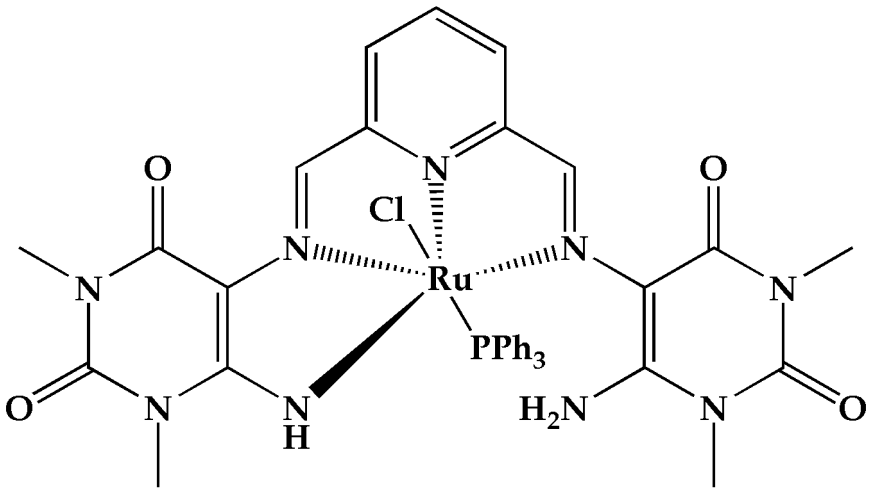

Figure 1.9: *Structure of the lead ruthenium(II) compound, [Ru(H3ucp)Cl(PPh3)] (**1**) (H4ucp = 2,6-bis-((6-amino-1,3-dimethyluracilimino)methylene)pyridine.*

The proliferation of T2DM in the human body can be deterred by metal complexes that scavenge specific ROS; resulting in cardioprotective effects.[18] One such example is the inorganic compound, AMD6221 (ruthenium[hydrogen(diethylenetrinitrilo)pentaacetato]chloride) which is a selective nitric oxide neutralizer see, **Figure 1.10**. This metal complex promoted cardiovascular regulation in STZ-induced diabetic rats where the therapeutic effects included lower mean blood pressure in metal-based drug-treated STZ-induced diabetic rats compared to the analogous parameters of the untreated rats.

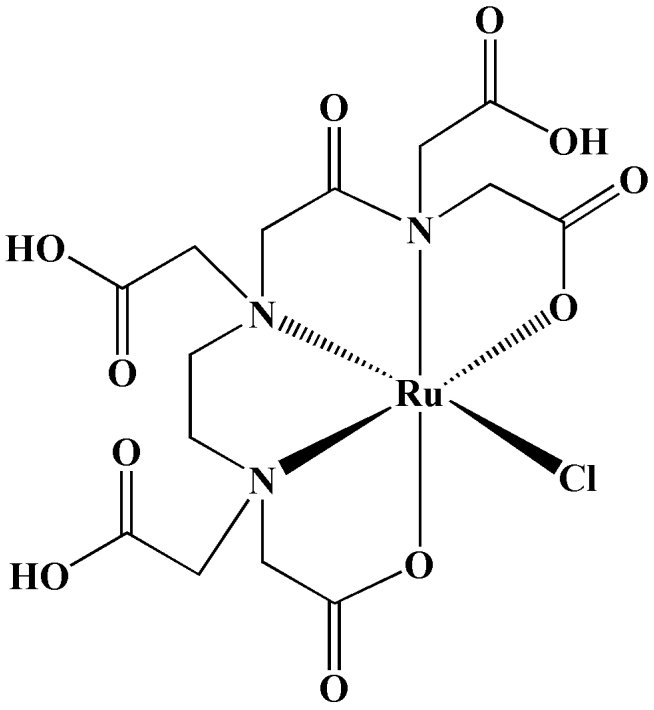

Figure 1.10: *Structure of the synthetic antioxidant, AMD6221.*

1.1.3.5 Ruthenium compounds with other mechanisms of actions

Ruthenium red has been widely used as an inorganic dye for histological bio-assays but this oxybridged trinuclear metal compound also possesses therapeutic activities for pancreatic diabetes, see **Figure 1.11**.[17] Symptomatic signs of prediabetes often manifest in the form of endothelial dysfunction followed by vascular dementia. However, co-administration of ruthenium red and an established peroxisome proliferator-activated receptor gamma (*PPAR-γ*) competitor, pioglitazone led to improved blood-sugar and Ca^{2+} levels accompanied by lower inflammation and oxidative stress of the brain blood vessels at the *in vivo* level.

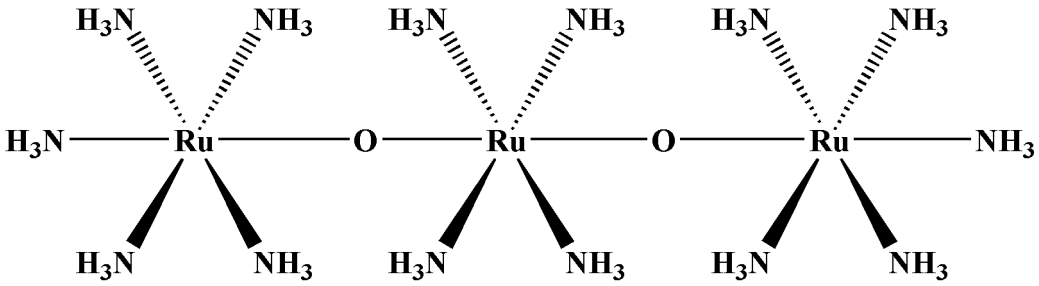

Figure 1.0.11: *Structure of the inorganic ryanodine receptor antagonist, ruthenium-red.*

The dipeptidyl peptidase-4 (DPPIV) enzyme has been implicated as one of the causes of T2DM as DPPIV impedes the action of the glucagon-like peptide-1 (GLP-1) to signal the release of key hormones that are involved in insulin release.[49] For instance, a natural extract, curcumin has shown complementary anti-inflammatory and dipeptidyl peptidase-4 (DPPIV) inhibitory activities. Advantageously, the inherent medicinal properties were significantly enhanced for their corresponding chloro-curcuminato-organoruthenium(II) complexes which suggest stronger interactions occurring between the respective metal complexes and the enzyme, see **Figure 1.12**. Molecular docking simulations suggest that the deactivation of the DPPIV enzyme is encouraged by favourable interactions with amino acids within the S1 and S2 pockets of the enzyme.

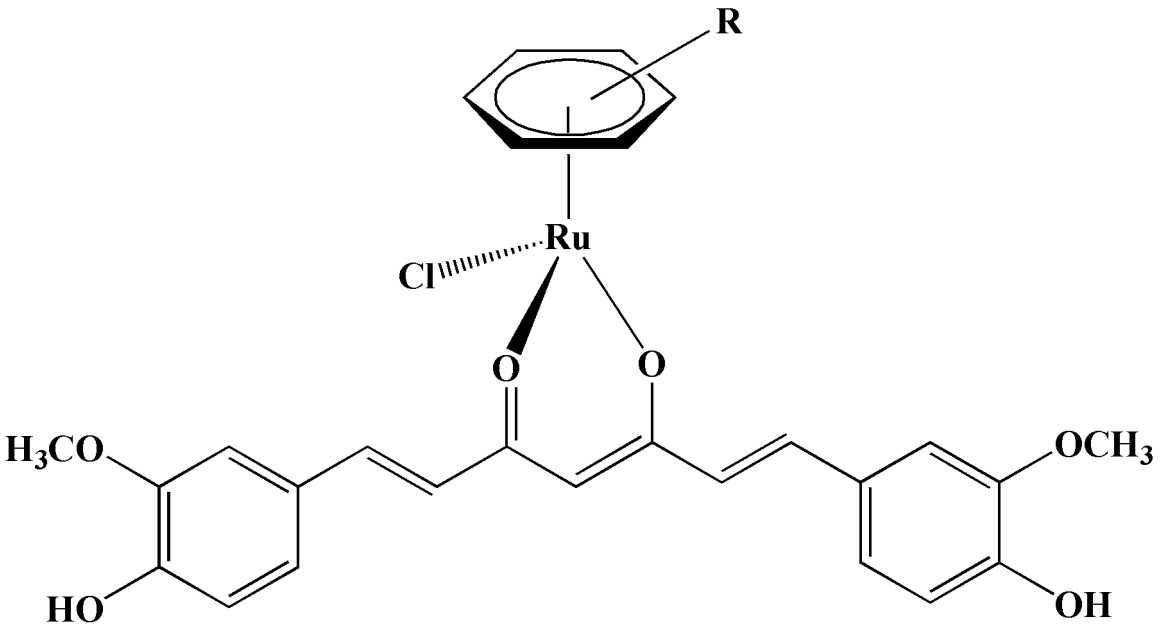

Figure 1.12: *Generic structure of the curcuminato organoruthenium(II) complexes where* ***R*** *can be p-^{i}PrC$_6$H$_4$Me, C$_6$H$_6$ or C$_6$Me$_6$.*

1.2 Future directions to improved metal-based anti-diabetic drug therapy

The use of ruthenium compounds in T2DM therapy offers tremendous potential but there is still some background work to be conducted before the vision can be realised. In particular, pharmacokinetic profiles of candidate drugs need to be generated which should afford more insight into their *in vivo* stabilities and biodistribution patterns.[50] This is especially imperative for ruthenium compounds containing labile co-ligands

that can undergo substitution with biological nucleophiles. Although various ruthenium complex systems have been shown to distinctively interact with relevant physiological targets, there is still a lack of comprehensive *in vivo* studies in diabetic rats to ascertain their capabilities to improve insulin expression and glucose homeostasis. [51] The feasibility of the animal studies is also emphasized by assessments to determine whether these metal-based compounds are benign and if not, to understand their toxicological traces for the improvement of drug design strategies. In addition, insulin injections can be regarded as primitive, tedious and uncomfortable as opposed to oral-administration and transdermal patches, which can offer more facile administration of drugs.[51] Incorporation of ruthenium anti-diabetic drugs into biodegradable polymers can promote more stability in the acidic conditions within the gastrointestinal tract while those imbedded in transdermal patches can ensure progressive drug administration.[52]

1.3 Nanomaterial-based drug delivery system (NMDDSs)

Direct injections are uncomfortable to patients, especially to younger children or infants. [53]Modern therapy needs to cater for more convenient drug administration methods which enhances bio-availabilities and that leads to higher drug efficacies. For instance, administration of drugs through oral methods, transdermal supports or depositories are currently widely in practice. Although, established pharmaceuticals have been incorporated into bulk polymer matrixes; studies focussing on the nanomaterial-based drug delivery systems are rare.[54]

In particular, NMDDS with embedded oral-administered anti-diabetic drugs must be biocompatible and display the same physiological action of insulin through various mechanisms of actions. In addition, NMDDSs must facilitate drug mobility across various biological barriers such as the acidic region of gastrointestinal (GI) tract, followed by controlled drug-release kinetics in the small intestines.[55]

More specifically, ENF is a continuous nanofiber structure created in the submicron between 100 – 1000 nm using high-voltage electrostatics on polymer solutions. These

structures are known as ENFs (electrospun nanofibers). Their capacity to encapsulate a wide range of drugs due to their surface area-to-volume ratio and their tunable porosity make them great candidates for effective and targeted delivery due to their unique properties.[56] ENFs can be easily assembled into 3-dimensional porous scaffolds that are interconnected to facilitate the delivery of drugs or other bioactive substances to targeted sites.[57,58] The ease of manipulation and formation of ENFs into various structures, of higher loading capacity, and smaller fibre diameters for better penetration are some of the advantages of nanofibers over other DDSs.[59]

1.4 Natural and synthetic polymers

There are close correlations between the applications and the composition of polymeric DDSs. Generally, polymeric DDSs can either be comprised of natural or synthetic polymers or a combination thereof, *viz.* semi-synthetic polymers, see **Figure 1.13**. Semi-synthetic polymers are created by chemically combining natural and synthetic compounds to modify the functional groups of natural polymers.[60] More specifically, Chitosan (CS) is a biomass-derived biodegradable polymer which has been widely used as a drug-delivery system.[61] CS has shown to be good blending agent to combine hydrophobic and hydrophilic synthetic polymers in different proportions to develop drug carriers.[62] In fact, the complementary structural features of CS polymer blends, such as the overall cationic charge at as well as the hydroxyl and amino groups along the CS polymer chains, render unique structure-activity relationships with respect to drug delivery applications.[61, 62]

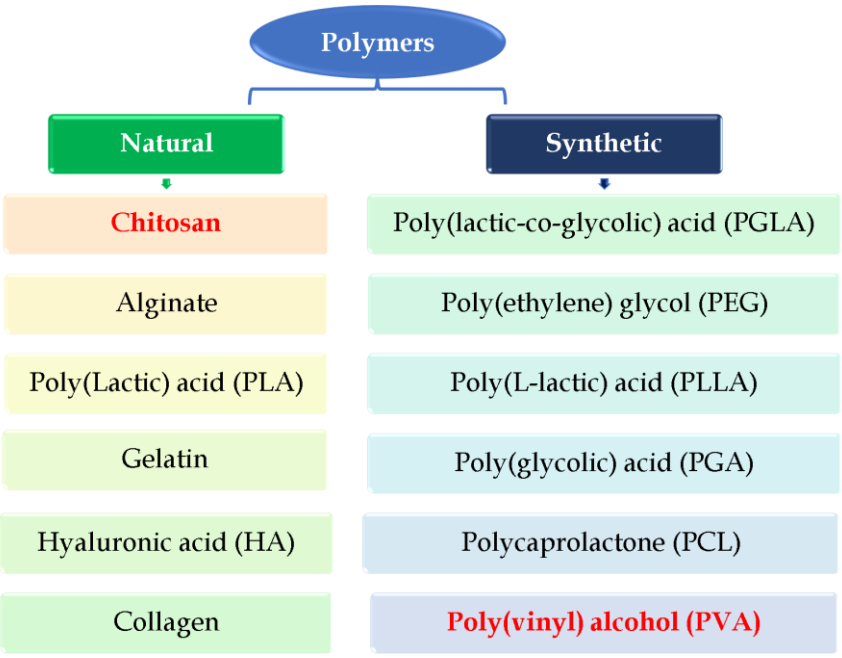

Figure 1.13: *Categories of polymers and the most used polymers in each category for DDSs. The polymers used in this research project: Poly(vinyl) alcohol (PVA) and Chitosan (CS) are highlighted in red.*[63]

Other polymeric DDSs include the combination of poly(ethylene) oxide (PEO) and polycaprolactone (PCL) used to investigate endocytosis in cells.[64] Also, targeting drugs have been incorporated into polymer capsules for diabetes treatment to reduce toxicity and associated side effects.[65] This blend of synthetic polymers has been used as transdermal and oral DDSs for applications such as tissue engineering and wound dressing materials.[63] The most important feature of polymer blending apart from mechanical robustness and reduced material cost it is the ability to negate toxicity in *in vivo* application. For example, commonly used synthetic/natural polymers such as PLGA, PCL and PLA have disadvantages such as slow degradation and biocompatibility issues due to the formation of acidic and toxic degradation products.[66,67]

1.5 Electrospun nanofibers in oral DDSs

There has been upsurge in the design of electrospun nanofibers (ENFs) for drug delivery applications.[68] ENFs have numerous benefits over bulk polymers and their blends such as the higher surface area-to-volume ratio affording superior drug load capacities as slower drug diffusion rates.[69] The most promising advantage of ENFs lies in the nanofabrication technique, electrospinning used to attain these polymeric fibres with diameters at the nanoscale. This top-down nanofabrication method is highly versatile where the solution, instrumental and ambient parameters can be conveniently to adjust the surface morphology, diameter and mechanical properties of the ENFs can be adjusted. Subsequently, these structural features and polymer elasticity have a significant influence on the dissolution rates of drug-ENF nanocomposites.[70] Pharmaceuticals can also be imbedded *via* an *in situ* electrospinning where the bulk polymer/s and drug are pre-mixed prior to electrospinning. Alternatively, a post functional strategy can be employed which involves the covalently linking of the drug to the pre-fabricated ENFs.[71, 68]

Typical illustrations of ENFs as NMDDSs rapid-dissolving polyvinyl alcohol (PVA) and Soluplus (SP)-based nanofiber mat loaded with Angelica Gigas Nakai (AGN) extract. The rendered ENF nanoconjugate, AGN-PVA-SP featured a mean diameter of 170 nm and an entrapment efficiency of over 80%. Structural and dissolution experiments demonstrated that the network structure of the AGN extract has been altered after nanoconjugation from a crystalline state to an amorphous state which enhanced the aqueous solubility.[72]

Similarly, an FDA-approved anti-diabetic drug, Repaglinide (Rg) with limited solubility, has been encapsulated into PVA-PVP ENFs for oral administration. The optimized polymeric nanohybrid has a smooth surface morphology with substantially wide average diameter of 600 – 800 nm. It is hypothesized that the aforementioned physical properties resulted in high load capacity where 90% of the drug was released

from the ENF matrix in 10 minutes. Consequently, high RG bio-availability was attained during anti-diabetic *in vivo* experiments when the RG-PVA-PVP ENFs were administered to Streptozotocin (STZ) diabetic rats which culminated into considerable reduction in the rise of blood glucose levels between the defined data collection interval of 30 and 120 minutes, when compared to both the free drug-administered and the control groups.[73]

Interestingly, the RG dosage kinetics could be retarded through its incorporation into a PVA core while polymethyl methacrylate (PMMA) was used as the coating agent. *In vitro* experiments revealed favourable prolonged drug release rate from the PVA-PMMA polymeric drug carrier. In order to ascertain the mechanism of Repaglinide release, experimental *in vitro* release data were fitted to various models. It was found that the RG diffusion and polymeric drug carrier erosion are the primary modes of drug release which followed a kinetic zero order trace. The biochemical and pathological analyses of albino rats administered with the nanocomposite showed no appreciable change. Thus, the dissolution rates of drugs can be tailored by imbedding them into core-shell but the nature and the ratios of the polymers is critical during co-*axial* electrospinning and the nature of the constituent polymers.[74]

Moreover, gradient drug release profiles can be induced by the nanoconjugation of drugs into ENFs where the initial release at higher concentrations was immediate followed by dissipating drug exposures overtime. This administration method is especially applicable for patients with substantial irregularities in their blood-glucose levels and hence, this class of ENF-drug combinations can encourage a sustained drug concentration in the bloodstream. This therapeutic effect is demonstrated by the GLZ-PVA-PGLA ENFs containing the second-generation sulfonylurea, Gliclazide (GLZ) where the optimized formulation adopted a biphasic drug release profile with rapid initial and sustained release of GLZ.[75]

The feasibility of ENF-drug combinations as an oral-administered therapy is further rationalized by insulin-containing PVA–NaAlg nanofiber patch which was applied

below the tongue of the diabetic rat. Interestingly, the drug-loaded PVA–NaAlg nanofiber patch possesses the strongest adhesion than the PVA polymer and the PVA–NaAlg ENFs only, according to the results of the mucoadhesive strength test. The drug was released gradually and under control in the in vitro drug release activity, showing significant differences from the commercial formulation and confirming that insulin was administered in its active state. The first burst release of insulin is necessary for the intended therapeutic effect where first order kinetics controlled the release of insulin. Additionally, there is sufficient evidence to suggest that the composite ENFs may be well-suited for sublingual insulin delivery, since about 99% of the experimental formulation and encapsulation efficacy supported this theory.[76]

The drive behind the use of PVA-CS ENFs is their inherent favourable attributes gathered from their parent polymers. For example, the amino groups in the C2 position of the Chitosan backbone change chemically in response to pH fluctuations which could be a structural tool for facilitating pH-dependent drug release.[77] It is anticipated that the conducive stereo-electronic properties of CS will induce prospective strong intermolecular interactions and coordinative bonding with the ruthenium complexes.[78] However, due to the strong molecular interactions, it can be challenging to obtain ultra-thin and defect-free CS nanofibers by electrospinning in acidic media. To circumvent the aforementioned phenomenon, pre-mixing CS with polyvinyl alcohol (PVA) leads to a bulk polymer blend with a critical charge density which lead to the formation of ENFs with smaller average diameter and less defects.[79] Indicative to CS, PVA is water soluble and biodegradable which makes PVA-CS ENFs an attractive option for DDS development. The high affinities of the constituent polymers are portrayed by their complementary hydrogen-bonding interactions in **Figure 1.14**. High crystallinity of the polymer has also been shown to reduce the drug release rate because the crystalline regions contain less water than the amorphous regions.[80] Therefore, the semi-crystalline molecular structure of PVA can be used to dilute CS and reduce the crystallinity of the CS network**.**

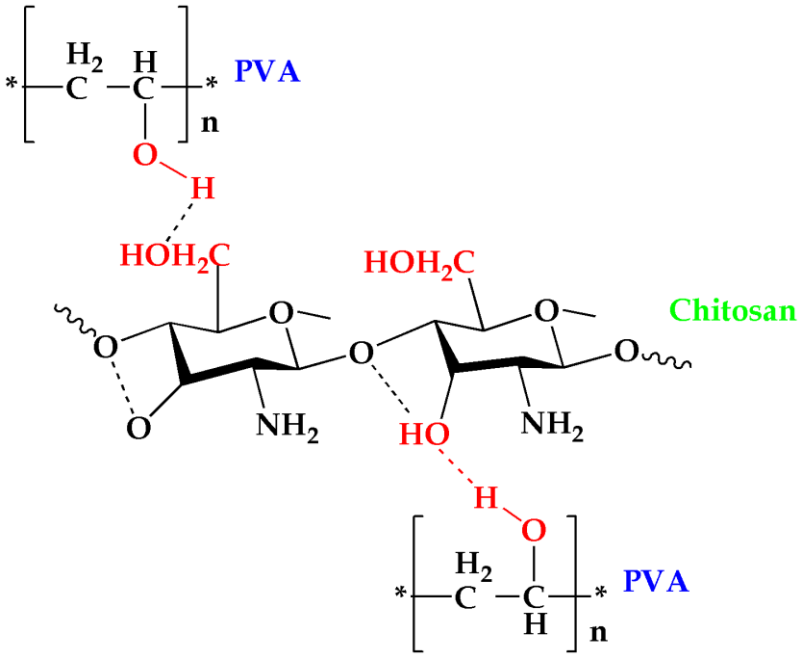

Figure 1.14 : *A perspective view of the possible intermolecular and intramolecular hydrogen interactions occurring between PVA and CS polymer units.*[73]

Evidentially, it has been shown that the electrospinning of a PVA and CS mixture in a 70:30 volume-to-volume ratio led to the formation of homogenous and bead-free ENFs. The average fibre diameter was 172.7 ± 56.8 nm, and the swelling ratio was 229%.[81] The MTT assay demonstrated well-attached cells with an increasing rate of proliferation and no signs of cytotoxicity in the cultured adipose tissue mesenchymal stem cells in the presence of ENFs in an *in vitro* cell culture study.

1.6 Rationale of the research study

Given the facts that our leading ruthenium-based anti-diabetic drug, $[Ru^{II}(H_3ucp)Cl(PPh_3)]$ displayed high anti-diabetic effects in STZ-diabetic rats with no observable harmful ailments, the next phase in this multidisciplinary bioinorganic research project was to gain an understanding of the mechanism of anti-diabetic activity. The plausibility of this research study is extensively rationalized within the previous section where the relevance of ruthenium in bioinorganic chemistry is described followed by a brief overview of the current status of ruthenium-based insulin-enhancing agents. The design of NMDDSs for the oral administration of drugs and as motivated, the incorporation of this class of anti-diabetic metal compounds into biodegradable ENFs could lead to more convenient and effective administration compared to current established therapies. The strategy of the research study described the specific research aims and objectives listed below:

1.6.1 Research aims:

1. The anti-diabetic metal-based drug, $[Ru^{II}(H_3ucp)Cl(PPh_3)]$ was resynthesized and the purity confirmation was conducted.
2. Derivatives of the aforementioned metal complex were synthesized and comprehensively characterized.
3. The aqueous stabilities of the metal complexes were conducted in aqueous media
4. Stabilities of the metal complexes were assessed in a pH range of 1.5 and 7.4.
5. BSA Serum Albumin (BSA) binding affinities of the respective metal complexes were evaluated.
6. The inhibitory activities of the ruthenium complexes were tested towards hIAPP amyloid fibrils or BSA amyloid fibrils.
7. The radical scavenging capabilities of the ruthenium complexes were explored.
8. The *in vitro* anti-diabetic studies of the selected novel metal complexes were determined.
9. The metal complexes were imbedded into the matrix of bio-degradable polymers blends *via* electrospinning and the nanofabricated ENFs were characterized.

10. The dissolution behaviours of the resultant electrospun nanofibers were interrogated in aqueous media.

1.6.2 Specific research objectives

1. The lead candidate drug was re-synthesized and its structure confirmed by NMR and IR spectroscopy, TOF-Mass spectrometry as well as Elemental Analysis.
2. Similar experimental procedures were employed in the synthesis of the analogues. The new ligands and metal complexes were characterized by various physicochemical techniques.
3. The aqueous stabilities of the metal complexes were monitored (2% PBS: 98% DMSO, anhydrous DCM, anhydrous DMSO and in excess LiCl: DMSO) by temperature-controlled UV-Vis spectrophotometry.
4. Indicatively, the stabilities of the metal complexes were tested in a pH range of 1.5 and 7.4, which were monitored by UV-Vis spectrophotometry. During these experiments, the pH values of the standardized metal complex solutions (in DMSO: UPW) were altered by standardized solutions of HCl and NaOH, respectively.
5. BSA and competitive (warfarin and ibuprofen) binding affinities of the metal complexes were examined by biomolecular titrations monitored by Photoluminescence.
6. The hIAPP and BSA amyloid fibril inhibitory activities of the metal complexes were investigated Photoluminescence and TEM.
7. AutoDock was utilized to study the rigid molecular docking between selected metal complexes and the receptor amylin.
8. The *in vitro* cell viability and glucose metabolism of selected metal complexes were investigated on Chang liver cell lines using MTT assay and recorded by microplate spectrophotometer.
9. Electrospun nanofibers were nanofabricated by optimizing their blend ratio using solutions of biodegradable polymers (PVA and CS), 0.09% (9 mg) of

respective metal compounds were imbedded in ENFs and characterized by SEM-EDX, FTIR.

10. The dissolution kinetics of the resultant metal complex-ENF composites was monitored by temperature-controlled UV-Vis spectrophotometry at pH 1.5 and 7.4 for 24 h, respectively.

1.7 References

(1) Kerru, N.; Singh-Pillay, A.; Awolade, P.; Singh, P. Current anti-diabetic agents and their molecular targets: A review. *European Journal of Medicinal Chemistry* **2018**, *152*, 436-488.

(2) Paudel, S.; Tran, T.; Owen, A. J.; Smith, B. J. The contribution of physical inactivity and socioeconomic factors to type 2 diabetes in Nepal: A structural equation modelling analysis. *Nutrition, Metabolism and Cardiovascular Diseases* **2020**. Rice Bradley, B. H. Dietary Fat and Risk for Type 2 Diabetes: a Review of Recent Research. *Curr Nutr Rep* **2018**, *7* (4), 214-226.

(3) Wei, W.; Liu, Q.; Tan, Y.; Liu, L.; Li, X.; Cai, L. Oxidative Stress, Diabetes, and Diabetic Complications. *Hemoglobin* **2009**, *33* (5), 370-377.

(4) Bishu, K. G.; Jenkins, C.; Yebyo, H. G.; Atsbha, M.; Wubayehu, T.; Gebregziabher, M. Diabetes in Ethiopia: A systematic review of prevalence, risk factors, complications, and cost. *Obesity Medicine* **2019**, *15*, 100132.

(5) Ceriello, A.; deValk, H. W.; Guerci, B.; Haak, T.; Owens, D.; Canobbio, M.; Fritzen, K.; Stautner, C.; Schnell, O. The burden of type 2 diabetes in Europe: Current and future aspects of insulin treatment from patient and healthcare spending perspectives. *Diabetes Research and Clinical Practice* **2020**, *161*, 108053.

(6) Organization, W. H. *Diabetes*. 2020. https://www.who.int/news-room/fact-sheets/detail/diabetes (accessed 2020 22.06/2020).

(7) Suwannaphant, K.; Laohasiriwong, W.; Puttanapong, N.; Saengsuwan, J.; Phajan, T. Association between Socioeconomic Status and Diabetes Mellitus: The National Socioeconomics Survey, 2010 and 2012. *J Clin Diagn Res* **2017**, *11* (7), LC18-LC22. Ferdi, N. E. H.; Abla, K.; Chenchouni, H. Effect of Socioeconomic Factors and Family History on the Incidence of Diabetes in an Adult Diabetic Population from Algeria. *Iran J Public Health* **2016**, *45* (12), 1636-1644. PubMed. Mutyambizi, C.; Booysen, F.; Stokes, A.; Pavlova, M.; Groot, W. Lifestyle and socio-economic inequalities in diabetes prevalence in South Africa: A decomposition analysis. *PLoS One* **2019**, *14* (1), e0211208-e0211208.

(8) Davidsson, L.; Alkhabbaz, E.; Vijayan, V.; Alhubail, A.; Shaltout, A.; Alkandari, H. Intermediate hyperglycaemia, insulin resistance and metabolic syndrome among obese Arab children (12–17 years old) in Kuwait. *Primary Care Diabetes* **2020**.

(9) Mendez, C. E.; Walker, R. J.; Eiler, C. R.; Mishriky, B. M.; Egede, L. E. Insulin therapy in patients with type 2 diabetes and high insulin resistance is associated with increased risk of complications and mortality. *Postgraduate Medicine* **2019**, *131* (6), 376-382.2019.1643635. Mizokami-Stout, K.; Cree-Green, M.; Nadeau, K. J. Insulin resistance in type 2 diabetic youth. *Curr Opin Endocrinol Diabetes Obes* **2012**, *19* (4), 255-262.

(10) Peng, M.; Yang, X. Controlling diabetes by chromium complexes: The role of the ligands. *Journal of Inorganic Biochemistry* **2015**, *146*, 97-103.

(11) Graham, G. G.; Punt, J.; Arora, M.; Day, R. O.; Doogue, M. P.; Duong, J.; Furlong, T. J.; Greenfield, J. R.; Greenup, L. C.; Kirkpatrick, C. M.; Ray, J.E,; Timmins, P.; Kenneth M Williams, K.M. Clinical Pharmacokinetics of Metformin. *Clinical Pharmacokinetics* **2011**, *50* (2), 81-98.

(12) Meyer, J. A.; Spence, D. M. A perspective on the role of metals in diabetes: past findings and possible future directions. *Metallomics* **2009**, *1* (1), 32-41.

(13) Treviño, S.; Diaz, A. Vanadium and insulin: Partners in metabolic regulation. *Journal of Inorganic Biochemistry* **2020**, *208*, 111094, 1-19. Alghrably, M.; Czaban, I.; Jaremko, Ł.; Jaremko, M. Interaction of amylin species with transition metals and membranes. *Journal of Inorganic Biochemistry* **2019**, *191*, 69-76. Levina, A.; Lay, P. A. Metal-based anti-diabetic drugs: advances and challenges. *Dalton Transactions* **2011**, *40* (44), 11675-11686.

(14) Meggers, E.; Atilla-Gokcumen, G. E.; Bregman, H.; Maksimoska, J.; Mulcahy, S. P.; Pagano, N.; Williams, D. S. Exploring Chemical Space with Organometallics: Ruthenium Complexes as Protein Kinase Inhibitors. *Synlett* **2007**, *2007* (08), 1177-1189.

(15) Gong, G.; Xu, J.; Huang, X.; Du, W. Influence of methionine–ruthenium complex on the fibril formation of human islet amyloid polypeptide. *JBIC Journal of Biological Inorganic Chemistry* **2019**, *24* (2), 179-189.

(16) Han, Y.; Luo, Q.; Hao, X.; Li, X.; Wang, F.; Hu, W.; Wu, K.; Lü, S.; Sadler, P. J. Reactions of an organoruthenium anticancer complex with 2-mercaptobenzanilide a model for the active-site cysteine of protein tyrosine phosphatase 1B. *Dalton Transactions* **2011**, *40* (43), 11519-11529.

(17) Jain, S.; Sharma, B. Effect of ruthenium red, a ryanodine receptor antagonist in experimental diabetes induced vascular endothelial dysfunction and associated dementia in rats. *Physiology & Behavior* **2016**, *164*, 140-150.

(18) Hutchings, S. R.; Song, D.; Fricker, S. P.; Pang, C. C. Y. The ruthenium-based nitric oxide scavenger, AMD6221, augments cardiovascular responsiveness to noradrenaline in rats with streptozotocin-induced diabetes. *European Journal of Pharmacology* **2005**, *528* (1), 132-136.

(19) Antonyan, A.; De, A.; Vitali, L. A.; Pettinari, R.; Marchetti, F.; Gigliobianco, M. R.; Pettinari, C.; Camaioni, E.; Lupidi, G. Evaluation of (arene)Ru(II) complexes of curcumin as inhibitors of dipeptidyl peptidase IV. *Biochimie* **2014**, *99*, 146-152.

(20) Dömötör, O.; Enyedy, É. A. Binding mechanisms of half-sandwich Rh(III) and Ru(II) arene complexes on human serum albumin: a comparative study. *JBIC Journal of Biological Inorganic Chemistry* **2019**, *24* (5), 703-719.

(21) Muneebah, A.; Muhammad, H.; Christian, G. H. Ruthenium Anticancer Agents—From Cisplatin Analogues to Rational Drug Design. In *Encyclopedia of Inorganic and Bioinorganic Chemistry*, Wiley, 2017; pp 1-21.

(22) Alessio, E.; Messori, L. NAMI-A and KP1019/1339, Two Iconic Ruthenium Anticancer Drug Candidates Face-to-Face: A Case Story in Medicinal Inorganic Chemistry. *Molecules* **2019**, *24* (10).

(23) Merlino, A. Interactions between proteins and Ru compounds of medicinal interest: A structural perspective. *Coordination Chemistry Reviews* **2016**, *326*, 111-134.

(24) Coverdale, J. P. C.; Laroiya-McCarron, T.; Romero-Canelón, I. Designing Ruthenium Anticancer Drugs: What Have We Learnt from the Key Drug Candidates? *Inorganics* **2019**, *7* (3).

(25) Zeng, L.; Gupta, P.; Chen, Y.; Wang, E.; Ji, L.; Chao, H.; Chen, Z.-S. The development of anticancer ruthenium(II) complexes: from single molecule compounds to nanomaterials. *Chemical Society Reviews* **2017**, *46* (19), 5771-5804.

(26) Maikoo, S.; Chakraborty, A.; Vukea, N.; Dingle, L. M. K.; Samson, W. J.; de la Mare, J.-A.; Edkins, A. L.; Booysen, I. N. Ruthenium complexes with mono- or bis-heterocyclic chelates: DNA/BSA binding, antioxidant and anticancer studies. *Journal of Biomolecular Structure and Dynamics* **2020**, 1-12. Brabec, V.; Kasparkova, J. Ruthenium coordination compounds of biological and biomedical significance. DNA binding agents. *Coordination Chemistry Reviews* **2018**, *376*, 75-94.

(27) Gong, G.; Wang, W.; Du, W. Binuclear ruthenium complexes inhibit the fibril formation of human islet amyloid polypeptide. *RSC Advances* **2017**, *7* (30), 18512-18522.

(28) He, L.; Wang, X.; Zhao, C.; Wang, H.; Du, W. Ruthenium complexes as novel inhibitors of human islet amyloid polypeptide fibril formation. *Metallomics* **2013**, *5* (12), 1599-1603.

(29) Ma, L.; Fu, Y.; Yu, L.; Li, X.; Zheng, W.; Chen, T. Ruthenium complexes as inhibitors of human islet amyloid polypeptide aggregation, an effect that prevents beta cell apoptosis. *RSC Advances* **2015**, *5* (23), 17405-17412.

(30) Brender, J. R.; Hartman, K.; Nanga, R. P. R.; Popovych, N.; de la Salud Bea, R.; Vivekanandan, S.; Marsh, E. N. G.; Ramamoorthy, A. Role of Zinc in Human Islet Amyloid

Polypeptide Aggregation. *Journal of the American Chemical Society* **2010**, *132* (26), 8973-8983.

(31) Zhu, D.; Gong, G.; Wang, W.; Du, W. Disaggregation of human islet amyloid polypeptide fibril formation by ruthenium polypyridyl complexes. *Journal of Inorganic Biochemistry* **2017**, *170*, 109-116.

(32) Atrián-Blasco, E.; Gonzalez, P.; Santoro, A.; Alies, B.; Faller, P.; Hureau, C. Cu and Zn coordination to amyloid peptides: From fascinating chemistry to debated pathological relevance. *Coordination Chemistry Reviews* **2018**, *371*, 38-55.

(33) Irving, E.; Stoker, A. W. Vanadium Compounds as PTP Inhibitors. *Molecules* **2017**, *22* (12), 1-10.

(34) Ong, J. X.; Yap, C. W.; Ang, W. H. Rational Design of Selective Organoruthenium Inhibitors of Protein Tyrosine Phosphatase 1B. *Inorganic Chemistry* **2012**, *51* (22), 12483-12492.

(35) Sacco, F.; Seelig, A.; Humphrey, S. J.; Krahmer, N.; Volta, F.; Reggio, A.; Marchetti, P.; Gerdes, J.; Mann, M. Phosphoproteomics Reveals the GSK3-PDX1 Axis as a Key Pathogenic Signaling Node in Diabetic Islets. *Cell Metabolism* **2019**, *29* (6), 1422-1432.e1423.

(36) Pandey, M. K.; DeGrado, T. R. Glycogen Synthase Kinase-3 (GSK-3)-Targeted Therapy and Imaging. *Theranostics* **2016**, *6* (4), 571-593.

(37) Lee, J.; Kim, M.-S. The role of GSK3 in glucose homeostasis and the development of insulin resistance. *Diabetes Research and Clinical Practice* **2007**, *77* (3, Supplement), S49-S57.

(38) Kramer, T.; Schmidt, B.; Lo Monte, F. Small-Molecule Inhibitors of GSK-3: Structural Insights and Their Application to Alzheimer's Disease Models. *International Journal of Alzheimeris Disease* **2012**, *2012*, 381029, 1-32.

(39) Zhang, L.; Carroll, P.; Meggers, E. Ruthenium Complexes as Protein Kinase Inhibitors. *Organic Letters* **2004**, *6* (4), 521-523.

(40) Atilla-Gokcumen, G. E.; Williams, D. S.; Bregman, H.; Pagano, N.; Meggers, E. Organometallic Compounds with Biological Activity: A Very Selective and Highly Potent Cellular Inhibitor for Glycogen Synthase Kinase 3. *ChemBioChem* **2006**, *7* (9), 1443-1450. Bregman, H.; Meggers, E. Ruthenium Half-Sandwich Complexes as Protein Kinase Inhibitors:

An N-Succinimidyl Ester for Rapid Derivatizations of the Cyclopentadienyl Moiety. *Organic Letters* **2006**, *8* (24), 5465-5468.

(41) Bregman, H.; Carroll, P. J.; Meggers, E. Rapid Access to Unexplored Chemical Space by Ligand Scanning around a Ruthenium Center: Discovery of Potent and Selective Protein Kinase Inhibitors. *Journal of the American Chemical Society* **2006**, *128* (3), 877-884.

(42) Atilla-Gokcumen, G. E.; Pagano, N.; Streu, C.; Maksimoska, J.; Filippakopoulos, P.; Knapp, S.; Meggers, E. Extremely Tight Binding of a Ruthenium Complex to Glycogen Synthase Kinase 3. *ChemBioChem* **2008**, *9* (18), 2933-2936. Atilla-Gokcumen, G. E.; Di Costanzo, L.; Meggers, E. Structure of anticancer ruthenium half-sandwich complex bound to glycogen synthase kinase 3β. *Journal of Biological Inorganic Chemistry* **2011**, *16* (1), 45-50.

(43) Maksimoska, J.; Feng, L.; Harms, K.; Yi, C.; Kissil, J.; Marmorstein, R.; Meggers, E. Targeting large kinase active site with rigid, bulky octahedral ruthenium complexes. *Journal of the American Chemical Society* **2008**, *130* (47), 15764-15765.

(44) Feng, L.; Geisselbrecht, Y.; Blanck, S.; Wilbuer, A.; Atilla-Gokcumen, G. E.; Filippakopoulos, P.; Kräling, K.; Celik, M. A.; Harms, K.; Maksimoska, J.; Marmorstein, R.; Frenking, G.; Knapp, S.; Lars-Oliver, E.; Meggers, E. Structurally Sophisticated Octahedral Metal Complexes as Highly Selective Protein Kinase Inhibitors. *Journal of the American Chemical Society* **2011**, *133* (15), 5976–5986.

(45) Mabuza, L. P.; Gamede, M. W.; Maikoo, S.; Booysen, I. N.; Ngubane, P. S.; Khathi, A. Effects of a Ruthenium Schiff Base Complex on Glucose Homeostasis in Diet-Induced Pre-Diabetic Rats. *Molecules* **2018**, *23* (7).

(46) Maikoo, S.; Dingle, L. M. K.; Chakraborty, A.; Xulu, B.; Edkins, A. L.; Booysen, I. N. Synthetic, characterization and cytotoxic studies of ruthenium complexes with Schiff bases encompassing biologically relevant moieties. *Polyhedron* **2020**, *184*, 114569.

(47) Mabuza, L. P.; Gamede, M. W.; Maikoo, S.; Booysen, I. N.; Ngubane, P. S.; Khathi, A. Cardioprotective effects of a ruthenium(II) Schiff base complex in diet-induced prediabetic rats. *Diabetes Metab Syndr Obes* **2019**, *12*, 217-223.

(48) Mabuza, L. P.; Gamede, M. W.; Maikoo, S.; Booysen, I. N.; Nguban, P. S.; Khathi, A. Hepatoprotective Effects of a Ruthenium(II) Schiff Base Complex in Rats with Diet-Induced Prediabetes. *Current Therapeutic Research* **2019**, *91*, 66-72.

(49) Li, N.; Wang, L.-J.; Jiang, B.; Li, X.-q.; Guo, C.-l.; Guo, S.-j.; Shi, D.-Y. Recent progress of the development of dipeptidyl peptidase-4 inhibitors for the treatment of type 2 diabetes mellitus. *European Journal of Medicinal Chemistry* **2018**, *151*, 145-157.

(50) Lentz, F.; Drescher, A.; Lindauer, A.; Henke, M.; Hilger, R. A.; Hartinger, C. G.; Scheulen, M. E.; Dittrich, C.; Keppler, B. K.; Jaehde, U. Pharmacokinetics of a novel anticancer ruthenium complex (KP1019, FFC14A) in a phase I dose-escalation study. *Anticancer Drugs* **2009**, *20* (2), 97-103. Li, F.; Gorle, A. K.; Ranson, M.; Vine, K. L.; Kinobe, R.; Feterl, M.; Warner, J. M.; Keene, F. R.; Collins, J. G.; Day, A. I. Probing the pharmacokinetics of cucurbit[7, 8 and 10]uril: and a dinuclear ruthenium antimicrobial complex encapsulated in cucurbit[10]uril. *Organic & Biomolecular Chemistry* **2017**, *15* (19), 4172-4179.

(51) Thakkar, S.; Misra, M. Electrospun polymeric nanofibers: New horizons in drug delivery. *European Journal of Pharmaceutical Sciences* **2017**, *107*, 148-167. Ravikumar, R.; Ganesh, M.; Senthil, V.; Ramesh, Y. V.; Jakki, S. L.; Choi, E. Y. Tetrahydro curcumin loaded PCL-PEG electrospun transdermal nanofiber patch: Preparation, characterization, and in vitro diffusion evaluations. *Journal of Drug Delivery Science and Technology* **2018**, *44*, 342-348.

(52) Villemin, E.; Ong, Y. C.; Thomas, C. M.; Gasser, G. Polymer encapsulation of ruthenium complexes for biological and medicinal applications. *Nature Reviews Chemistry* **2019**, *3* (4), 261-282. Lemmerman, L. R.; Das, D.; Higuita-Castro, N.; Mirmira, R. G.; Gallego-Perez, D. Nanomedicine-Based Strategies for Diabetes: Diagnostics, Monitoring, and Treatment. *Trends Endocrinol Metab* **2020**, *31* (6), 448- 458.

(53) Frid, A. H.; Kreugel, G.; Grassi, G.; Halimi, S.; Hicks, D.; Hirsch, L. J.; Smith, M. J.; Wellhoener, R.; Bode, B. W.; Hirsch, I. B.; Smith, M.J.; Wellhoener, R.; Bode , W.; B Hirsch, I.; Kalra, S.; Ji, L.; Strauss, W.K.; New Insulin Delivery Recommendations. *Mayo Clinic Proceedings* **2016**, *91* (9), 1231-1255.

(54) Ezike, T. C.; Okpala, U. S.; Onoja, U. L.; Nwike, C. P.; Ezeako, E. C.; Okpara, O. J.; Okoroafor, C. C.; Eze, S. C.; Kalu, O. L.; Odoh, E. C.; Nwadike, U.G.; Ogbodo, J. O.; Umeh , B.U.; Ossai, E.C.; Nwanguma, B.C. Advances in drug delivery systems, challenges and future directions. *Heliyon* **2023**, *9* (6), e17488.

(55) Wong, C. Y.; Al-Salami, H.; Dass, C. R. Potential of insulin nanoparticle formulations for oral delivery and diabetes treatment. *J Control Release* **2017**, *264*, 247-275.

(56) Gugulothu, D.; Barhoum, A.; Afzal, S. M.; Venkateshwarlu, B.; Uludag, H. Structural Multifunctional Nanofibers and their Emerging Applications. In *Handbook of Nanofibers*, Barhoum, A., Bechelany, M., Makhlouf, A. Eds.; Springer International Publishing, **2018**, 1-41.

(57) Xu, T.; Ding, Y.; Liang, Z.; Sun, H.; Zheng, F.; Zhu, Z.; Zhao, Y.; Fong, H. Three-dimensional monolithic porous structures assembled from fragmented electrospun nanofiber mats/membranes: Methods, properties, and applications. *Progress in Materials Science* **2020**, *112*, 100656.

(58) CeCe, R.; Jin, L.; Islam, M.; Korvink, J.; Sharma, B. An Overview of the Electrospinning of Polymeric Nanofibers for Biomedical Applications Related to Drug Delivery. *Advanced Engineering Materials* **2023**, *26*.1-19.

(59) Hu, X.; Liu, S.; Zhou, G.; Huang, Y.; Xie, Z.; Jing, X. Electrospinning of polymeric nanofibers for drug delivery applications. *Journal of Controlled Release* **2014**, *185*, 12-21.

(60) Simionescu, B. C.; Ivanov, D. Natural and Synthetic Polymers for Designing Composite Materials. In *Handbook of Bioceramics and Biocomposites*, Antoniac, I. V. Ed.; Springer International Publishing, 2014; pp 1-54.

(61) Bernkop-Schnürch, A.; Dünnhaupt, S. Chitosan-based drug delivery systems. *European Journal of Pharmaceutics and Biopharmaceutics* **2012**, *81* (3), 463-469.

(62) Imani, R.; Yousefzadeh, M.; Nour, S. Functional Nanofiber for Drug Delivery Applications. In *Handbook of Nanofibers*, Barhoum, A., Bechelany, M., Makhlouf, A. S. H. Eds.; Springer International Publishing, 2019, 775-829.

(63) Kundu, J.; Pati, F.; Hun Jeong, Y.; Cho, D.-W. Chapter 2 - Biomaterials for Biofabrication of 3D Tissue Scaffolds. In *Biofabrication*, Forgacs, G., Sun, W. Eds.; William Andrew Publishing, 2013; pp 23-46.

(64) Li, Y.-L.; Nguyen, V.; Hsieh, M.-F. Endocytosis Pathways of the Folate Tethered Star-Shaped PEG-PCL Micelles in Cancer Cell Lines. *Polymers* **2014**, *6*, 634-650.

(65) Chen, D.; Han, S.; Zhu, Y.; Hu, F.; Wei, Y.; Wang, G. Kidney-targeted drug delivery via rhein-loaded polyethyleneglycol-co-polycaprolactone-co-polyethylenimine nanoparticles for diabetic nephropathy therapy. *Int J Nanomedicine* **2018**, *13*, 3507-3527.

(66) Ma, S.; Feng, X.; Liu, F.; Wang, B.; Zhang, H.; Niu, X. The pro-inflammatory response of macrophages regulated by acid degradation products of poly(lactide-co-glycolide) nanoparticles. *Eng Life Sci* **2021**, *21* (10), 709-720.

(67) S, S.; G, A.; Bajaj, G.; John, A.; Chandran, S.; Vijay kumar, V.; Ramakrishna, S. A review on the recent applications of synthetic biopolymers in 3D printing for biomedical applications. *Journal of Materials Science: Materials in Medicine* **2023**, *34*.1-22.

(68) Sridhar, R.; Lakshminarayanan, R.; Madhaiyan, K.; Amutha Barathi, V.; Lim, K. H. C.; Ramakrishna, S. Electrosprayed nanoparticles and electrospun nanofibers based on natural

materials: applications in tissue regeneration, drug delivery and pharmaceuticals. *Chemical Society Reviews* **2015**, *44* (3), 790-814.

(69) Nafo, W. Hydrogel Biomaterials for Drug Delivery: Mechanisms, Design, and Drugs. 2022.

(70) Haider, A.; Haider, S.; Kang, I.-K. A comprehensive review summarizing the effect of electrospinning parameters and potential applications of nanofibers in biomedical and biotechnology. *Arabian Journal of Chemistry* **2018**, *11* (8), 1165-1188.

(71) Gaydhane, M. K.; Sharma, C. S.; Majumdar, S. Electrospun nanofibres in drug delivery: advances in controlled release strategies. *RSC Advances* **2023**, *13* (11), 7312-7328.

(72) Nam, S.; Lee, J. J.; Lee, S. Y.; Jeong, J. Y.; Kang, W. S.; Cho, H. J. Angelica gigas Nakai extract-loaded fast-dissolving nanofiber based on poly(vinyl alcohol) and Soluplus for oral cancer therapy. *Int J Pharm* **2017**, *526* (1-2), 225-234.

(73) Thakkar, S.; More, N.; Sharma, D.; Kapusetti, G.; Kalia, K.; Misra, M. Fast dissolving electrospun polymeric films of anti-diabetic drug repaglinide: formulation and evaluation. *Drug Development and Industrial Pharmacy* **2019**, *45* (12), 1921-1930.

(74) Dhana Lekshmi, U. M.; Poovi, G.; Kishore, N.; Reddy, P. N. In vitro characterization and invivo toxicity study of repaglinide loaded poly (methyl methacrylate) nanoparticles. *Int J Pharm* **2010**, *396* (1-2), 194-203.

(75) Panda, B. P.; Wei, M. X.; Shivashekaregowda, N. K. H.; Patnaik, S. Design, Fabrication and Characterization of PVA/PLGA Electrospun Nanofibers Carriers for Improvement of Drug Delivery of Gliclazide in Type-2 Diabetes. *Proceedings* **2021**, *78* (1), 14.

(76) Gupta, A.; G.Rath; Goyal, A.; Mathur, R. B.; Dhakate, S. Electrospun composite nanofiber-based transmucosal patch for anti-diabetic drug delivery. *Journal of Materials Chemistry* **2013**,1-9.

(77) Joseph, S. M.; Krishnamoorthy, S.; Paranthaman, R.; Moses, J. A.; Anandharamakrishnan, C. A review on source-specific chemistry, functionality, and applications of chitin and chitosan. *Carbohydrate Polymer Technologies and Applications* **2021**, *2*, 100036.

(78) Tan, Q.; Kan, Y.; Huang, H.; Wu, W.; Lu, X. Probing the Molecular Interactions of Chitosan Films in Acidic Solutions with Different Salt Ions. *Coatings* **2020**, *10* (11), 1052.

(79) Abbas, W. A.; Sharafeldin, I. M.; Omar, M. M.; Allam, N. K. Novel mineralized electrospun chitosan/PVA/TiO2 nanofibrous composites for potential biomedical applications: computational and experimental insights. *Nanoscale Advances* **2020**, *2* (4), 1512-1522.

(80) Herdiana, Y.; Wathoni, N.; Shamsuddin, S.; Muchtaridi, M. Drug release study of the chitosan-based nanoparticles. *Heliyon* **2022**, *8* (1), e08674.
(81) Al-Madhagy, G.; Alghoraibi, I.; Darwich, K.; Hajeer, M. Y. Evaluation of the Chemical, Morphological, Physical, Mechanical, and Biological Properties of Chitosan/Polyvinyl Alcohol Nanofibrous Scaffolds for Potential Use in Oral Tissue Engineering. *Cureus* **2022**, *14* (10), 1-18.

Chapter 2

Materials and methods

2.1 The handling of ruthenium precursors:

The metal precursors and the isolated ruthenium compounds were perceived as potentially toxic and environmentally harmful. For instance, in the presence of strong oxidants, these aforementioned substances react to form ruthenium tetroxide which is a highly toxic and volatile gas. Consequently, a number of safety precautions were taken when handling the synthesized ruthenium compounds and their metal precursors. These common precautions included wearing dust masks, gloves and the use of certified fume cupboards in which all coordination reactions were carried out.[1,2]

2.2 Materials

2.2.1 Metal precursors:

The metal precursor, *cis*-$[Ru(bipy)_2Cl_2]$ and *trans*-$[RuCl_2(PPh_3)_2]$were purchased at 97% purity from Sigma-Aldrich and no additional purification was carried out before use.

2.2.2 Laboratory chemicals:

All solvents were of analytical grade and obtained commercially from Sigma-Aldrich. Organic precursors, used for the synthesis of the ligands, were procured from the same supplier and their purities were deemed adequate; refer to **Table 2.1**.

Table 2.1: Organic precursors that were used in the formation of the respective ligands.

Name	**Purity**
2-Pyridinecarboxaldehyde	99%
5,6-Diamino-1,3-dimethyluracil hydrate	Technical grade
5,6-Diaminouracil hydrate	≥98%
5-Diaminouracil	97%

2-Quinolinecarboxaldehyde	97%
2,6-Pyridinedicarboxaldehyde	97%
Tetrabutylammonium hexafluorophosphate	98%
Phosphate buffered saline (PBS) tablets	-
Human islet amyloid polypeptide (hIAPP)	-
Bovine serum albumin	-
2,2-Di(4-tert-octylphenyl)-1-picrylhydrazyl (DPPH)	98%
Griess reagent	98%
Sodium nitroprusside	98%
L-Ascorbic acid	99%
Warfarin	98%
Ibuprofen	98%

2.3 Methods

An Elga Purelab Ultra system produced ultrapure water. Electronic spectra were collected using a Cary 60 UV-Vis spectrophotometer with a temperature-controlled multi-cuvette holder, and the extinction coefficients (ε) are given in M^{-1} cm^{-1}. Melting point ranges were determined with a Stuart SMP3 melting point apparatus. Fluorescence measurements were performed using a 1 cm quartz emission cell and a Perkin Elmer LS-45 fluorescence spectrometer equipped with a Xenon lamp source. Elemental analysis data was obtained using a CHNS-O Flash 2000 Organic Elemental Analyzer. Powder X-ray diffractograms (PXRD) were obtained using a miniflex600 Powder X-ray diffractometer. Scanning electron microscope (SEM) micrographs with accompanying electron dispersive X-ray (EDX) spectrums were acquired using a Zeiss EVO LS15 microscope operating under high vacuum conditions. Solid-state infrared spectra were recorded on a Perkin-Elmer Spectrum 100 from 4000 to 350 cm^{-1}. ^{1}H and ^{31}P NMR spectral data were acquired on a Bruker Avance 400 MHz spectrometer. All NMR spectra were recorded in DMSO-d_6. High-resolution mass spectra were obtained on a Waters Micromass LCT Premier TOF-MS instrument.

2.3.1 *Theory and instrumentation of electrospinning:*

Electrospinning is a low-cost, simple-to-use method for assembling polymers into NMDDSs. **Figure 2.1** depicts a schematic diagram of the electrospinning procedure

and the instrumentation set-up showing a flow pump, a spinner, a collector unit (*viz.* flat conductive plate) and a high-voltage power source which are typically the key components of the electrospinning process. In particular, the open circuit connection from the spinneret to the high voltage source which in turn are linked to the collector and the latter and spinneret are oppositely charged during the electrospinning process.

At the onset of the electrospinning process, the polymer solution is injected into the spinneret from a syringe linked to the flow pump generally at constant flowrate. Simultaneously, the opposing voltages are applied to the spinneret and collector unit. Polymer extrusion occurs once the Taylor cone appearing at the tip of the electrode is overcome by exceeding the surface tension of the polymer solution as the collector unit attracts the oppositely charge polymer stream. Subsequently, solvent evaporation occurs as the polymer jet travel between the collector unit. The electrospinning process is concluded when the ENFs are accumulated on the collector. The structural features of ENFs can be manipulated through alterations of instrumental, polymer solution and ambient parameters.[3]

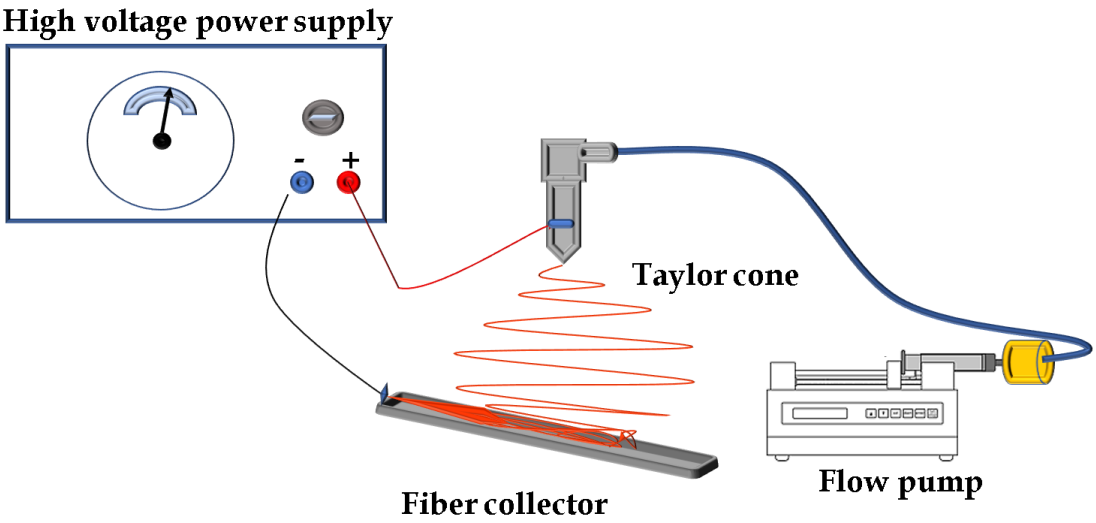

Figure 2.1: *Illustration of electrospinning setup.* [3]

2.3.2 Synthesis of free ligands:

2.3.2.1 Previously reported ligands

The following ligands were isolated as previously reported: 6-amino-1,3-dimethyl-5-((pyridin-2-ylmethylene)amino)pyrimidine-2,4-(1H, 3H)-dione (urpy),[4] 6-amino-5-((2-aminobenzylidene)amino)-1,3-dimethylpyrimidine-2,4-(1H, 3H)-dione (urdpy),[5] 2,6-bis-((uracilimino)methylene)pyridine (urdp)[6] and 2,6-bis-((6-amino-1,3-dimethyluracilimino)methylene)pyridine (H_4ucp).[7]

2.3.2.2 (5E)-5-((Pyridin-2-yl)methyleneamino)-6-aminopyrimidine-2,4(1H,3H)-dione (urpda)

A volume of 20 mL methanol was used to dissolve urpda (0.500 g; 2.16 mmol) and 2-pyridinecarboxaldehyde (0.2057 cm^3; 2.16 mmol) were weighed and mixed together and then the condensation reaction was performed at elevated temperatures while refluxing the reaction mixture for 3 h. The resultant bright orange solution was allowed to cool to room temperature, filtered and a bright orange precipitate was washed with cold methanol as well as diethyl ether. Yield = 73%; m.p. 114 – 116 °C. IR (ν_{max}/cm^{-1}): ν(N-H) (m) 3410, 3195 (br), ν(C=O) 1726, ν(C=N) 1609 see, **Figure 2.2**. ^{1}H NMR (295 K/d_6-DMSO/ppm): 10.75 -10.65 (br, d, 2H, H7N, H6N); 9.63 (s, 1H, H1), 8.63 (d, 1H, H2); 8.34 (d, 1H, H5); 8.02 (t, 1H, H4); 7.48 (t, 1H, H3); 7.08 (br, s, 2H, $N8H_2$), see **Figure 2.3**. UV-Vis (DMSO, λ_{max} (ε, M^{-1} cm^{-1})): 255 nm (57600), 360 nm (88000), sh, 456 nm (1600) see **Figure 2.4**.

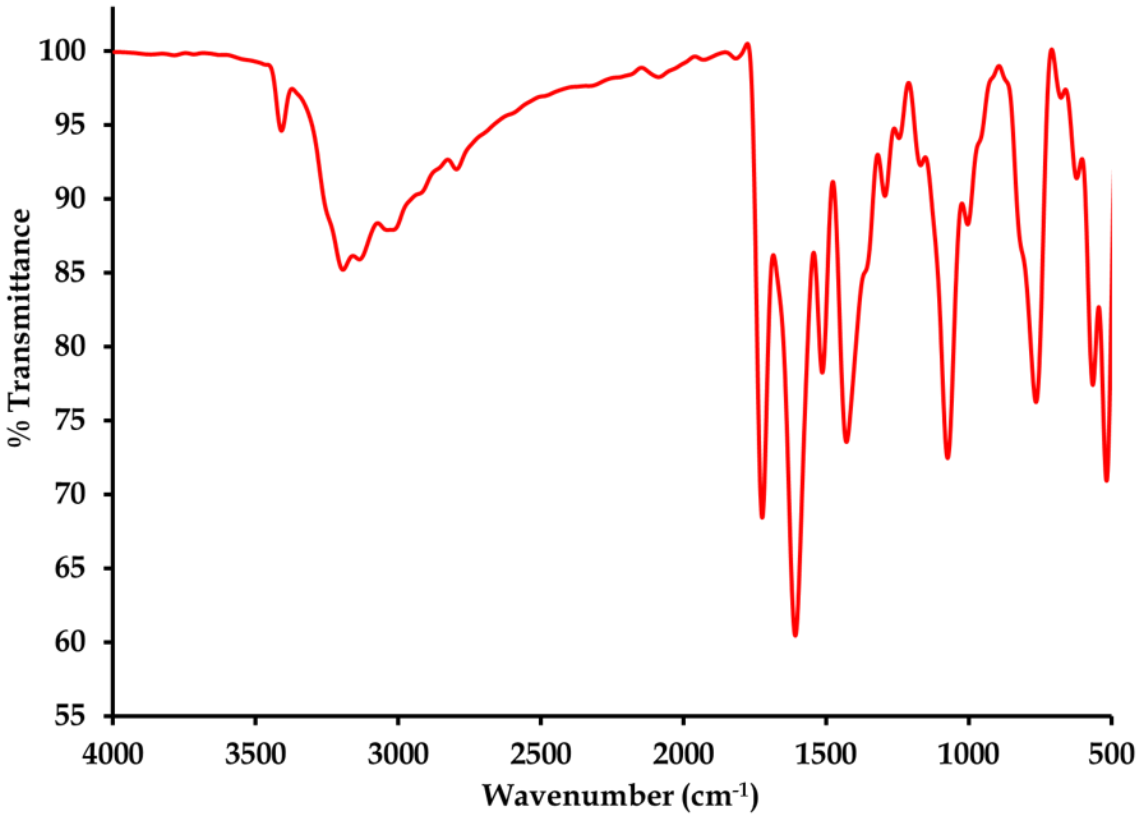

Figure 2.2: *Overlay IR spectrumof the urpda free-ligand between 4000 and 500 cm^{-1}.*

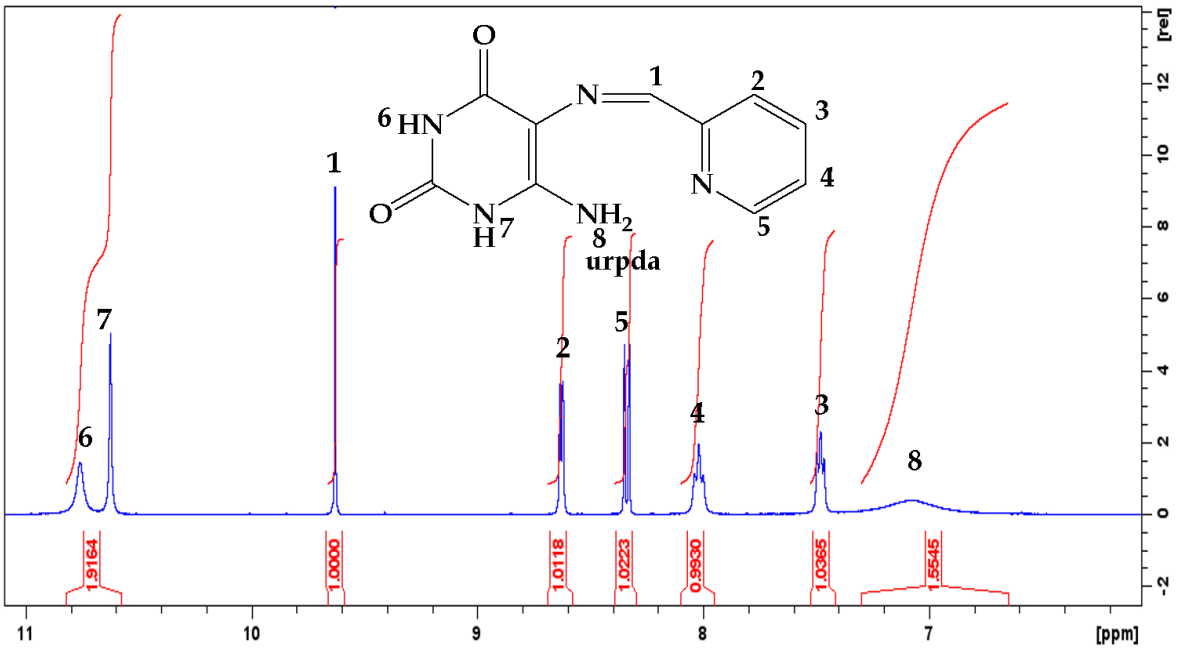

Figure 2.3: *^{1}H NMR spectrum of urpda free-ligand.*

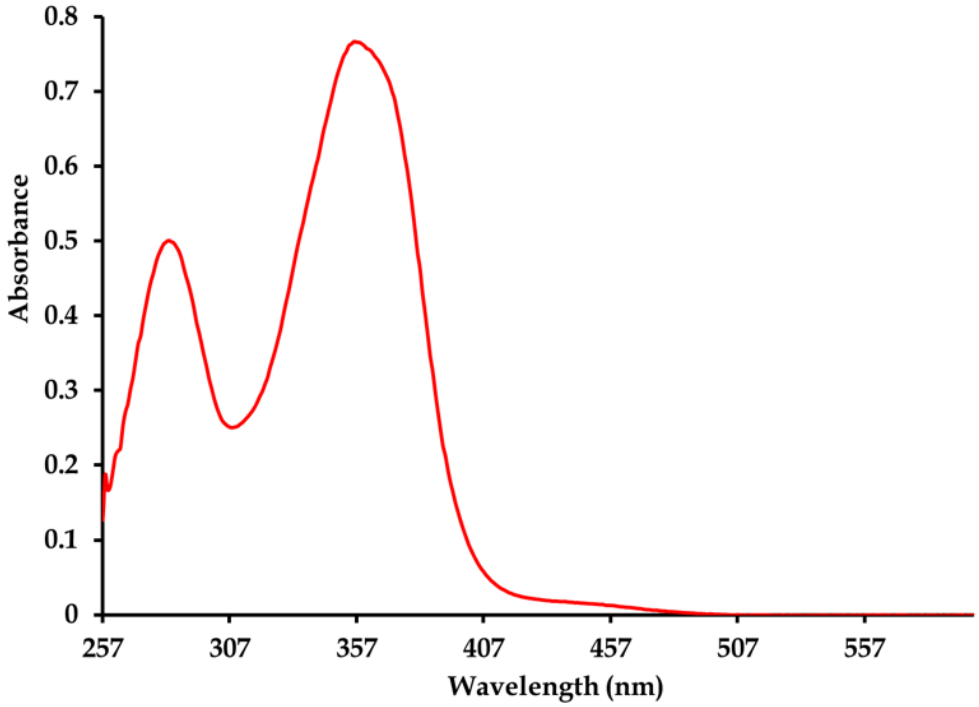

Figure 2.4: *UV-vis spectrum of the urpda free-ligand.*

2.3.2.3 *(5E)-5-((quinolin-2-yl)methyleneamino)-6-aminopyrimidine-2,4(1H,3H)-dione* ***(urqda)***.

A 1:1 molar reaction between 5,6-diaminouracil (0.500 g; 1.88 mmol) and 2-quonolinecarboxaldehyde (0.2951, 1.88 mmol) were refluxed for 3 hours in methanol (20 mL). The resulting light-yellow solution was allowed to cool to room temperature, filtered and a yellow precipitate was washed with cold methanol and finally with diethyl ether. Yield = 80%; m.p. 115 – 118 °C. IR (ν_{max}/cm^{-1}): v(N-H) 3373 (m, br), v(C=O) 1708 (m, sh), v(C=N) 1666 (s), see **Figure 2.5**. ^{1}H NMR (295K/d_6-DMSO/ppm): 10.72 -10.59 (d, 2H, H1N, H2N); 9.81 (s, 1H, H4); 8.56 (d, 1H, H5); 8.33 (d, 1H, H10); 8.02- 7.96 (dd, 2H, H6, H9); 7.76 (td, 1H, H7); 7.59 (td, 1H, H8); 6.98 (br, s, 2H, N3H$_2$) see, **Figure 2.6**. UV-Vis (DMSO, λ_{max} (ε, M^{-1} cm^{-1})): 289 nm (7900), 315 nm (9200), sh, 328 nm (9400), 342 nm (9700), 358 nm (8400, 420 nm (1100) see, **Figure 2.7**.

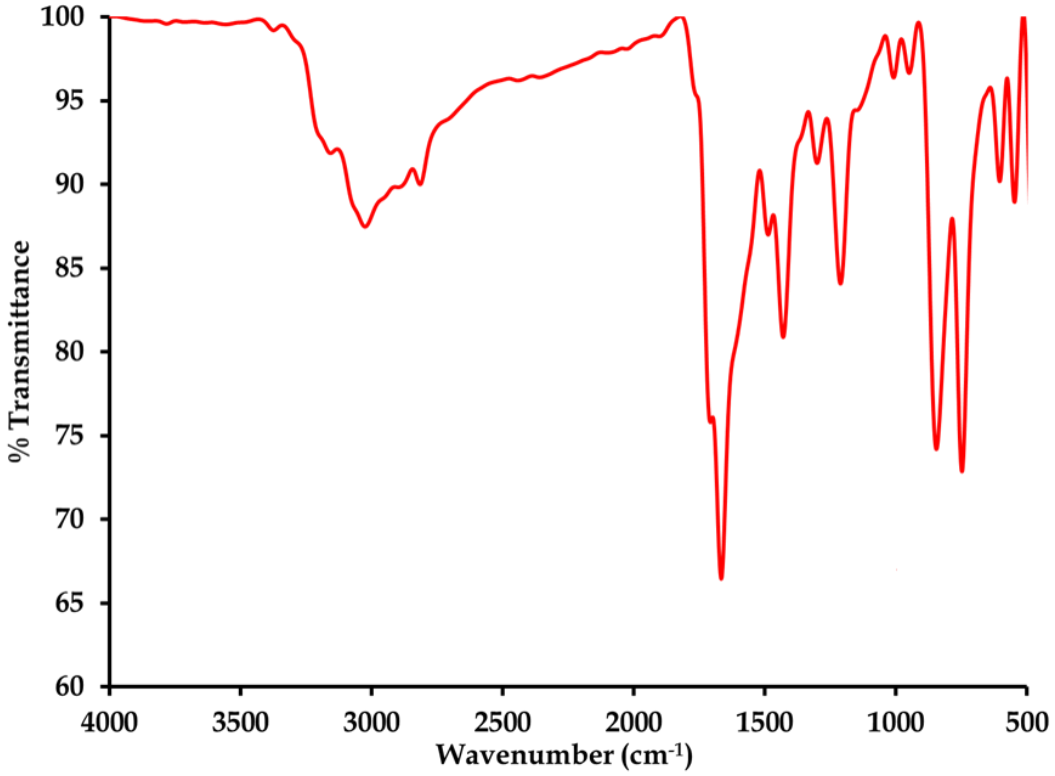

Figure 2.5*: IR spectrum of the urqda free-ligand between 4000 and 500 cm-1.*

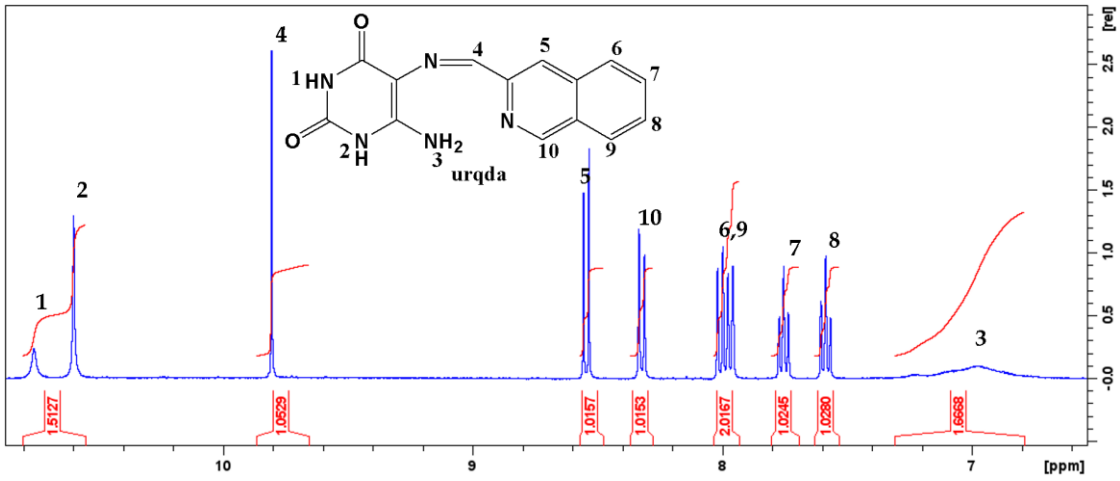

Figure 2.6: *1H NMR spectrum of the urqda free-ligand.*

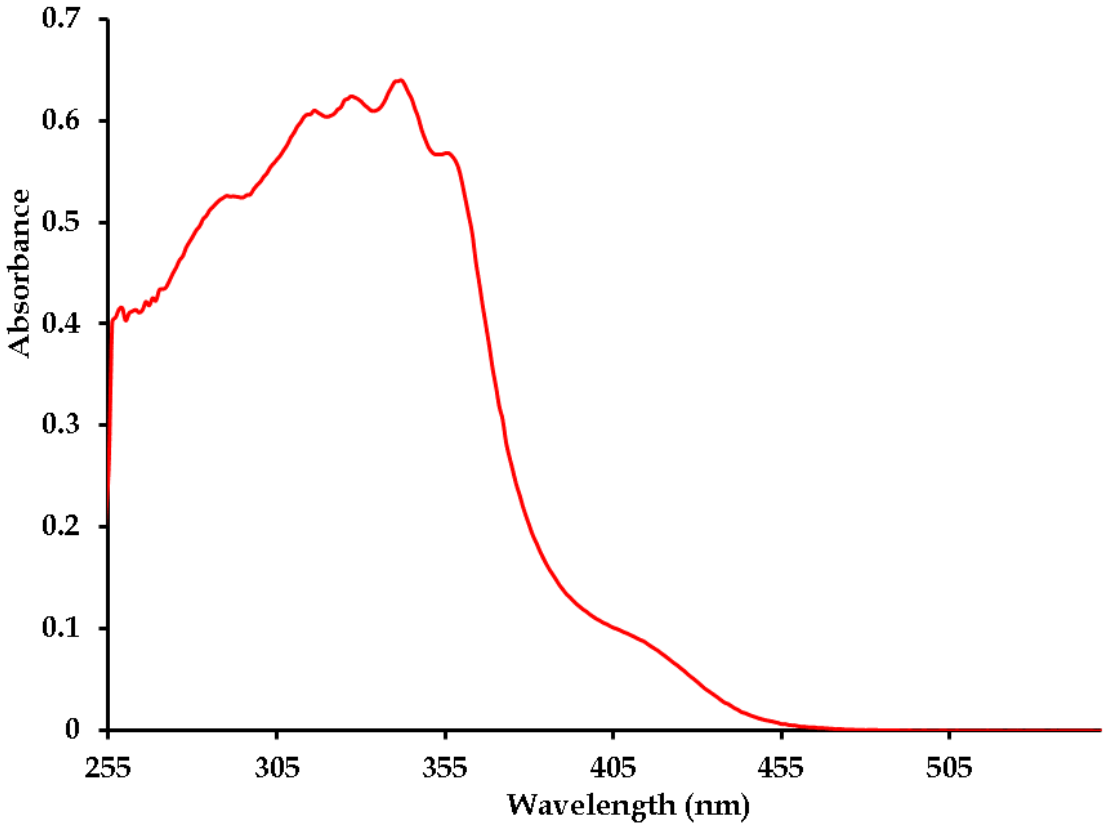

Figure 2.7: *UV-vis spectrum of the urqda free-ligand.*

2.3.3 Computational modelling

Indicative of the reported computational studies conducted on parent metal complex **1** ([Ru^{II}(H_3ucp)Cl(PPh_3)]), tandem geometry and frequency simulations of novel compounds, were performed using Gaussian 09W. In particular, the calculations were executed at the Density Functional Theory (DFT) level and the B3LYP functionals were applied. In addition, a hybrid basis set was used where the non-metals and metal were assigned to the 6-311G^{++} (d, p) and the LANL2DZ basis sets, respectively.[8] Starting conformers of the individual metal compounds were generated directly from their corresponding solid-state structures after removing solvent molecules of recrystallization and counter-ions.

2.3.4 *Molecular docking*

PatchDock was utilized to study the rigid molecular docking between the ligand (i.e. metal complex) and the receptor (i.e. biomolecule).[9] More specifically, the algorithms are applied to search suitable vacant spaces (i.e. patches) where the static ligand can fit. Complementary intermolecular interactions are determined based on the nature of the receptor, which dictates the orientation of the ligand within the binding site. For PatchDock parameters, a clustering RMSD and a complex type of protein small ligand were used in these simulations.

2.3.5 *Single X-ray crystallography*

Crystallographic raw data of the novel metal complexes were obtained using a Bruker Apex Duo coupled to an Oxford Instruments Cryostat set which was set to temperatures in the range of 100 K. Concurrently, an Incoatec microsource conducted phi and omega scans at 30 W power and 0.50^{o} frame widths with the aid of APEX2.[10] In addition, the X-ray Cu(K_{α}) radiation source was tuned to a wavelength of 1.54178 Å.

Data processing was initiated using the SAINT program by reducing the respective data sets with the aid of standard Lorentz and polarization correction factors, scan speed scaling and outlier rejection. Afterward, data correction was implemented using semi-empirical multi-scan absorption adjustment (SADABS).[10, 11] The intermediary structures were rendered from data analysis using direct methods, WinGX and SHELX-2016.[12, 13] More specifically, the structures were fully resolved by refining the non-hydrogen atoms which were obtained by the process of mapping the variation in electron densities was refined with SHELX-2016.[13] Furthermore, disordered molecules of crystallization were squeezed out of the crystal lattice of the respective compounds which afforded X-ray data sets with acceptable R-factor.[14]

2.3.6 Electronic spectrophotometric titrations

Fluorescence spectroscopy was used to analyse the interactions between respective compounds– and BSA, wherein their Stern-Volmer quenching constant (K_{SV}) was obtained by using the Stern-Volmer equation (1):[15]

$$\frac{I_0}{I} = 1 + K_{sv}[\text{Complex}] \quad (\mathbf{1})$$

In equation (2), Io and I are the emission intensities in the absence and presence of a metal complex. The slope of equation (2) was used to deduce the K_{SV} values. K_{SV} is related to the associative rate constant, k_q (M^{-1} s^{-1}) by equation (2):

$$k_q = K_{sv}/(\tau_0 \ = 10^{-8}\ \text{s}) \quad (\mathbf{2})$$

where τ_0 is the average lifetime of the excited state of the biomolecule (10^{-8} s) without the quencher. The binding constants (K_b) and the binding number (n) were then determined using equation (3):

$$\text{Log}\frac{I_0 - I_0}{I_0} = \text{Log}\ K_b + n\ \text{Log}[\text{complex}] \quad (\mathbf{3})$$

where K_b is the binding constant of each metal complex with BSA and n is the number of binding sites as obtained from the slopes of the plots of data according to equation (3).

2.3.7 Radical scavenging studies

The DPPH radical scavenging assay performed with minor adjustments, for **2-10** using a previously published protocol.[7] A 0.03 mM solution of DPPH was prepared with anhydrous DMSO, while a 0.2 mM solution was prepared with methanol. Then, 600 μL of the 0.2 mM DPPH solution and 90 μL of **2–10** were mixed and the mixture was allowed to stand for 30 min at room temperature in a dark room. We measured the absorbance values of the sample solutions at 518 nm using a UV-Vis spectrophotometer. In the same measurements, ascorbic acid was used as a positive sequester control reagent and DPPH solution in methanol was used as a negative sequester control.

A standard assay was used to evaluate the ability of **2-10** to scavenge nitric oxide (NO) radicals.[7,16] To create a negative control, 1.8 mL of Greiss-IIosvay nitrite reagent was added to 0.2 mL of nitroprusside (20 mM) in PBS (pH 7.4). Aliquots of 2 mL of the negative control were added to each of the 0.3 mM solutions of **2-10** (0.03 mM). Under the same conditions as for the DPPH assay, the above solutions were incubated for three hours. The absorbance values were then measured at 540 nm. A positive control solution containing 0.03 mM ascorbic acid was also prepared, incubated with DPPH in the same way as compounds **2-10** and its absorbance measured. The percentage radical scavenging activities (% RSA) of compounds **2-10** was calculated using equation (**4**), where A_{bs}(DPPH or NO radicals) is the absorbance of the control and $A_{0(nc)}$ is the absorbance of each metal compound after they were added to the negative control after incubation. The % RSA of **2-10** and ascorbic acid was determined using equation **4**:

$$\% \text{ RSA } = \frac{A_{0(NC)} - A_S}{A_{0(NC)}} \text{ X } 100 \% \qquad (\mathbf{4})$$

2.4 References

(1) Catena, R.; Ozcan, A.; Zivanovic, N.; Bodenmiller, B. Enhanced multiplexing in mass cytometry using osmium and ruthenium tetroxide species. Cytometry. Part A : the journal of the International Society for Analytical Cytology **2016**, 89(5), 491-7.

(2) Rosli, N.; Ming, L.; Mahadi, A.; Wattanasiriwech, S.; Lim, R.; Thotagamuge, R. Ruthenium Dye (N3) Removal from Simulated Wastewater Using Bamboo Charcoal and Activated Bamboo Charcoal. Key Engineering Materials **2018**, 765, 92-98.

(3) Xue, J.; Wu, T.; Dai, Y.; Xia, Y. Electrospinning and Electrospun Nanofibers: Methods, Materials, and Applications. Chemical Reviews **2019**, 119 (8), 5298-5415.

(4) Cherayath, Sr.; Alice, J.; Prabhakaran, C. P. Palladium(II) complexes of Schiff bases derived from 5-amino-2,4-(1H, 3H)pyrimidinedione (5-aminouracil) and 1,2-dihydro-1,5-dimethyl-2-phenyl-4-amino-3H-pyrazol-3-one. Transition Metal Chemistry **1990**, 15 (6), 449-453.

(5) Booysen, I.; Hlela, T.; Ismail, M.; Gerber, T.; Hosten, E.; Betz, R. (E)-6-Amino-1,3-dimethyl-5-[(pyridin-2-yl-methyl-idene)amino]-pyrimidine-2,4(1H,3H)-dione. Acta Crystallogr Sect E Struct Rep Online **2011**, 67 (Pt 9), o2289.

(6) Koz, G.; Özdemir, N.; Astley, D.; Dinçer, M.; Astley, S. T. Synthesis, spectroscopic and structural characterization of cobalt(II) complex with uracil-containing 2,6-diformylpyridine ligand: Theoretical studies on the ligand and pentagonal-bipyramidal [Co(L)(H2O)2]2+ and [Zn(L)(H2O)2]2+ cations. Journal of Molecular Structure **2010**, 966 (1), 39-47.

(7) Maikoo, S.; Dingle, L. M. K.; Chakraborty, A.; Xulu, B.; Edkins, A. L.; Booysen, I. N. Synthetic, characterization and cytotoxic studies of ruthenium complexes with Schiff bases encompassing biologically relevant moieties. Polyhedron **2020**, 184, 1-10.

(8) Brink, A.; Visser, H. G.; Roodt, A. Novel imino rhenium(I) tricarbonyl complexes of salicylidene-derived ligands: Synthesis, X-ray crystallographic studies, spectroscopic characterization and DFT calculations. Polyhedron **2013**, 52, 416-423.

(9) Schneidman-Duhovny, D.; Inbar, Y.; Nussinov, R.; Wolfson, H. J. PatchDock and SymmDock: servers for rigid and symmetric docking. Nucleic Acids Res **2005**, 33 (Web Server issue), W363-367.

(10) Bruker APEX2, SAINT and SADABS (2010). Bruker AXS Inc. Madison., Wisconsin, USA.; Bruker AXS Inc. Madison.

(11) Blessing, R. H. An empirical correction for absorption anisotropy. Acta crystallographica. Section A, Foundations of crystallography **1995**, 51 (Pt 1), 33-38.

(12) Farrugia, L. WinGX and ORTEP for Windows: an update. J. Appl. Crystallogr. **2012**, 45 (4), 849-854.

(13) Sheldrick, G. A short history of SHELX. Acta Crystallogr. A **2008**, 64 (1), 112-122.

(14) Dolomanov, O. V.; Bourhis, L. J.; Gildea, R. J.; Howard, J. A. K.; Puschmann, H. OLEX2: a complete structure solution, refinement and analysis program. Journal of Applied Crystallography **2009**, 42 (2), 339-341. Bourhis, L.; Dolomanov, O.; Gildea, R.; Howard, J.; Puschmann, H. The anatomy of a comprehensive constrained, restrained refinement program for the modern computing environment –Olex2 dissected. Acta Crystallographica Section A **2015**, 71 (Pt 1), 59-75.

(15) Paul, H.; Mukherjee, T.; Mukherjee, M.; Mondal, T. K.; Moirangthem, A.; Basu, A.; Zangrando, E.; Chattopadhyay, P. Ruthenium(II) complexes of pyrrole-azo ligands: cytotoxicity, interaction with calf thymus DNA and bovine serum albumin. Journal of Coordination Chemistry **2013**, 66 (15), 2747-2764.

(16) Vijayabaskaran, M.; Venkatesaramurthy, N.; Babu, G.; Perumal, P.; Jayakar, B. In vitro antioxidant evaluation of Pseudarthria viscida Linn. Int J Curr Pharmaceut Res **2010**, 2, 21-23.

Chapter 3

Bovine serum albumin uptake and polypeptide disaggregation studies of hypoglycaemic ruthenium(II) uracil Schiff-base complexes

3.1 Introduction

Diabetes mellitus is a chronic disease induced by the insufficient production of insulin by the pancreas (Type I diabetes mellitus) or by irregular metabolism of blood glucose as a result of the improper use of insulin (Type II diabetes mellitus, T2DM).[1] Significant causes of T2DM are high carbohydrate- and cholesterol-containing diets accompanied by limited physical exercise. At the same time, free radicals have also been associated with the distortion of the pancreatic β-cells.[2] Advancement of T2DM generally induces secondary medical conditions in diabetic patients ranging from cardiovascular ailments to failure of excretory organs and, in more aggravated cases, to blindness and limb amputations.[3]

Amelioration of T2DM progression requires closely managed intervention using oral-administered drugs. This intervention has been associated with common gastrointestinal and other serious side effects.[4] Consequently, the increasing morbidity associated with T2DM and the current management drugs have led to a search for an alternative therapeutic agent with a different mechanism of activity.[5] The emergence of nitrogen-donor ruthenium compounds as chemical quenchers of human islet amyloid polypeptide (hIAPP, otherwise known as amylin) aggregation has provided a new avenue for discovering candidate metal-based anti-diabetic drugs.[6]

Transition metal complexes have displayed promising insulin-mimetic activities via various mechanism of activities. In particular, it has been reported that alterations in the ruthenium cores and the stereo-electronic properties of the organic chelators afforded new ruthenium analogues that can reverse amylin oligomerization.[7] Consequently, these derivatives could potentially restore the physiological damage of

the pancreatic β-cells.[8] One of the main driving forces behind the unfolding of amylin aggregates is the hydrolysis of labile chloro ligands of ruthenium compounds followed by direct coordination while displacing aqua co-ligands of the intermediate ruthenium compound.[6] Alternatively, the structural features of the ruthenium compound can encourage non-covalent interactions between it and the amylin oligomers.[9] In turn, the restoration or the preservation of amylin strands within the pancreatic β-cells leads to an improved regulation of the blood glucose levels.

Literature trends have illustrated that certain d-block metal cations and transition metal complexes exhibit various coordination modes and non-coordinative binding towards amylin or its aggregates.[6, 8, 10] For instance, copper(II) ions primarily disrupt amylin self-aggregation through direct coordination to protein residues in close proximity of the amylin disulphide bridges while reducing acute toxicity of the pancreatic β-cells. Another study reported that zinc(II) cations showed preferential binding affinities for the histidine residues (His18) of amylin, in a concentration-dependent manner, rendering varying degrees of amyloidosis inhibition. However, elevated concentrations of these essential metal cations have induced misfolding of amylin. This unexpected adverse effect on amylin can be circumvented by the use of selected d-block metal complexes with organic ligands of conducive electronic and steric properties. Intriguingly, metal complexes of gold(III) or ruthenium(II) with ligands of appropriate steric factors have displayed unique coordination modes with amylin, leading to concentration-dependent amylin disaggregation or fibrillation inhibition. Furthermore, the dimeric ruthenium(II) complexes have rendered higher amylin disaggregation capabilities than their structurally-related monomeric species. In addition, both gold and ruthenium complexes have coordinated through various amide donor sites of amylin. More specifically, manipulation of the electronic effects of pi-conjugated ligands within the coordination spheres of ruthenium compounds have improved the aqueous solubility for amylin disaggregation.

Previous studies using our lead ruthenium(II) compound with a tridentate uracil diimine chelator, [Ru(H_3ucp)Cl(PPh_3)] (**1**) (H_4ucp = 2,6-bis-((6-amino-1,3-

dimethyluracilimino)methylene)pyridine, see **Figure 3.1**) showed anti-diabetic potential as the compound was not only able to restore glucose homeostasis in a diet-induced pre-diabetic rat model, but it also prevents complications associated with the accumulation of reactive oxygen species.[11] In this study, the substituents on the uracil rings were changed to investigate the influence of steric and electronic effects on the structure and activity of ruthenium complexes structurally-related to **1**. Therefore, the metal complexes, cis-$[Ru(bpy)_2(urdp)]Cl_2$ (**2**) (urdp = 2,6-bis-((uracilimino)methylene)pyridine), trans-$[RuCl_2(PPh_3)(urdp)]$ (**3**), and cis-$[Ru(bpy)_2(H_4ucp)](PF_6)_2$ (**4**) were synthesized and fully characterized. Metal complex cations of **2** and **4** were kinetically inert in solution while **1** and **2** underwent substitution of the chloro co-ligands. Affinities of **2 – 4** towards the bovine serum albumin (BSA) were evaluated as pre-determining steps to examine their physiological transportability. Electronic titrations of the new metal complexes **2 – 4** with the amylin and its oligomers were conducted to assess their capabilities to stop aggregation or initiate disaggregation of the latter. The in vitro glucose metabolism studies of the novel metal complexes in liver (Chang) cells reveal that **3** exhibits the highest activity.

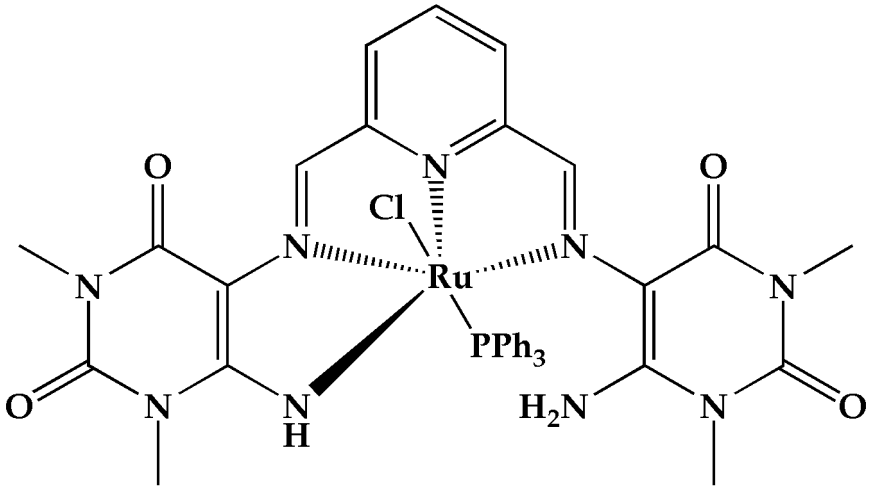

Figure 3. 1: *Structure of the lead ruthenium(II) compound, $[Ru(H_3ucp)Cl(PPh_3)]$ (**1**) (H_4ucp = 2,6-bis-((6-amino-1,3-dimethyluracilimino)methylene)pyridine).*

3.2. Experimental

3.2.1 Synthesis of cis-[Ru(bipy)$_2$(urdp)]Cl$_2$ (**2**)

The metal complex was prepared by reacting cis-[Ru(bipy)$_2$Cl$_2$] (0.100 g, 0.21 mmol) with urdp (0.07295 g, 0.21 mmol) in a solvent mixture of ethanol (16 mL) and water (4 mL), which was heated under reflux in an inert atmosphere for 8 h. The red precipitate was filtered, washed several times with water and dried, resulting in a dark red precipitate. After that, the precipitate was dissolved in acetonitrile (4 mL) and layered with diethyl ether, forming dark red X-ray quality crystals. To attain acceptable elemental analysis (EA) data, the red crude precipitate was alternatively re-dissolved in a saturated solution (15 mL) of ammonium hexafluorophosphate in analytical-grade acetonitrile: dichloromethane (1:1). Thereafter, it was layered with di-ethyl ether, to yield dark red crystals of cis-[Ru(bpy)$_2$(urdp)](PF$_6$)$_2$•CH$_2$Cl$_2$. These crystals were then dried in a vacuum oven for 5 days. Yield: (0.06 g, 82%); mp = 164.3 – 167.8 °C; elemental analysis for $C_{35}H_{27}F_{12}N_{11}O_4P_2Ru$•$CH_2Cl_2$: calcd, C = 37.88%, H = 2.56%, N = 13.50%; found, C = 37.84%, H = 2.66%, N = 13.80%; IR (ATR, cm^{-1}): ν_{N-H} 3634, 3325 (w), $\nu_{C=O}$ 1717 (m), 1679 (m, sh), $\nu_{C=N}$ 1648, 1627, 1600 (m); ^{1}H NMR (400 MHz, DMSO-d$_6$): δ_H Uracil: 11.26, 11.24 (2x s, 2H, N2-H, N6-H), 7.48, 6.64 (2x s, 2H, CH); 9.34, 8.76 (2 x s, 2H, CH=N (H-5, 11); Pyr: 8.41 (dd, J=7.7, 1.4 Hz, 1H), 8.18 (t, J=7.8 Hz, 1H), 7.86 (dd, J=7.9, 1.4 Hz, 1H); Bipyr A: 8.79 (br d, J=8.0 Hz, 1H), 8.28 (td, J=7.8, 1.5 Hz), 7.69 (ddd, J=7.6, 5.8, 1.1, 1H), 8.30 (br d, J=5.6 Hz); Bipyr B: 8.64 (br d, J=8.0 Hz, 1H), 8.05 (td, J=7.9, 1.3 Hz, 1H), 7.27 (td, J=6.1, 1.0 Hz, 1H), 7.44 (dd, J=5.6, 1.0 Hz, 1H); Bipyr C: 8.63 (br d, J=8.1 Hz, 1H), 8.12 (dd, J=7.8, 1.5 Hz, 1H), 7.58 (ddd, J=7.6, 5.6, 1.1 Hz, 1H); Bipyr D: 8.57 (d, J=8.1 Hz, 1H), 7.89 (td, J=7.8, 1.2 Hz, 1H), 7.22 (td, J=6.0, 1.0 Hz), 7.55 (br d, J=5.6 Hz, 1H) see; UV/Vis (MeOH): 292 nm (14300), 371 nm (sh, 4460), 435 nm (2980), 503 nm (2120) see, **Figure 3.2**; ESI-(+)-TOF-MS (DMSO): m/z 766.1235 [M–H-2Cl]; calcd for $C_{35}H_{26}Cl_2N_{11}O_4{}^{102}Ru$, 766.1213.

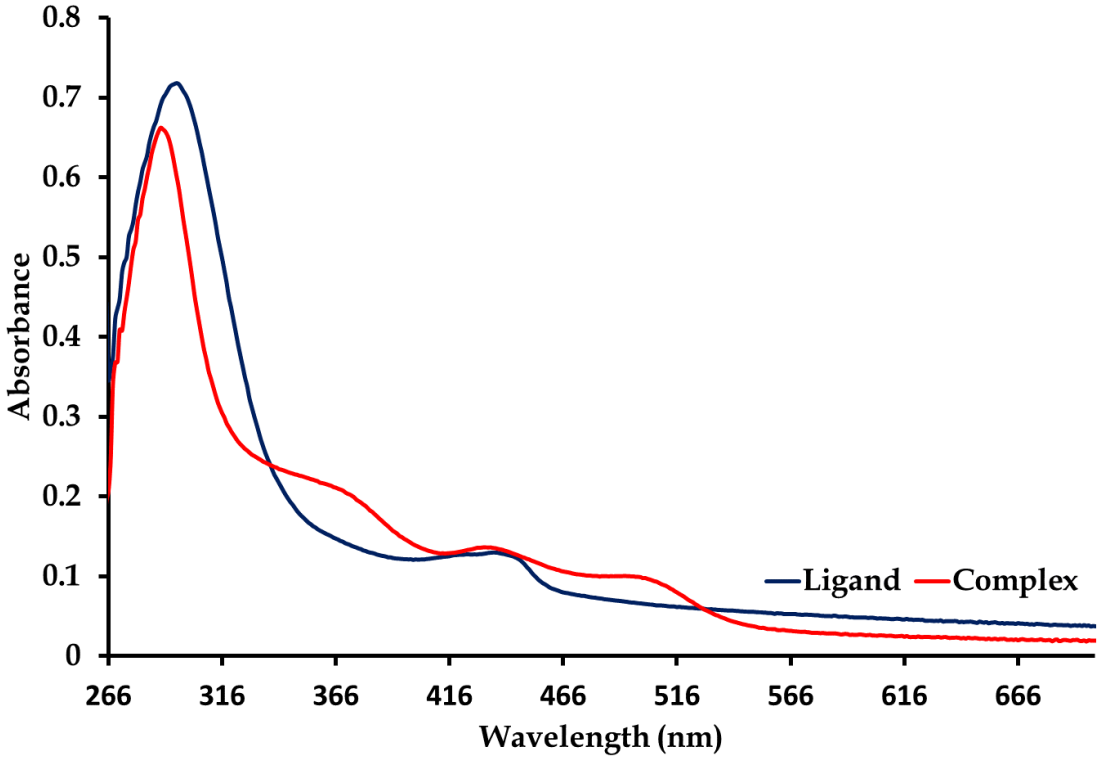

Figure 3. 2: *Overlay UV-Visible absorption spectrum of complex 2 and the free-ligand, urdp.*

3.2.2 Synthesis of trans-[$RuCl_2(PPh_3)$(urdp)] (**3**)

The 1:1 molar coordination reaction between urdp (0.03685 g; 0.104 mmol) and trans-[$RuCl_2(PPh_3)_3$] (0.100 g; 0.104 mmol) was conducted in methanol (20 mL) which was heated until reflux for 3 h. A maroon precipitate was filtered by gravity and washed with diethyl ether. After that, it was dissolved in a mixture of pyridine: tetrahydrofuran in a volume-to-volume ratio of 3:7. The resultant solution was then layered with hexane. Cubic-shaped, violet-colored crystals grew from the slow diffusion of hexane into the solvent mixture of **3** over a period of 12 days. Yield: (0.080 g, 98%); mp = 244.3 – 246.8 °C; elemental analysis for $C_{33}H_{26}Cl_2N_7O_4PRu \bullet 2(H_2O)$: calcd, C = 48.13%, H = 3.67%, N = 11.90%; found: C = 48.17%, H = 3.32%, N = 11.70%; IR (ATR, cm^{-1}): ν_{N-H} 3465 (br, w), $\nu_{C=O}$ 1675 (br, vs), $\nu_{C=N}$ 1629 (sh, s), 1594 (sh, m), $\nu_{Ru-PPh3}$ 691 (s); ^1H NMR (400 MHz, DMSO-d_6): δ 11.5 (s, 2H, N1-H, N7-H), 11.29 (s, 2H, N2-H, N6-H), 8.89 (s, 2H, H-5, H-11), 8.52 (s, 2H, H-15, H-1), 7.58 (d, J=7.7 Hz, 2H, H-7, H-9), 7.46 (dd, J=8.3, 7.4 Hz, 1H, H-8); 7.22 – 7.02 (m, 15H, PPh_3); UV/Vis (MeOH): 273 nm (4540), 324 nm (sh, 2610), 358 nm (2780), 393 nm (sh, 2450), 460 nm

(sh, 980), 565 nm (440) see, **Figure 3.3**; ESI-(-)-TOF-MS (DMSO): m/z 750.0333 [M-2H-Cl]; calcd for $C_{33}H_{24}N_7O_4PCl^{102}Ru$, 750.0359.

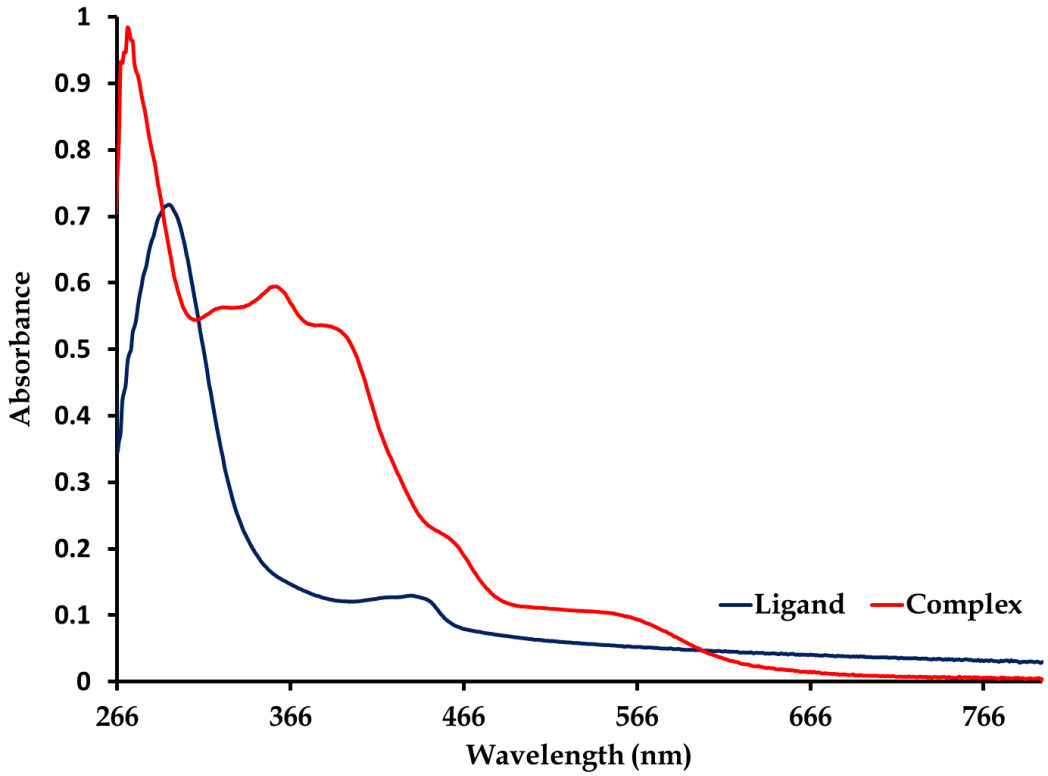

Figure 3. 3: *Overlay UV/ UV-Visible absorption spectra of complex* ***3*** *and the free-ligand, urdp.*

3.2.3 Synthesis of cis-$[Ru(bpy)_2(H_4ucp)](PF_6)_2 \bullet (tppt)$ (**4**)

An equimolar reaction mixture of cis-$[Ru(bpy)_2Cl_2]$ (0.20 g, 0.38 mmol) and H_4ucp (0.15 g, 0.38 mmol) in a mixture of ethanol (16 mL) and distilled water (4 mL) were heated until reflux under a nitrogen atmosphere for 8 h. Afterwards, an aqueous solution of ammonium hexafluorophosphate (≈ 0.25 g in 15 mL water) was introduced into the reaction vessel and the mixture was heated to reflux temperature for the next 0.5 h. The reaction mixture was then cooled to room temperature, forming a red precipitate. This precipitate was collected by gravitational filtration, washed several times with water and dried, affording a dark-red powder. A concentrated solution of the powder in acetonitrile was layered with diethyl ether. Slow diffusion of the latter into the acetonitrile layer yielded red single crystals of XRD quality. Yield: (0.125 g,

49%); mp = 281.2 – 284.9 °C; elemental analysis for $C_{51}H_{49}F_{12}N_{19}O_8P_2Ru \bullet 3H_2O$: calcd, C = 40.81%, H = 3.69%, N = 17.73%; found: C = 40.92%, H = 3.90%, N = 17.41%; IR (ATR, cm^{-1}): ν_{N-H} 3540 (w), 3351 (br, w), $\nu_{C=O}$ 1681 (s), $\nu_{C=N}$ 1598 (s); ^1H NMR (400 MHz, DMSO-d_6): δ_H CH=N: 9.25 (s, 1H), 91,3 (s, 1H); Pyr: 8.28 (dd, J 8.0, 1.4 Hz, 1H), 7.99 (t, J 7.0 Hz, 1H), 8.18 (dd, J 7.9, 1.5 Hz); Bipyr A: 9.00 (dd, J 5.7, 1.1 Hz, 1H), 7.57 (td, J 7.7, 1.4 Hz, 1H), 8.02 (J 7.9, 1.6 Hz, 1H), 8.55 (br d, J 7.6, 1H); Bipyr B: 8.75 (br d, J 8.2 Hz, 1H), 8.26 (td, J 7.9, 1.4 Hz, 1H), 7.69 (ddd, J 7.3, 5.6, 1.2 Hz, 1H), 8.55 (br d, J 7.6 Hz, 1H); Bipyr C: 8.50 (br d, J 8.4 Hz, 1H), 7.82 (dd, td, J 8.1, 1.5 Hz, 1H), 7.25 (ddd, J 7.1, 5.7, 1.2 Hz, 1H), 7.58 (dd, J 5.8, 1.2 Hz, 1H); Bipyr D: 8.55 (br d, J 7.6 Hz, 1H), 7.92 (td, J 7.9, 1.6 Hz, 1H), 7.17 (ddd, J 7.7, 5.6, 1.2 Hz, 1H), 7.38 (br d, J 5.6 Hz, 1H), Uracil: 7.46 (br s, NH_2, 2H), 6.09 (br s, NH_2, 2H), 3.32, 3.061, 3.056, 2.74 (4 x s, 12H, 4 x CH_3); UV/Vis (MeOH): 283 nm (199740), 417 nm (79300), 515 nm (sh, 29400) see, **Figure 3.4**; ESI-(+)-TOF-MS (DMSO): m/z 852.2070 [M-H-2PF_6]; calcd, 852.2057.

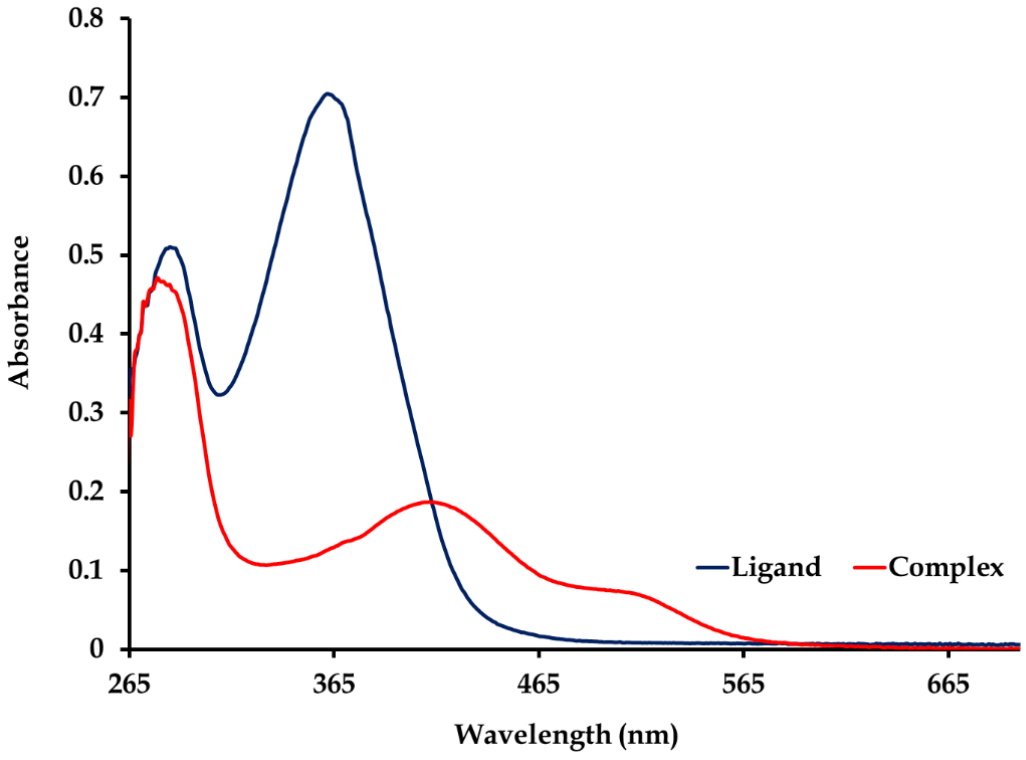

Figure 3. 4: *Overlay UV-Visible absorption spectra of complex* ***4*** *and its ligand, H_4ucp.*

3.2.4 X-ray diffraction

Crystal structure refinement details of only **2** and **3** (CCDC numbers 2202412 and 2202413) are found in **Table 3.1** since a low-resolution solid structure of **4** did not show the presence of the $[Cl]^-$ counter-ions but a 5,6-diamino-1,3-dimethyl-2,4-dioxopyrimidine (tppt) molecule found in its crystal lattice.

Furthermore, pyridine molecules of crystallization were squeezed out of the crystal lattice of **3**.[16]

Table 3. 1: *Crystal and structure refinement data for **2** and **3**.*

Compound	**2**•H_2O	**3**•$5C_5H_5N$
Chemical formula	$C_{35}H_{29}Cl_2N_{11}O_5Ru$	$C_{58}H_{51}Cl_2N_{12}O_4PRu$
Formula weight	855.66	1183.04
Temperature (K)	100(2)	102(2)
Crystal system	Monoclinic	Monoclinic
Space group	$P2_1/c$	$P2_1/n$
Unit cell dimensions (Å, °)	a = 9.6637(3)	a = 13.1749(3)
	b = 14.2268(4)	b = 19.4693(4)
	c = 25.4731(6)	c = 20.9466(5)
	α = 90	α = 90
	β = 91.1190(10)	β = 100.833(1)
	γ = 90	γ = 90
Crystal size (mm)	0.34 × 0.07 × 0.045	0.15 × 0.13 × 0.08
V ($Å^3$)	3501.46(17)	5277.2(2)
Z	4	4
Density (calc.) (Mg/m^3)	1.623	1.489
Absorption coefficient (mm^{-1})	5.55	4.12
F (000)	1736	2432
θ range for data collection (deg)	3.5°; 72.3°	3.1°; 67.5°
Index ranges	-11 ≤ h ≤ 9 -17 ≤ k ≤ 17 -31 ≤ l ≤ 31	-15 ≤ h ≤ 15 -23 ≤ k ≤ 23 -25 ≤ l ≤ 25
Reflections measured	76788	113041
Observed reflections (I > 2σ (I)	6267	9482
Independent reflections	6763	4729
Data/ restraints/ parameters	6267/ 3/ 493	9419 / 0/ 433
Goodness of fit on F^2	1.09	1.10
Observed R; wR^2	0.026; 0.072	0.052; 0.155
R_{int}	0.040	0.027

3.2.5 Computational details

Indicative of the reported computational studies conducted on parent metal complex **1**, tandem geometry and frequency simulations of **2 – 4** were performed using Gaussian 09W. In particular, the calculations were executed at the Density Functional Theory (DFT) level, and the B3LYP functionals were applied. In addition, a hybrid basis set was used where the non-metals and metal were assigned to the 6-311G^{++} (d, p) and the LANL2DZ basis sets, respectively.[17] Starting conformers of the individual metal compounds were generated directly from their corresponding solid-state structures after removing solvent molecules of recrystallization and counter-ions.

3.2.6 Molecular docking

PatchDock was utilized to study the rigid molecular docking between the ligand (i.e. metal complex) and the receptor (i.e. biomolecule).[18] More specifically, the algorithms are applied to search suitable vacant spaces (patches) where the static ligand can fit. Complementary intermolecular interactions are determined based on the nature of the receptor, which dictates the orientation of the ligand within the binding site. For PatchDock parameters, a clustering RMSD of **4** and a complex type of protein small ligand were used in these simulations.

3.2.7 Transmission electron microscopy (TEM)

TEM micrographs were captured using a JEOL 1400 microscope. TEM samples **1-4** were prepared by incubating amylin at 50 μM in the presence or absence of the respective metal complexes (at 160 μM) for 72 h at a physiological temperature of 37 °C. Subsequently, the HIAPP fibers were negatively stained with uranyl acetate. The positive control is the TEM micrograph of amylin alone. ImageJ software was used to obtain the estimated sizes of the particles.[19]

3.2.8 Stability studies

The aqueous stabilities of the respective metal complexes **1-4** were evaluated by monitoring their electronic spectra at a physiological temperature of 37 °C for 24 h at 1-h intervals to simulate in vivo conditions.[13] Standard (1 mM) solutions of different metal complexes were prepared in aqueous PBS containing 2% DMSO (v/v). UV-Visible absorption spectra of **1** and **3** in anhydrous DMSO saturated with lithium chloride were also recorded at hourly intervals for 24 h to check the kinetic stability towards chloride ligand exchange by DMSO. Electronic spectra of **1** and **3** were also evaluated in a high-purity non-coordinative solvent, dichloromethane (DCM), to contrast with the possible displacement of chloride co-ligands from these metal complexes by DMSO solvent molecules.

3.2.9 Cell viability and in vitro glucose metabolism studies

Cell viability was conducted in the Chang liver cell lines to assess the cytotoxic effects of ruthenium complexes. The assessment used the 3-(4,5-dimethylthiazol-2-yl)-2,5-diphenyltetrazolium bromide (MTT) assay originally described by Mosmann.[20] Trypsinisation and seeding of cells into 96-well plates at a seeding density of 1.8 x 10^4 cells/well followed thereafter and the cells were incubated for 24h to allow attachment and growth of cells to semi-confluency. Thereafter, the cells were incubated with three different ruthenium complexes (**2**, **3** and **4**) with three doses (12.5, 25 and 50 µmol/L) at 37^{o}C for 12, 24 and 48 h, respectively. After each incubation period, the treatment media was discarded, and the cells were re-immersed in 20 µL MTT salt solution (5 mg MTT in 1 mL 0.1M PBS) and 100 µL culture media. The cells were incubated for 4 h to allow for the formation of blue formazan crystals. The MTT solution was then replaced with DMSO (100 µL/well) and incubated for 1 h at 37 °C. The optical density of the formazan product was quantified using spectrophotometry (Bio-Tek µQuant, Winooski, VT, USA) at 570/690. The percentage cell viability was then calculated as follows:

$$\% \text{ Cell Viability} = \frac{\text{Average OD of treated cells}}{\text{verage OD of control cells}} \text{ X } 100\ \% \qquad (\mathbf{1})$$

A well-established cell culture protocol was used in this study.[21] The glucose utilization experiments were conducted as previously described by Ventera et al.[22] with slight modifications. Glycogen analysis was performed in liver cells harvested at 48 h. Glycogen assays were conducted using a well-established laboratory protocol by Musabayane et al.[23]

3.3 Results and discussion

3.3.1 Synthesis and spectral characterization

The parent metal compound **1** was resynthesized as reported, and its purity was confirmed by elemental analysis.[12] A structural analog of **1**, the diamagnetic ruthenium(II) complex **3** was synthesized by the coordination reaction of trans-$[RuCl_2(PPh_3)_2]$ with urdp where it acted as a neutral tridentate chelator in **1**, see **Scheme 3.1**. The bis-uracil diimines, urdp (in **2**) and H_4ucp (in **4**) coordinate via their mutual $N_{pyridyl}N_{imino}$ donor set to the cis-$[Ru(bpy)_2]^{2+}$ core. Two chloride anions stabilize the complex cation of **2** while a co-crystallized 1,3,6,8-tetramethylpyrimidopteridin-2,4,5,7-tetrone (tppt) molecule was also observed in the low-resolution X-ray structure of **4**. It has been reported that tppt can be formed by the reaction of 5,6-diamino-1,3-dimethyluracil (H_2ddd) with various transition metal species, which suggests that H_4ucp underwent hydrolysis and the resultant H_2ddd undergoes oxidative deamination followed by condensation to yield tppt.[24] However, the presence of the $[PF_6]^-$ counter-ions in **4** was confirmed by elemental analysis.

The new compounds **2–4** are red crystalline materials that are fully soluble in DMF and DMSO, partial solubility in alcoholic media, and insoluble in non-polar solvents. In particular, the metal complex salts **2** and **4** illustrate good solubility in the aprotic solvent acetonitrile, and as expected, **2 – 4** completely dissolve in the high boiling point solvents DMF and DMSO. Noticeably, higher conversion yields for **2** and **3** were obtained, whereas the yield of **4** was impacted by the conversion of half the molar ratio of its free-ligand, H_4ucp converting to tppt.

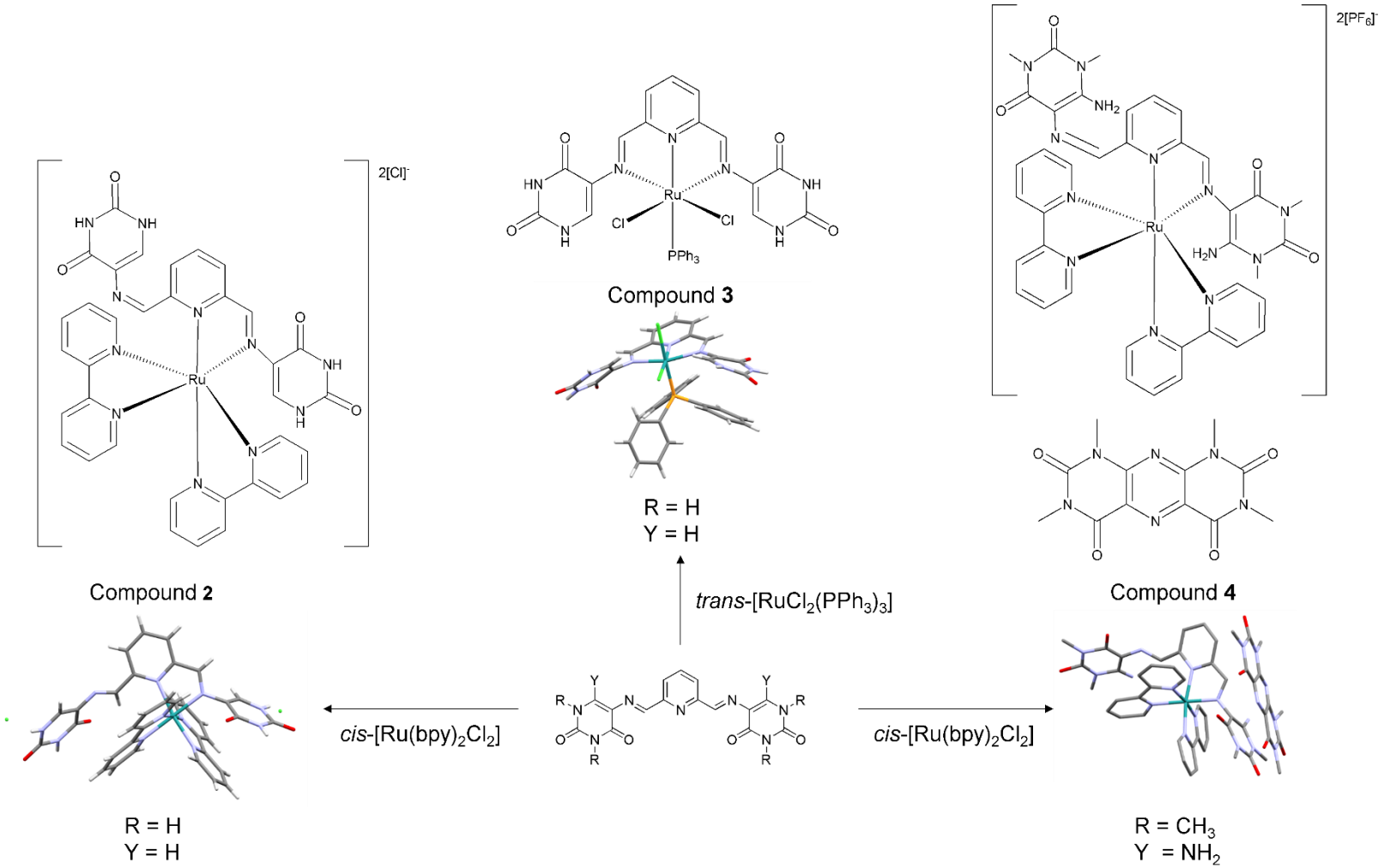

Scheme 3. 1: *Synthetic scheme illustrating the formation of* **2 – 4**. *The low-resolution solid structure of* **4** *did not show the presence of the* $[PF_6]^-$ *counter-ions, but a 1,3,6,8-tetramethylpyrimidopteridin-2,4,5,7-tetrone (tppt) molecule was found in its crystal lattice.*

3.3.2 Computational studies

Method validation was established based on the close correlation of the geometrical parameters between the starting and optimized compounds, see **Figure 3.5.** Minor deviations in the computed and experimental geometrical parameters can be accounted for by the absence of inter- and intramolecular interactions in the gas-phase computed molecule as was experienced in the X-ray crystal structure.[25] Frequency calculations were also carried out at the same level of theory to ensure that each optimized structure is a global minimum on the potential energy surface.

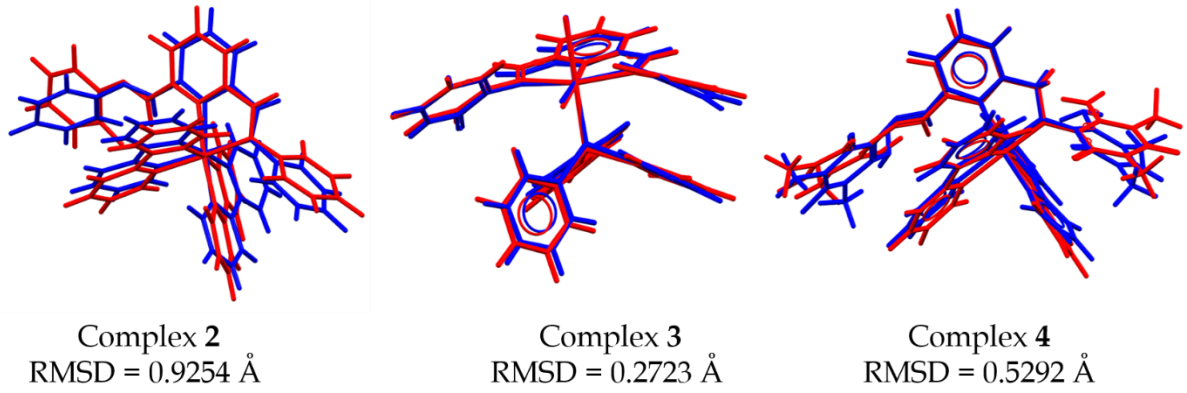

Figure 3. 5: *The corresponding super-imposed optimized and computed structures of* **2** *–* **4** *with their respective root mean square deviation (RMSD) values. The red structures are the optimized structures, while the blue structures are their corresponding experimental structures.*

Characteristic of Schiff bases coordinating through the imino nitrogen atoms, the experimental IR spectra of **2** [ν(C=N) at 1648, 1627, and 1600 cm^{-1}], **3** [ν(C=N) at 1629 and 1594 cm^{-1}] and **4** [ν(C=N) at 1598 cm^{-1}] illustrate that their imino bands vibrate at different energies than the corresponding infrared stretches of the free-ligands: H_4ucp [ν(C=N) at 1586 cm^{-1}] and urdp [ν(C=N) at 1628 cm^{-1}], see **Figures 3.6 - 3.8**. Computationally, the higher degrees of freedom of the uncoordinated imino bonds induce vibrations with higher energies occurring at lower frequencies (1677 cm^{-1} for **2** and 1625 cm^{-1} for **4**) in comparison to the coordinated imino bonds vibrating at 1665 cm^{-1} for **2** and 1619 cm^{-1} for **4**. In the case of **3**, the Schiff base functionality manifests in the form of a weak broad vibration found at 1630 cm^{-1}, which is accounted for by

the symmetrical imino bonds experiencing rigidity in stabilizing the ruthenium(II) center.

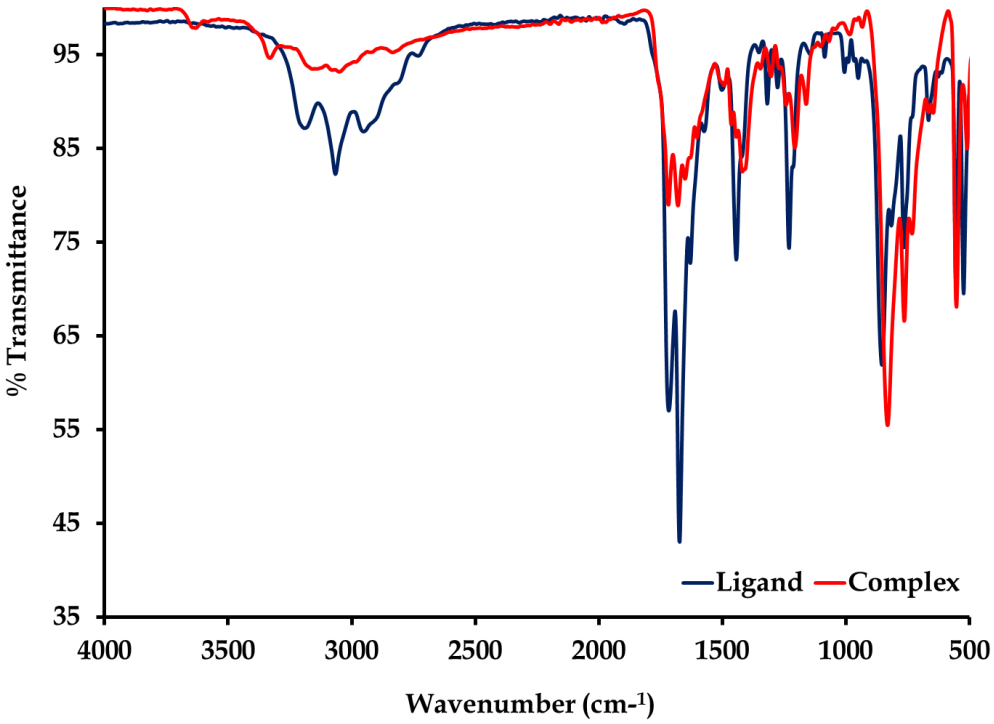

Figure 3. 6: *Overlay IR spectrum of the free-ligand, urdp, and complex* **2** *between 4000 and 650 cm-1.*

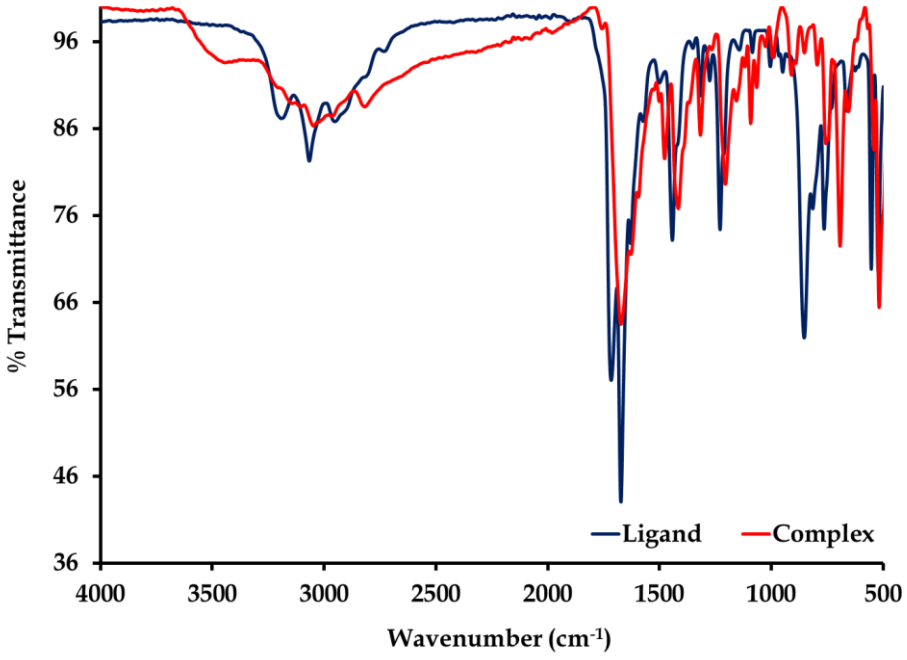

Figure 3. 7: *Overlay IR spectra of the free-ligand, urdp, and complex* **3** *between 4000 and 500 cm-1.*

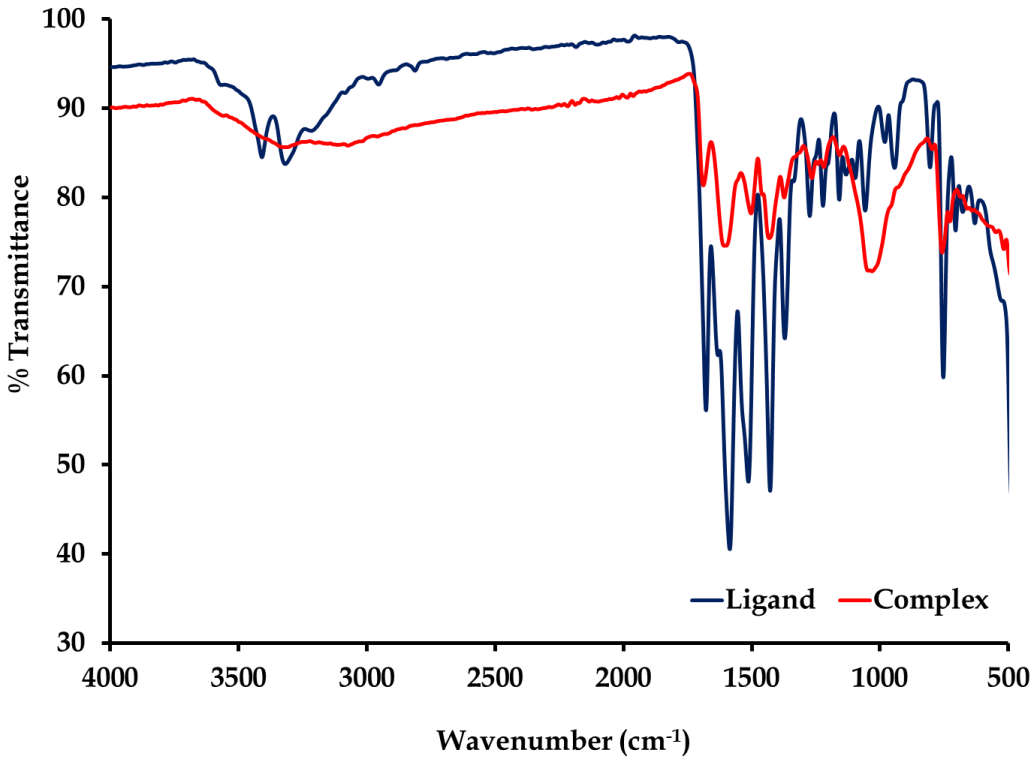

Figure 3. 8: *Overlay IR spectra of the free-ligand, H_4ucp, and complex* **4** *between 4000 and 500 cm^{-1}.*

In the overlay IR spectra of **3** and its free-ligand urdp, it is evident that the uracil ketonic vibrations have coalesced (at 1675 cm^{-1}) in comparison to the free ligand's two infrared stretches found at 1717 and 1679 cm^{-1}. In contrast, the corresponding signals in **2** (at 1717 and 1679 cm^{-1}) and **4** (at 1681 cm^{-1}) are found essentially at the same frequencies as those of the corresponding free-ligand: H_4ucp (at 1681 cm^{-1}). Similarly, the related computed uracil C=O bonds of respective compounds vibrate intensely in a similar trend where for **2,** two vibrational bands occurred at 1666 and 1655 cm^{-1}, while solitary stretches for **3** (at 1684 cm^{-1}) and **4** (at 1763 cm^{-1}) were observed.

The solid-state FTIR spectrum of **3** illustrates the distinctive vibration of the ruthenium-to-phosphorus bond, which was typical of other comparable ruthenium compounds with ν(Ru-PPh_3) signals in the range 683 and 694 cm^{-1}. [30] As expected; other commonalities could also be found between the actual respective overlay infrared spectrum of the free-ligands and the respective metal complexes in terms of their ν(NH) signals. In particular, the stretches of the metal complexes (at 3634 and

3325 cm^{-1} for **2**, at 3465 cm^{-1} for **3,** and 3540 cm^{-1} for **4**) were found in similar positions as those of the different free ligands. These experimental assignments were further supported by the calculated bond stretches appearing at 3616, 3607, 3586, 3583 cm^{-1} for **2**, 3632, 3604 cm^{-1} at **3**, for 3617, 3630 (symmetrical) and 3740, 3754 (asymmetrical) cm^{-1} at **4**.

For instance, in the HOMO configuration of **2**, the electron density is found on a non-coordinating uracil group and the diimino(pyridyl) chelating unit. In contrast, in its LUMO configuration, a noticeable accumulation of electron density occurs on the pyridyl ring. These computational trends support the experimental ligand-based electronic transitions of **2** while computationally, reduction in the d-orbital electron cloud within the LUMO surface compared to the HOMO surface shows that the actual charge transfer band is an MLCT electronic transition.

The HOMO surface of **3** displayed minimal electron density contributions from the diimine ligand. In contrast, extensive stabilization of the HOMO configuration is afforded by the prominent electron density of the metal center and the chloro co-ligands. Visible reductions of the chlorides' frontier orbitals are observed within the LUMO configuration, which suggest charge transfers occurred from the aforementioned ligands to the metal center, which, in turn, means that the experimental CT-band is LMCT-based. Computational evidence for the experimental intra-ligand electronic transition manifests computationally in the form of high electron density residing on the diimino(pyridyl) moiety.

Experimental vibrational band assignments for the different metal compounds **2–4** were made with the aid of frequency calculations conducted at the DFT level using the pre-specified hybrid base set, see **Figure 3.9**. A detailed discussion of these simulated and experimental IR spectra can be found in the online supporting information document. Furthermore, overlay UV-Visible absorption spectra of the novel ruthenium compounds and their corresponding free ligands were recorded in analytical grade DMSO due to the high solubility of the former in the solvent. The experimental electronic spectra of these metal complexes have distinctive charge

transfer bands at higher wavelengths. The nature of these electronic transitions was established by evaluating their computed frontier orbitals.[26] Computed frontier orbitals of **2 – 4** illustrate significant contributions from the Schiff-base chelating ligands, which in turn corroborates the presence of prominent experimental intra-ligand-based transitions, refer to **Table 3.2**. A detailed discussion is given in the supporting information document.

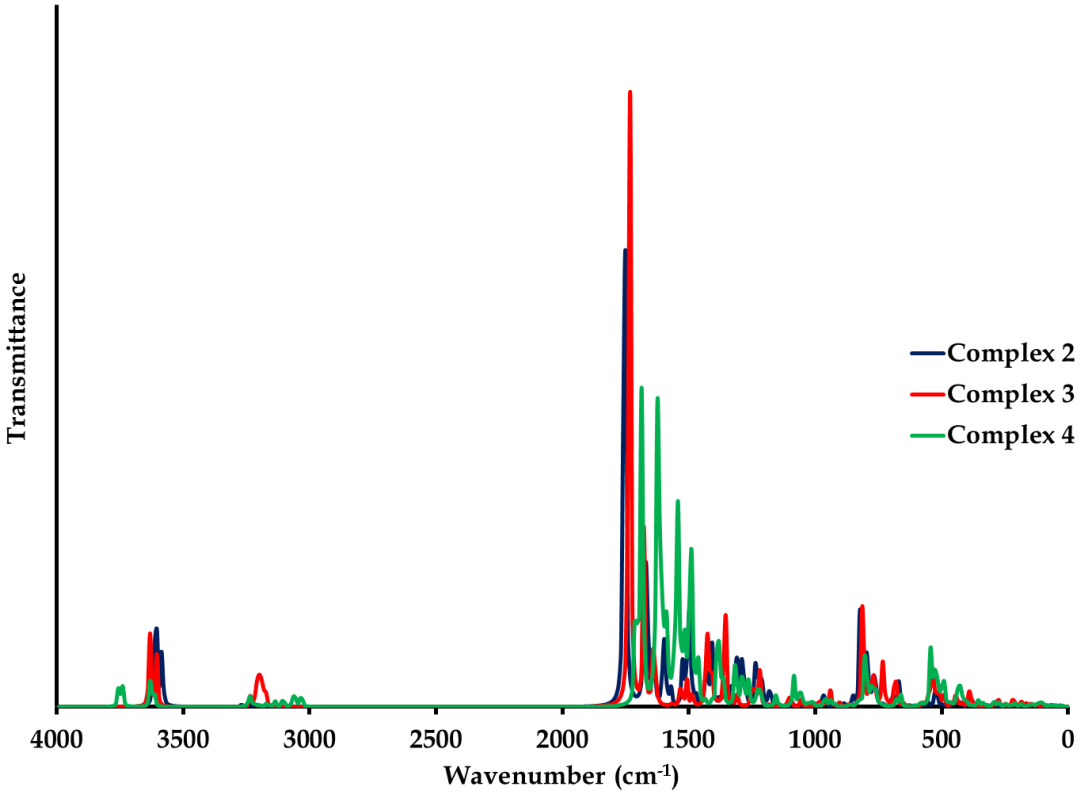

Figure 3. 9: *Overlay of calculated IR spectra of* ***2 – 4****.*

Pivotal in understanding the mechanism of activities for ruthenium-based anti-cancer drugs is to assess the stabilities in aqueous and organic media. It is well known that many ruthenium compounds are considered pro-drugs that are activated through in vivo hydrolysis. Subsequently, the labile Ru-H_2O bonds of the active specie allow interaction with the biological target of concern through its aqua-ligand displacement.[27]

Time-dependent UV-Vis spectrophotometric experiments were used to evaluate the solution stabilities of **1 – 4**, see **Figures 3.10 – 3.13**. To provide context to this study, it is important to note that the in vitro and in vivo studies conducted on reference

compound **1** were done in a 2% DMSO - 98% PBS UPW (ultrapure water) mixture.[12] Therefore, the electronic spectra of **2–4** were also monitored in the solution mixture mentioned above at a physiological temperature over 24 h with 1 h data collection intervals. No significant electronic spectral changes were observed for **2** and **4**, which implies that these compounds retain their structural integrities in solution, see **Figure 3.10** and **Figure 3.11**. However, solvatochromic effects are evident when comparing the electronic spectra of each metal complex conducted within the solvent mixture and methanol, respectively.[28] Metal complexes **1** and **3** containing the chloro co-ligands displayed characteristic electronic spectral changes associated with hydrolysis when their solution stabilities were recorded in 2% DMSO - 98% PBS, see **Scheme 3.2**, **Figures 3.12 - 3.13**.[29]

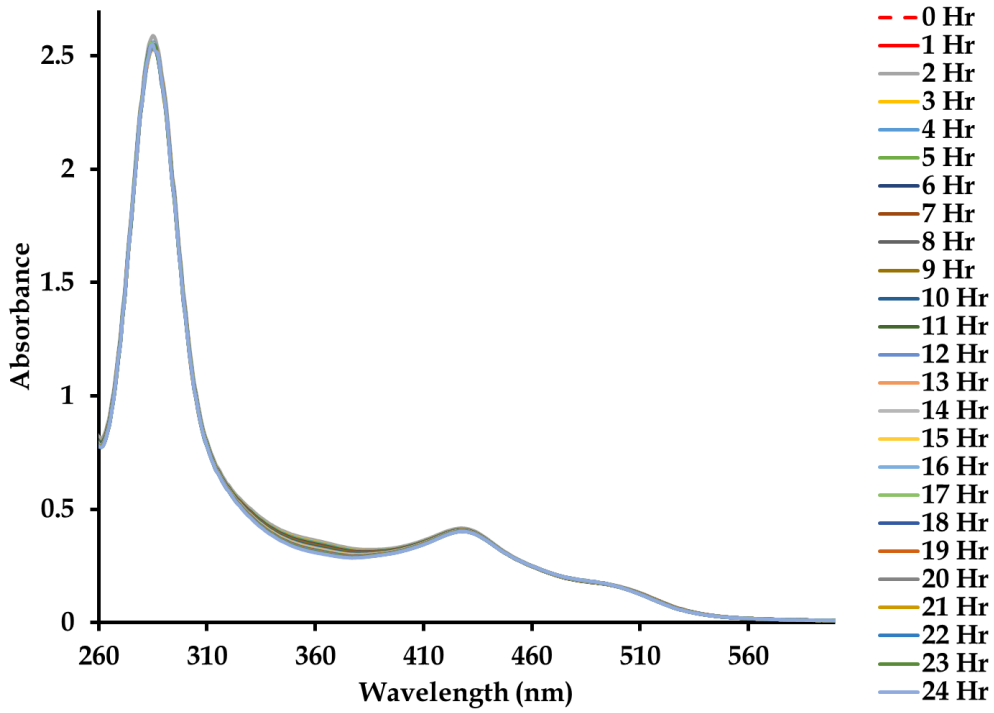

Figure 3. 10: *Time-dependent stability study conducted on* **2** *in a 2%: 98% (v:v) DMSO-PBS solution (250 µM, 298 K) monitored over 24 h period using UV-Vis spectrophotometry.*

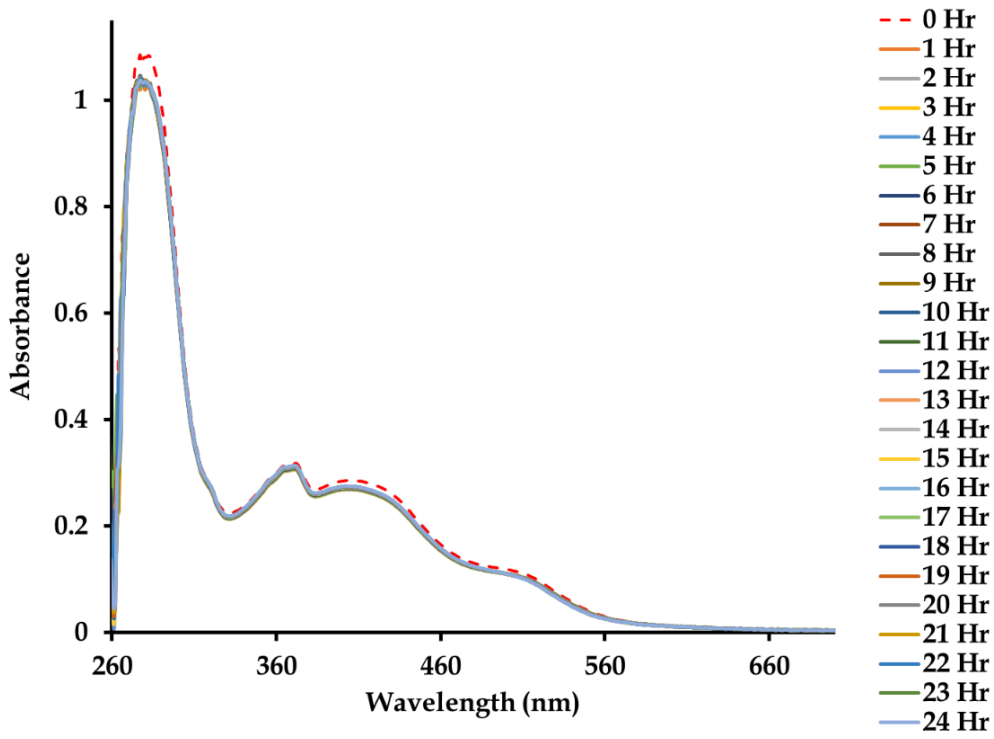

Figure 3. 11: *Time-dependent stability study conducted on* ***4*** *in a 2%: 98% (v:v) DMSO-PBS solution (250 µM, 298 K) monitored over 24 h period using UV-Vis spectrophotometry.*

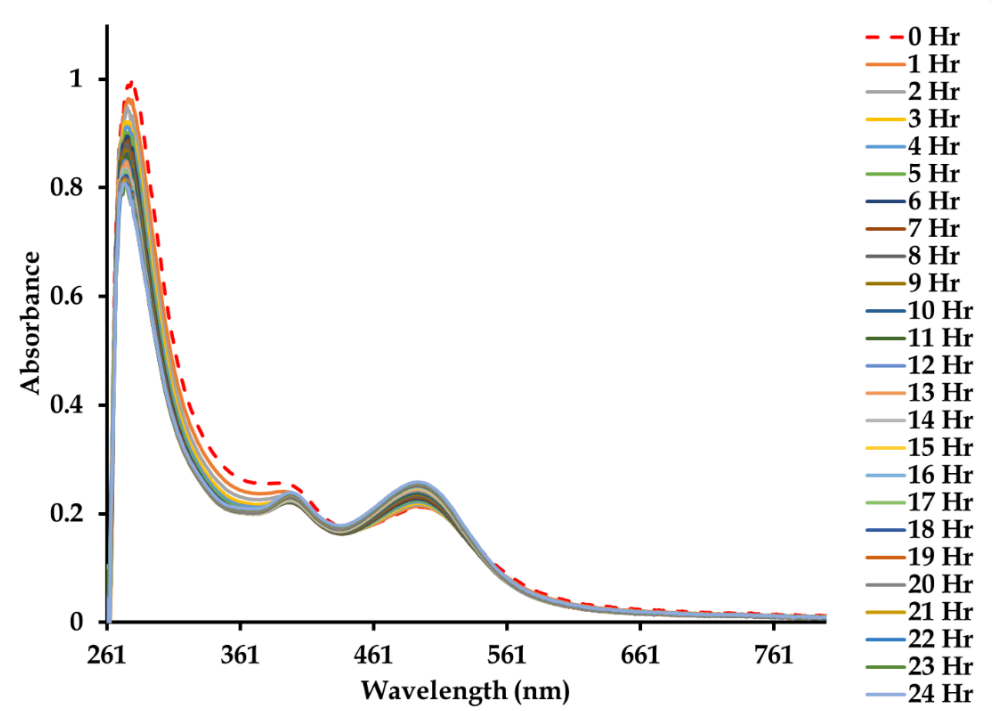

Figure 3. 12: *Time-dependent stability study conducted on* ***1*** *in a 2%: 98% (v:v) DMSO-PBS solution (250 µM, 298 K) monitored over 24 h period using UV-Vis spectrophotometry.*

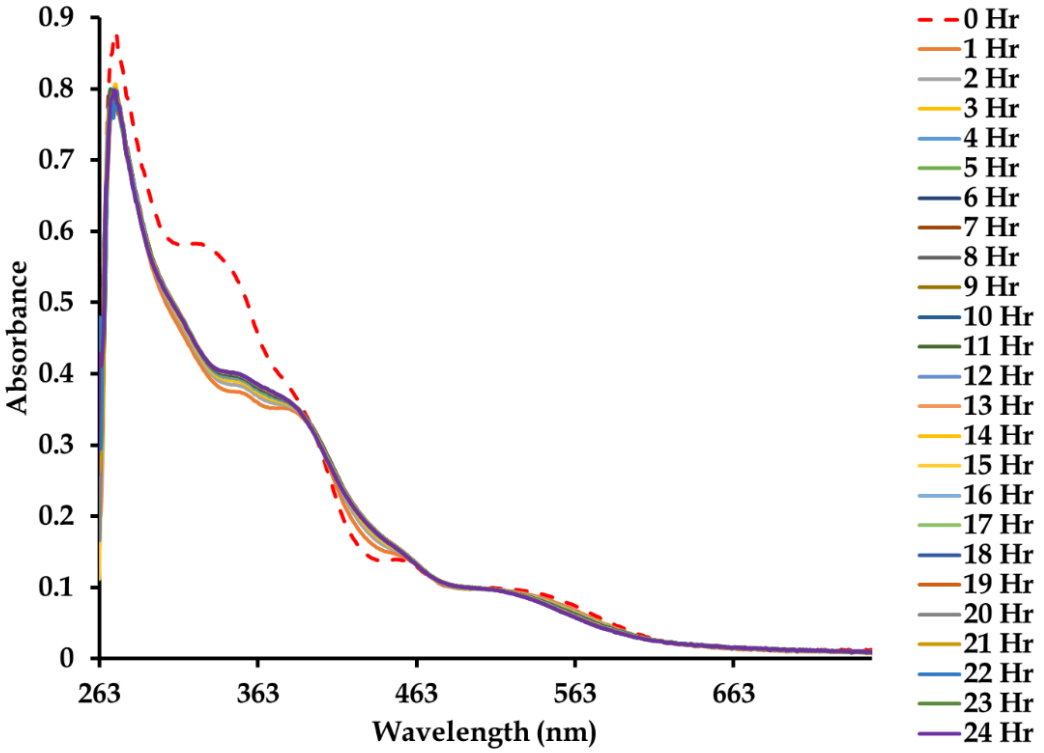

Figure 3. 13: *Time-dependent stability study of* ***3*** *in 2% (v:v) DMSO-PBS solution (250 µM, 298 K, 24 h) monitored by UV-Visible absorption spectrophotometry.*

The stabilities of complexes **1** and **3** were also assessed in analytical-grade DMSO. The resultant electronic spectral profiles confirmed the displacement of the chloro co-ligands by the solvent, see **Figures 3.14 - 3.15**. More specifically, for **1**, the intraligand transition occurring at 277 nm undergoes hypochromism while a hypsochromic shift of the CT-band from 512 nm to 530 nm was observed. The formation of Ru-DMSO species of **3** is evident from the well-defined isosbestic points observed at 354 nm and 462 nm, which suggest that the chloro co-ligand substitutions do not occur simultaneously.[30] Additionally, the decreasing CT bands at 336 and 350 nm are interlinked through the first isosbestic point with the CT bands at 372 and 392 nm, which underwent progressive hypochromism and eventually coalesced into a broad band at 383 nm. This experimental observation supports the first substitution of the chloro co-ligand by a water molecule. The second chloro substitution is illustrated by the more diffused isosbestic point at 462 nm, which is accompanied by shifts in the intra-ligand transitions and CT bands. This emphasizes the redistribution of electron

density within the Schiff-base chelating ligand. In particular, there is a blue shift of the CT band at 476 nm to 473 nm and a decrease in the intensity of the CT band at 571 nm.

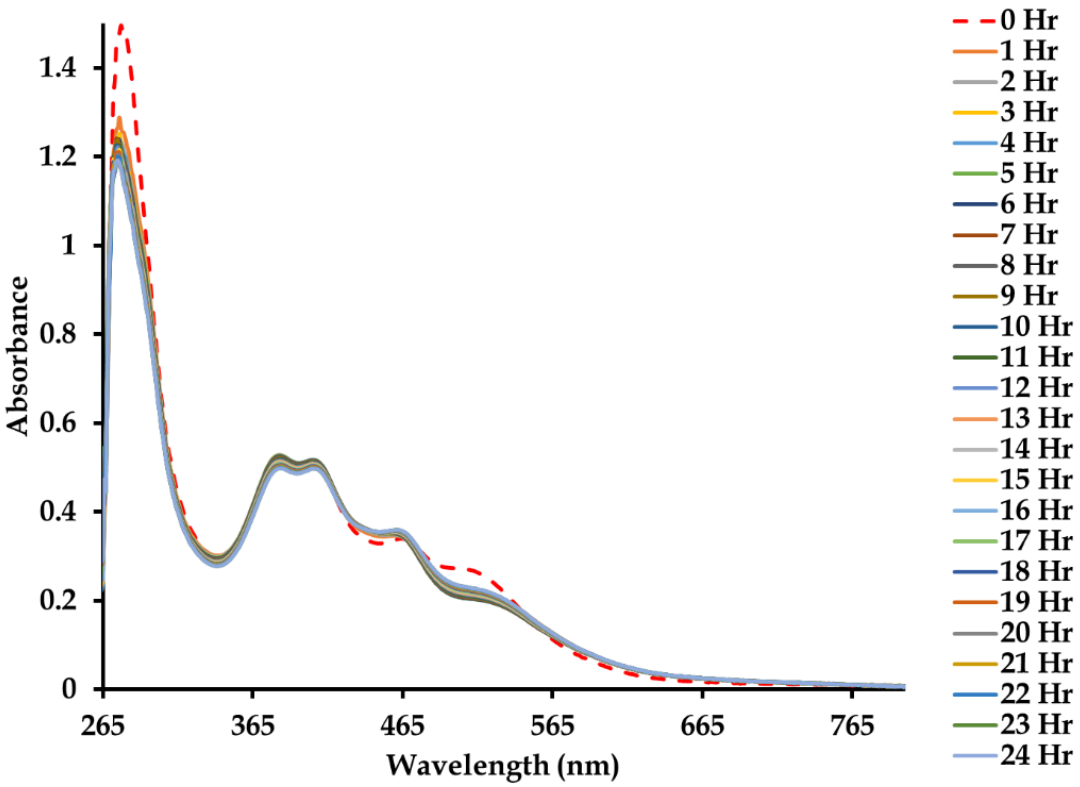

Figure 3. 14: *Time-dependent stability study of* ***1*** *in DMSO (10^{-5} M, 298 K, 24 h) monitored by UV-Visible absorption spectrophotometry.*

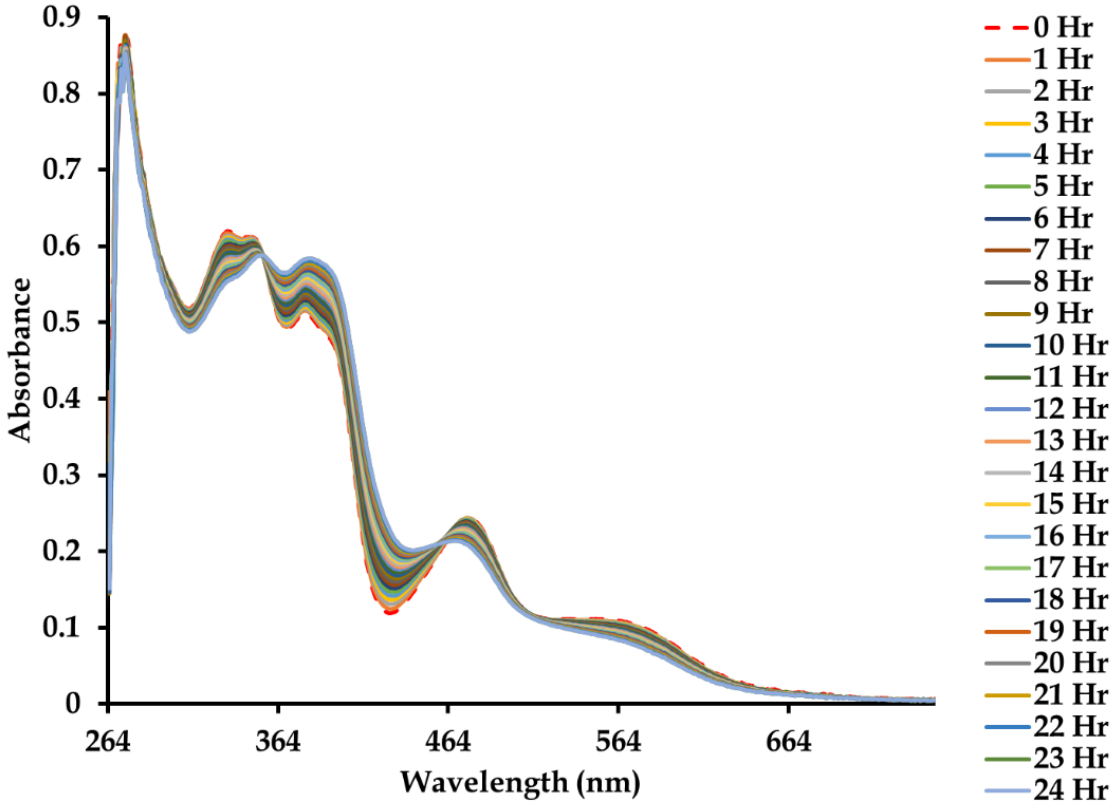

Figure 3. 15: *Time-dependent stability study of* ***3*** *in DMSO (10^{-5} M, 298 K, 24 h) monitored by UV-Visible absorption spectrophotometry.*

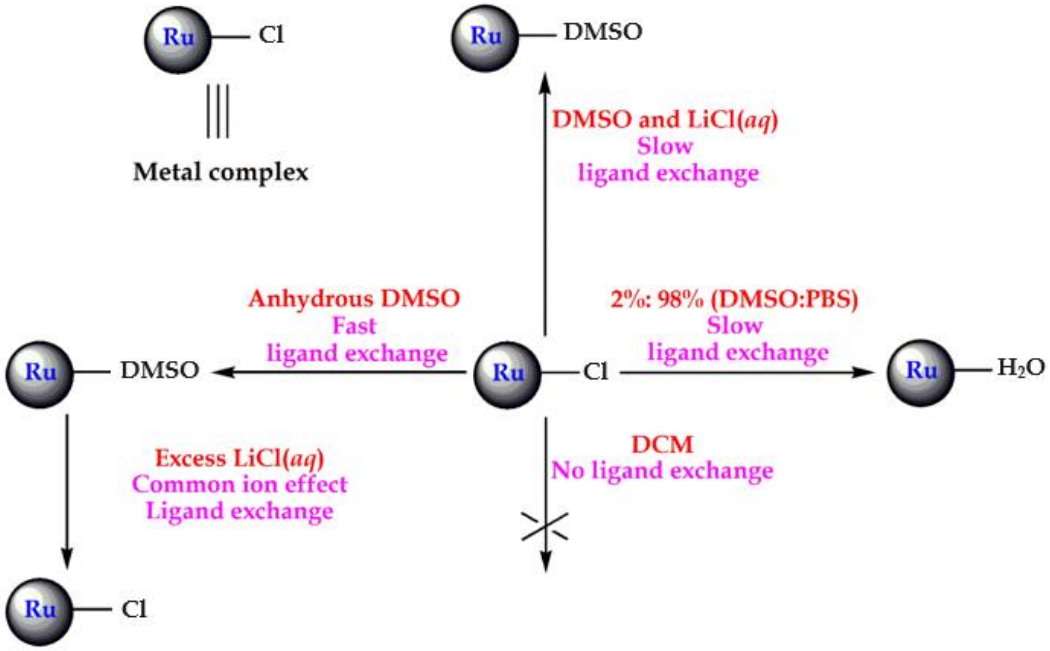

Scheme 3. 2: *Pictorial representation of the stabilities of* ***1*** *and* ***3*** *in different solution media.*

Afterward, the solution stabilities of **1** and **3** were recorded in a saturated aqueous solution of lithium chloride, and the observed electronic spectral changes were synonymous with retardation of halide displacements from the coordination sphere of diamagnetic ruthenium(II) compounds by water, see **Figures 3.16** and **3.17**. The suppression of the chloro substitution and its seemingly slower kinetics could be readily rationalized by the common-ion effect. As expected, no ligand substitution took place in the non-coordinative solvent dichloromethane (DCM), see **Figures 3.18** and **3.19**.[30] Hence, as per **Scheme 3.2**, it was concluded that the chloro-containing metal complexes undergo rapid ligand displacement with DMSO before hydrolysis in the phosphate-buffered saline solvent mixture.

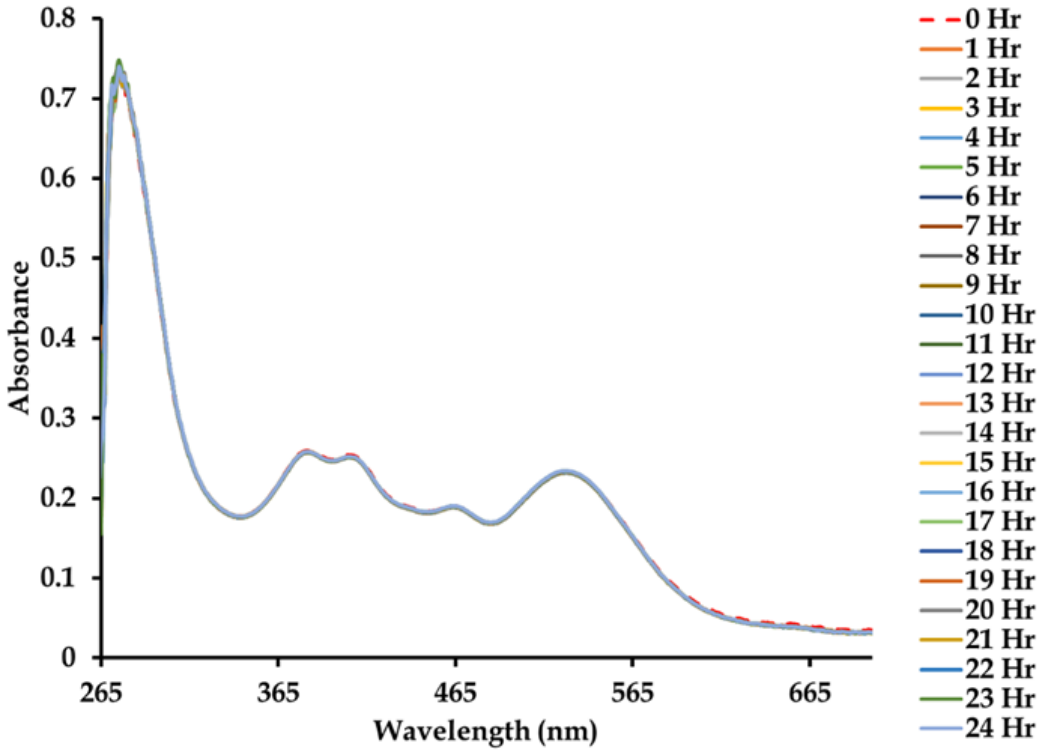

Figure 3. 16: *Time-dependent stability study of* ***1*** *in a solution of DMSO and saturated LiCl (10^{-5} M, 298 K, 24 h) monitored by UV-Visible absorption spectrophotometry.*

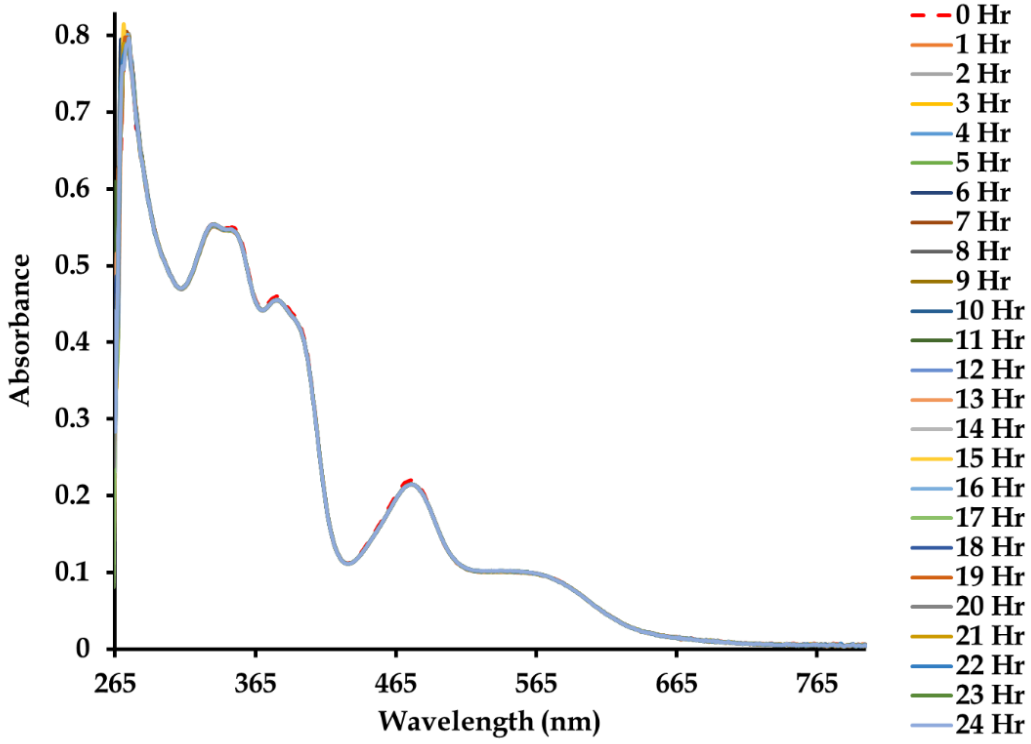

Figure 3. 17: *Time-dependent stability study of* ***3*** *in a solution of DMSO and saturated LiCl (10^{-5} M, 298 K, 24 h) monitored by UV-Visible absorption spectrophotometry.*

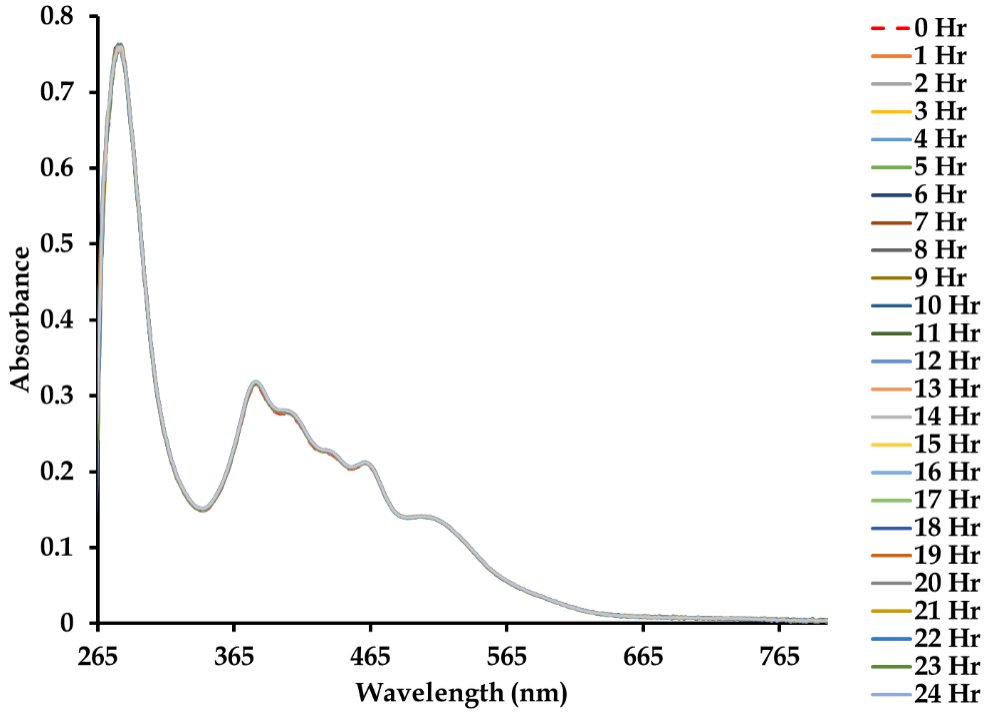

Figure 3. 18: Time-dependent stability study of **1** in DCM (10^{-5} M, 298 K, 24 h) monitored by UV-Visible absorption spectrophotometry.

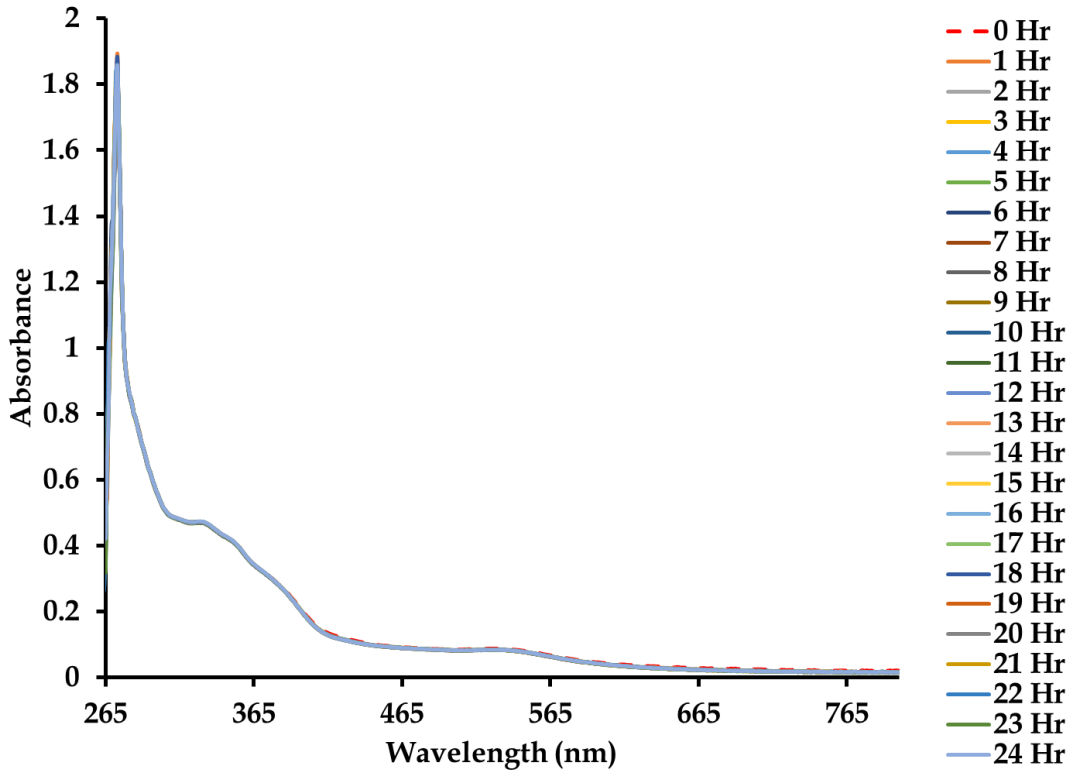

Figure 3. 19: *Time-dependent stability study of 3 in DCM (10^{-5} M, 298 K, 24 h) monitored by UV-Vis spectrophotometry.*

Computed energies of the optimized conformers justify the trends in their solution stabilities; refer to **Table 3.2**. Noteworthy is that the calculated band gaps (ΔE) of **1** or **3** are more significant than that of **2** but lower than that of **4**. The anomalous band gap energy of **4** is ascribed to the difference in energies of the respective HOMOs of **2** and **4.** Tandemly, the former experience enhanced stabilization by the inductive transfer of electron density of the methyl groups into the uracil rings.[31] Moreover, the Ru metal centers of **1** and **3** bear lower computed natural population analysis (NPA) charges than those of the counterparts **2** and **4** since the former complexes are coordinated with two chloride anions compared to the neutral N-donors of the latter complexes.[32]

Table 3. 2: *Summary of the computational data of metal complexes* ***1*** *-* ***4****. Band gap energies are expressed in electron volt (eV).*

Parameter	**1**	**2**	**3**	**4**
NPA charge of Ru atom	-0.109	+0.640	-0.137	+0.640
Band-gap energy (eV)	2.469	3.037	2.727	2.3508
HOMO surface	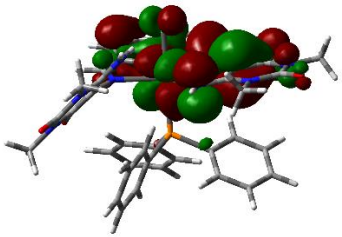	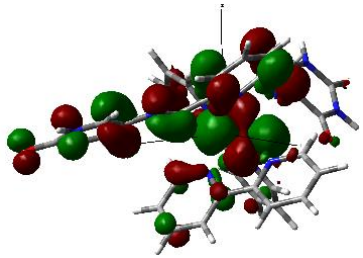	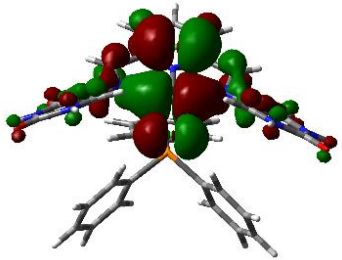	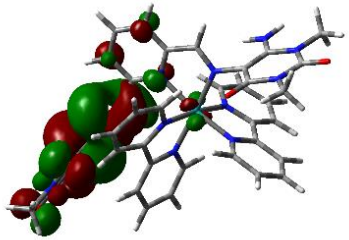
LUMO surface	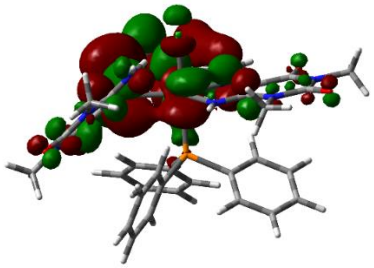	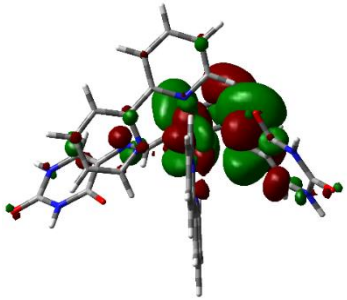	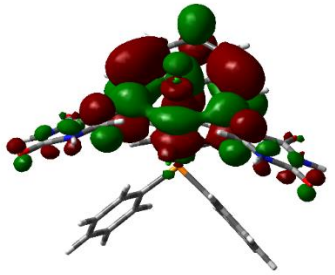	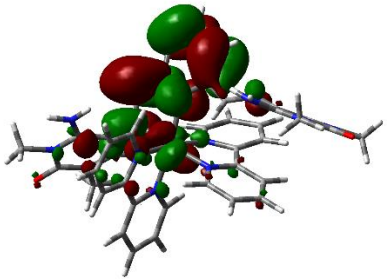

Comparing the one-dimensional proton ^{1}H NMR spectra in deuterated DMSO of the novel metal complexes (**2-4**) and their corresponding free-ligands, distinctive differences are noticed in the positions where the respective imino singlets are resonating, see **Figures 3.20– 3.22**. The structurally similar metal complex salts **2** and **4** produced nearly identical signals when comparing the Schiff-base signals with those of the related free ligands. More specifically, the symmetrical free Schiff-base ligands afford one imino signal (H_4ucp at δ_H 9.70 and urdp at δ_H 9.54 ppm) integrating for two protons each in the respective ^{1}H NMR spectra. In contrast, the coordinated Schiff-base chelators are asymmetrical based on the fact that the imino singlets occur at different positions (at δ_H 9.26, 9.13 ppm for **2,** and at δ_H 9.31, 8.77 ppm for **4**).

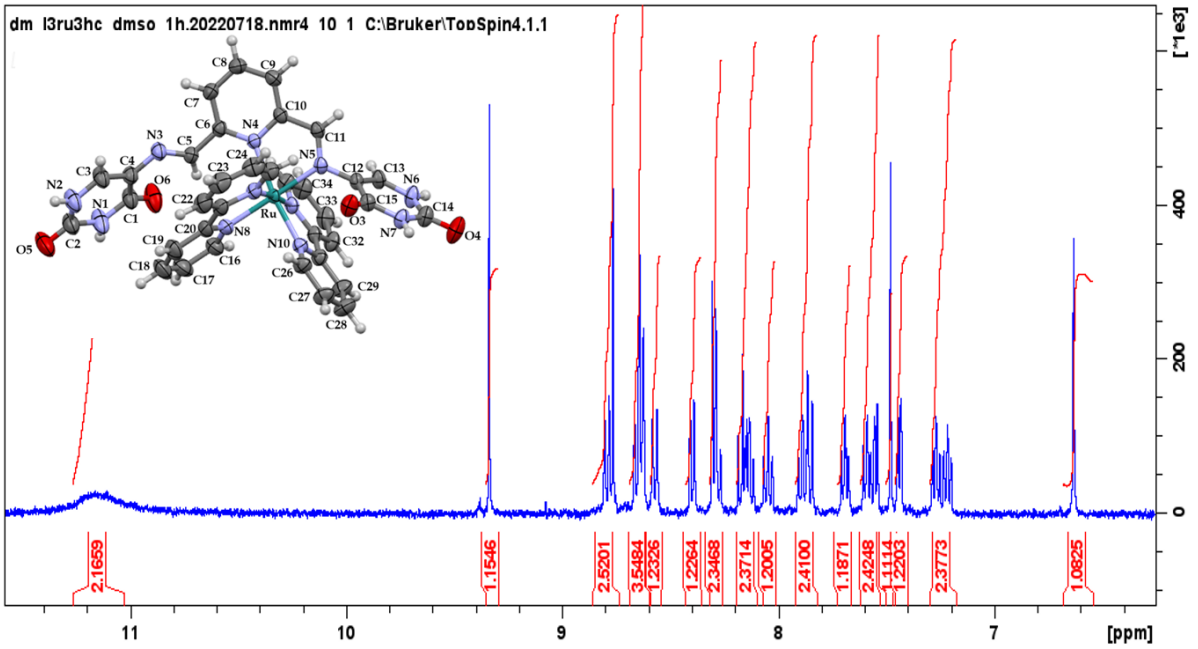

Figure 3. 20: *^{1}H NMR spectrum of* **2**.

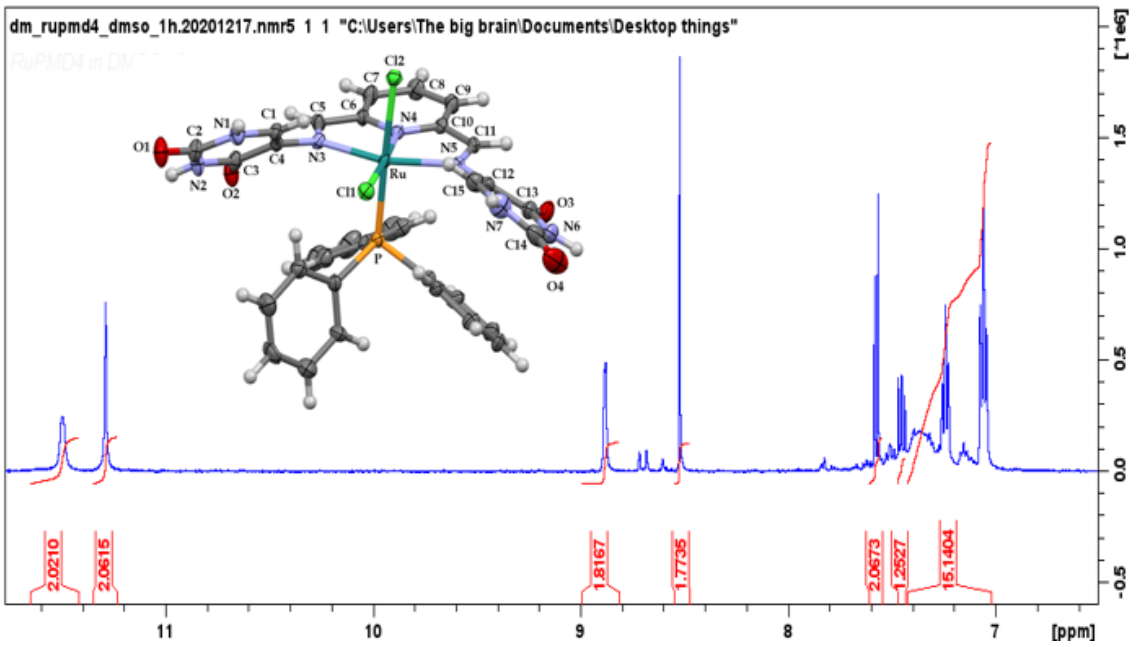

Figure 3. 21: *^{1}H NMR spectrum of* ***3****.*

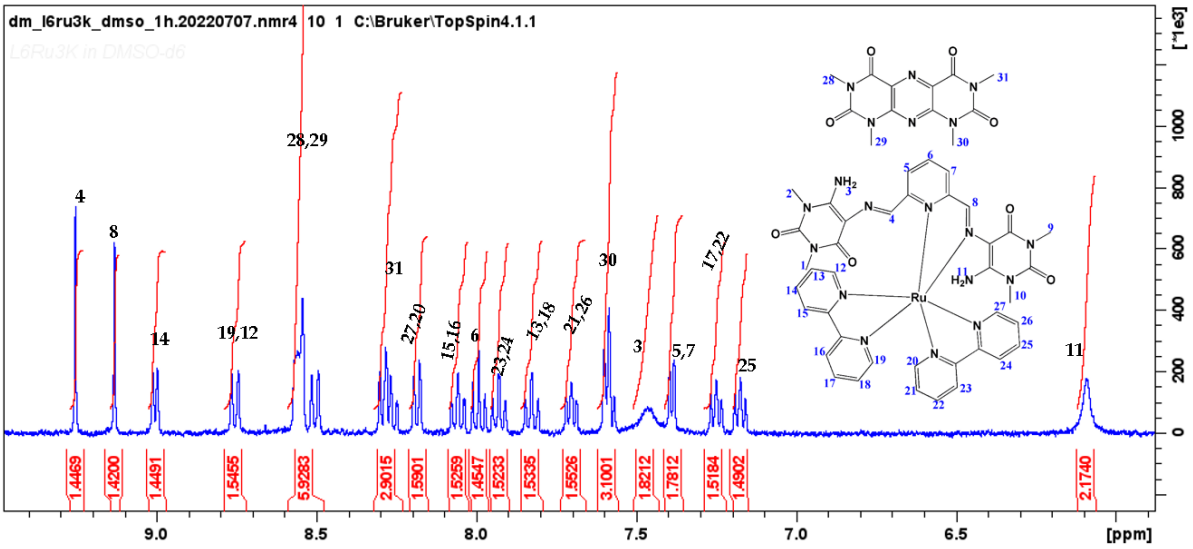

Figure 3. 22: *^{1}H NMR spectrum of* ***4****.*

As expected, the symmetry retainment of the urdp Schiff-base chelator in **3** leads to the imino protons resonating as one signal, similar to what is found in the ^{1}H NMR spectrum of its free-ligand. In addition, there is a distinctive upfield shift in the imino singlet of **3** (at δ_H 9.35 ppm) when compared to its free-ligand (urdp at δ_H 9.54 ppm), which is a typical spectral feature for Schiff-bases coordinating to a cis-[$RuCl_2(PPh_3)$] moiety. [30] Time-dependent ^{1}H NMR studies of **3** collected in DMSO-d_6 corroborated that this metal complex is susceptible to chloro displacement by the DMSO solvent

molecules. In particular, a general up-field shift is noticed for all the original signals accompanied by the appearance of new peaks in the aromatic region, see **Figure 3.23**. This trend is corroborated by the ^{31}P NMR spectrum of **3**, having two signals of different intensities, which indicate major and minor species in solution, see **Figure 3.24**.

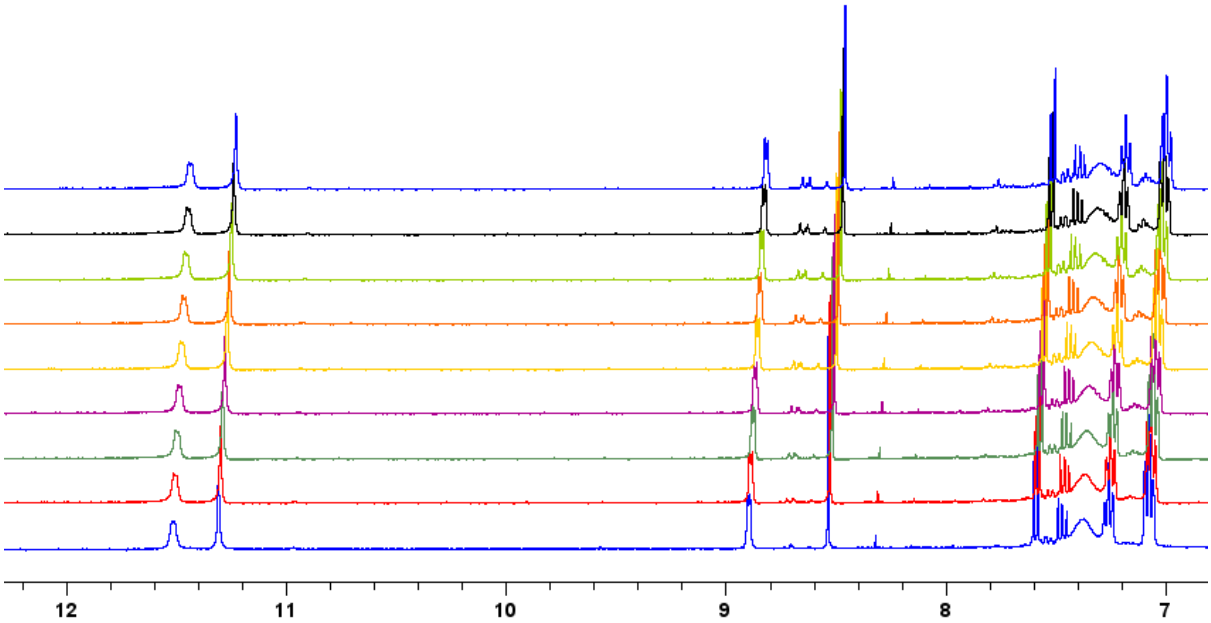

Figure 3. 23: *Time-dependent NMR study of* **3** *collected in 20-minute intervals for 3 h.*

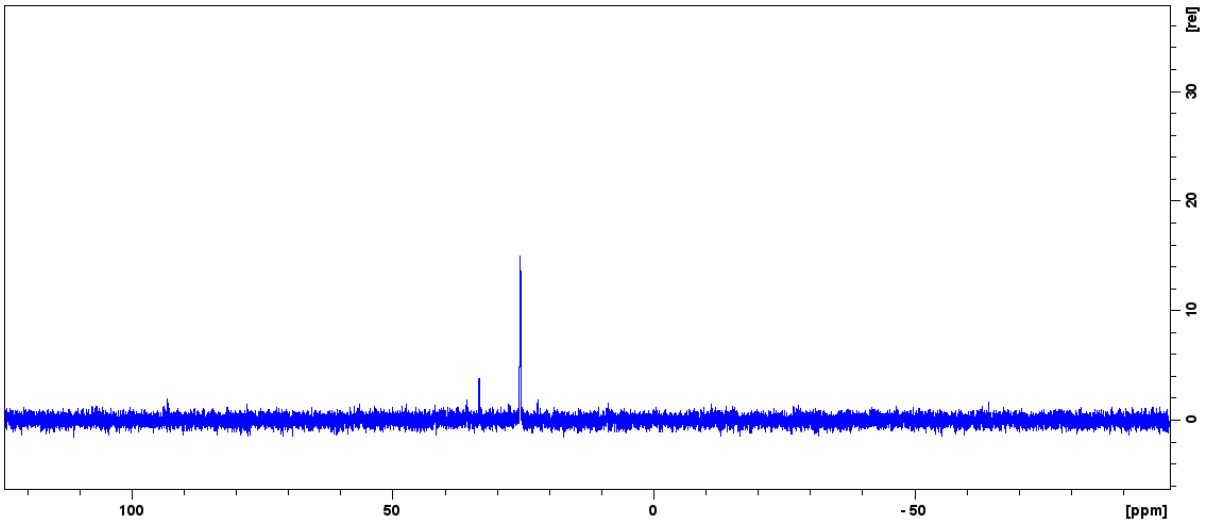

Figure 3. 24: *^{31}P NMR spectrum of compound* **3** *in DMSO-d_6.*

The different coordination modes of urdp in **2** and **3** are reflected in the uracil imino signals when the ^{1}H NMR spectra are compared to each other and the free Schiff-base ligand. The uracil N-H protons of urdp resonate at δ_H 11.01 ppm as a broad singlet. In

comparison, the analogous signals of metal complex **2** appear as individual peaks at δ_H 11.26 ppm (integrated for 2 protons), 7.50 ppm (singlet integrated for 1 proton), and 6.64 ppm (singlet integrated for 1 proton). Similarly, for **3**, the uracil N-H protons resonate as singlets at δ_H 11.5 and 11.29 ppm in deuterated DMSO.

Extensive correlations are found within cis-$[Ru(bipy)_2]^{2+}$ moieties and bridging pyridyl rings of the isostructural metal compounds **2** and **4,** whereby a large number of overlapping ^{1}H NMR signals are observed within the respective 1D NMR spectra. Subsequently, with the aid of COSY NMR spectral analysis, insight into the nature of these coalescing ^{1}H NMR peaks was obtained, see **Figures 3.25** and **3.26**. These ^{1}H NMR spectral assignments were initiated by specifying the multiplicity of each signal and relating it to the expected signal found in the structure. After that, structural corroboration was done by establishing bond connectivities via signals within the same aromatic system. For illustrative purposes shown in **Figure 3.25**, the correlations of the bridging protons for **2** are shown.

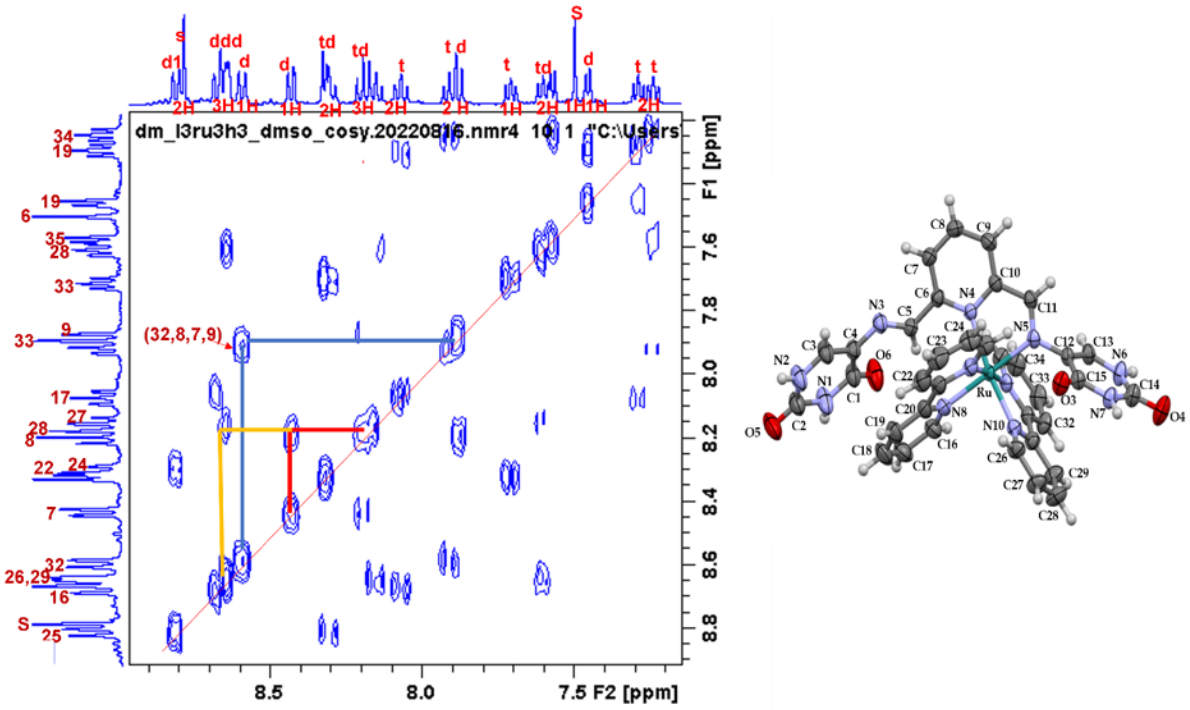

Figure 3. 25: *COSY NMR spectrum of* **2**. *The coloured lines depict the correlations between the bridging pyridyl protons.*

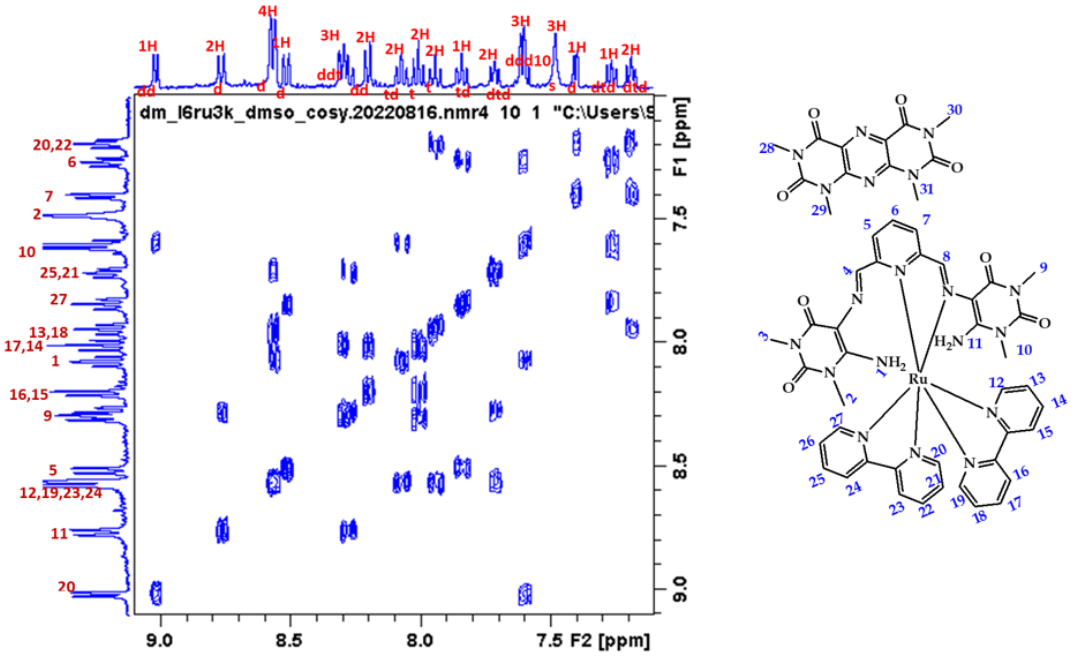

Figure 3. 26: *COSY NMR spectrum of* ***4****.*

High-resolution mass spectrometric analysis showed isotopic patterns due to the pseudo-molecular ions of the respective metal complexes. For example, the mass spectra for **2** and **4** showed typical isotopic peaks centered at 766.1235 ($[M - H - 2Cl]^+$) for **2** and at m/z = 750.0359 ($[M - H - 2PF_6]^+$) for **4**. The detected ion peaks for **2** and **4** were due to the loss of a single proton (deprotonation) and the respective counter ions from the parent salts. For complex **3**, the loss of one of the coordinated chloride ligands and two protons resulted in a fragment ion with an isotopic peak pattern centred at m/z = 750.0333, for $[M - 2H - Cl]^-$, see **Figures 3.27- 3.29**.

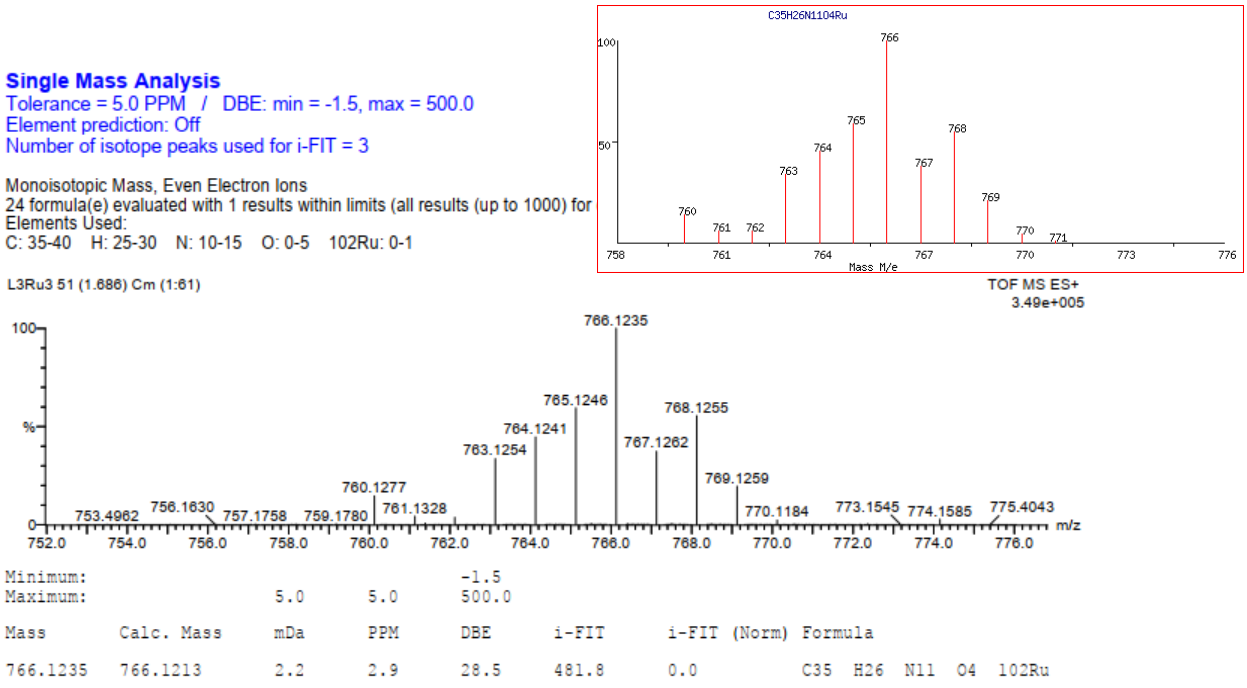

Figure 3. 27: *TOF-ESI-(+)-MS spectrum of complex* **2**. *Inset: The simulated mass isotopic pattern of* **2**.

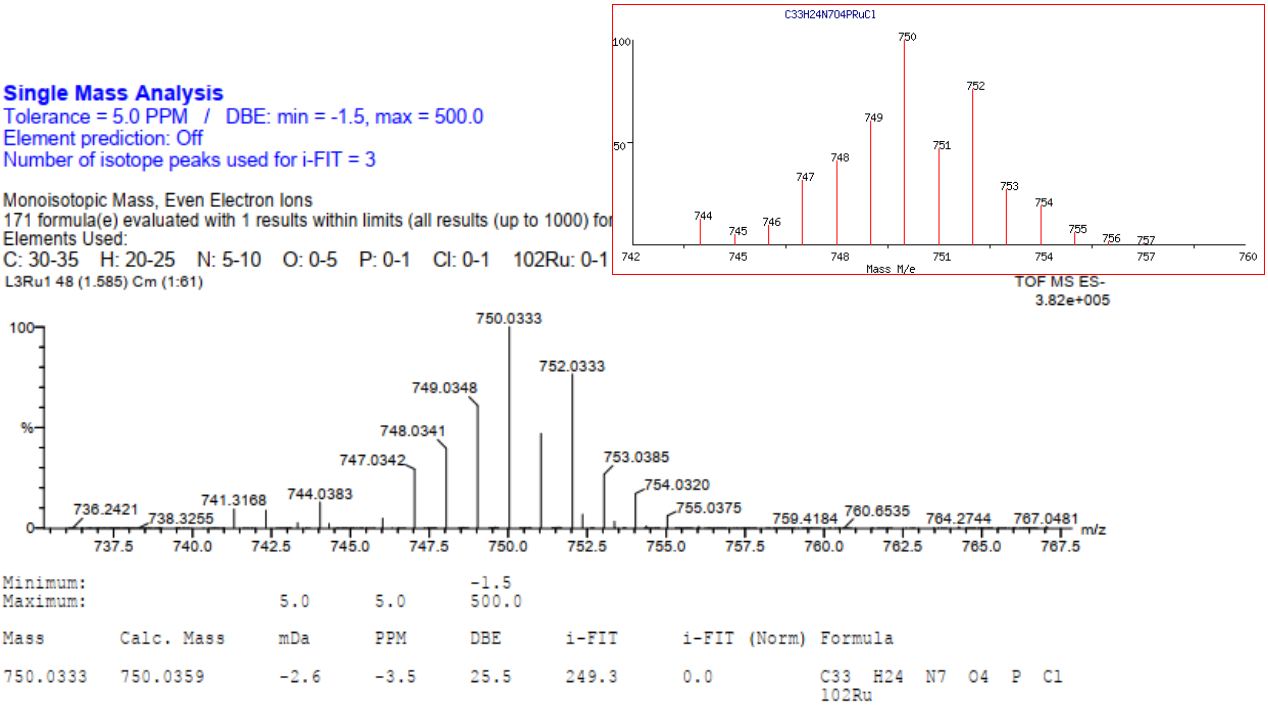

Figure 3. 28: *TOF-ESI-(+)-MS spectrum of complex* **3**. *Inset: The simulated mass isotopic pattern of* **3**.

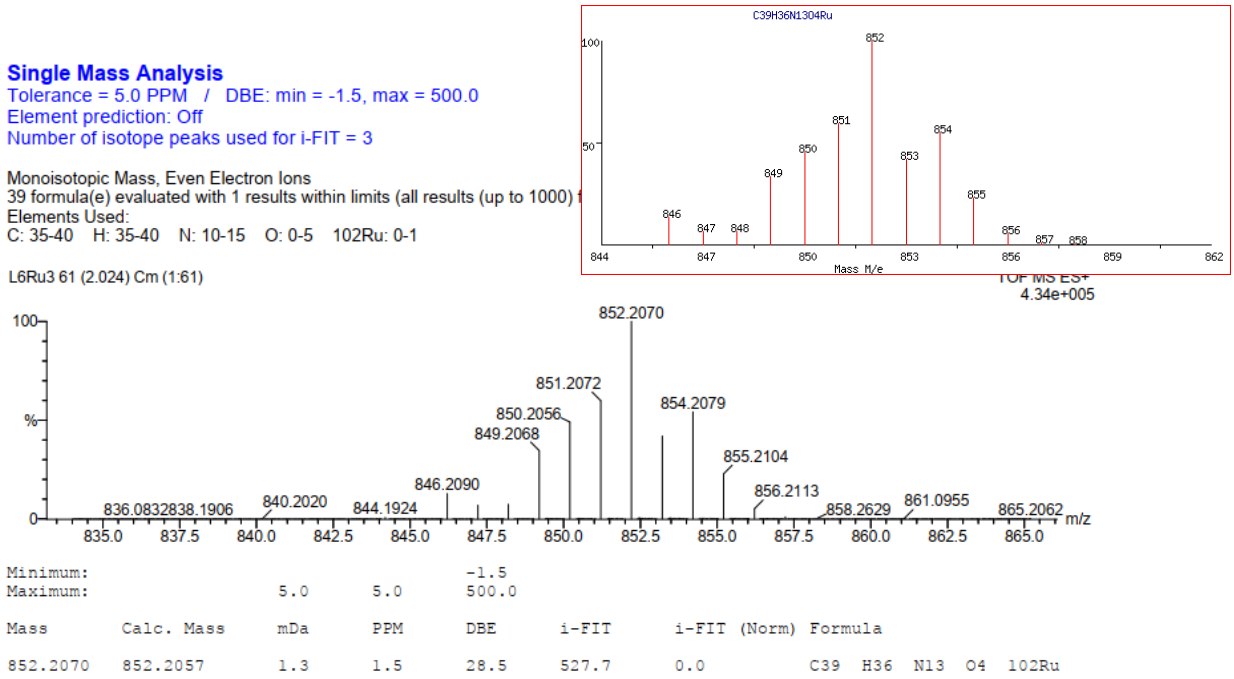

Figure 3. 29: *TOF-ESI-(+)-MS spectrum of complex* ***4****. Inset: Simulated mass isotopic pattern of* ***4****.*

3.3.3 Single Crystal X-ray Diffraction Studies

Individual monoclinic unit cells of **2** and **3** display four molecules orientated according to the $P2_1/c$ and $P2_1/n$ space groups, respectively. The respective crystal lattices are stabilized by intermolecular bonding. In particular, hydrogen-bonded dimers of **3** are rendered from classical interactions between uracil amines and the chloro co-ligands of neighboring molecules, see **Figure 3.30**. Similarly, molecules of **2** are cross-linked along the [a]-axis by bridging intermolecular interactions with the aqua solvent molecules of recrystallization and chloride counter-ions, se **Figure 3.31**.

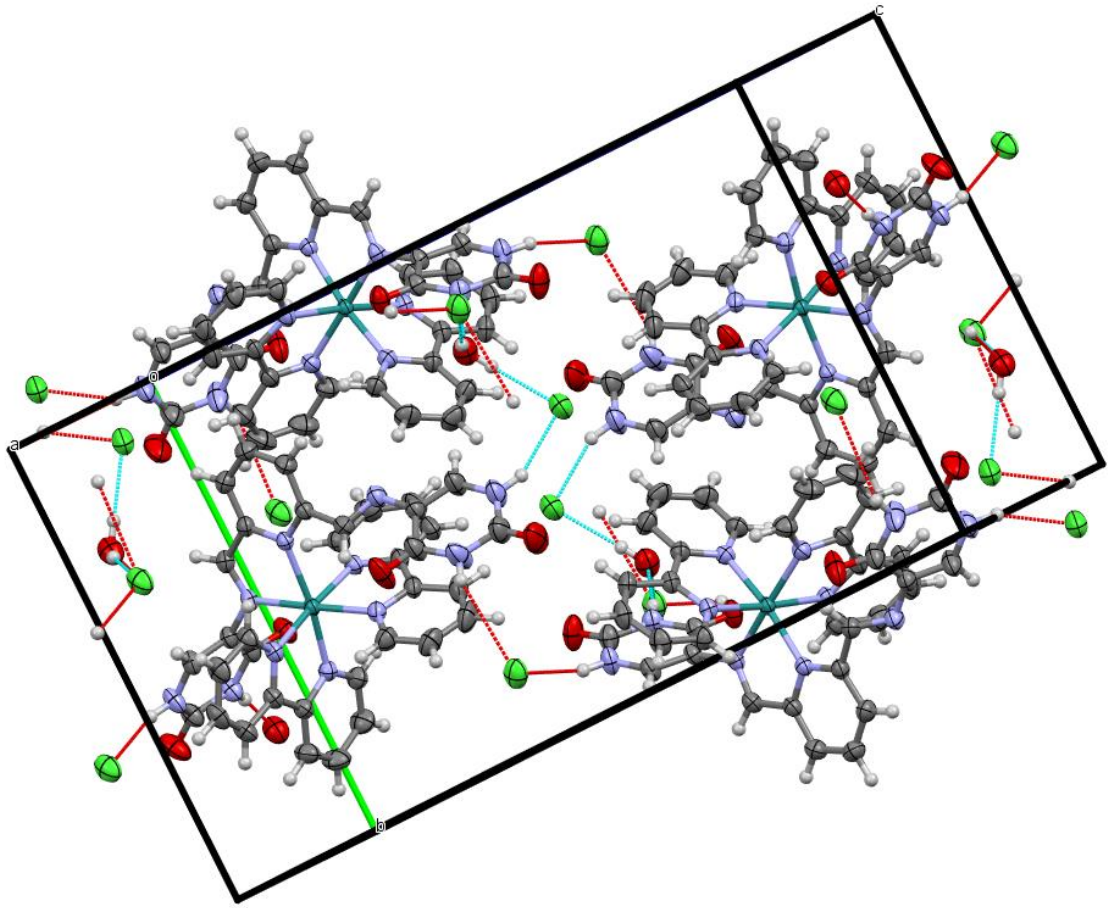

Figure 3. 30: *Monoclinic unit cell of* **2** *illustrating the hydrogen-bonding contacts:* $N7-H\cdots O7 = 1.982$ *Å,* $N6-H\cdots Cl1 = 2.295$ *Å,* $N1-H\cdots Cl1_B = 3.076$ *Å,* $N2\text{-}H6\cdots Cl2 = 2.268$ *Å,* $Cl1\cdots H_B\text{-}O\text{-}H_C = 2.268$ *Å and* $Cl2\cdots H_C\text{-}O\text{-}H_B = 2.268$ *Å.*

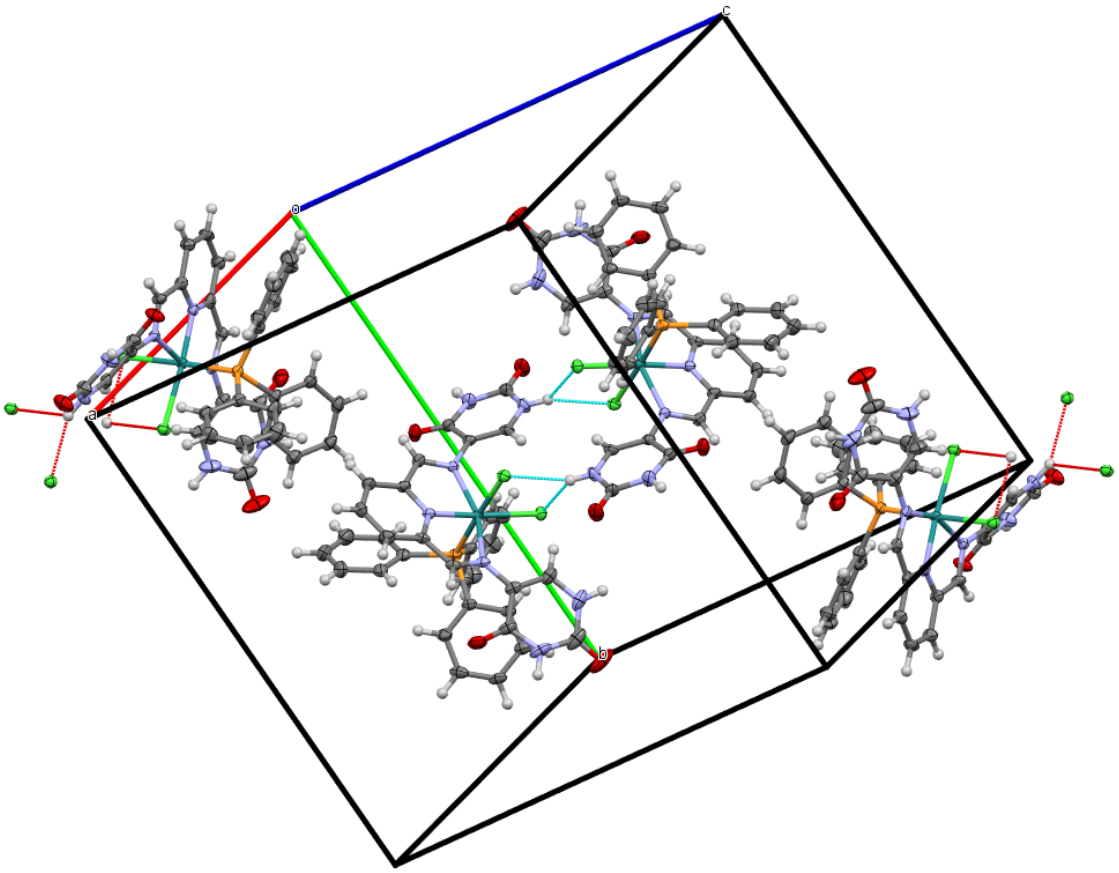

Figure 3. 31*: Monoclinic unit cell of* ***3*** *showing the classical intermolecular hydrogen-bonding interactions within the dimer: NA7 – HA ··· Cl2B/ NB7 – HB ··· Cl2A = 2.399 Å and NA7 – HA ··· Cl1B/ NB7 – HB ··· Cl1A = 2.774 Å.*

Each metal complex displays a distorted octahedral geometry caused by the constrained five-membered chelate rings, N4-Ru-N5 = 77.45(6)° for **2**, N3-Ru-N4 = 78.5(1)° and N4-Ru-N5 = 78.1(1)° for **3**, respectively. Consequently, non-linearity is observed within bond angles between the trans-axial coordination bonds [N4-Ru-N10 = 171.32(7)°, N8-Ru-N5 = 176.63(7)°, N7-Ru-N11 = 175.56(7)° for **2** and P-Ru-Cl2 = 177.65(4)° and N4-Ru-Cl1 = 176.2(1)° for **3**] while the N3-Ru-N5 [153.5(1)°] bond angle is significantly lower than 180°.

A notable difference in the coordination modes of urdp in **2** and **3**, it coordinates bidentately, while in the latter, it coordinates tridentately. The variable coordination modes can be ascribed to the combined steric demands of the bipyridyl co-ligands in **2,** which are absent in **3**. Furthermore, the C-$(C=N)_{imino}$ angles of **2** are smaller than the

idealized 120°, with C6-C5-N3 = 118.7(2)° for the uncoordinated imino chain and C10-C11-N5 = 116.8(2)° for the coordination imino chain of **2**. For **3**, where both imino nitrogens are coordinated to the ruthenium, bond angles of C6-C5-N3 = 117.2(4)° and C10-C11-N5 =117.4(4)° were observed, in respective **Figures 3.32 - 3.33**. As shown in **Table 3.3** Analogous coordination effects are also manifested in the imino bond lengths [C5-N3 (free chain) = 1.273(3) Å; C11-N5 (coordinated chain) = 1.284(3) Å for **2** and 1.296(6) Å; 1.295(6) Å for **3**], respectively. In addition, the higher degrees of freedom of the uncoordinated uracilimino methylene group of **2** resulted in a slightly lower dihedral angle of the uracil moiety with respect to the basal plane [N4N8N10N5] of 65.79°. At the same time, the coordinated chain is constrained to an angle of 67.92°. In **3**, where both uracilimino methylene groups are coordinated, the uracil moieties intersect the basal plane by 41.23° and 31.45°.

The ruthenium-to-halide bonds of **3** [Ru-Cl1 = 2.447(1) Å and Ru-Cl2 = 2.456(1) Å] differ since they are experiencing variable trans-influences from the pyridyl nitrogen and triphenylphosphine phosphorous donor atoms. The bond lengths of Ru-Cl of **3** and the Ru-N_{imino} bonds, Ru-N4 = 2.126(2) Å for **2** and Ru-N3 = 2.106(3) Å; Ru-N5 = 2.104(4) Å for **3**, are comparable to those found in other diamagnetic ruthenium benzohydrazone-derived Schiff base compounds, e.g. [(η^6-p-cymene)Ru(L_1)Cl] (HL_1 = 3-methoxy-N'-((3-methylthiophen-2-yl)methylene)benzohydrazide) with Ru-Cl and Ru-N_{imino} bond lengths of 2.4238(7) Å and 2.058(3) Å, respectively.[33] The difference of the Schiff base chelator bond lengths, Ru-$N_{pyridyl}$ of **2** [Ru-N4 = 2.126(2) Å] and **3** [Ru-N4 = 1.944(4) Å], is accounted for by the higher electronegativity of the Cl1 donor atom in **3** as opposed to the N10 donor atom in **2**. The bond distances between the individual bipyridyl nitrogen donor atoms and ruthenium [Ru-$N_{pyridyl}$ bonds ranging 2.050(2) - 2.077(2) Å] in **2** are similar to those observed for the bond lengths between ruthenium and the central imino pyridyl nitrogens of **2** and **3**.[34]

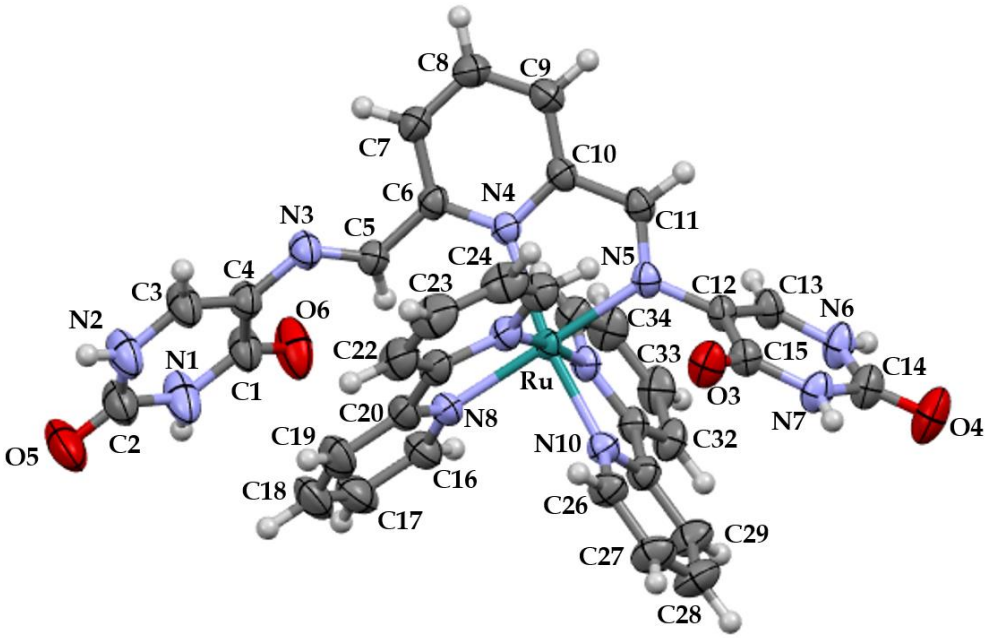

Figure 3. 32: *Molecular structure of* **2***, shown with 50% probability displacement ellipsoids and the selected atom-numbering scheme. The water molecule of recrystallization and the chloride counter-ions have been omitted for clarity.*

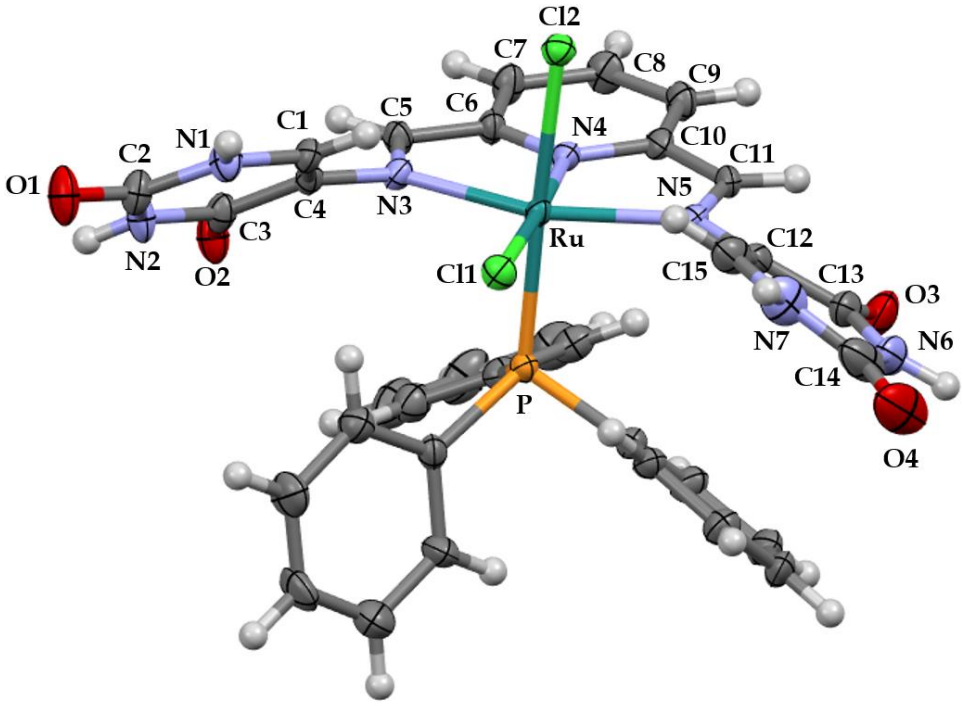

Figure 3. 33: *Molecular structure of* **3***, shown with 50% probability displacement ellipsoids and the selected atom-numbering scheme.*

Table 3. 3: *Selected bond lengths (Å) and angles (°) for* ***2*** *and* ***3.***

Bond lengths	**2**	**3**
Ru-N3	-	2.106(3)
Ru-N4	2.126(2)	1.944(4)
Ru-N5	2.050(2)	2.104(4)
Ru-N8	2.067(2)	-
Ru-N9	2.063(1)	-
Ru-N10	2.048(2)	-
Ru-N11	2.059(2)	-
Ru-Cl1	-	2.447(1)
Ru-Cl2	-	2.456(1)
Ru-P	-	2.303(1)
C5-N3	1.273(3)	1.296(6)
C11-N5	1.284(3)	1.295(6)
Bond angles		
N3-Ru-N4	-	78.5(1)
N4-Ru-N5	77.45(6)	78.1(1)
N8-Ru-N11	78.35(7)	-
N10-Ru-N11	78.61(7)	-
N4-Ru-N10	171.32(7)	-
N8-Ru-N5	176.63(7)	-
N7-Ru-N11	175.56(7)	-
C6-C5-N3	118.7(2)	117.2(4)
C10-C11-N5	116.8(2)	117.4(4)
P-Ru-Cl2	-	177.65(4)
N3-Ru-N5	-	156.5(1)
N4-Ru-Cl1	-	176.2(1)

3.3.4 BSA interaction studies

A well-defined biodistribution pattern of a drug is closely correlated to its reversible uptake by human serum albumin (HSA), a key drug transport protein.[35,36] As HSA is a structural analog of BSA, the latter is often used as a prototype to model the affinities between HSA and drugs.[37] Among the many analytical techniques used to determine the interactions between BSA and metal complexes, fluorescence spectroscopy is the most widely employed technique to investigate the solution BSA affinities and binding strengths of transition metal complexes.[38] The tryptophan residues of BSA are fluorescent, and the binding of metal complexes to BSA typically induces fluorescence quenching. In particular, ruthenium complexes have occupied various binding sites, which are largely dictated by the nature of the BSA binding sites (within the subdomains IIA and IIIA) and the stereo-electronic properties of the metal complexes.[30]

Biomolecular titrations between the drug carrier BSA and metal complexes **2–4** were monitored by fluorescence spectroscopy. During the standard additions of each metal complex to BSA, a gradual loss in the protein's emission intensity was observed, accounting for the respective metal complexes binding to BSA. Of particular interest is that the metal complexes induce minor blue shifts in the BSA peak maximum; see **Figures 3.34 - 3.36**. This characteristic spectral change is synonymous with metal complexes interacting with the tryptophan residue of the BSA through non-covalent short contacts.[39] Consequently, these metal complexes could be interacting with the tryptophan residue through hydrogen-bonding and ion-dipole interactions (for **2** and **4** only), which in turn conceals the tryptophan groups within the hydrophobic microenvironment of BSA, subdomain IIA.

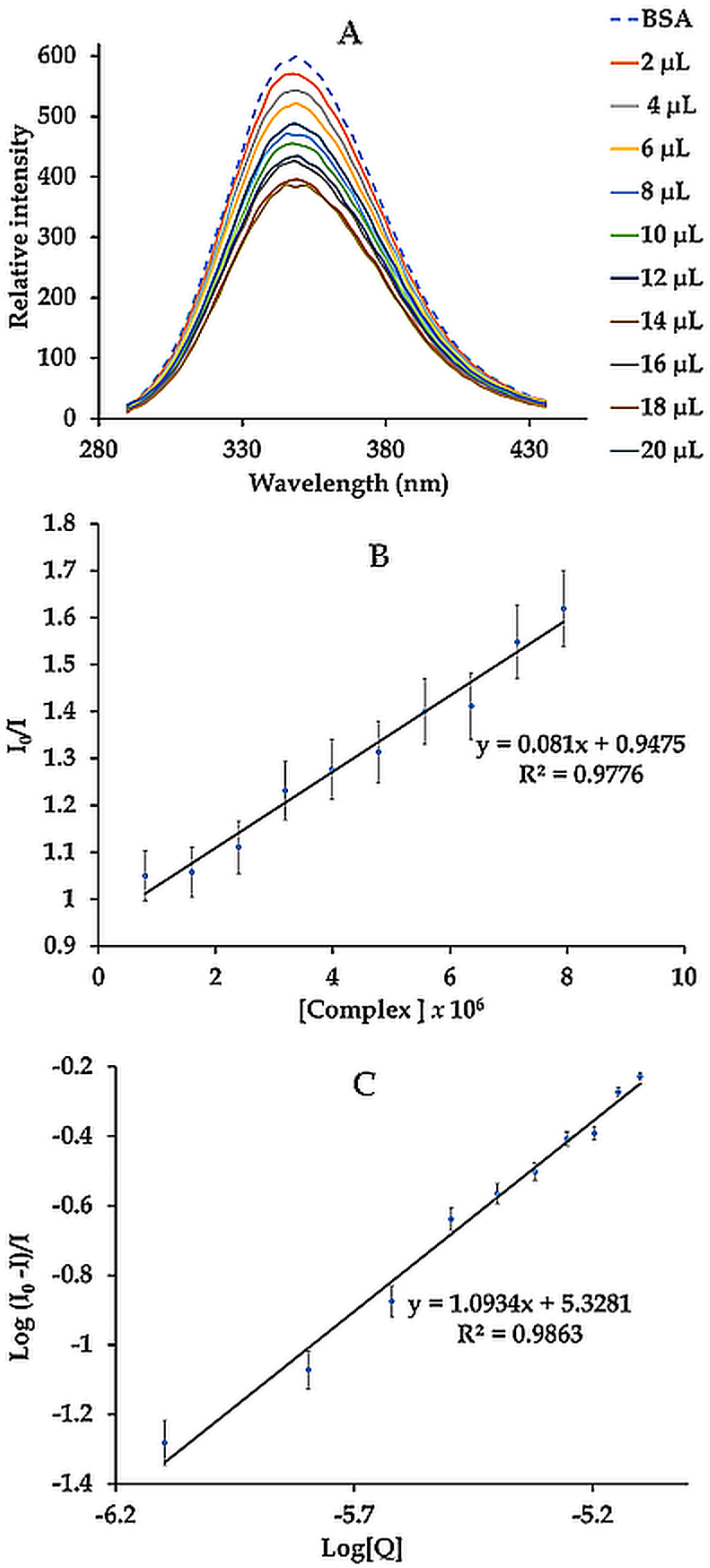

Figure 3. 34: *Fluorometric titration of BSA (preloaded with ibuprofen/warfarin) with complex* **2** *(excitation wavelength = 280 nm). (A) Stern-Volmer plot and the linear regression plot (B) of Log(I_0-I/I_0) vs Log[Q]. The relative standard addition of each data point (n = 3) was below 5%.*

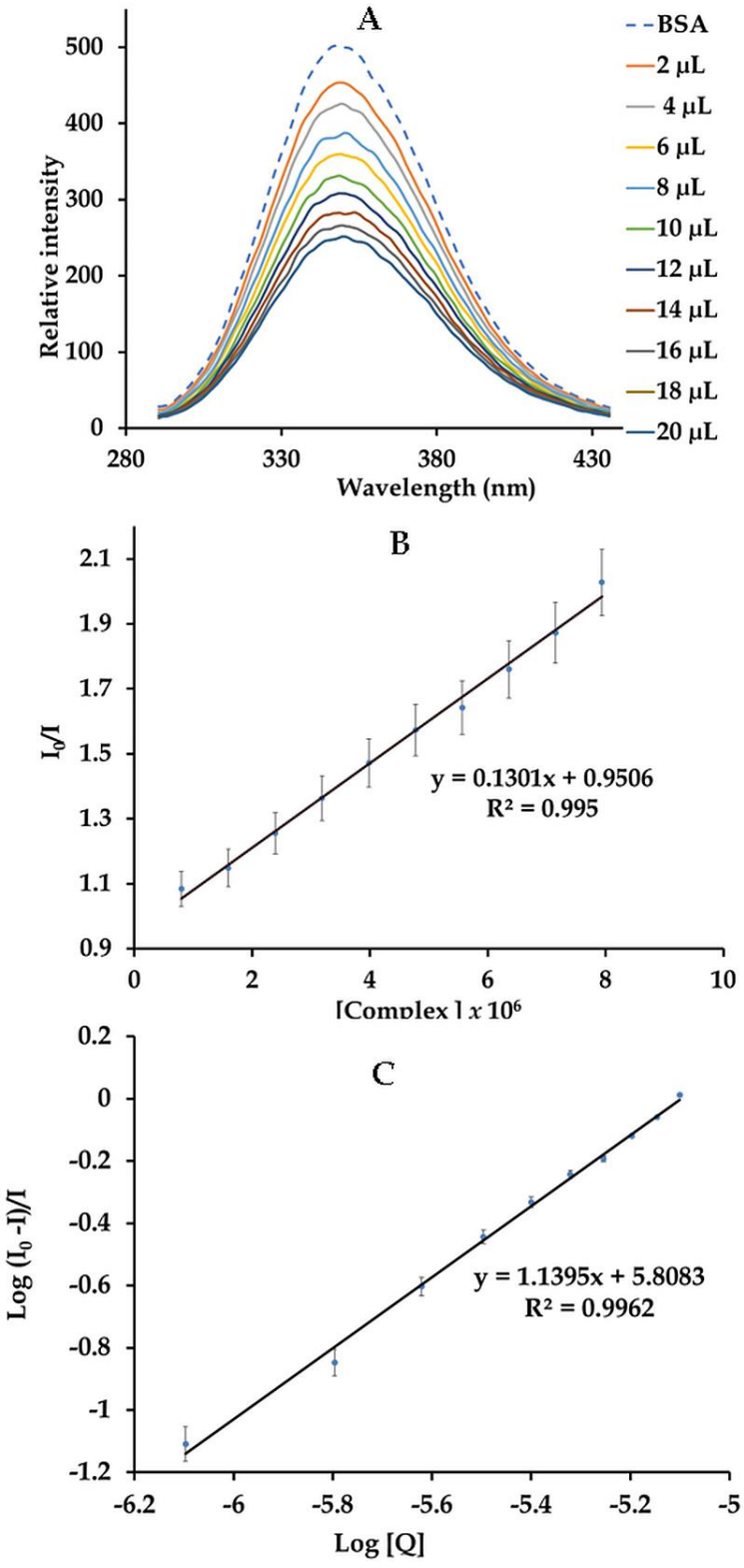

Figure 3. 35: *Fluorometric titration of BSA (preloaded with ibuprofen/warfarin) with complex **3** (excitation wavelength = 280 nm). (A) Stern-Volmer plot and the linear regression plot (B) of Log(I_0-I/I_0) vs Log[Q]. The relative standard addition of each data point (n = 3) was below 5%.*

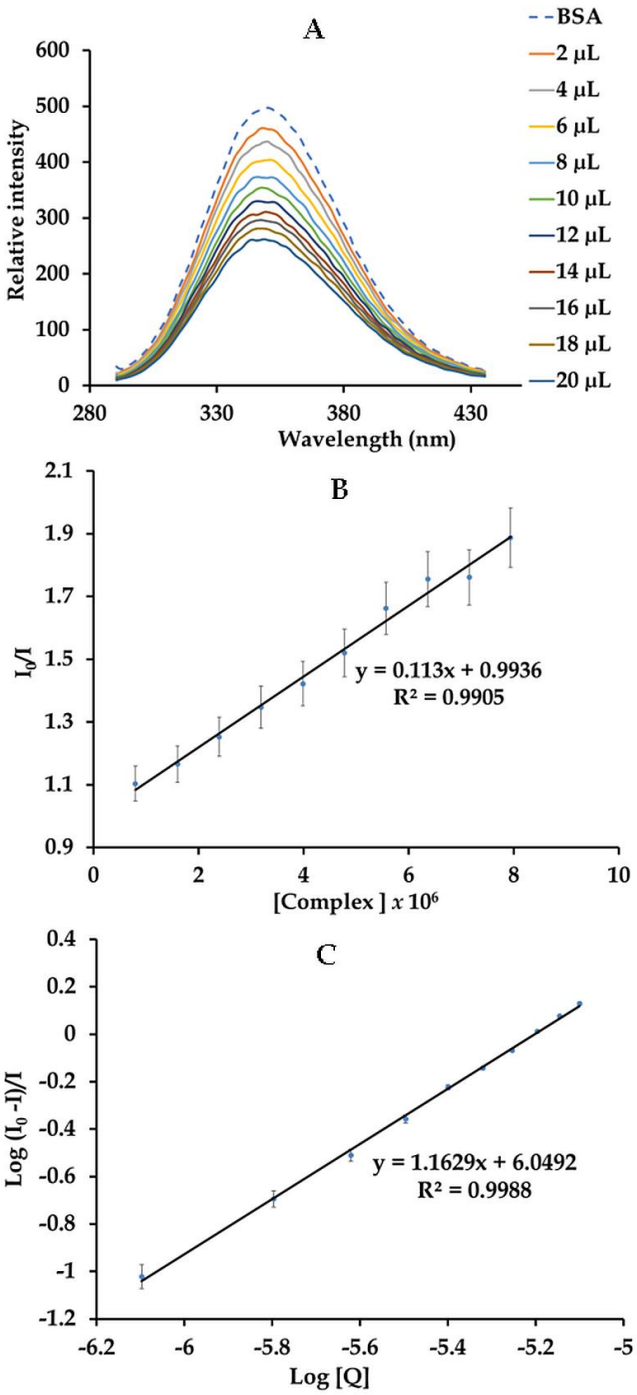

Figure 3. 36: *Fluorometric titration of BSA (preloaded with ibuprofen/warfarin) with complex* **4** *(excitation wavelength = 280 nm). (A) Stern-Volmer plot and the linear regression plot (B) of Log(I₀-I/I₀) vs Log[Q]. The relative standard addition of each data point (n = 3) was below 5%.*

To corroborate the preferential protein binding of these metal complexes within the BSA subdomain IIA, the protein interaction studies were extended to competitive binder displacement studies, which were carried out by taking note of quenching capacities and binding strengths of each metal complex in the presence and absence of the site markers. It has been established through various literature trends that specific site markers can bind into preferential BSA microenvironments. Specifically, warfarin and ibuprofen are site markers known to bind in site I and II domains, respectively.[40]

No informative relationships could be derived from the Stern-Volmer constants (K_{SV}); only **2** showed a minor increase in the K_{SV} constants during the titrations with BSA samples preloaded with different site markers. However, regarding the trends in the intrinsic binding (K_b) constants, metal complex **4** exhibited indiscriminate binding within the protein subdomains of concern since the K_b values decrease for the BSA preloaded with the separate site markers in comparison to the BSA with metal complex only, see **Figures 3.37 - 3.38** .[41] However, in the instances for the competitive binding studies conducted with **2** and **3** in the presence of ibuprofen, increases in the K_b values were observed; these trends are tentatively assigned to cooperative binding effects.[42] No alterations in the order of the K_b values are observed for the BSA-warfarin systems titrated against the aforementioned metal complexes, which implies that **2** and **3** are preferential domain II binders. Although this conclusion is derived from the experimental trends, it is important to note that multiple BSA binding sites are still probable.

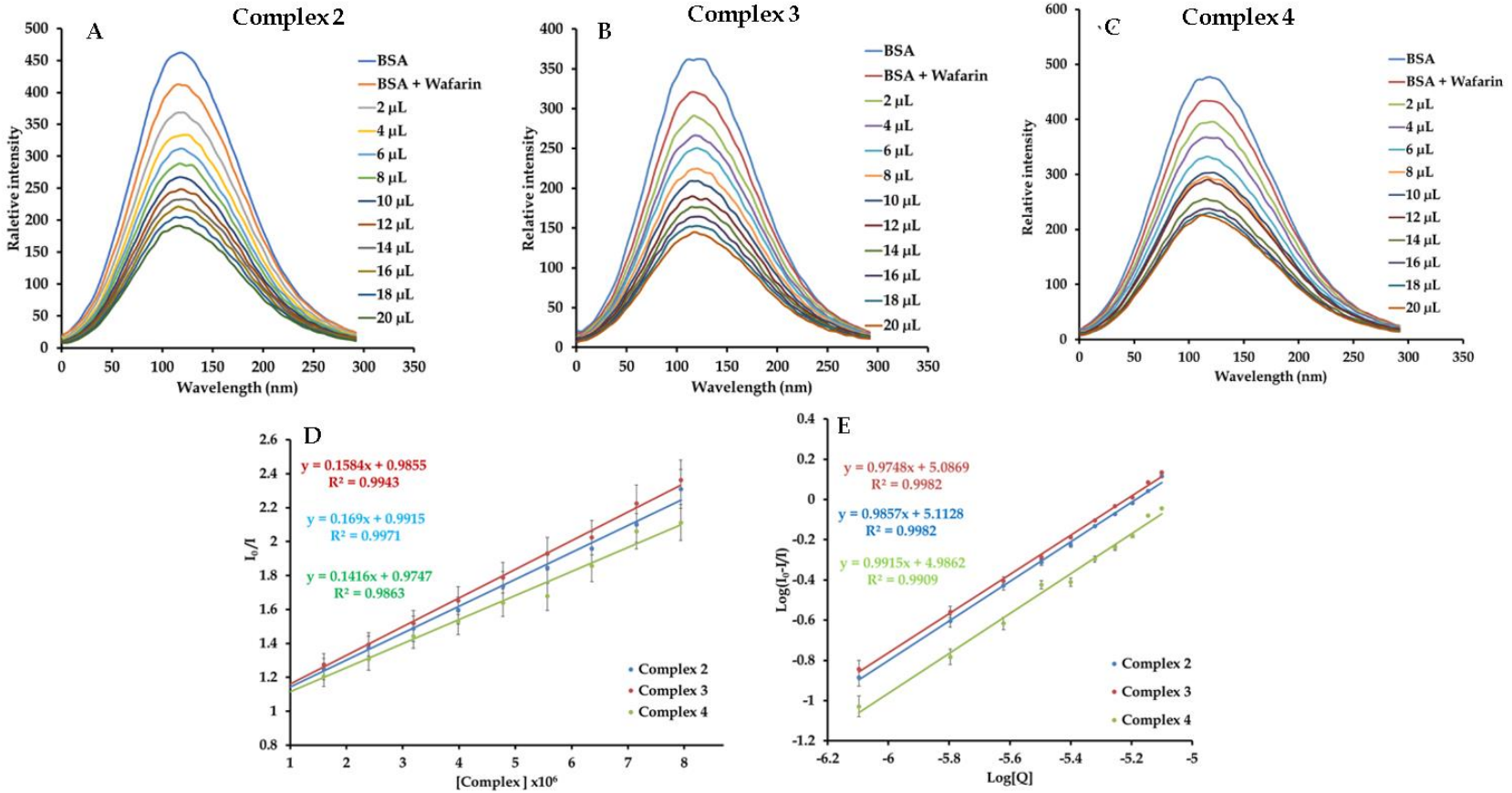

Figure 3. 37: *Fluorescence emission spectral profiles of BSA (A-C) with equimolar amounts of warfarin upon the addition of* **2** *-* **4** *and the Stern-Volmer plots, (D) (I_0/I) vs [Q (***2** *-* **4***)], (E) Log(I_0-I/I) vs Log[Q (***2** *-* **4***)] and the respective regression data. The relative standard deviation of each data point (n = 3) was below 5%.*

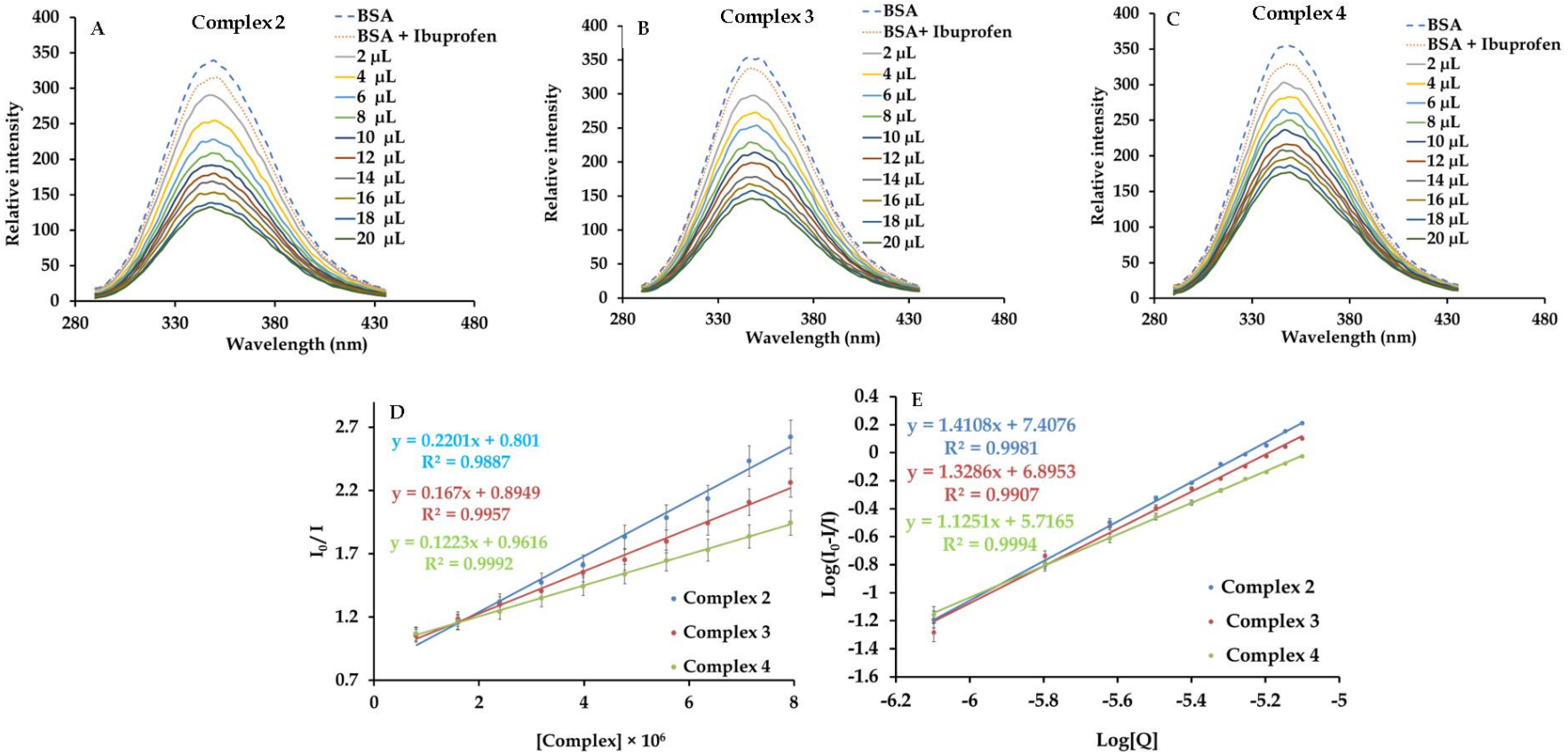

Figure 3. 38: *Fluorescence emission spectral profiles of BSA (A-C) with equimolar amounts of ibuprofen upon the addition of* **2** *-* **4** *and the Stern-Volmer plots, (D) (*I_0/I*) vs [Q (***2** *-* **4***)], (E) Log(*I_0*-I/I) vs Log[Q (***2** *-* **4***)] and the respective regression data. The relative standard deviation of each data point (n = 3) was below 5%.*

Generally, the respective metal complexes are moderate to strong binders, as shown in the magnitude of their binding constants (10^4 - 10^6 M^{-1}). The fluorescence quenching data for compounds **2–4** obtained from the Stern–Volmer equation (k_q) were found in the range of 1.13×10^{12} – 8.30×10^{12} M^{-1} s^{-1}, which suggests a static quenching mechanism, see **Table 3.4**.[43] These analytical parameters were comparable to other ruthenium compounds containing nitrogen-donor chelating ligands.[30, 44] The magnitude of the binding constants suggest strong interactions between the BSA transporter protein and the individual metal complexes (**2 - 4**) which will ensure their efficient delivery to the pancreatic β-cells that is essential for glucose homeostasis. In fact, literature trends substantiate that HSA has shown target specificity towards pancreatic cells. For instance, an HSA nanocomposite has shown chemotherapeutic activity towards pancreatic cancer where HSA serves as a drug delivery agent.[45] In addition, the versatility of HSA is shown by its application as a sensor for pancreatic cancer and the use of this serum albumin as an inhibitor of amylin aggregation.[46]

Table 3. 4: *Non-covalent interaction parameters calculated from the BSA fluorescence spectroscopic titrations with the metal complexes* **2**–**4**.

Compound	No site marker			Binding site(s)	Ibuprofen			Warfarin		
	K_{sv} (M^{-1})	k_q (M^{-1} s^{-1})	K_b (M^{-1})	n	K_{sv} (M^{-1})	k_q (M^{-1} s^{-1})	K_b (M^{-1})	K_{sv} (M^{-1})	k_q (M^{-1} s^{-1})	K_b (M^{-1})
2	8.1×10^{4}	8.1×10^{12}	2.1×10^{5}	1.0934	2.20×10^{5}	2.20×10^{12}	2.6×10^{7}	1.58×10^{5}	1.58×10^{12}	1.2×10^{5}
3	1.30×10^{5}	1.30×10^{12}	6.4×10^{5}	1.1395	1.67×10^{5}	1.67×10^{12}	7.9×10^{6}	1.69×10^{5}	1.69×10^{12}	1.22×10^{5}
4	1.13×10^{5}	1.13×10^{12}	1.1×10^{6}	1.1629	1.22×10^{5}	1.22×10^{12}	5.21×10^{5}	1.42×10^{5}	1.42×10^{12}	9.7×10^{4}

3.3.5 hIAPP interaction studies

Self-aggregation of the human islet amyloid polypeptide (hIAPP, amylin) has been implicated as one of the leading causes of β-cell apoptosis.[47] Subsequently, this leads to lower bio-availability of insulin to regulate blood-glucose levels leading to prediabetes. To halt the progression of prediabetes to fully-fledged type 2 diabetes mellitus (DM) or to provide an effective therapy for DM, medicinal agents are required to induce disaggregation of amylin oligomers. Organoruthenium compounds have shown the capability of inhibiting amylin misfolding, which is often primarily induced through short-range intermolecular interactions or direct covalent bonding. At the same time, secondary facilitation can be rendered through radical scavenging capabilities of reactive oxygenated species by the metal complexes.[6]

Firstly, we incubated our separate metal complex solutions prepared in 2% DMSO-98% PBS with amylin dissolved in PBS, followed by TEM analysis, see **Figure 3.39**. As expected, the micrograph of amylin only (micrograph scale at 0.5 μm) illustrated the misfolded strands of the polypeptide in the form of larger clusters.[48] The amylin sample exposed to lead metal complex **1** illustrated correction of the misfolded oligomers to afford strands with an average particle length of 6.1 nm. However, metal complex **2** induced the formation of smaller spherical oligomers with an average diameter of 19.15 nm. Furthermore, metal complexes **3** and **4** afforded significantly irregular-shaped smaller amylin oligomers with mean particle sizes of 5 and 7.2 nm, respectively. Based on the TEM analysis, it is evident that complex **3** performs superior in promoting the disaggregation of the misfolded amylin.

Thereafter, we embarked on an investigation to probe the nature of the interactions between the metal complexes and amylin, see **Figure 3.40**. The fluorescence titrations of the individual metal complexes against amylin revealed hyperchromism for **1** and **3** while the metal complex cations **2** and **4** induces hypochromism. As per literature trends, hypochromism during hIAPP fluorescence titrations indicates non-covalent interactions such as hydrogen-bonding or ion-dipole interactions between the

biomolecule and the different metal complexes.[49] In addition, there is a distinctive blue-shift of **2** observed in its emission wavelength maximum, which can be attributed to the unfolding of the protein/disaggregation process.[50] Fluorescence quenching activities of **2** (30.61%) and **4** (31.60%) were within the range of other ruthenium-based complexes.[7]

In the case of the fluorescence spectroscopic titrations done using the chloro-containing metal complexes **1** and **3**, the susceptibility to hydrolysis may lead to simultaneous displacement of the aqua co-ligands and direct binding of the respective metal complexes to amylin. In the process, different covalently-linked amylin-metal complexes (adducts of **1** or **3**) are rendered as evidenced by the presence of intersections between the electronic spectra of the separate metal complexes, at each addition of **1** or **3**.[51] Also noteworthy is that the adducts of **1** and **3** with amylin have fluorescent intensity profiles similar to that of amylin and which increases with each addition of each metal complex (**1** or **3**). In fact, biomolecular interaction capabilities of **1** and **3** are comparable to other studies conducted with NAMI A and its derivative when interacting with other biomolecules.[52,53]

Furthermore, the simulated Log P values for the respective metal compounds were determined by Molinspiration calculation program in an octanol:water biphasic system.[54] The large values for **2** (Log P = 10.25) and **4** (Log P = 10.20) suggest that these metal compounds bind to the hydrophobic sites of amylin while the aqua derivatives of **1** (Log P = -3.05) and **3** (Log P = -3.29) would bind weakly to those hydrophobic sites.[55]

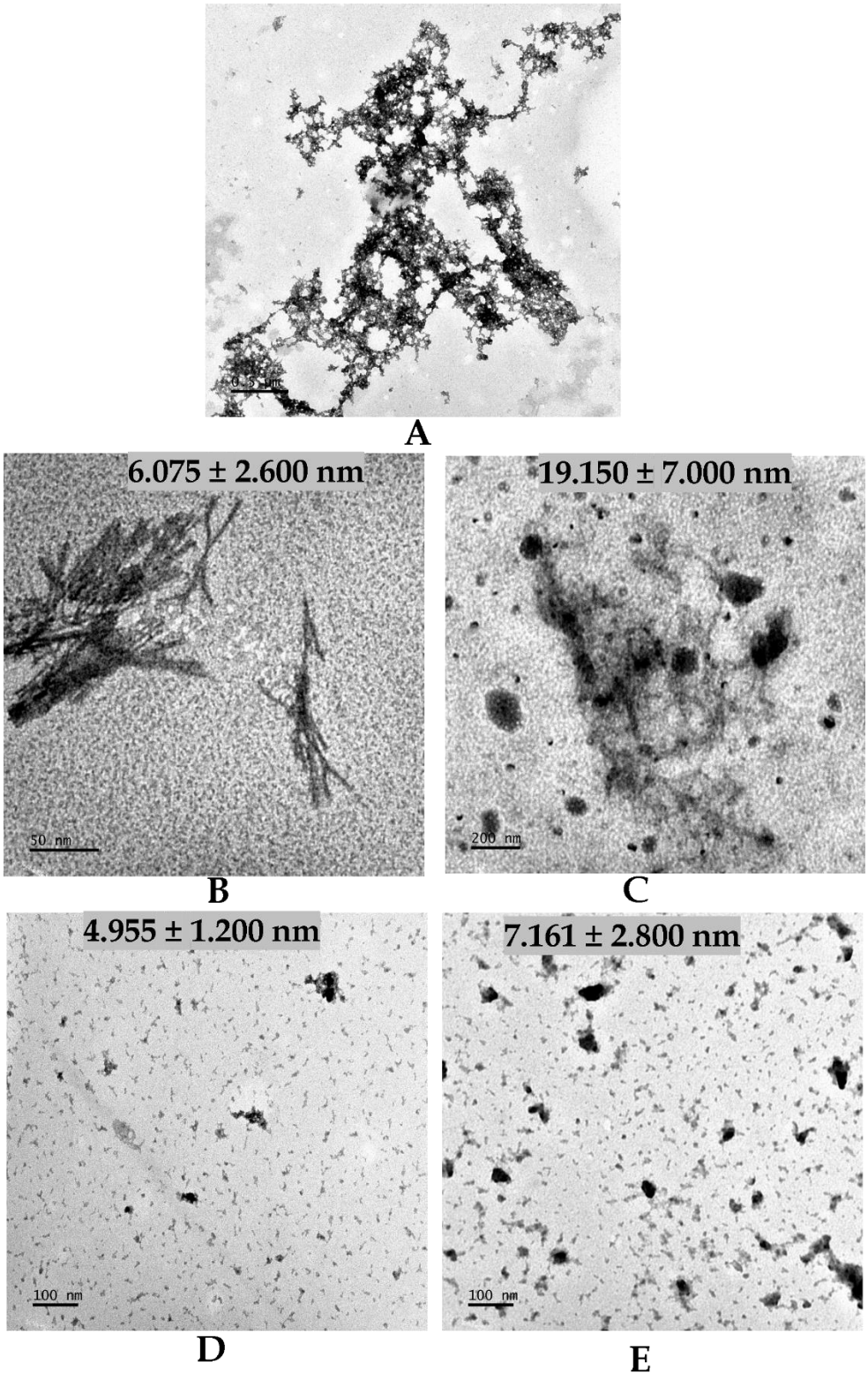

Figure 3. 39: *TEM micrographs illustrating (**A**) the aggregated amylin (50 µM) and (**B**-**E**) after exposure of standard aliquots (160 µM) of the respective metal complexes for 72 h at physiological temperature. Uranyl acetate was used as a staining negative control.*

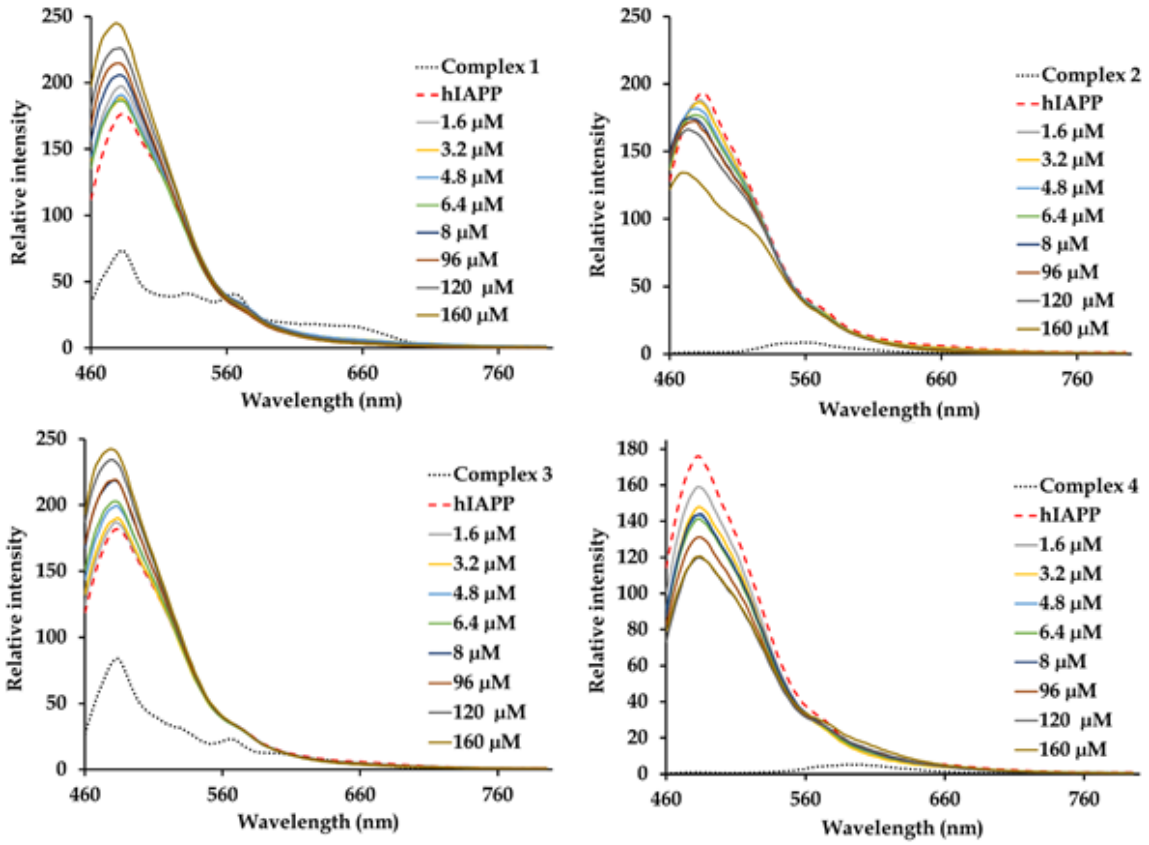

Figure 3. 40: *Quenching titrations between the fluorescent conjugate of 10 µM amylin - 2.5 µM THT and the respective metal complexes (excitation wavelength = 432 nm).*

3.3.6 In vitro anti-diabetic studies

The liver is crucial in maintaining blood glucose homeostasis by coordinating glucose storage, utilization, and production.[56] Increased hepatic glucose production (HGP) resulting from elevated gluconeogenesis is the leading cause of increased blood glucose levels in the diabetic state.[57] In addition, the impairment of liver cells to control glucose metabolism is closely linked to the distortion and failure of amylin function in the pancreas.[58] Hence, new drugs that alleviate insulin resistance and normalize the impaired hepatic glycogen synthesis, as well as the excessive gluconeogenesis in T2DM, are essential for regulating glucose metabolism. In this study, we evaluated the potential of **2 – 4** to simultaneously promote glycogen synthesis and inhibit gluconeogenesis in cultured liver (Chang) cell lines, refer to **Table 3.5**.

The cell viability of the individual ruthenium complexes in Chang cell lines was assessed using the MTT assay, see **Figure 3.41**. The results show that the Chang cells treated with 12.5 and 25 µg/mL ruthenium complexes (**2 - 4**) have minor increases in cell viability (highest cell viability of 119%) when compared to the control group after 12 or 24 h treatment periods. However, a dose dependent decrease was observed at higher doses over the 48 h treatment period when compared to the control group with the lowest cell viability obtained being 80%. Therefore, higher concentrations required for the antiproliferation of the Chang cells.

Table 3. 5: *The effects of complex* **2**- **4** *on glycogen synthesis in the liver cells after 48 h. Values are presented as means ± SEM (n = 6) in each group. These metal complexes had molar concentrations of 14.92 µM for* **2**, *15.87 µM for* **3**, *8.64 µM for* **4** *for the first doses (12.5 µg mL^{-1}); 29.85 µM for* **2**, *31.74 µM for* **3**, *17.28 µM for* **4** *for the second doses (25 µg mL^{-1}); and 59.69 µM for* **2**, *63.49 µM for* **3**, *34.55 µM for* **4** *for the third doses (50 µg mL^{-1}).*

Drug		Glucose (mmol L^{-1})	Glycogen (mmol cells^{-1})
Control		8.5±0.57	0.64±0.07
Complex 2	Dose µg mL^{-1}		
	12.5	6.8±0.46*α	0.72±0.03*α
	25	6.5±0.78*α	0.78±0.02*α
	50	6.0±0.96*	0.83±0.04*
Insulin	4	4.3±0.45*	1.00±0.04*
Control		8.5±0.59	0.64±0.07
Complex 3	Dose µg mL^{-1}		
	12.5	6.4±0.76*α	0.78±0.03*α
	25	6.1±0.78*	0.84±0.06*
	50	5.2±0.55*	0.90±0.06*
Insulin	4	4.3±0.45*	1.00±0.02*
Control		8.5±0.67	0.64±0.06
Complex 4	Dose µg mL^{-1}		
	12.5	6.7±0.78*α	0.70±0.04*α
	25	6.5±0.92*α	0.78±0.04*α
	50	6.1±0.45*	0.84±0.06*
Insulin	4	4.3±0.52*	1.00±0.02*

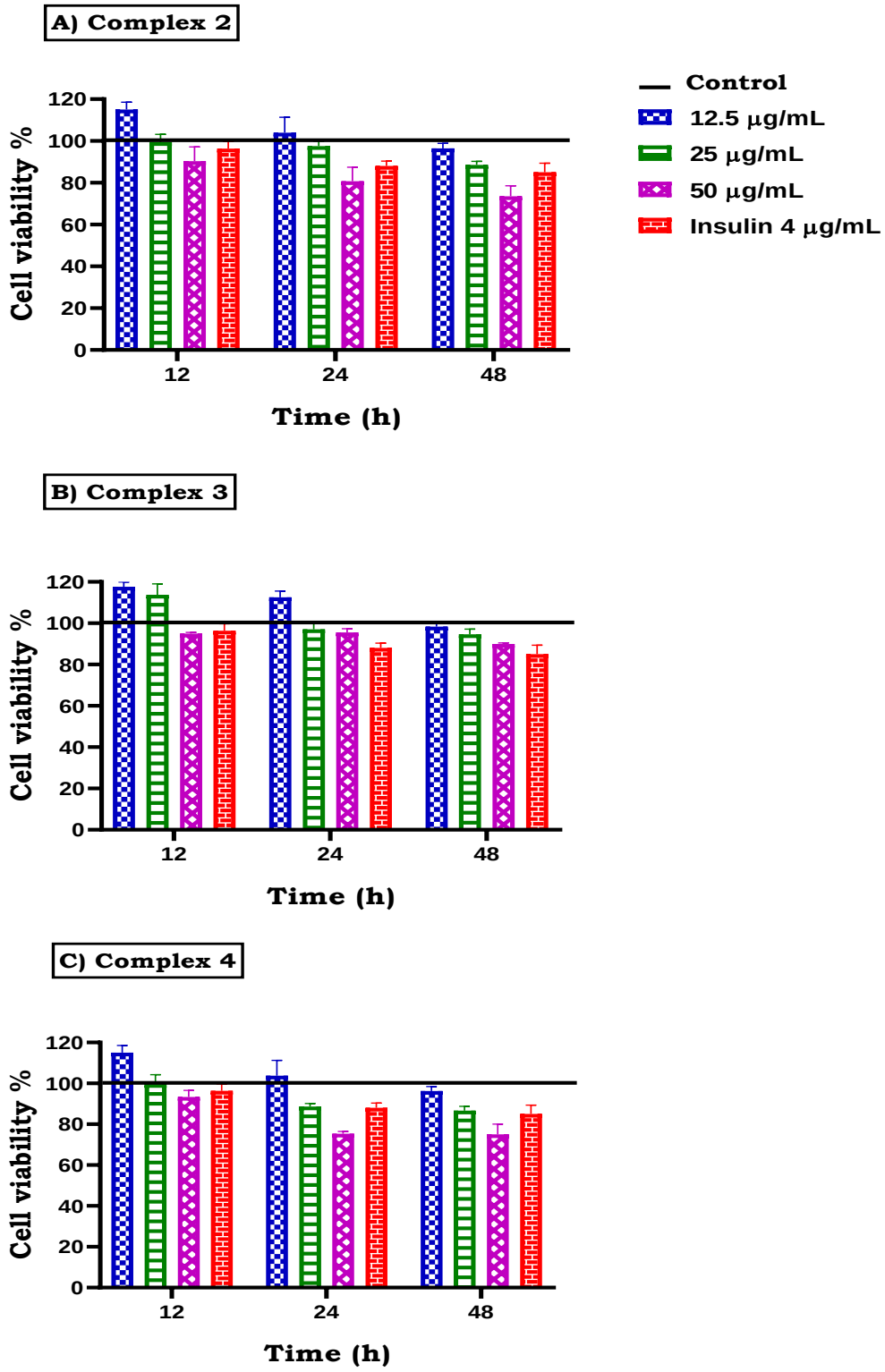

Figure 3. 41: *The effects of ruthenium complexes (A) complex* **2**, *(B) complex* **3** *and (C) complex* **4** *on cell viability in Chang liver cell line after 12, 24 and 48 h treatment period.*

The drug dosages, glucose concentrations, and time intervals applied in these bio-evaluations were pre-determined from preliminary experiments. [23] The effects of the individual metal complexes **2 – 4** on glucose utilization in cultured liver (Chang) cell lines were deduced by measuring the glucose concentration in the media after incubating cells with the different metal complexes over 0, 12, 24, and 48 h, see **Figure 3.42**. The control group showed a steady decline in glucose concentrations over a 48 h experimental period. In contrast to the kinetic trends for the control group, the administration of different doses of **2 – 4** or insulin (positive control at 4 μg mL^{-1}) significantly ($p < 0.05$) decreased media glucose concentrations, especially after a 48 h incubation period where all metal complexes had reduced the glucose concentration by less 10%.

Complex **3** was the most effective in reducing the media glucose concentration in the liver cells. At all three treatment dosages, the steady-state glucose concentration was lower than that of insulin-treated cells, suggesting insulin-mimetic effects, see **Figure 3.42B**. The values were also lower than those induced by insulin. This superior in vitro activity of **3** (relative to **2** and **4**) is synonymous with the ability of the lead metal complex **1** to promote glucose-lowering effects in streptozotocin (STZ)-diabetic rats. From the results of the aqueous stability and biomolecular interaction of the chloro-containing complexes **1** and **3**, it is concluded that these complexes tend to undergo aqua co-ligand substitution before they can directly coordinate with amylin. This transformation is central to the mechanism of the anti-diabetic activity.[59]

However, even at the highest dose (50 μg mL^{-1}), 2 – 4 are less effective than insulin (4 μg mL^{-1}). The observed decrease of glucose concentration in the solution media implied its increased utilization by the liver cells in the presence of various metal complexes or insulin. Thus, additional insight into the mechanism can be gained because these metal complexes boost glucose metabolism in the liver in a similar manner to that of insulin, of which the administration is known to induce increased glucose utilization by liver cells. This is also evidenced by a sharp decline in media glucose concentrations in these experiments compared to the control. Insulin promotes glucose utilization indirectly through increasing glycogen synthesis.[21] The

steady decline in media glucose concentration in the presence of **2 – 4** may be attributed to the impairment of the glucose transporter isoform 2 (GLUT2). GLUT2 controls the glucose utilization pathways in the liver depending on the circulating concentration levels in the bloodstream.[60] In the cell, excess glucose is rapidly phosphorylated to glucose 6-phosphate by the enzyme glucokinase and subsequently metabolized by glycolysis and incorporated into glycogen.[61] Thus, malfunctioning or genetic mutation of GLUT2 or glucokinase has been shown to impair glucose homeostasis and subsequently lead to the development of T2DM.[62]

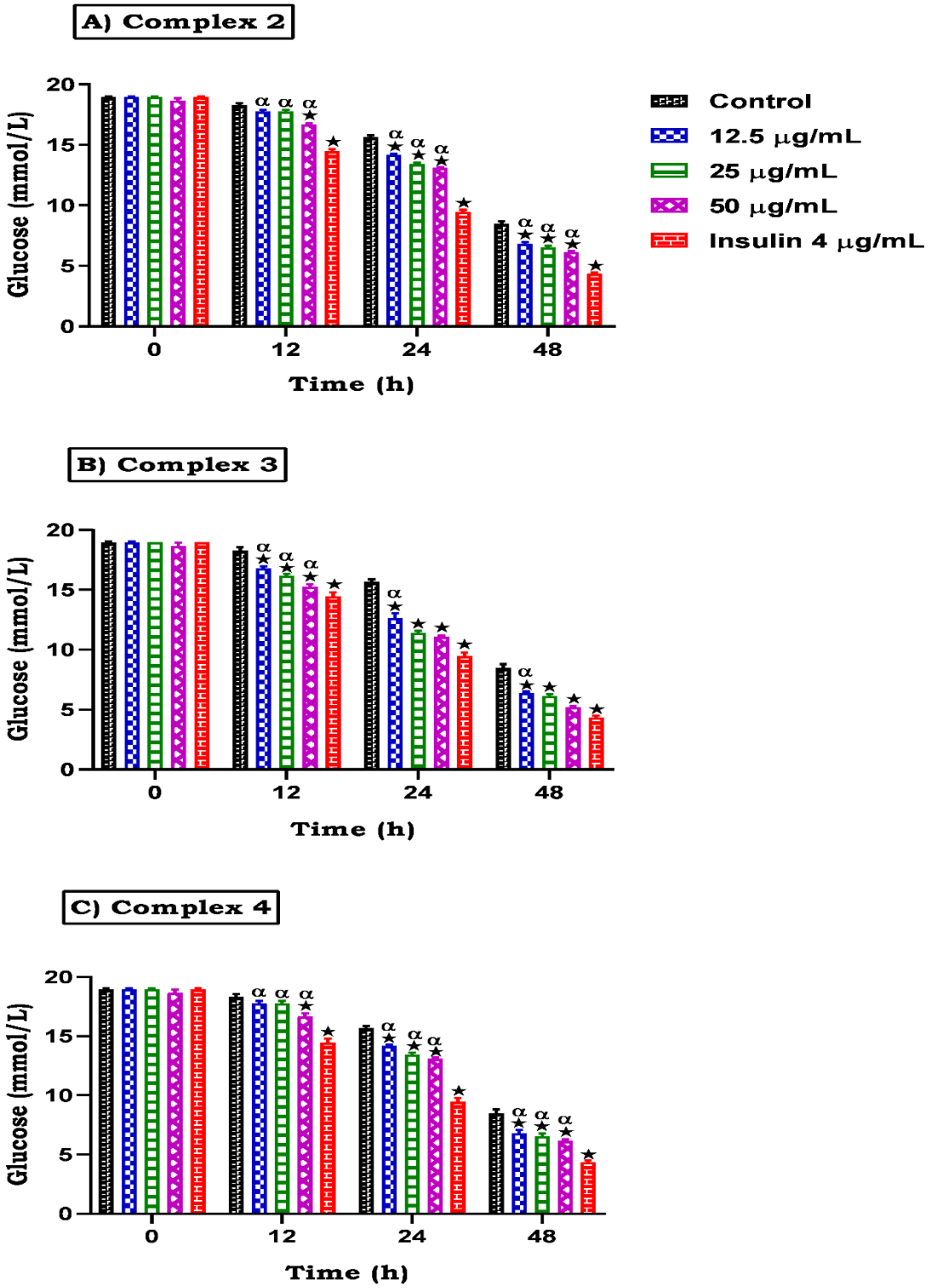

Figure 3. 42: *The effects of A) complex* **2**, *B) complex* **3,** *and C) complex* **4** *on glucose utilization in the liver (Chang) cell line after 0, 12, 24, and 48 h. Values are presented as means ± SEM (n = 6) in each group. *p < 0.05 compared to control,* $\boldsymbol{a}_p$ *< 0.05 compared to insulin at corresponding time.*

3.3.7 Molecular docking

PatchDock was utilized to study the rigid molecular docking between the ligand (metal complex) and the receptor (biomolecule).[18] More specifically, the algorithms are applied to search suitable vacant spaces (patches) where the static ligand can fit. Complementary intermolecular interactions are determined based on the nature of the receptor, which dictates the orientation of the ligand within the binding site. For PatchDock parameters, a clustering RMSD of 4 and a complex type of protein small ligand were used in these simulations.

Amylin structure (PDB ID: 2L86) was obtained from the Protein Database Centre, and the receptor was obtained from the latter using AutoDockTools.[63] In particular, the extra molecules of the recrystallization were omitted, and then all non-polar hydrogens were merged. YasaraView was used to produce perspective views and evaluate close contacts within the binding sites of the biomolecule and respective metal complexes.[64]

Molecular docking of the different optimized structures for the aqua analogs of **1** and **3** and metal complex cations **2** and **4** to the horseshoe-shaped amylin was performed using a rigid docking algorithm. Even though amylin can adopt several orientations in solutions, this static and blind docking method can provide input into the nature of intermolecular interactions occurring during the experimental amylin fluorescence titrations and TEM analysis. The results of these simulations show that the optimized conformers occupy a common binding site in the amylin cavity, see **Figures 3.43** and **3.44**. This molecule-receptor binding mode was also comparable to the binding of the pentapeptide inhibitor Phe-Leu-Pro-Asn-Phe (FLPNF) with amylin, where FLPNF has various reinforcing close contacts within the hydrophobic cavity of amylin.[65] For metal complex **1** cation-amylin adduct, of particular interest is that there is a direct overlap of the O-H bond of aqua co-ligand with NH and C atoms of L-Arginine 11 residue, which suggest that there is a high probability of displacement of the aqua ligand followed by covalent linking to amylin. This computational data substantiates the fluorescence spectral trends observed upon titrating metal complex **1** with amylin. Computationally, this adduct is stabilized by secondary interactions with the

phenylalanine 11 residue. However, for **3**, no overlapping was observed for its di-aqua co-ligands with the amino acids of its receptor.

The optimized metal complex cations **2** and **4** adopted comparable close contacts with amylin due to their nearly identical structural features. Firstly, no overlapping of electron density between the receptor and the aforementioned small molecules, which ruled out covalent bonding. Instead, these simulated adducts were stabilized by classical and non-classical hydrogen bonding. For example, the optimized conformer **2** forms close contacts with the overarching side amylin chains, see **Figures 3.45** and **3.46**.

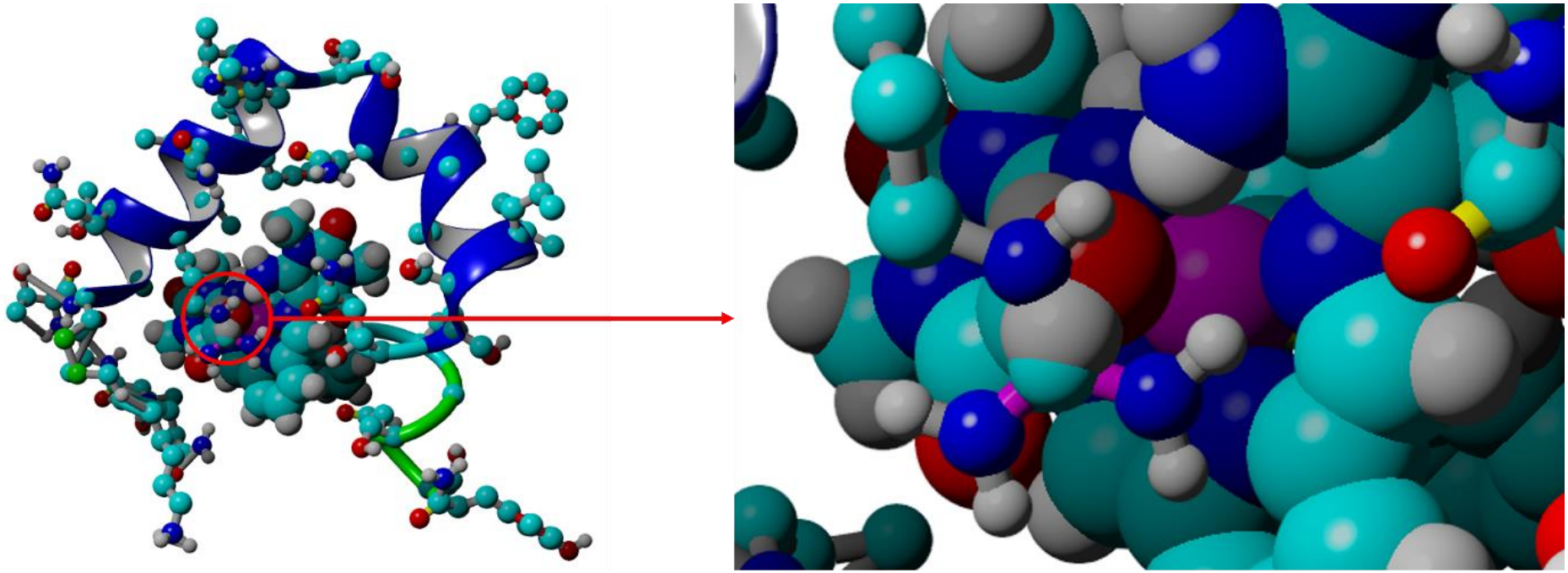

Figure 3. 43: *The primary interaction between the aqua analogue of* ***1*** *and amylin where the direct overlap of the O-H bond of the aqua co-ligand with NH and the C atoms of the L-Arginine 11 residue is observed.*

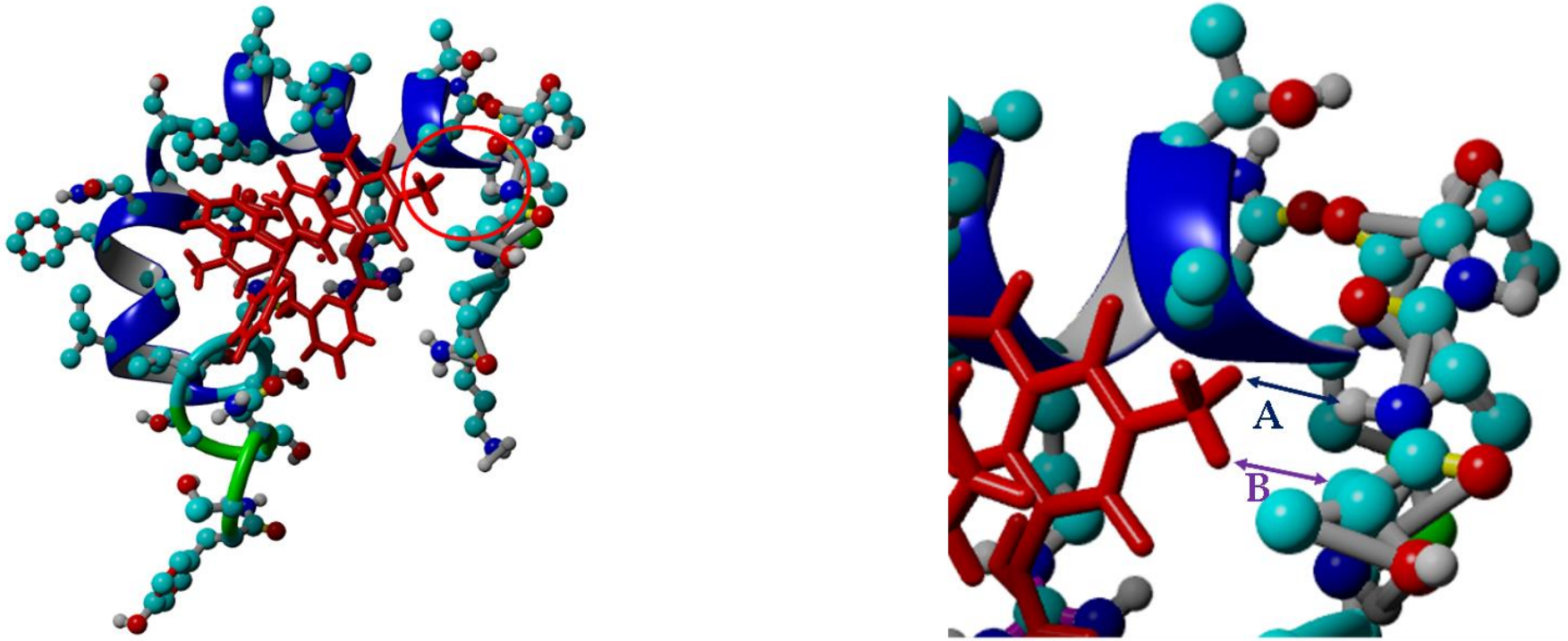

Figure 3. 44: *Secondary interactions: A = 2,486 Å and B = 2,597 Å occurring between amylin's phenylalanine 11 residue and the aqua analogue of* ***1****.*

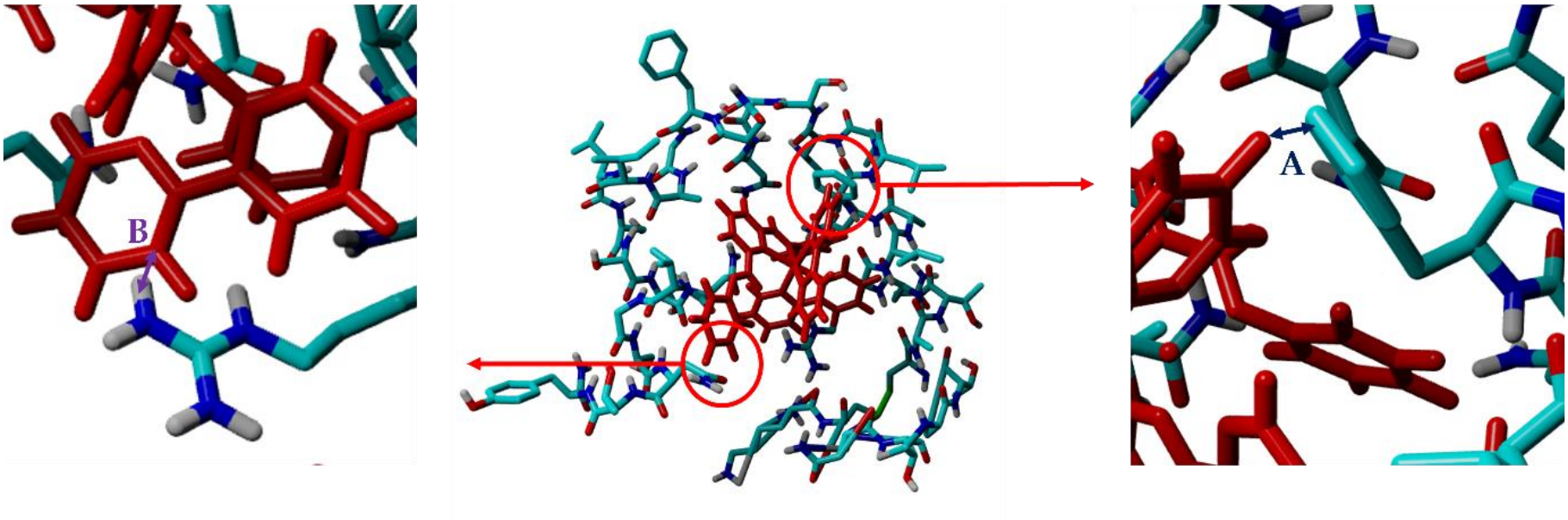

Figure 3. 45: *Primary interactions occurring between amylin and the metal complex cation* **2***: **A** = 1,266 Å shows the close contact with the phenylalanine 15 residue, while **B** = 0,762 Å shows interactions with the L-Arginine 11 residue.*

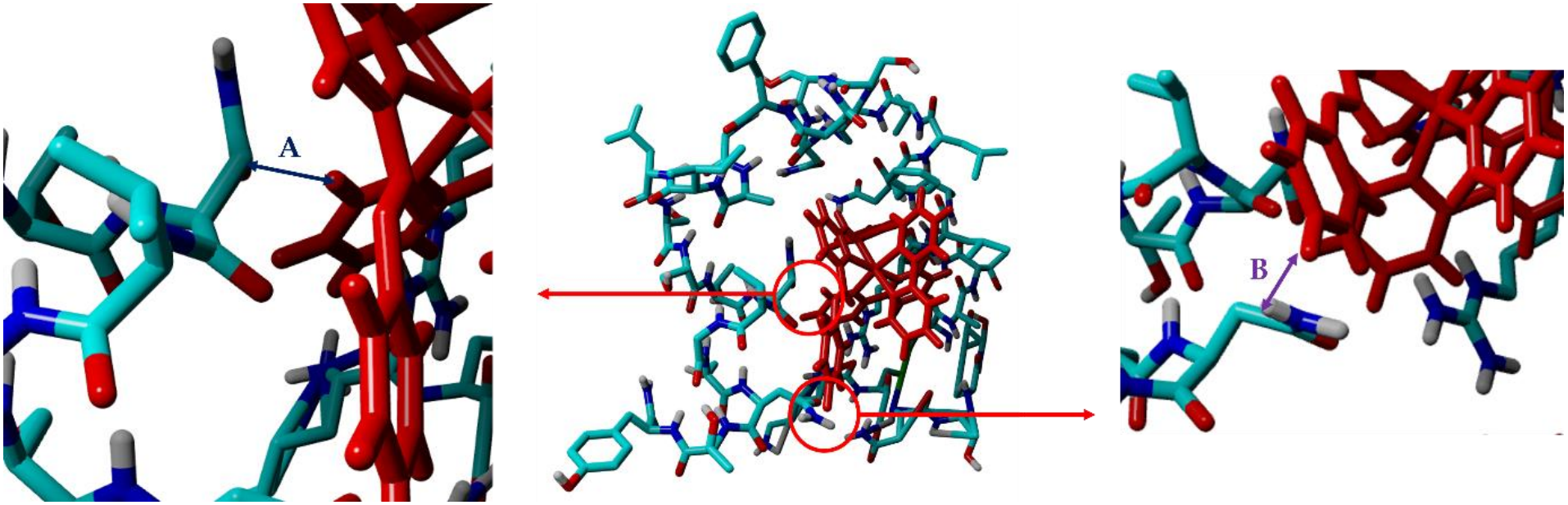

Figure 3. 46: *Secondary interactions between amylin and the metal complex cation* ***2****: **A** = 1,990 Å with the asparagine 31 residue and **B** = 1,739 Å with the asparagine 35 residue.*

3.4 References

(1) Sohrabi, M.; Binaeizadeh, M. R.; Iraji, A.; Larijani, B.; Saeedi, M.; Mahdavi, M. A review on α-glucosidase inhibitory activity of first row transition metal complexes: a futuristic strategy for treatment of type 2 diabetes. RSC Advances **2022**, 12 (19), 12011-12052, 10.1039/D2RA00067A. DOI: 10.1039/D2RA00067A. WHO. Diabetes. World Health Organization, https://www.who.int/health-topics/diabetes#tab=tab_1 (accessed 2023 26/07/2023).

(2) Salimi, A.; Chatterjee, S.; Yong Lee, J. Histidine Tautomerism Driving Human Islet Amyloid Polypeptide Aggregation in the Early Stages of Diabetes Mellitus Progression: Insight at the Atomistic Level. Chemistry – An Asian Journal **2021**, 16 (17), 2453-2462. Siboto, A.; Akinnuga, A. M.; Khumalo, B. N.; Ismail, M. B.; Booysen, I. N.; Sibiya, N. H.; Ngubane, P. S.; Khathi, A. The effects of a [3+1] oxo-free rhenium (V) compound with uracil-derived ligands on selected parameters of glucose homeostasis in diet-induced pre-diabetic rats. Obesity Medicine **2020**, 19, 100258, 1-8.

(3) Garg, P.; Duggal, N. Type 2 diabetes mellitus, its impact on quality of life and how the disease can be managed-a review. Obesity Medicine **2022**, 35, 100459, 1-11.

(4) Shurrab, N. T.; Arafa, E.-S. A. Metformin: A review of its therapeutic efficacy and adverse effects. Obesity Medicine **2020**, 17, 100186, 1-6.

(5) Kim, D.; Alshuwaykh, O.; Sandhu, K. K.; Dennis, B. B.; Cholankeril, G.; Ahmed, A. Trends in All-Cause and Cause-Specific Mortality Among Individuals With Diabetes Before and During the COVID-19 Pandemic in the U.S. Diabetes Care **2022**, 45 (6), e107-e109.

(6) Maikoo, S.; Makayane, D.; Booysen, I. N.; Ngubane, P.; Khathi, A. Ruthenium compounds as potential therapeutic agents for type 2 diabetes mellitus. European Journal of Medicinal Chemistry **2021**, 213, 1-11.

(7) He, L.; Wang, X.; Zhao, C.; Wang, H.; Du, W. Ruthenium complexes as novel inhibitors of human islet amyloid polypeptide fibril formation†. Metallomics **2013**, 5 (12), 1599-1603.

(8) Bhowmick, D. C.; Kudaibergenova, Z.; Burnett, L.; Jeremic, A. M. Molecular Mechanisms of Amylin Turnover, Misfolding and Toxicity in the Pancreas. Molecules **2022**, 27 (3), 1-24.

(9) Gong, G.; Wang, W.; Du, W. Binuclear ruthenium complexes inhibit the fibril formation of human islet amyloid polypeptide. RSC Advances **2017**, 7 (30), 18512-18522, 10.1039/C6RA28107A.

(10) Alghrably, M.; Czaban, I.; Jaremko, Ł.; Jaremko, M. Interaction of amylin species with transition metals and membranes. Journal of Inorganic Biochemistry **2019**, 191, 69-76.

(11) Mabuza, L. P.; Gamede, M. W.; Maikoo, S.; Booysen, I. N.; Ngubane, P. S.; Khathi, A. Amelioration of risk factors associated with diabetic nephropathy in diet-induced pre-diabetic rats by an uracil-derived diimine ruthenium(II) compound. Biomedicine & Pharmacotherapy **2020**, 129, 110483.

(12) Bruker APEX2, SAINT and SADABS (2010). Bruker AXS Inc. Madison., Wisconsin, USA.; Bruker AXS Inc. Madison.

(13) Blessing, R. H. An empirical correction for absorption anisotropy. Acta crystallographica. Section A, Foundations of crystallography **1995**, 51 (Pt 1), 33-38.

(14) Farrugia, L. WinGX and ORTEP for Windows: an update. J. Appl. Crystallogr. **2012**, 45 (4), 849-854.

(15) Sheldrick, G. A short history of SHELX. Acta Crystallogr. A **2008**, 64 (1), 112-122.

(16) Dolomanov, O. V.; Bourhis, L. J.; Gildea, R. J.; Howard, J. A. K.; Puschmann, H. OLEX2: a complete structure solution, refinement and analysis program. Journal of Applied Crystallography **2009**, 42 (2), 339-341. Bourhis, L.; Dolomanov, O.; Gildea, R.; Howard, J.; Puschmann, H. The anatomy of a comprehensive constrained, restrained refinement program for the modern computing environment –Olex2 dissected. Acta Crystallographica Section A **2015**, 71, 59–75.

(17) Brink, A.; Visser, H. G.; Roodt, A. Novel imino rhenium(I) tricarbonyl complexes of salicylidene-derived ligands: Synthesis, X-ray crystallographic studies, spectroscopic characterization and DFT calculations. Polyhedron **2013**, 52, 416-423.

(18) Schneidman-Duhovny, D.; Inbar, Y.; Nussinov, R.; Wolfson, H. J. PatchDock and SymmDock: servers for rigid and symmetric docking. Nucleic Acids Res **2005**, 33 (Web Server issue), W363-367.

(19) Schneider, C. A.; Rasband, W. S.; Eliceiri, K. W. NIH Image to ImageJ: 25 years of image analysis. Nature Methods **2012**, 9 (7), 671-675.

(20) Mosmann, T. Rapid colorimetric assay for cellular growth and survival: application to proliferation and cytotoxicity assays. J Immunol Methods **1983**, 65 (1-2), 55-63.

(21) Chen, Y.; Liu, H.; Wang, Y.; Yang, S.; Yu, M.; Jiang, T.; Lv, Z. Glycosaminoglycan from Apostichopus japonicus inhibits hepatic glucose production via activating Akt/FoxO1 and inhibiting PKA/CREB signaling pathways in insulin resistant hepatocytes. Food & Function **2019**, 10 (11), 7565-7575.

(22) van de Venter, M.; Roux, S.; Bungu, L. C.; Louw, J.; Crouch, N. R.; Grace, O. M.; Maharaj, V.; Pillay, P.; Sewnarian, P.; Bhagwandin, N.; et al. Antidiabetic screening and scoring of 11 plants traditionally used in South Africa. Journal of Ethnopharmacol **2008**, 119 (1), 81-86.

(23) Mabuza, L. P.; Gamede, M. W.; Maikoo, S.; Booysen, I. N.; Ngubane, P. S.; Khathi, A. Effects of a Ruthenium Schiff Base Complex on Glucose Homeostasis in Diet-Induced Pre-Diabetic Rats. Molecules **2018**, 23 (7), 1721, 1-7.

(24) Booysen, I.; Gerber, T.; Mayer, P. Oxidation of 5,6Diamino1,3-dimethyl-2,4-dioxopyrimidine by Perrhenate: the crystal structure of 1,3,6,8-Tetramethylpyrimidopteridine-2,4,5,7-tetrone. Journal of The Brazilian Chemical Society - JBCS **2008**, 19, 199-202.

(25) Jadoo, B.; Booysen, I. N.; Akerman, M. P. Synthesis, characterization and DNA binding studies of rhenium(I) and (V) compounds with Schiff bases derived from 4-aminotetrahydropyran. Polyhedron **2017**, 126, 159-165.

(26) van der Westhuizen, D.; Slabber, C. A.; Fernandes, M. A.; Joubert, D. F.; Kleinhans, G.; van der Westhuizen, C. J.; Stander, A.; Munro, O. Q.; Bezuidenhout, D. I. A Cytotoxic Bis(1,2,3-triazol-5-ylidene)carbazolide Gold(III) Complex Targets DNA by Partial Intercalation. Chemistry – A European Journal **2021**, 27 (32), 8295-8307.

(27) Geisler, H.; Westermayr, J.; Cseh, K.; Wenisch, D.; Fuchs, V.; Harringer, S.; Plutzar, S.; Gajic, N.; Hejl, M.; Jakupec, M. A.; Philipp Marquetand, P.; Kandioller, W. Tridentate 3-Substituted Naphthoquinone Ruthenium Arene Complexes: Synthesis, Characterization, Aqueous Behavior, and Theoretical and Biological Studies. Inorganic Chemistry **2021**, 60 (13), 9805-9819. Cetinbas, N.; Webb, M. I.; Dubland, J. A.; Walsby, C. J. Serum-protein interactions with anticancer Ru(III) complexes KP1019 and KP418 characterized by EPR. JBIC Journal of Biological Inorganic Chemistry **2010**, 15 (2), 131-145. Webb, M. I.; Walsby, C. J. Control of ligand-exchange processes and the oxidation state of the antimetastatic Ru(iii) complex NAMI-A by interactions with human serum albumin. Dalton Transactions **2011**, 40 (6), 1322-1331, 10.1039/C0DT01168A. Webb, M. I.; Walsby, C. J. EPR as a probe of the intracellular speciation of ruthenium(iii) anticancer compounds†. Metallomics **2013**, 5 (12), 1624-1633. Webb, M. I.; Walsby, C. J. Albumin binding and ligand-exchange processes of the Ru(iii) anticancer agent NAMI-A and its bis-DMSO analogue determined by ENDOR spectroscopy. Dalton Transactions **2015**, 44 (40), 17482-17493.

(28) Mai, S.; Ashwood, B.; Marquetand, P.; Crespo-Hernández, C. E.; González, L. Solvatochromic Effects on the Absorption Spectrum of 2-Thiocytosine. The Journal of Physical Chemistry B **2017**, 121 (20), 5187-5196.

(29) Karges, J.; Heinemann, F.; Maschietto, F.; Patra, M.; Blacque, O.; Ciofini, I.; Spingler, B.; Gasser, G. A Ru(II) polypyridyl complex bearing aldehyde functions as a versatile synthetic precursor for long-wavelength absorbing photodynamic therapy photosensitizers. Bioorg Med Chem **2019**, 27 (12), 2666-2675. Wiśniewska, J.; Fandzloch, M.; Muzioł, T.; Łakomska, I. The hydrolysis of a ruthenium(III) complex with triazolopyrimidine ligands and mechanistic insights into its anticancer activity. Inorganic Chemistry Communications **2019**, 109, 107567, 1-6. Elsayed, S. A.; Harrypersad, S.; Sahyon, H. A.; El-Magd, M. A.; Walsby, C. J. Ruthenium(II)/(III) DMSO-Based Complexes of 2-Aminophenyl Benzimidazole with In Vitro and In Vivo Anticancer Activity. Molecules **2020**, 25 (18), 4284, 1-26.

(30) Maikoo, S.; Xulu, B.; Mambanda, A.; Mkhwanazi, N.; Davison, C.; de la Mare, J. A.; Booysen, I. N. Biomolecular interactions of cytotoxic ruthenium compounds with

thiosemicarbazone or benzothiazole Schiff base chelates. ChemMedChem **2022**, 17 (20), 1-15.

(31) Mutua, G. K.; Bellam, R.; Jaganyi, D.; Mambanda, A. The role of N,N-chelate ligand on the reactivity of (η6-p-cymene)Ru(II) complexes: kinetics, DNA and protein interaction studies. Journal of Coordination Chemistry **2019**, 72 (17), 2931-2956.

(32) Mambanda, A.; Ongoma, P.; Gichumbi, J.; Omondi, R. O.; Hunter, L. A.; Kanyora, A. K. Crystal structures of half-sandwich Ru(II) complexes, [(η6-p-Cymene)(3-chloro-6-(1H-pyrazol-1-yl)pyridazine)Ru(X)]BF4, (X = Cl, Br, I). Molbank **2022**, 2022, 1-14. (4), M1477. Nikolić, S.; Grgurić-Šipka, S.; Djordjević, I. S.; Dahmani, R.; Dekanski, D.; Vidičević, S.; Tošić, J.; Mitić, D.; Grubišić, S. Half-sandwich ruthenium(II)-arene complexes: synthesis, spectroscopic studies, biological properties, and molecular modeling. Journal of Coordination Chemistry **2019**, 72 (1), 148-163.

(33) Soh, C.; Kollipara, M. R.; Banothu, V.; Diengdoh, D. F.; Kaminsky, W.; Rymmai, E. K. Synthesis and molecular structure of arene ruthenium(II) complexes containing benzhydrazone derivative ligands with antibacterial and antioxidant properties. Journal of Molecular Structure **2022**, 1269, 133775.

(34) Kumari, M.; Bera, S. K.; Lahiri, G. K. Noninnocence of the deprotonated 1,2-bis((1H-pyrrol-2-yl)methylene)hydrazine bridge in diruthenium frameworks – a function of co-ligands. Dalton Transactions **2021**, 50 (28), 9891-9903.

(35) Rout, D.; Sharma, S.; Agarwala, P.; Upadhyaya, A. K.; Sharma, A.; Sasmal, D. K. Interaction of Ibuprofen with Partially Unfolded Bovine Serum Albumin in the Presence of Ionic Micelles and Oligosaccharides at Different λex and pH: A Spectroscopic Analysis. ACS Omega **2023**, 8 (3), 3114-3128.

(36) Suryawanshi, V. D.; Walekar, L. S.; Gore, A. H.; Anbhule, P. V.; Kolekar, G. B. Spectroscopic analysis on the binding interaction of biologically active pyrimidine derivative with bovine serum albumin. Journal of Pharmaceutical Analysis **2016**, 6 (1), 56-63.

(37) Ketrat, S.; Japrung, D.; Pongprayoon, P. Exploring how structural and dynamic properties of bovine and canine serum albumins differ from human serum albumin. Journal of Molecular Graphics and Modelling **2020**, 98, 107601, 1-8.

(38) Bellam, R.; Jaganyi, D.; Robinson, R. S. Heterodinuclear Ru–Pt Complexes Bridged with 2,3-Bis(pyridyl)pyrazinyl Ligands: Studies on Kinetics, Deoxyribonucleic Acid/Bovine Serum Albumin Binding and Cleavage, In Vitro Cytotoxicity, and In Vivo Toxicity on Zebrafish Embryo Activities. ACS Omega **2022**, 7 (30), 26226-26245.

(39) Maikoo, S.; Booysen, I. N.; Xulu, B.; Rhyman, L.; Ramasami, P. Stabilization of the ruthenium (II) and -(III) centres by chelating N-donor ligands: Synthesis, characterization, biomolecular affinities and computational studies. Journal of Molecular Structure **2021**, 1244, 130986, 1-14.

(40) Hadidi, S.; Feizi, F. Study on the interaction of antiviral drug 'Tenofovir' with human serum albumin by spectral and molecular modeling methods. Spectrochimica acta. Part A, Molecular and biomolecular spectroscopy **2014**, 138C, 169-175.

(41) Li, Z.-M.; Wei, C.-W.; Zhang, Y.; Wang, D.-S.; Liu, Y.-N. Investigation of competitive binding of ibuprofen and salicylic acid with serum albumin by affinity capillary electrophoresis. Journal of chromatography. B, Analytical technologies in the biomedical and life sciences **2011**, 879, 1934-1938.

(42) Zhivkova, Z. D. Studies on drug-human serum albumin binding: the current state of the matter. Curr Pharm Des **2015**, 21 (14), 1817-1830.

(43) Topală, T.; Bodoki, A.; Oprean, L.; Oprean, R. Bovine Serum Albumin Interactions with Metal Complexes. Clujul Med **2014**, 87 (4), 215-219.

(44) Mandal, P.; Kundu, B. K.; Vyas, K.; Sabu, V.; Helen, A.; Dhankhar, S. S.; Nagaraja, C. M.; Bhattacherjee, D.; Bhabak, K. P.; Mukhopadhyay, S. Ruthenium(ii) arene NSAID complexes: inhibition of cyclooxygenase and antiproliferative activity against cancer cell lines. Dalton Trans **2018**, 47 (2), 517-527. Maikoo, S.; Chakraborty, A.; Vukea, N.; Dingle, L. M. K.; Samson, W. J.; de la Mare, J.-A.; Edkins, A. L.; Booysen, I. N. Ruthenium complexes with mono- or bis-heterocyclic chelates: DNA/BSA binding, antioxidant and anticancer studies. Journal of Biomolecular Structure and Dynamics **2021**, 39 (11), 4077-4088. de Melo, A. C. C.; Santana, J.; Nunes, K.; Rodrigues, B. L.; Castilho, N.; Gabriel, P.; Moraes, A. H.; Marques, M. A.; de Oliveira, G. A. P.; de Souza Í, P.; Terenzi, H.; Pereira-Maia, E.C. New Heteroleptic Ruthenium(II) Complexes with

Sulfamethoxypyridazine and Diimines as Potential Antitumor Agents. Molecules **2019**, 24 (11), 1-16.

(45) Kim, G. nab-Paclitaxel for the treatment of pancreatic cancer. Cancer Manag Res **2017**, 9, 85-96. Giordano, G.; Pancione, M.; Olivieri, N.; Parcesepe, P.; Velocci, M.; Di Raimo, T.; Coppola, L.; Toffoli, G.; D'Andrea, M. R. Nano albumin bound-paclitaxel in pancreatic cancer: Current evidences and future directions. World J Gastroenterol **2017**, 23 (32), 5875-5886.

(46) Wasko, J.; Wolszczak, M.; Kaminski, Z. J.; Steblecka, M.; Kolesinska, B. Human Serum Albumin Binds Native Insulin and Aggregable Insulin Fragments and Inhibits Their Aggregation. Biomolecules **2020**, 10 (10), 1366, 1-24. Haeri, H. H.; Tomaszewski, J.; Phytides, B.; Schimm, H.; Möslein, G.; Niedergethmann, M.; Hinderberger, D.; Gelos, M. Identification of Patients with Pancreatic Cancer by Electron Paramagnetic Resonance Spectroscopy of Fatty Acid Binding to Human Serum Albumin. ACS Pharmacology & Translational Science **2020**, 3 (6), 1188-1198.

(47) Tan, J.; Zhang, J.; Luo, Y.; Ye, S. Misfolding of a Human Islet Amyloid Polypeptide at the Lipid Membrane Populates through β-Sheet Conformers without Involving α-Helical Intermediates. Journal of the American Chemical Society **2019**, 141 (5), 1941-1948.

(48) Ridgway, Z.; Lee, K. H.; Zhyvoloup, A.; Wong, A.; Eldrid, C.; Hannaberry, E.; Thalassinos, K.; Abedini, A.; Raleigh, D. P. Analysis of Baboon IAPP Provides Insight into Amyloidogenicity and Cytotoxicity of Human IAPP. Biophys J **2020**, 118 (5), 1142-1151. Xu, Y.; Maya-Martinez, R.; Guthertz, N.; Heath, G. R.; Manfield, I. W.; Breeze, A. L.; Sobott, F.; Foster, R.; Radford, S. E. Tuning the rate of aggregation of hIAPP into amyloid using small-molecule modulators of assembly. Nature Communications **2022**, 13 (1), 1040, 1-15. Fortin, J.; Benoit-Biancamano, M.-O.; C.-Gaudreault, R. Discovery of Ethyl Urea Derivatives as Inhibitors of Islet Amyloid Polypeptide Fibrillization and Cytotoxicity. Canadian Journal of Physiology and Pharmacology **2015,** 94(3), 341-6.

(49) Maikoo, S.; Makayane, D.; Booysen, I. N.; Ngubane, P.; Khathi, A. Ruthenium compounds as potential therapeutic agents for type 2 diabetes mellitus. European Journal of Medical Chemistry **2021**, 213, 113064, 1-15.

(50) Duy, C.; Fitter, J. How aggregation and conformational scrambling of unfolded states govern fluorescence emission spectra. Biophys J **2006**, 90 (10), 3704-3711.

(51) Alberti, E.; Zampakou, M.; Donghi, D. Covalent and non-covalent binding of metal complexes to RNA. J Inorg Biochem **2016**, 163, 278-291.

(52) Bacac, M.; Hotze, A. C.; van der Schilden, K.; Haasnoot, J. G.; Pacor, S.; Alessio, E.; Sava, G.; Reedijk, J. The hydrolysis of the anti-cancer ruthenium complex NAMI-A affects its DNA binding and antimetastatic activity: an NMR evaluation. J Inorg Biochem **2004**, 98 (2), 402-412.

(53) Vargiu, A. V.; Robertazzi, A.; Magistrato, A.; Ruggerone, P.; Carloni, P. The hydrolysis mechanism of the anticancer ruthenium drugs NAMI-A and ICR investigated by DFT-PCM calculations. J Phys Chem B **2008**, 112 (14), 4401-4409.

(54) Molinspiration. https://www.molinspiration.com/services/properties.html (accessed 2023 22/11/2023).

(55) Matos, M. J.; Vazquez-Rodriguez, S.; Santana, L.; Uriarte, E.; Fuentes-Edfuf, C.; Santos, Y.; Muñoz-Crego, A. Synthesis and Structure-Activity Relationships of Novel Amino/Nitro Substituted 3-Arylcoumarins as Antibacterial Agents. Molecules **2013**, 18 (2), 1394-1404.

(56) Chadt, A.; Al-Hasani, H. Glucose transporters in adipose tissue, liver, and skeletal muscle in metabolic health and disease. Pflügers Archiv-European Journal of Physiology **2020**, 472, 1273-1298.

(57) Tan, Y.; Miao, L.; Xiao, J.; Cheang, W. 3, 3′, 4, 5′-Tetramethoxy-trans-stilbene improves insulin resistance by activating the IRS/PI3K/Akt pathway and inhibiting oxidative stress. Current Issues in Molecular Biology **2022**, 44 (5), 2175-2185.

(58) O'Rahilly, S. Molecular aspects of non-insulin-dependent diabetes. Eye (Lond) **1993**, 7 (Pt 2), 214-217.

(59) Mabuza, L. P.; Gamede, M. W.; Maikoo, S.; Booysen, I. N.; Ngubane, P. S.; Khathi, A. Cardioprotective effects of a ruthenium (II) Schiff base complex in diet-induced prediabetic rats. Diabetes Metab Syndr Obes **2019**, 12, 217-223.

(60) Liu, P.; Jiang, L.; Kong, W.; Xie, Q.; Li, P.; Liu, X.; Zhang, J.; Liu, M.; Wang, Z.; Zhu, L.; et al. PXR activation impairs hepatic glucose metabolism partly via inhibiting the HNF4α–GLUT2 pathway. Acta Pharmaceutica Sinica B **2022**, 12 (5), 2391-2405.

(61) Agius, L.; Chachra, S.; Ford, B. The protective role of the carbohydrate response element binding protein in the liver: the metabolite perspective. Frontiers in Endocrinology **2020**, 11, 594041, 1-12.

(62) Stanley, S.; Moheet, A.; Seaquist, E. Central mechanisms of glucose sensing and counterregulation in defense of hypoglycemia. Endocrine Reviews **2019**, 40 (3), 768-788.

(63) Shi, Y.; Lv, W.; Jiao, A.; Zhang, C.; Zhang, J. A Novel Pentapeptide Inhibitor Reduces Amyloid Deposit Formation by Direct Interaction with hIAPP. Int J Endocrinol **2019**, 2019, 9062032. Forli, S.; Huey, R.; Pique, M. E.; Sanner, M. F.; Goodsell, D. S.; Olson, A. J. Computational protein–ligand docking and virtual drug screening with the AutoDock suite. Nature Protocols **2016**, 11 (5), 905-919.

(64) Ismail, M. B.; Booysen, I. N.; Hosten, E.; Akerman, M. P. Synthesis, characterization and DNA interaction studies of tricarbonyl rhenium(I) compounds containing terpyridine Schiff base chelates. Journal of Organometallic Chemistry **2017**, 833, 1-9.

(65) Shi, Y.; Lv, W.; Jiao, A.; Zhang, C.; Zhang, J. A Novel Pentapeptide Inhibitor Reduces Amyloid Deposit Formation by Direct Interaction with hIAPP. International Journal of Endocrinology **2019**, 2019, 9062032, 1-9.

Chapter 4

Anti-amyloid aggregation and anti-hyperglycaemic activities of novel ruthenium(II) uracil Schiff base compounds

4.1 Introduction

Mutation of amylin within the pancreatic β-cells is typically induced by various endogenous factors such as exposure to elevated reactive oxygen species (ROS) and high pancreatic fat content.[1] In particular, the disordered arrangement of amylin strands leads to the formation of oligomers which undergo self-aggregation.[2] The resultant amyloidal plaques are associated with the causes of human pathological and immunological disorders such as cataracts, Diabetes Mellitus (DM) as well as Parkinson's and Alzheimer's diseases.[3]

Multiple studies have shown that amyloid fibrils develop from the misfolding of several unrelated proteins such as human islet amyloid polypeptide (hIAPP),[4] $A\beta_{1-40}$,[5] insulin,[6] lysozyme,[7] α-synuclein,[8] and albumins such as human serum albumin (HSA)[9] which all share a common cross-β-sheet structure. More specifically, bovine serum albumin (BSA) is a model globular protein and has been extensively studied due to its close homology to human serum albumin (HSA) function as well as its lower cost and higher availability than HSA.[10] BSA is a crucial chaperone (i.e. biomolecular vesicle) serum protein which payloads includes biomolecules, essential ions and therapeutic drugs. This biomolecule has three domains (viz. I, II, and III) which are each sub-divided into two sub-domains (viz. A and B).[11] Previous studies have illustrated that BSA can be precursor of amyloid fibril structures where the mutation can be induced by physical conditions such as pH below 4 and thermal denaturation by temperatures above 55 °C.[12,13]

Numerous studies in the literature have reported on the prevention of amyloid fibrillization using biocompatible inhibitors such as small peptides,[14] osmolytes,[15] as well metal-based complexes.[16] Furthermore, structure-activity relationship (SAR) studies of ruthenium compounds have established that the steric and electronic features of the chelating ligands as well as the nature of the metal cores are pivotal for modulating their BSA fibrillation inhibitory activities.[17, 18] A prior account of ruthenium ions coordinated to a small biogenic molecule, 5-fluorouracil and its N-dimethyl derivative shows that they disrupt the formation of mature amyloid fibrils due to their strong interaction which is ascribed to the relatively less hindered structures compared to metal-based inhibitors with larger ligands.[19] We have demonstrated in chapter 3 that the diimine ruthenium(II) compound, [Ru(H_3ucp)Cl(PPh_3)] (**7**) (H_4ucp = 2,6-bis-((6-amino-1,3-dimethyluracilimino)methylene)pyridine) and its analogues: cis-[Ru(bipy)$_2$(urdp)]Cl_2 (**8**) (urdp = 2,6-bis-((uracilimino)methylene)pyridine), trans-[$RuCl_2$(PPh_3)(urdp)] (**9**), and cis-[Ru(bpy)$_2$(H_4ucp)](PF_6)$_2$ (**10**) can disaggregate amyloidal plaques in a concentration-dependent manner. Moreover, the proposed mechanism of activity of the chloro-containing metal compounds is initiated by ligand substitution followed by direct coordination with amylin aggregates. On the contrary, the bipyridine uracil Schiff base complex cations of **4** and **5** were kinetically inert and non-coordinatively interact with the amylin aggregates.

It is evident from the aforementioned ruthenium compounds that their uracil moieties induce amylin disaggregation activities and hence, the next phase is the advancement to the isolation of diamagnetic ruthenium compounds with less sterically-demanding mono-imine uracil ligands. Therefore, in this study, we report on the synthesis and structural elucidations of diamagnetic ruthenium(II) compounds: [(η^6-p-cymene)(Ru^{II}LCl] (L= urpda for **1,** urpy for **2,** urqd for **3**), cis-[Ru^{II}(bipy)$_2$L] (L = urpy for **4** and H_2dadp for **5**), trans-[Ru^{II}L (PPh_3)Cl_2] (L = urpda for **6**), with bidentate uracil Schiff base ligands: (urpda, 5-((pyridin-2-yl)methyleneamino)-6-aminouracil), (urqda, 5-

((quinolin-2-yl)methyleneamino)-6-aminouracil), (urdpy, 6-amino-1,3-dimethyl-5-((pyridin-2-ylmethylene)amino)uracil), (dadp, 5,6-diaminouracil) and (urpy, 5-((pyridin-2-yl)methyleneamino)uracil), see **Figure 4.1**.

As medicinally relevant ruthenium compounds are known to be pro-drugs that transform to their relating active aqueous species under physiological conditions,[18, 20] hence evaluations of the solution stabilities of **1 – 6** is a prerequisite prior to evaluating their biomolecular interaction affinities, radical scavenging and in vitro glucose metabolism activities. Excessive release of ROS into the bloodstream has been closely correlated with destruction of pancreatic β-cells,[21] the antioxidant activities of the mono-imine metal complexes along with the previously reported diimine ruthenium compounds **7 – 10** will be assessed. Structure-activity correlations between the mono- and diimines will be derived from comparative analysis of their in vitro glucose metabolism activities.

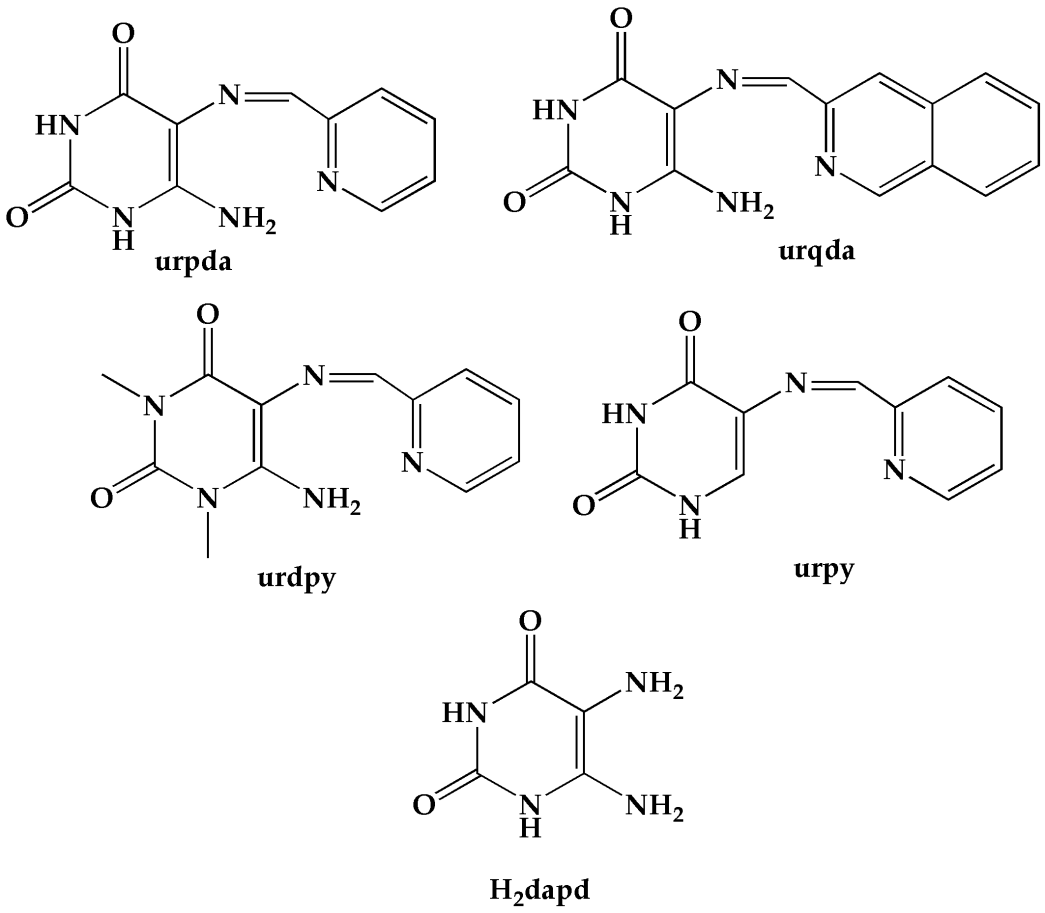

Figure 4. 1: *Structures of 5,6-diaminouracil (H_2dapd) and structurally-related uracil mono-imines.*

4.2 Experimental

4.2.1 *General synthetic procedure of the para-cymene ruthenium(II) Schiff base compounds:*
Amounts of 0.100 g (0.16 mmol) of the metal precursor, $[(\eta^6\text{-p-cymene})Ru(Cl)_2]_2$ were dissolved in dichloromethane (for **1**) or acetonitrile (for **2** and **3**) while two-fold molar quantities (0.32 mmol) of the respective uracil Schiff bases (0.0760 g for urpda, 0.051 g, for urdpy and 0.0667 g for urqda) were separately dissolved in 10 mL of alcoholic media (urdpa and urdpy in ethanol and urqda in methanol). The latter solutions were individually added in drops over 2 h to the different solutions of the metal precursor and thereafter, these reaction mixtures were stirred at room temperature for 16 h. Afterwards, 5 mL of an ethanolic suspension of ammonium salts (NH_4PF_6 for **1**, NH_4BF_4 for **2** and **3**) were introduced in a dropwise manner into the different reaction mixtures. Each of the reaction mixtures were filtered and from the various mother liquors, pale orange crystals suitable for single crystal X-ray analysis were grown via slow-evaporation over 4 days.

4.2.1.1 $[(\eta^6\text{-p-cymene})Ru(urpda)Cl)]$ (BF_4) (**1**)

Yield: (0.142 g, 81%); M.P. = 214 – 217°C; elemental analysis for $C_{20}H_{22}ClN_5O_2Ru \bullet [BF_4] \bullet [CH_2OH]$: calcd., C = 40.7%, H = 4.2%, N = 11.3%; found, C = 40.2%, H = 4.6%, N = 11.6%; IR (ν_{max}/cm^{-1}): υ(N–H) 3034 (w), ν(C=O) 1716 (m), ν(C=N) 1636 (m). ^{1}H NMR (295 K/d^6-DMSO/ppm): 11.04 (s, 1H, H4N); 9.55 (s, 1H, H17); 8.62 (s, 1H, H6); 8.23 - 8.03 (d, 2H, H3, H4); 7.86 (td, 1H, H4); 7.05 (s, 2H, $N3H_2$); 6.02 (d, 1H, N5H); 5.88 (d, 2H, H12, H11); 5.61 (d, 1H, H14); 2.19 (s, 3H, CH_3); 2.10 (d, 1H, H15); 1.21 (d, 1H, H1); 0.99 (dd, 6H, CH_3, CH_3). UV-Vis (DMF, λ_{max} (ε, M^{-1} cm^{-1})): 268 nm (15500), 419 nm (5600), 504 nm (2100).

4.2.1.2 [(η^6-p-cymene)Ru(urdpy)Cl](BF$_4$) (**2**)

Yield: (0.156 g, 85%); M.P: 209 – 212°C. Elemental analysis for $C_{22}H_{26}ClN_5O_2Ru$•[BF_4]$_2$• [H_2O] • $CNCH_3$ • CH_2CH_3OH: calcd., C = 38.7%, H = 4.6%, N = 10.4%; found, C = 38.4%, H = 4.8%, N = 10.8%; IR (ν_{max}/cm^{-1}): υ(N–H) 3048 (w), ν(C=O) 1706 (m), ν(C=N) 1625 (m); ^{1}H NMR (295 K/d^6-DMSO/ppm): 9.58 (d, 1H, H1); 8.99 (s, 1H, H6); 8.33 – 8.26 (m, 2H, H17, H21); 7.89 (t, 1H, H3); 7.49 (t, 1H, H2); 7.10 (s, 2H, N3H); 6.23 (d, 1H, H4); 5.83 (dd, 2H, H18, H19); 5.69 (d, 1H, H13); 3.46 (s, 3H, CH_3); 3.31 (s, 3H, CH_3); 2.20 (s, 3H, CH_3); 0.98 (dd, 6H, CH_3, CH_3). UV-Vis (DMF, λ_{max} (ε, M^{-1} cm^{-1})): 272 nm (19000); 433 nm (6700); 509 nm (2500).

4.2.1.3 [(η^6-p-cymene)(Ru(urqda)Cl](BF$_4$) (**3)**

Yield: (0.101 g, 76%); M.P: 210 – 214 ^{o}C. Elemental analysis for $C_{24}H_{23}ClN_4O_2Ru$• [BF_4]•$CNCH_3$]•$CNCH_3$: calcd., C = 43.1%, H = 3.8%, N = 9.4%; found, C = 43.2%, H = 3.8%, N = 9.7%; IR (ν_{max}/cm^{-1}):): υ(N–H) 3040 (w), ν(C=O) 1717 (m), ν(C=N) 1575 (m). ^{1}H NMR (295K/d$_6$-DMSO/ppm): 11.76 (d, 2H, H3N, H4N); 9.29 (s, 1H, H10); 8.91 (d, 1H, H7); 8.70 (d, 1H, H1); 8.40 (t, 2H, H2, H3); 8.29 (d, 1H, H8); 8.15 (td, 1H, H4); 8.01 (t, 1H, H22); 6.22 (dd, 2H, H20, H17); 5.98 (d, 1H, H21); 5.64 (d, 1H, H18); 2.28 (s, 3H, CH_3); 0.92 (s, 3H, CH_3); 0.81 (s, 3H, CH_3). UV-Vis (DMF, λ_{max} (ε, M^{-1} cm^{-1})): 274 nm (13400), sh, 327 nm (7500), 381 nm (9400), sh, 464 nm (4400), 562 nm (1700).

4.2.2 *General synthetic procedure of the bipyridine ruthenium(II) Schiff base compounds*:
Equimolar coordination reactions between cis-[$Ru(bipy)_2Cl_2$] (0.100 g, 0.21 mmol) with urpy (0.046 g, 0.21 mmol) or H_2dapd (0.0322 g, 0.21 mmol) in ethanol: water mixture (v: v = 16 mL + 4 mL) where the respective reaction mixtures were heated until reflux under an inert atmosphere for 8 h.

4.2.2.1 cis-[$Ru(bipy)_2(urpy)](BF_4)_2$ (**4**)

Subsequently, a red precipitate formed which was filtered, washed several times with water, and dried, resulting in a dark red precipitate. The precipitate was re-dissolved in acetonitrile (4 mL) and layered with diethyl ether to render dark red crystals of **4** after 8 days. Yield: (0.13 g, 87%); M.P: 182.7–184.5. Elemental analysis for $C_{30}H_{24}N_8O_2Ru \bullet [CNCH_3]_2 \bullet CH_3CH_2OH$: calcd., C = 37.9%, H = 3.5%, N = 12.6%; found, C = 37.5%, H = 3.9%, N = 12.9%; IR (ν_{max}/cm^{-1}): υ(N–H) 3079 (w), ν(C=O) 1693 (w), ν(C=N) 1596 (w). ^{1}H NMR (295K/d_6-DMSO/ppm): 10.71 (d, 2H, H3N, H4N); 9.14 (s, 1H, H6); 8.83 (dd, 2H, H11, H20); 8.76 (t, 2H, H2, H19); 8.67 (d, 1H, H14); 8.48 (d, 1H, H17); 8.27- 8.12 (m, 3H, H13, H29, H12); 8.11 (td, 1H, H4); 7.78 (d, 1H, H21); 7.71 (d, 1H, H30); 7.66 - 7.56 (m, 4H, H1, H2, H22, H23); 7.51 (t, 1H, H28); 7.37 (t, 1H, H3); 6.64 (s, 1H, H9); 2.14 (d, 2H, H24, H27).UV-Vis (DMF, λ_{max} (ε, M^{-1} cm^{-1})): 293 nm (17700); 352 nm (3000); 450 nm (2700), sh; 501 nm (2400).

4.2.2.2 cis-[$Ru(bipy)_2(dapd)$] (**5**)

A 5 mL volume of an ethanolic solution of NH_4BF_4 was added in a dropwise manner to the reaction mixture while stirring it at room temperature for 1 h to afford a red precipitate. The precipitate was collected by filtration, filtered, washed several times with water, and dried to get a dark red powder. The powder was redissolved in acetonitrile (4 mL) and layered with diethyl ether, which rendered dark red crystals of **5** after 2 days. Yield: (0.101 g, 76%); M.P: 242.9–238.2 ^oC. Elemental analysis for $C_{24}H_{22}N_8O_2Ru \bullet [PF_6] \bullet H_2O$: calcd, C = 40.2%, H = 3.1%, N = 15.4%; found, C = 40.5%, H =

3.1%, N = 15.4 %; IR (ν_{max}/cm^{-1}): ν(N–H) 3347, 3055 (w), ν(C=O) 1655 (w), ν(N-H) 1558 (m), ν(N-H) 1681 (w). ^{1}H NMR (295 K/d^6-DMSO/ppm): 9.85 (d, 1H, H5); 9.44 (d, 1H, H11); 8.76 (dd, 2H, H8, H14); 8.64 (t, 2H, H7, H12); 8.28 (t, 1H, H15); 8.21 (t, 1H, H24); 8.07 (td, 1H, H21); 7.93 (dt, 2H, H6, H13); 7.84 (t 1H, H17); 7.69 (d, 1H, H18); 7.51 (t, 1H, H22); 7.33 – 7.26 (m, 2H, H16, H23); 2.45 (s, 3H, N3H, N4H, N2H); 2.01 (s, 1H, N1H). UV-Vis (DMF, λ_{max} (ε, M^{-1} cm^{-1})): 296 nm (23000), 353 nm (2900), 485 nm (3200), 565 nm (1700).

4.2.2.3 Synthesis of trans-[Ru(urpda)(PPh_3)Cl_2] (**6**)

The 1:1 molar mixture of trans-[$Ru^{II}(PPh_3)_3Cl_2$] (0.100 g, 0.10 mmol) and urpda (0.037g, 0.10 mmol) in methanol (20 mL) was heated under reflux for 3 h. Thereafter, the mother liquor was allowed to cool to room temperature and a maroon precipitate was filtered off using a nylon Millipore membrane under vacuum and washed with diethyl ether. It was then re-dissolved in methanol (MeOH), and the resultant solution was layered with hexane. Cubic-shaped violet-coloured single crystals of **6** grew from the slow liquid evaporation in a 1:1 ratio of diethyl ether and methanol solution of **6**. Yield: (0.0115 g, 93%). MP: 203–206 ^{o}C. Elemental analysis for $C_{30}H_{24}N_8O_2Ru \bullet [CH_3CH_2OCH_2CH_3] \bullet H_2O$: calcd., C = 56.1%, H = 5.1%, N = 10.2%; found, C = 56.4%, H = 4.7%, N = 10.7%; IR (ν_{max}/cm^{-1}): ν(C=O) 1705 (m), ν(C=N) 1581 (m), ν(Ru-PPh_3) 689 (vs); ^{1}H NMR (295 K/ d^6-CD_6SO/ ppm): 8.12 (dd, 1H, H4); 7.94 -7.86 (m, 2H, H3, H2); 7.82 - 7.75 (m, 3H, H29, N3H, H1); 7.71 – 7.19 (m, 17H, PPh_3, N3H, N4H); ^{31}P NMR (295 K/ d^6-CD_6SO/ ppm): 34.80 (major), 26.20 (minor – aqua derivative). UV-Vis (DMSO, λ_{max} (ε, M^{-1} cm^{-1})): 270 nm (16000), 333 nm (5000), 373 nm (3900), 397 nm (4100), 428 nm (1700), 508 nm (1600).

4.2.3 Single Crystal X-ray Diffraction Studies.

Tables **4.1** and **4.2** contain the refined crystal structure details of **1- 6**.

Table 4. 1: *Crystal and structure refinement data for **1 – 3.***

Compound	**1** • $[PF_6]$ • CH_3OH	**2** • $[BF_4]_2$ • H_2O • CH_3CN • CH_2CH_3OH	**3** • $[BF_4]$ • CH_3CN• CH_3CN
Chemical formula	$C_{20}H_{23}ClF_2N_5O_2P_{0.5}Ru$	$C_{22}H_{26.69}BClF_4N_5O_2Ru$	$C_{24}H_{24.98}BClF_4N_4O_{2.49}Ru$
Formula weight	555.44	616.50	632.62
Temperature (K)	101.63(2)	104.76(2)	100.02(2)
Crystal system	Monoclinic	Monoclinic	Triclinic
Space group	C2/c	C2/c	P-1
Unit cell dimensions (Å, ^{o})	a = 19.1071(5) b = 11.3601(3) c = 21.9650(5) α = 90 β = 90.1140(10) γ = 90	a = 31.1220(6) b = 8.8014(2) c = 23.8118(5) α = 90 β = 124.6990(10) γ =90	a = 9.7041(10) b = 12.6693(14) c = 12.8191(14) α = 104.698(4) β = 107.478(4) γ = 111.415(4)
Crystal size (mm)	0.21 × 0.18 × 0.155	0.255 × 0.195 × 0.15	0.445 × 0.12 × 0.115
V ($Å^3$)	4767.7(2)	5362.5(2)	1276.9(2)
Z	8	8	2
Density (calc.) (Mg/m^3)	1.548	1.527	1.645
Absorption coefficient (mm^{-1})	7.041	6.153	0.780
F (000)	2244.0	2494.0	638.0
θ range for data collection (deg)	8.05°; 136.364°	6.91°; 144.458°	3.65°; 53.76°
Index ranges	-22 ≤ h ≤ 22 -13 ≤ k ≤ 13 -26 ≤ l ≤ 26	-38 ≤ h ≤ 38 -10 ≤ k ≤ 10 -29 ≤ l ≤ 29	-12 ≤ h ≤ 12 -16 ≤ k ≤ 16 -16 ≤ l ≤ 16
Reflections measured	40198	41853	50794

Observed reflections ($I > 2\sigma(I)$)	4251	4906	4127
Data/ restraints/ parameters	4362/0/296	5117/4/369	5476/2/377
Goodness of fit on F^2	1.051	1.055	1.030
Observed R; wR^2	0.0220, 0.0522	0.0242, 0.0631	0.0464; 0.1095
R_{int}	0.0306	0.0253	0.1334

Table 4. 2: *Crystal and structure refinement data for* ***4*** *-* ***6****.*

Compound	**4** • $(CNCH_3)_2$ • CH_3CH_2OH	**5** • $[PF_6]$ • H_2O	**6** • $CH_3CH_2OCH_2CH_3$ • H_2O
Chemical formula	$C_{30}H_{30}B_2F_8N_8O_5Ru$	$C_{27}H_{21.50}N_{5.50}O_2Ru$	$C_{15.75}H_{17}ClN_{2.50}O_{2.75}P_{0.50}Ru_{0.50}$
Formula weight	857.31	553.55	386.79
Temperature (K)	99.97(2)	105.86(2)	100.03(2)
Crystal system	Monoclinic	Triclinic	Triclinic
Space group	$P2_1/n$	P-1	P-1
Unit cell dimensions (Å, °)	a = 15.0081(15) b = 12.8923(13) c = 18.3017(18) α = 90 β = 104.259(4) γ = 90	a = 11.5656(4) b = 12.0179(4) c = 12.5582(4) α = 80.3340(10) β = 73.9390(10) γ = 65.7040(10)	a = 10.172(3) b = 11.566(4) c = 14.907(5) α = 84.146(15) β = 89.204(13) γ =72.135(13)
Crystal size (mm)	0.265 × 0.155 × 0.13	0.355 × 0.33 × 0.07	0.445 × 0.12 × 0.115
V ($Å^3$)	3432.1(6)	1525.91(9)	1660.2(9)
Z	4	2	4
Density (calc.) (Mg/m^3)	1.659	1.205	1.547
Absorption coefficient (mm^{-1})	0.553	4.412	0.731
F (000)	1728.0	560.0	790.0
θ range for data collection (deg)	3.91°; 55.21°	8.09°; 139.9°	2.746°; 53.734°
Index ranges	-19 ≤ h ≤ 19 -16 ≤ k ≤ 16 -23 ≤ l ≤ 23	-14 ≤ h ≤ 14 -14 ≤ k ≤ 14 -15 ≤ l ≤ 15	-12 ≤ h ≤ 12 -14 ≤ k ≤ 14 -18 ≤ l ≤ 18
Reflections measured	117788	37391	20609
Observed reflections (I > 2σ (I)	4319	5447	4173
Data/ restraints/ parameters	7411/0/500	5567/0/332	7029/0/352
Goodness of fit on F^2	0.942	1.087	1.026

Observed R; wR^2	0.0472; 0.1148	0.0313; 0.0881	0.0813, 0.2194
R_{int}	0.1614	0.0286	0.1161

4.2.4 Computational details

Insights into structural and electronic properties of **1 - 6** were computed at the density functional theory (DFT) level of complexity. Before the DFT calculations on the aforementioned metal complexes were performed, the counter ions and solvent of recrystallization were removed to prepare starting conformers. In addition, the computational calculations were conducted using the Gaussian 09W software package using the B3LYP (Becke, 3-parameter, Lee–Yang–Parr) function and LANL2DZ (Los Alamos National Laboratory 2 Double-Zeta) with a 6-311G^{++} (d, p) basis set, respectively.[22-23]

4.2.4.1 Data validation

Validation of the computational method was established by examining the differences between the geometric parameters of the optimized compounds and those of their corresponding solid-state structures, see **Figures 4.2** and **4.4**. Absence of intra- and intermolecular interactions in the X-ray crystal structures of the calculated molecules in the gas phase optimized structures, rationalizes the differences between the calculated and experimental geometric parameters. Frequency calculations performed at the same theoretical level, generate simulated vibrations with no negative Eigen values showing that each optimized structure are global minima on their relating potential energy surfaces.

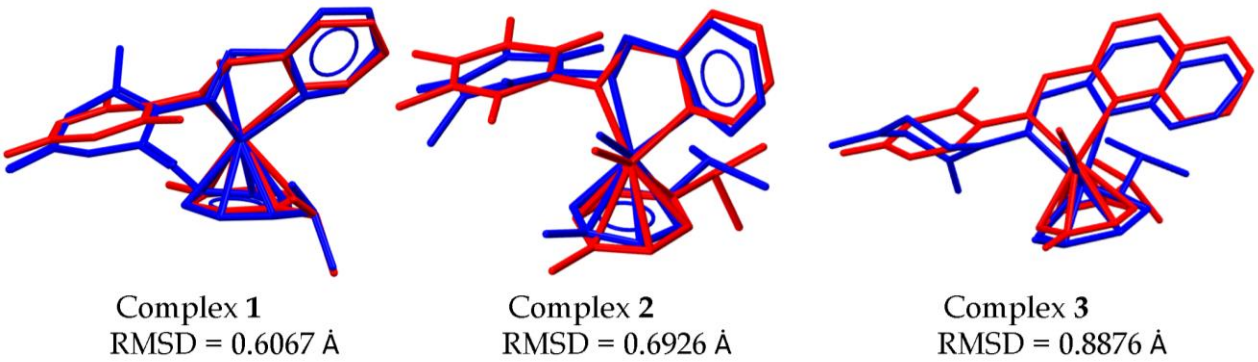

Figure 4. 2: *The corresponding super-imposed optimized and computed structures of* ***1 – 3*** *with their respective root mean square deviation (RMSD) values. The red structures are the optimized structures, while the blue structures are their corresponding experimental structures.*

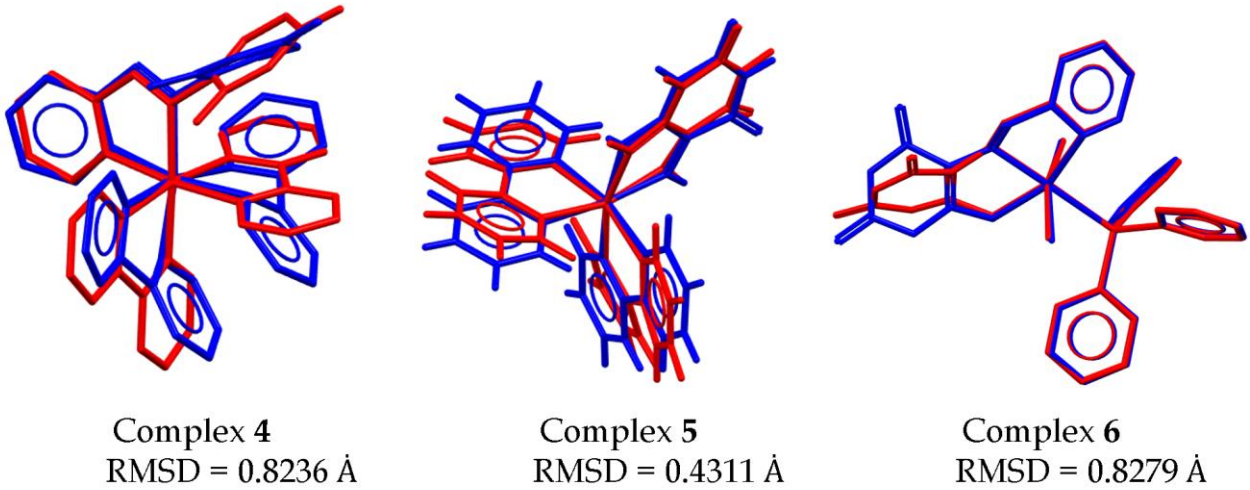

Figure 4. 3: *The corresponding super-imposed optimized and computed structures of* ***4 – 6*** *with their respective root mean square deviation (RMSD) values. The red structures are the optimized structures, while the blue structures are their corresponding experimental structures.*

4.2.5 Stability studies

The aqueous stabilities of the respective metal complexes **1- 6** were evaluated by monitoring their electronic spectra at a physiological temperature of 37 °C for 24 h at 1-h intervals to simulate in vivo conditions.[24] Standard solutions (1 mM) of different metal complexes were prepared in 2% DMSO (v: v) with 98% aqueous PBS buffer. UV-Visible absorption spectra of (**1-3** and **6**) in anhydrous DMSO saturated with lithium chloride were also recorded at hourly intervals for 24 h to check the kinetic stability towards chloride ligand exchange by DMSO. Electronic spectra of (**1-3** and **6**) were evaluated in the high-purity non-coordinative solvent, dichloromethane (DCM), to contrast with the possible displacement of chloride co-ligands from these metal complexes by DMSO solvent molecules.

4.2.6 Preparation of BSA amyloid fibrils

TEM micrographs were captured using a JEOL 1400 microscope. TEM samples were prepared by incubating amylin and BSA fibrils at 50 μM with 20 μM Thioflavin T (ThT) in the presence or absence of the respective metal complexes (at 75, 37.5, 18.75, 9.38, 4.69 μM for **1-6**) for 72 h at a physiological temperature of 37 °C, thereafter the prepared concentrations of BSA were induced at 55°C for 24 h to form amyloid fibrils, respectively. BSA fibrils were stained with formvar. The positive control is the TEM micrograph of amylin and BSA fibrils alone. ImageJ software was used to obtain the estimated sizes of the particles.[25]

4.3 Results and discussion

4.3.1 Synthesis and spectral characterization

The 1:1 molar coordination reactions between $[(\eta^6\text{-p-cymene})(RuCl_2)]_2$ with the uracil Schiff bases: urdpa, urpy, and urqda formed the organoruthenium(II) Schiff base complexes, $[(\eta^6\text{-p-cymene})(Ru^{II}(urdpa)Cl]$ (**1**), $[(\eta^6\text{-p-cymene})Ru^{II}urpyCl]$(**2**), $[(\eta^6\text{-p-cymene})(Ru^{II}(urqda)Cl]$ (**3**), respectively. The reaction of trans-$[RuCl_2(PPh_3)_2]$ with urpda led to the formation of the diamagnetic metal complex, cis-$[Ru^{II}(urpda)(PPh_3)Cl_2]$ (**6**), while the metal complexes: cis-$[Ru^{II}(bipy)_2(urpy)]$ (**4**) and cis-$[Ru^{II}(bipy)_2(dadp)]$ (**5**) were isolated from the relating reactions between cis-$[Ru^{II}(bipy)_2Cl_2]$ and urpy or H_2dadp. These novel ruthenium complexes were obtained in good yields with percentage yields above 76%. These monomeric metal complexes are highly soluble in aprotic non-volatile solvents such as DMF and DMSO but are partial soluble in alcoholic media.

Characteristic to the majority of the p-cymene organoruthenium complexes in literature.[29] The organic Schiff base ligands coordinated as neutral bidentate chelators ($N_{imino}N_{pyridyl}$ donor set for **1** and **2**, $N_{imino}N_{quinoline}$ for **3**) to the $[\eta^6$-p-cymene(Ru)Cl$]^+$ core where the metal complex cations are stabilized by $[PF_6]^-$ or $[BF_4]^-$ anions, see **Scheme 4.1**. As expected, the displacement of the labile co-ligands of the metal precursor, cis-$[Ru(bipy)_2Cl_2]$ by bidentate uracil ligands occurred to render the neutral octahedral metal complexes **4** and **5**. This trend in chemical reactivity adheres well with those found with higher steric demands of the diimine ligands rendered (1:2) metal complex cation: anions salts of **8** and **10**, respectively. This is re-emphasized that the stereo-electronic properties of uracil-derived Schiff base chelators have a profound on the coordination susceptibilities towards various ruthenium cores.

Therefore, it can be foreseen that the mono- and diimine ruthenium complexes will display different structure-activity relationship activities. Furthermore, the dadp chelating ligand in **5** has also stabilized the cis-Cl, trans-P-$RuCl_2(PPh_3)_2]$ unit render to a paramagnetic ruthenium(IV) complex, cis-Cl, trans-P-$[RuCl_2(PPh_3)_2(ddd)]$, [viz. 5,6-diamino-1,3-dimethyl uracil (H_2ddd)]. Mono-anionic tridentate coordination of

uracil iminos towards ruthenium(II) centres as seen in **6** are rare and another example reported before is 5-((thiophen-3-yl)methyleneamino)-6-amino-1,3-dimethyluracil (H_2tdp) in trans-[RuCl(PPh_3)$_2$(Htdp)] where the Htdp ligand acts as tridentate chelator through its amido and imino nitrogens as well as sulphur thiophene donor atoms.[26]

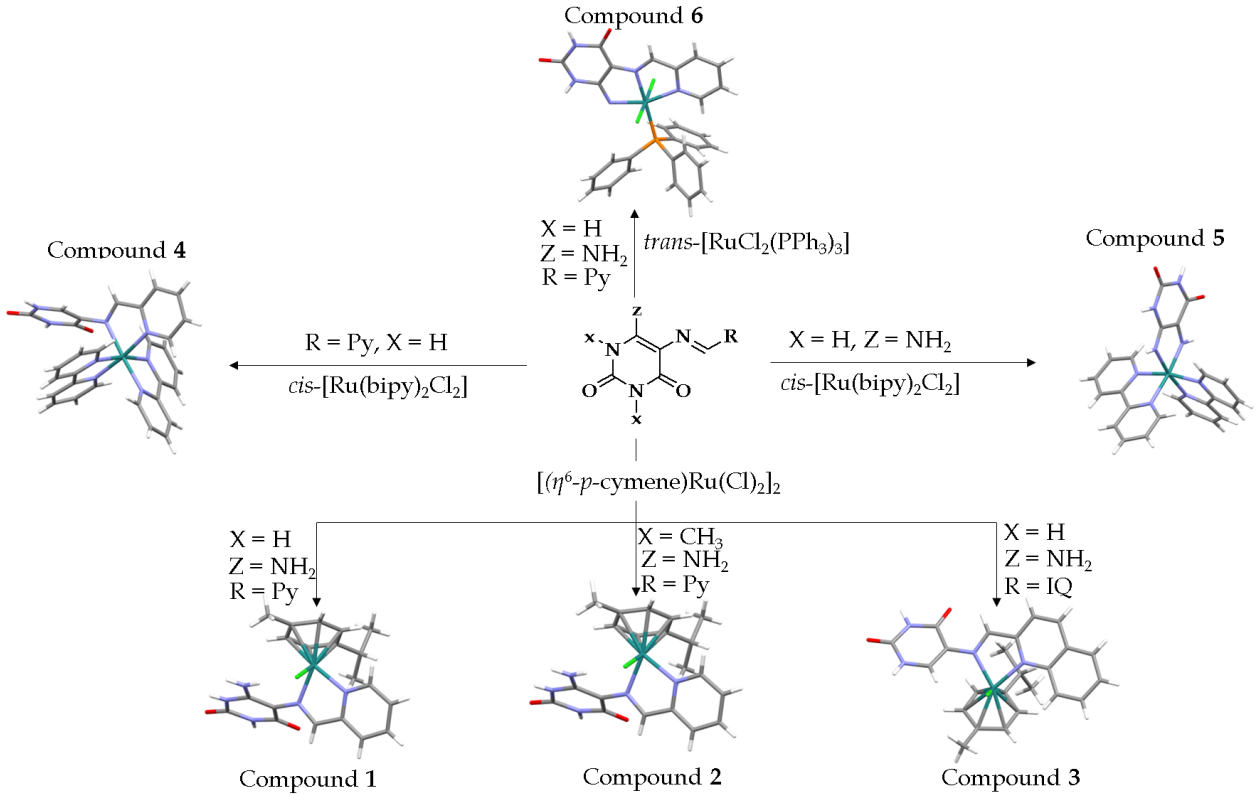

Scheme 4. 2: *Synthetic scheme illustrating the formation of* ***1 – 6****, where Py is (pyridine) and IQ is isoquinolone.*

The novel diamagnetic metal compounds were characterized using heteronuclear spectroscopy (viz. ^{1}H and ^{13}C NMR) as well as two-dimensional COSY NMR spectroscopy. The ^{31}P NMR spectrum of the diamagnetic metal complex **6** showed a singlet magnetic peak attributable to the trans-axial triphenylphosphine co-ligand at 26.1 ppm where a lower intensity peak is found downfield at 38.8 ppm can be accounted to the DMSO adduct upon displacement of the chloro co-ligand of **6**. see, **Figure 4.4**. Typical of Schiff bases coordinated to ruthenium(II) centres, the imino singlets are shielded occurring within the range of 7.82 - 7.75 ppm for **6** in comparison to the analogous signals of the metal complexes (at 9.55 ppm for **1**, 8.99 ppm for **2**, 9.29 ppm for **3** and 9.14 ppm for **4**) as observed in **Figures 4.5 – 4.10**, respectively. Discernment of the cis-$[Ru(bipy)_2]^{2+}$ and bridging pyridyl proton signals of the isostructural metal compounds **4** and **5** through analysis of their COSY NMR spectra, see **Figures 11** and **12**.

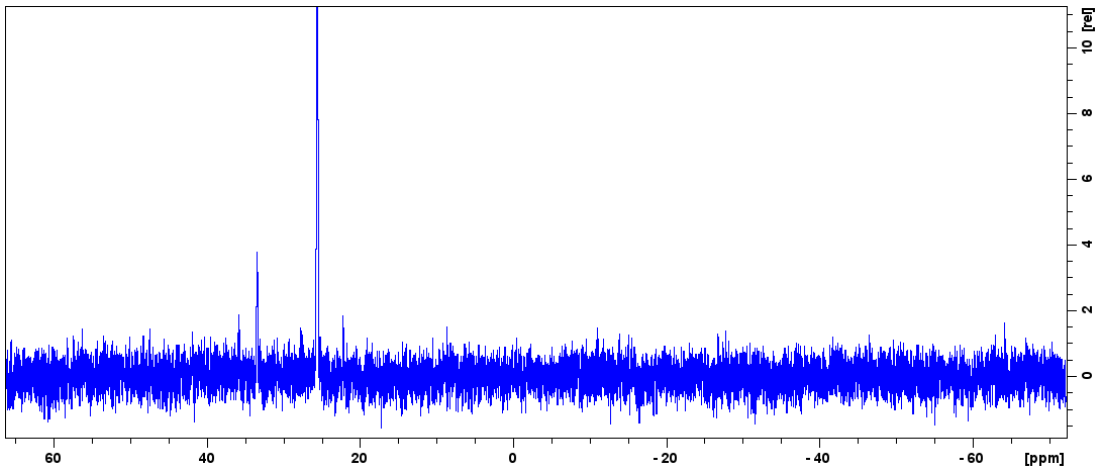

Figure 4. 4: *^{31}P NMR spectrum of **6** in deuterated DMSO-d_6.*

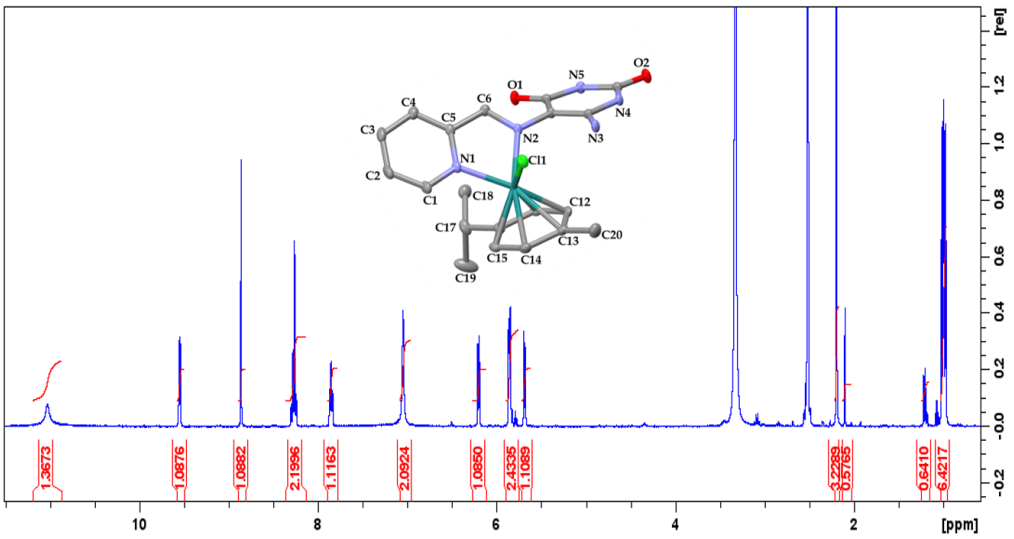

Figure 4. 5: *^{1}H NMR spectrum of* ***1****.*

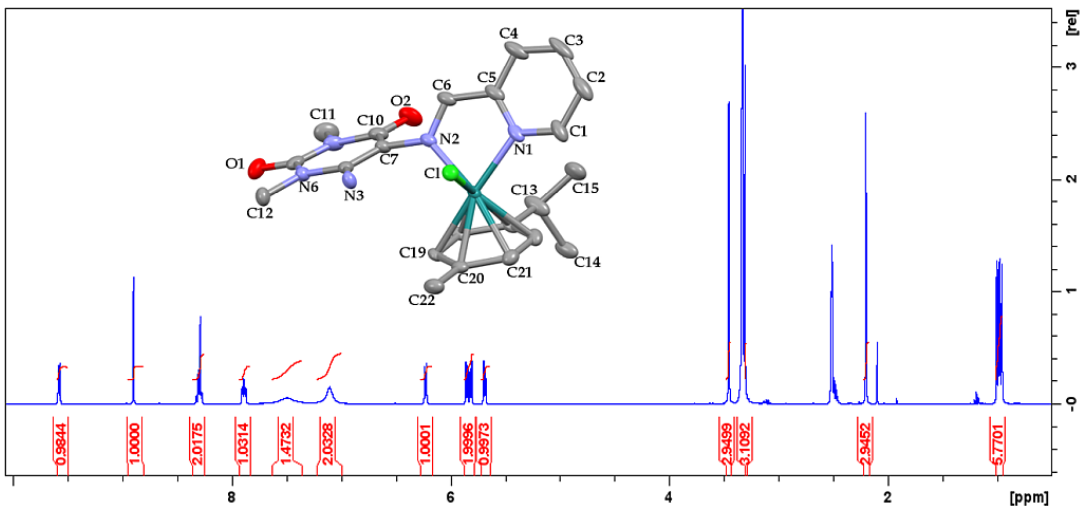

Figure 4. 6: *^{1}H NMR spectrum of* **2***.*

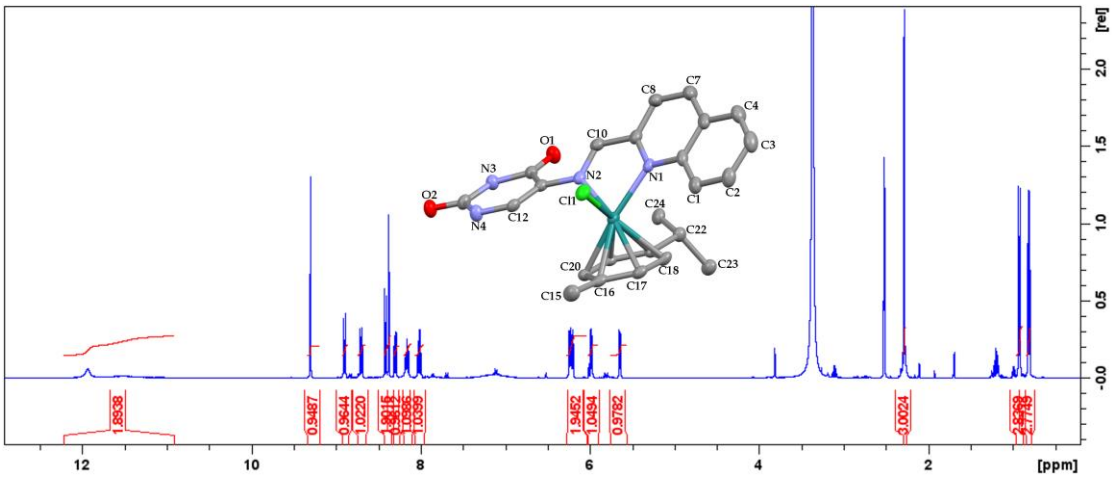

Figure 4. 7: *^{1}H NMR spectrum of* ***3****.*

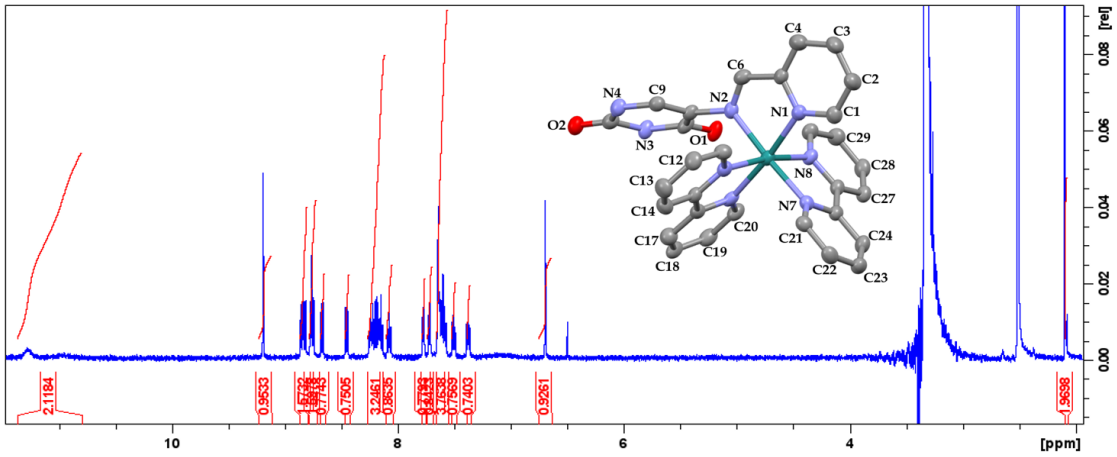

Figure 4. 8: *^{1}H NMR spectrum of* ***4****.*

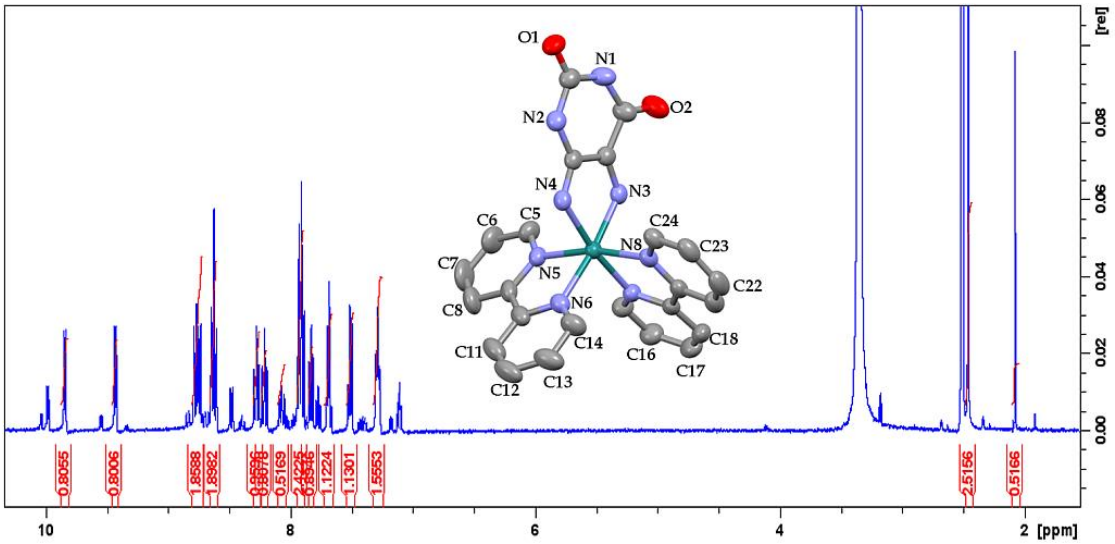

Figure 4. 9: *^{1}H NMR spectrum of* ***5****.*

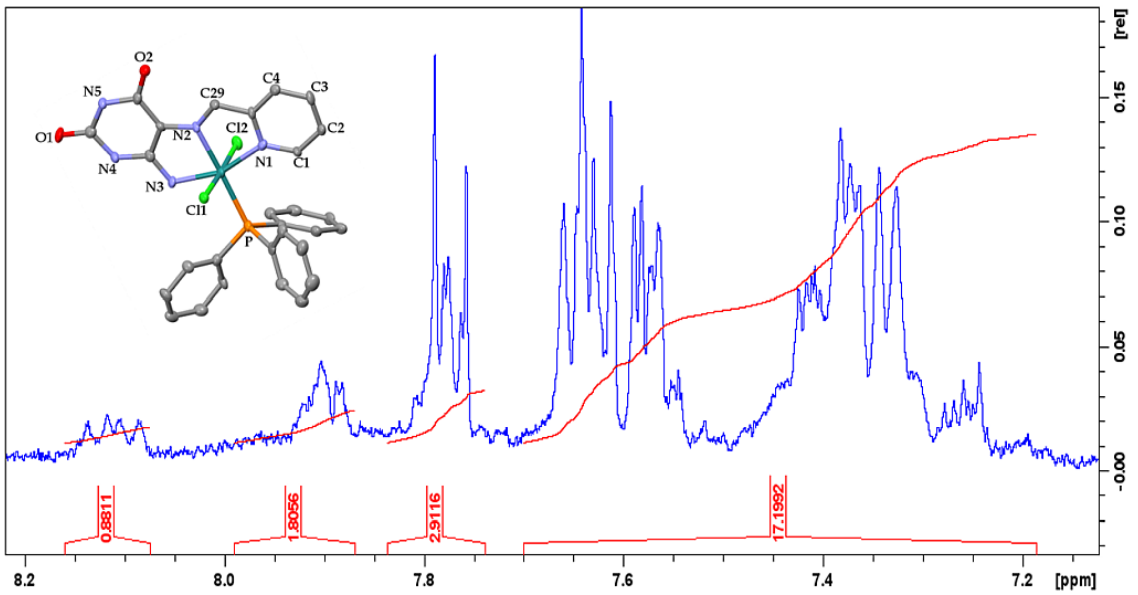

Figure 4. 10: *^{1}H NMR spectrum of* ***6****.*

For instance, in the COSY NMR spectrum of **4**, the doublet of H21 at 7.78 ppm correlate with H30 at 7.71 ppm as well as with H23 and H23 within the multiplets at 7.65 - 7.57 ppm, see **Figure 4.11**. Similarly, for **5**, H23 within the multiplets at chemical shift range of 7.23 – 7.26 ppm correlates with H24 at 8.21 ppm which in turn overlaps with protons at H22 at 7.51 ppm and H12 at 8.64 ppm, see **Figure 4.12**. As expected, there are comparatively large shielding effects for specific protons of **4** and **5** between (Δδ) 2.45 - 2.01 ppm. Interestingly for **5**, several minor peaks are found in its ^{1}H NMR spectrum which are reminiscent of metal complexes undergoing keto-enol tautomerization and in fact, this structural transformation also manifested in the time-dependent electronic spectral profiles of **5**.[27]

More specifically, the signals at 2.14 ppm (assigned to H24 and H27) for **4**, 2.45 ppm (assigned to N3H, N4H and N2H) and 2.01 ppm (assigned to N1H) for **5** are relatively up-field which may be attributed to ruthenium's larger diamagnetic anisotropic effect.[28] Furthermore, the ^{1}H NMR spectrum of **1** - **3** displayed three common resonance peaks in the range of 5.62 – 6.28 ppm, and the characteristic signals of the aliphatic protons of para-cymene moiety appearing in the regions of 2.1 ppm (singlet

for methyl group) and 0.99 ppm (doublet of doublets for the two methyl isopropyl groups) which agrees with other ruthenium complexes.[29]

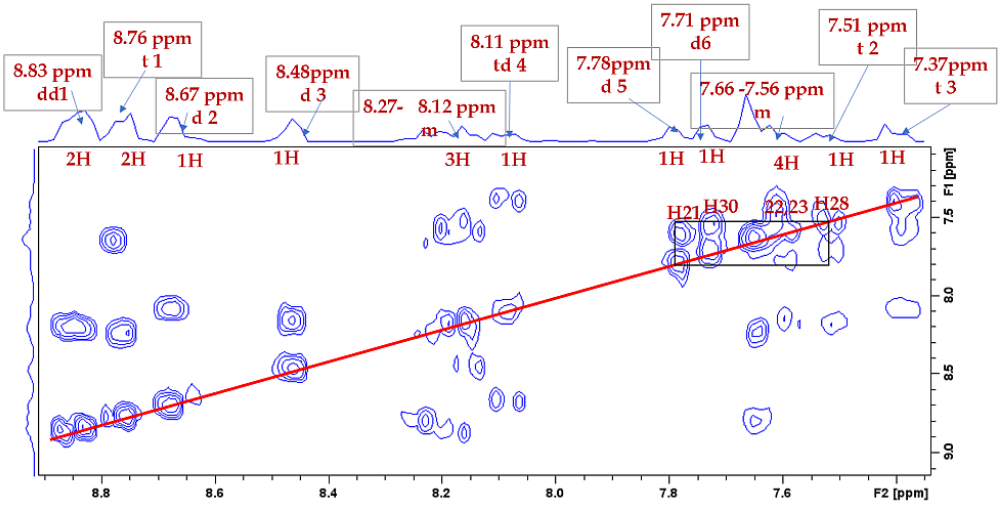

Figure 4. 11: *COSY NMR spectrum of* ***4****.*

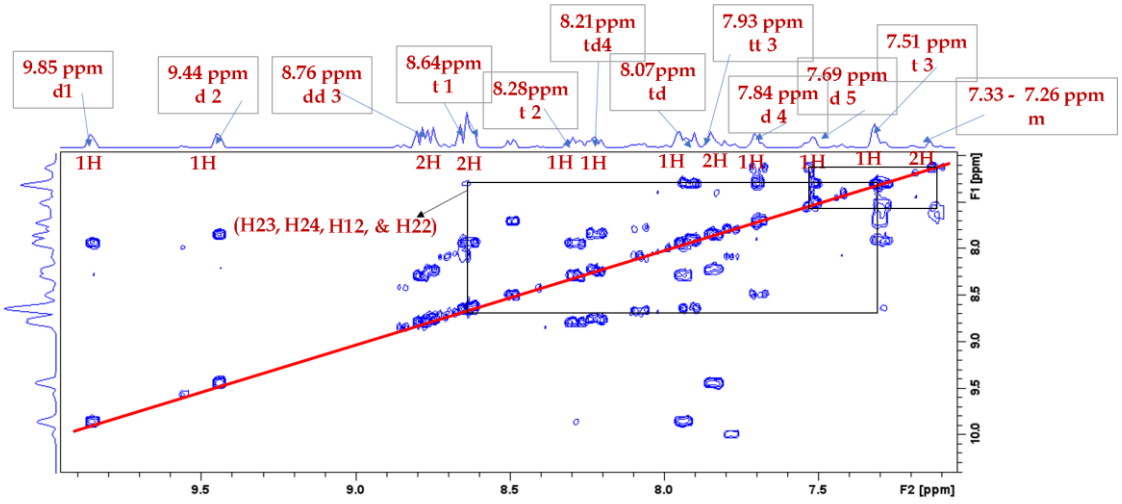

Figure 4. 12: *COSY NMR spectrum of* ***5****.*

Experimental vibrational band assignments of **1 - 6** were made with the aid of the DFT unscaled vibrational frequencies. The most prominent experimental IR bands are the ν(C=N), ν(C=O) and ν(NH). Imino bonds vibrate experimentally at 1636 cm^{-1} for **1**, 1625 cm^{-1} (for **2**), 1615 cm^{-1} (for **3**), 1596 cm^{-1} (for **4**) and 1579 cm^{-1} (for **6**). Another conclusive feature that the free ligands were coordinated to the different metal cores are that the free Schiff base functionality vibrates at different frequencies: urpda at

1609 cm^{-1}, urpdy at 1588 cm^{-1}, urpy at 1584 cm^{-1} and urqda at 1666 cm^{-1}, see **Figure 4.13 – 4.18**, respectively.[30]

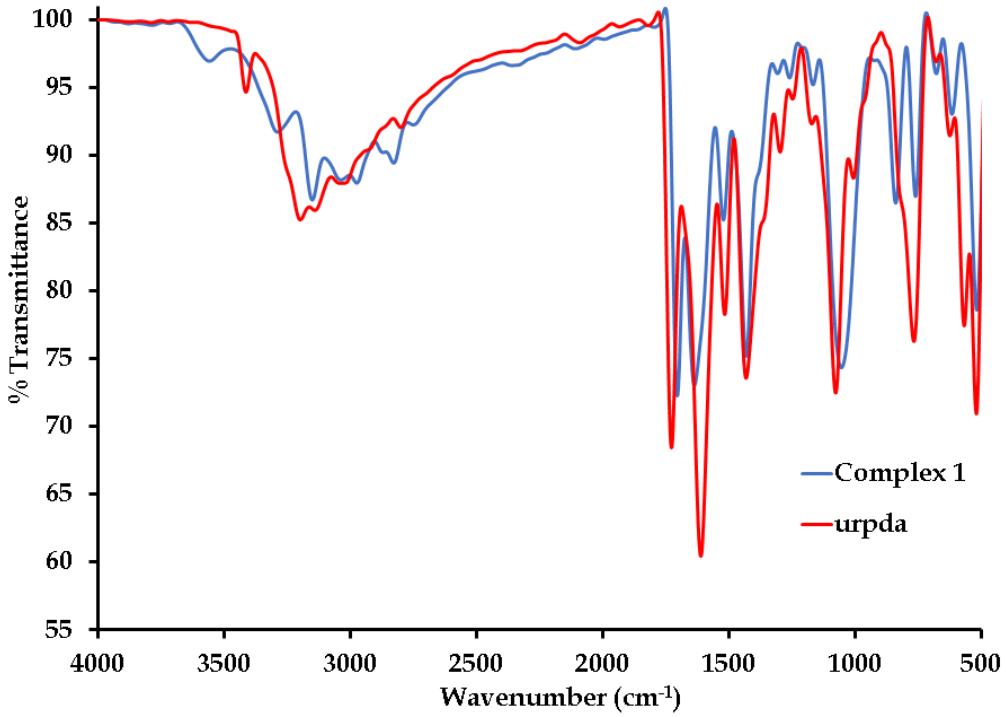

Figure 4. 13: *Overlay IR spectra of the urpda free-ligand and its metal complex* ***1*** *between 4000 and 500 cm^{-1}.*

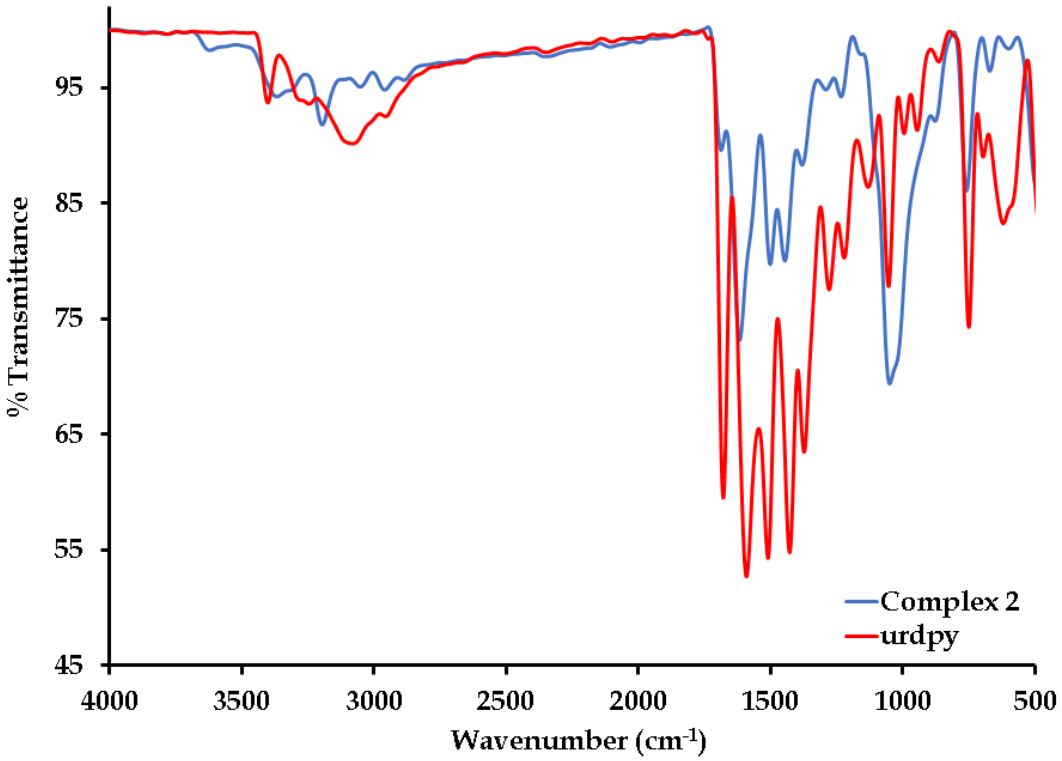

Figure 4. 14: *Overlay IR spectra of the urdpy free-ligand, and its metal complex* **2** *between 4000 and 500 cm-1.*

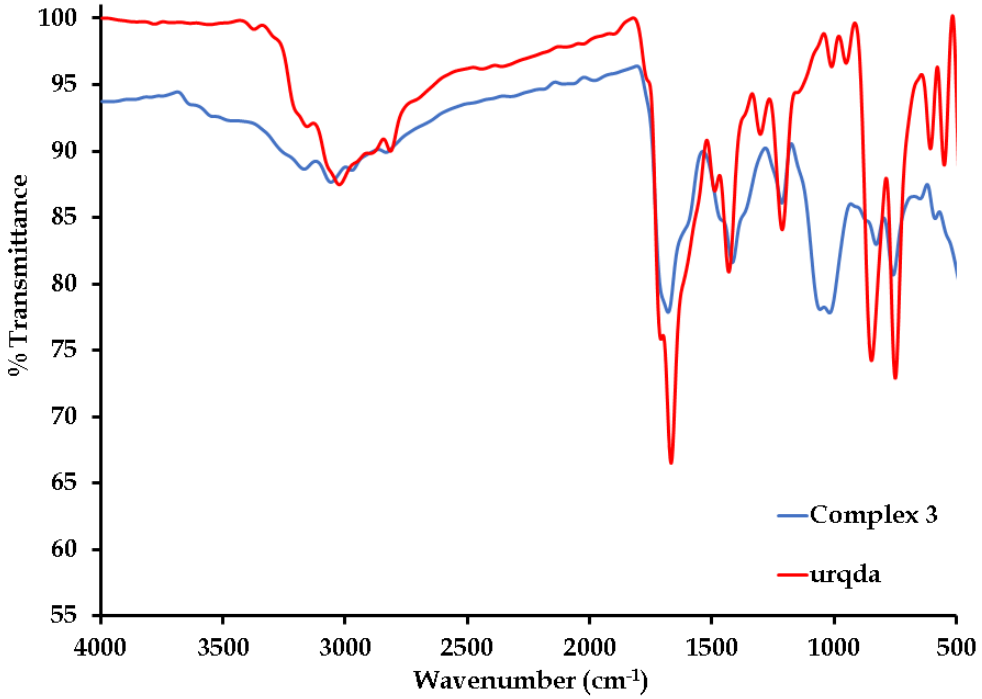

Figure 4. 15: *Overlay IR spectra of the urqda free-ligand and its corresponding metal complex* ***3*** *between 4000 and 500 cm-1.*

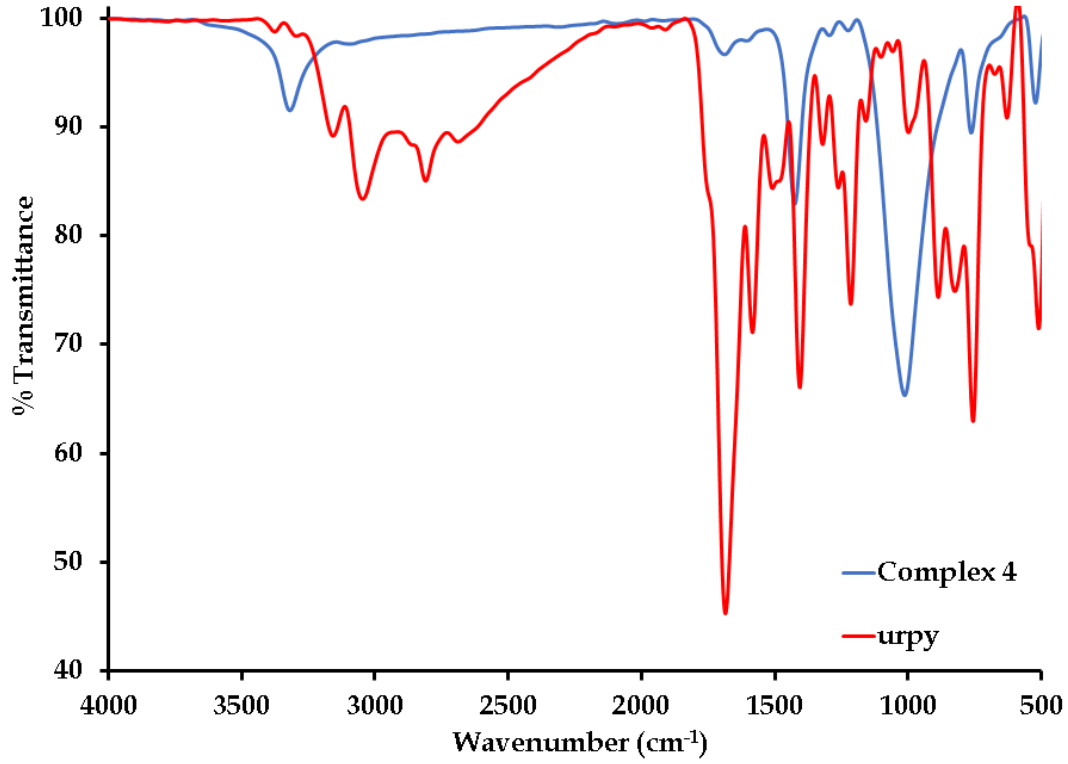

Figure 4. 16: *Overlay IR spectra of the urpy free-ligand and its corresponding metal complex* ***4*** *between 4000 and 500 cm-1.*

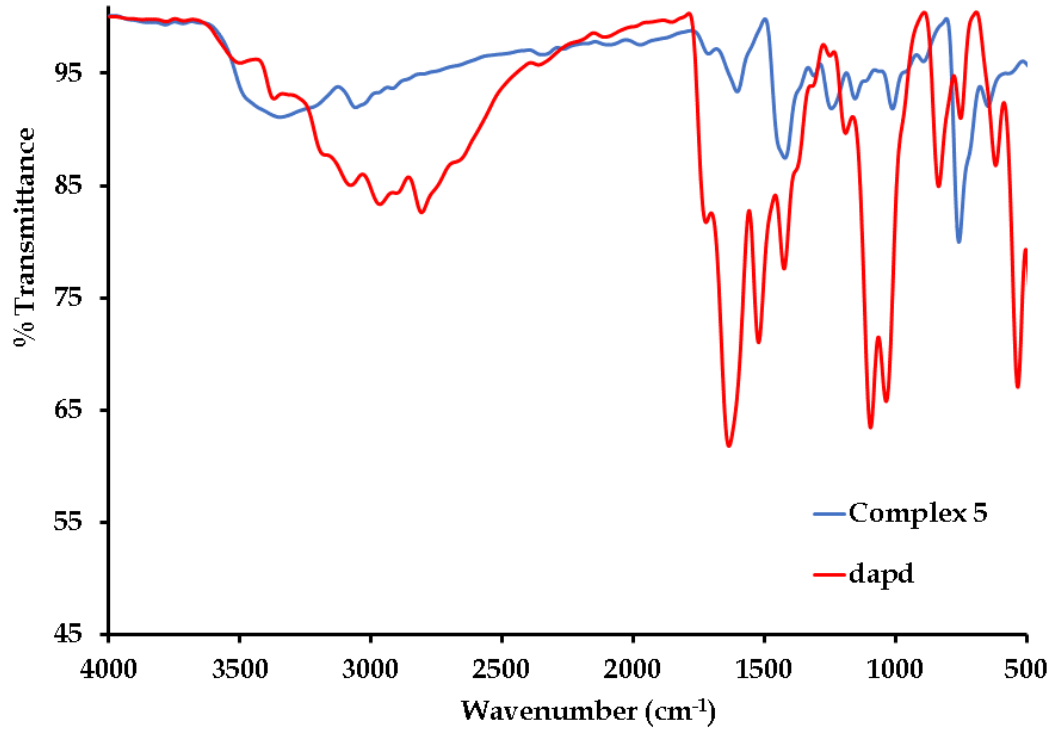

Figure 4. 17: *Overlay IR spectra of the free-ligand, dapd and its corresponding metal complex* ***5*** *between 4000 and 500 cm-1.*

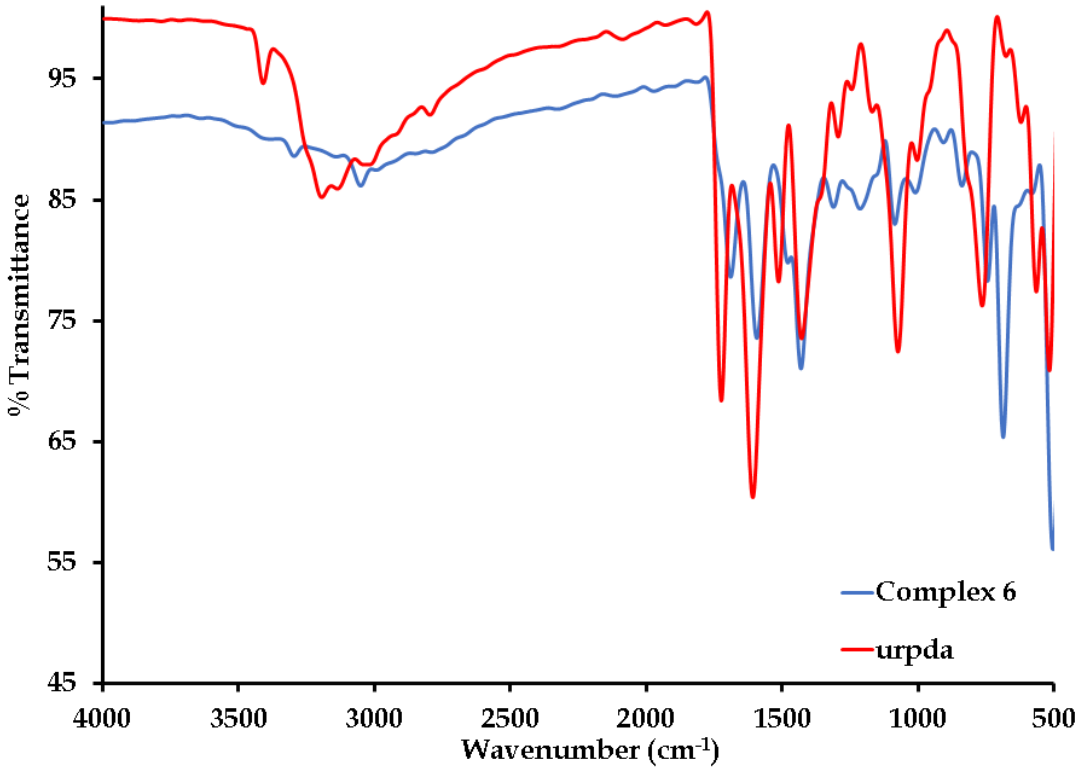

Figure 4. 18: *Overlay IR spectra of the free-ligand, urpda and its corresponding metal complex* ***6*** *between 4000 and 500 cm-1.*

Computationally, the coordinated imino bonds induce vibrations occurring at lower frequencies at 1578 cm $^{-1}$ for **1**, 1610 cm^{-1} for **2**, 1558 cm^{-1} for **3**, 1559 cm^{-1} for **4**, and 1560 cm^{-1} for **6**, see **Figure 4.19**. In the case of **5**, the absence of the imino vibrational band is observed in its solid-state FTIR spectrum and the hydrolysis of dpdp are confirmed with the presence of the broad medium intensity uracil amido bond vibrations found at 3300 cm^{-1} while its heterocyclic C-N bonds are found at the 1587 cm^{-1} and 1440 cm^{-1}, respectively. The respective IR spectra of the free-ligands: urpda, urpdy, urpy, urqda, and dapd) shows strong bands at 1726 cm^{-1},1678 cm^{-1}, 1684 cm^{-1}, 1713 cm^{-1} and 1635 cm^{-1} which are ascribed to ν(C=O), respectively.

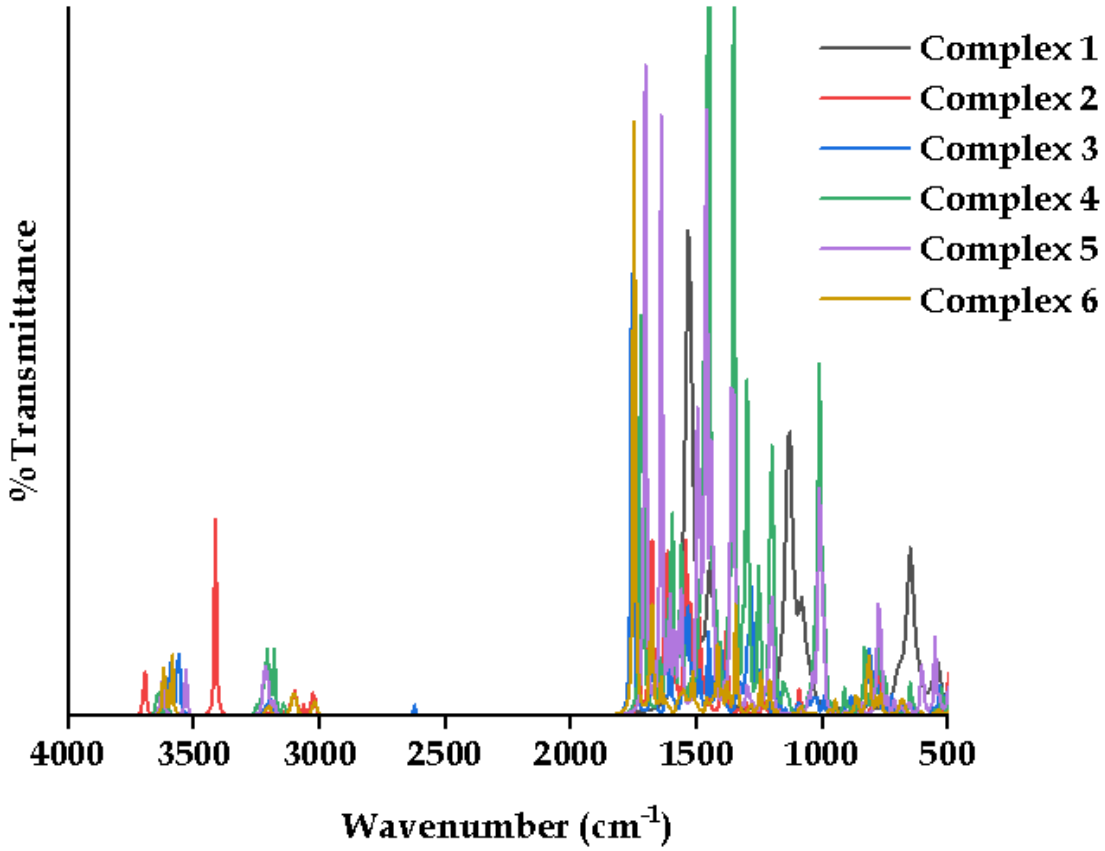

Figure 4. 19: *Overlay calculated IR spectra of* ***1*** *–* ***6****.*

The characteristic region of a localized ketonic band in the spectra of the ruthenium complexes is usually between 1620 – 1719 cm^{-1}.[31-32] Similarly, the majority of related computed uracil C=O vibrational bands falls within the aforementioned limits where two vibrational bands of each metal complex were observed at 1750 and 1560 cm^{-1} (for **1**), 1705, and 1621 cm^{-1} for (**5**), at 1719 cm^{-1} and 1649 cm^{-1} for (**4**) as well as 1757 cm^{-1} and 1560 cm^{-1} for (**6**). On the other hand, solitary stretches for these analogous signals for **2** at 1682 cm^{-1} were observed while for **3**, several ketonic stretches occurred at 1749 cm^{-1}, 1681 cm^{-1}, and 1514 cm^{-1}. Similarly, the related experimental vibrational frequencies of uracil C=O bonds for the respective metal compounds vibrate as medium intensity vibrational bands at 1716 cm^{-1} (for **1**), 1706 cm^{-1} (for **2**), 1717 cm^{-1} (for **3**) 1705 cm^{-1} (for **5**), whereas **4** and **5** vibrates weakly at 1693 and 1655 cm^{-1}, respectively.

The UV-Vis spectra of the diamagnetic metal complexes with pi-conjugated ligand systems usually show common absorbances below 400 nm which attributes to intra-ligand π-π* transitions dominance.[33] Several charge transfer (CT) bands are found at more red-shifted regions between 400 and 600 nm: at 419 nm, 504 nm for **1**, 419 nm, 433 nm, 509 nm, , 504 nm for **2**, 464, 562 nm for **3**, 450, 501 nm for **4**, 450, 501 nm for **5** and 485, 565 nm for **6** see, **Figures 4.20 – 4.25.** Furthermore, indicative of literature trends, the diamagnetic ruthenium complexes afforded no d-d electronic transitions due to their low-spin d^6 electron configurations.[34]

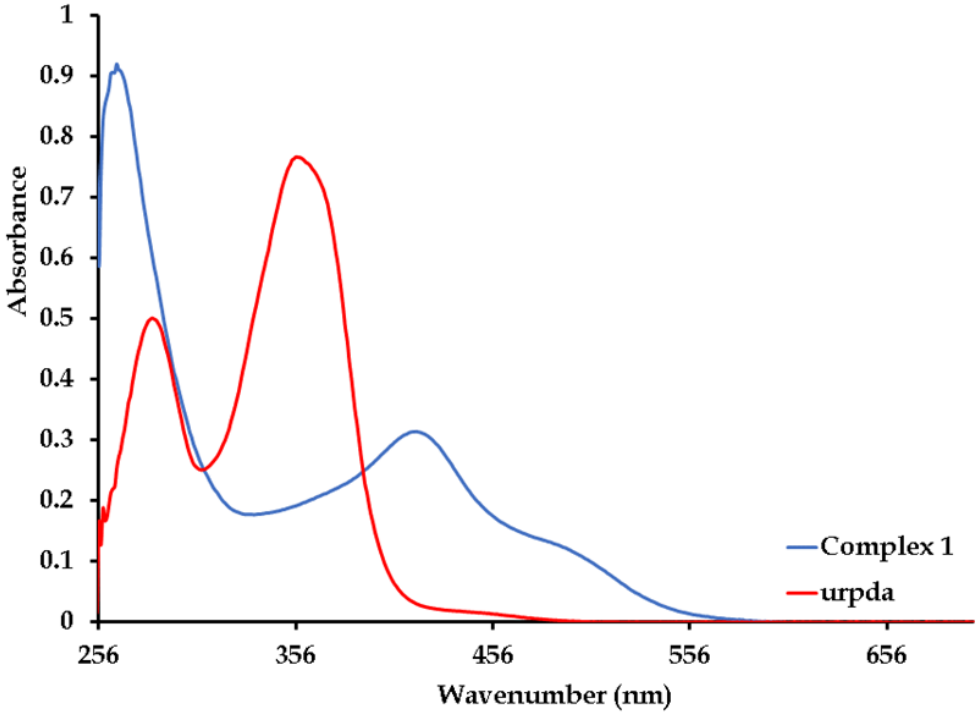

Figure 4. 20: *Overlay UV-vis spectra of **1** and its corresponding free-ligand, urpda.*

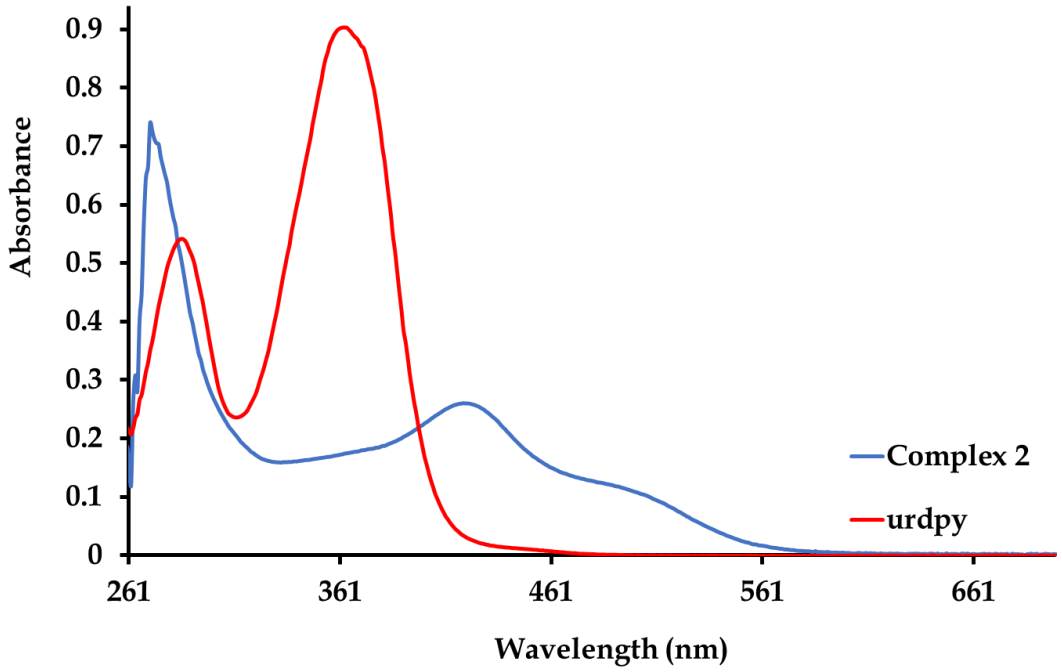

Figure 4. 21: *Overlay UV-vis spectra of* **2** *and its corresponding free-ligand, urdpy.*

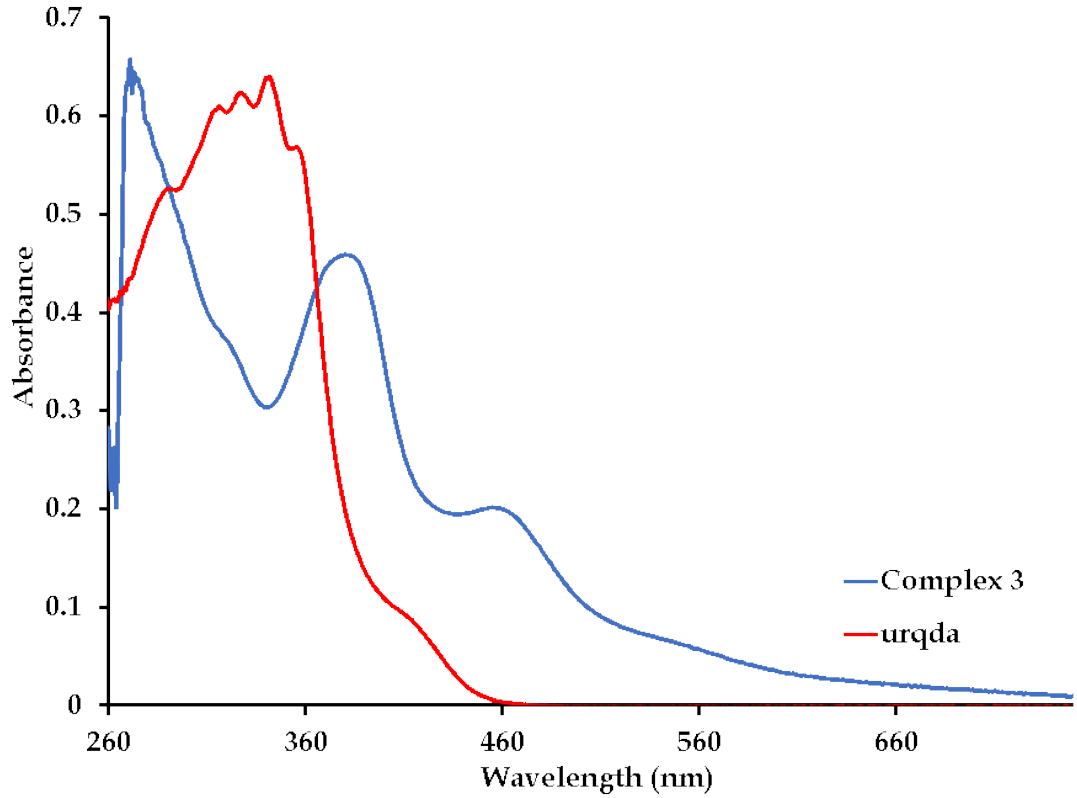

Figure 4. 22: *Overlay UV-vis spectra of* **3** *and its corresponding free-ligand, urqda.*

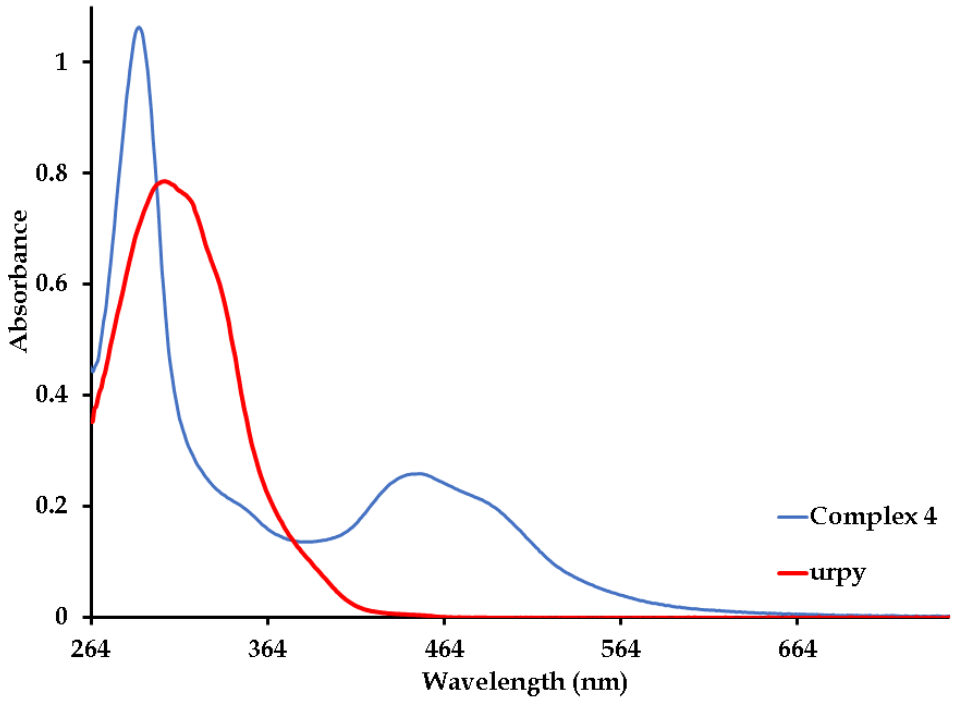

Figure 4. 23: *Overlay UV-vis spectra of* ***4*** *and its corresponding free-ligand, urpy.*

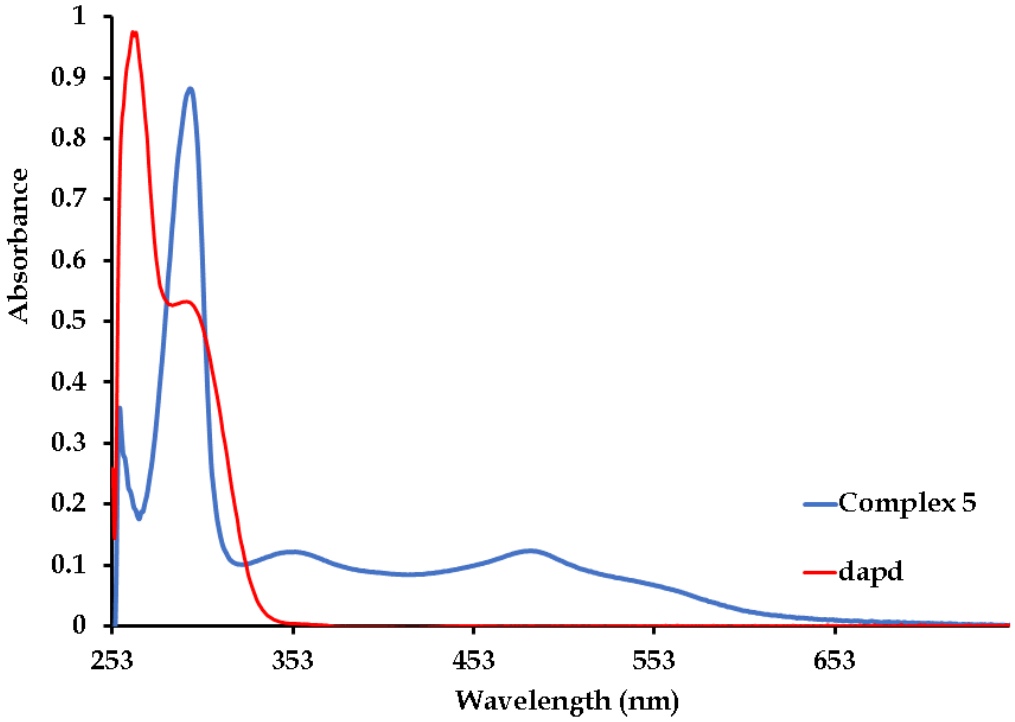

Figure 4. 24: *Overlay UV-vis spectra of* ***5*** *and its corresponding free-ligand, dapd.*

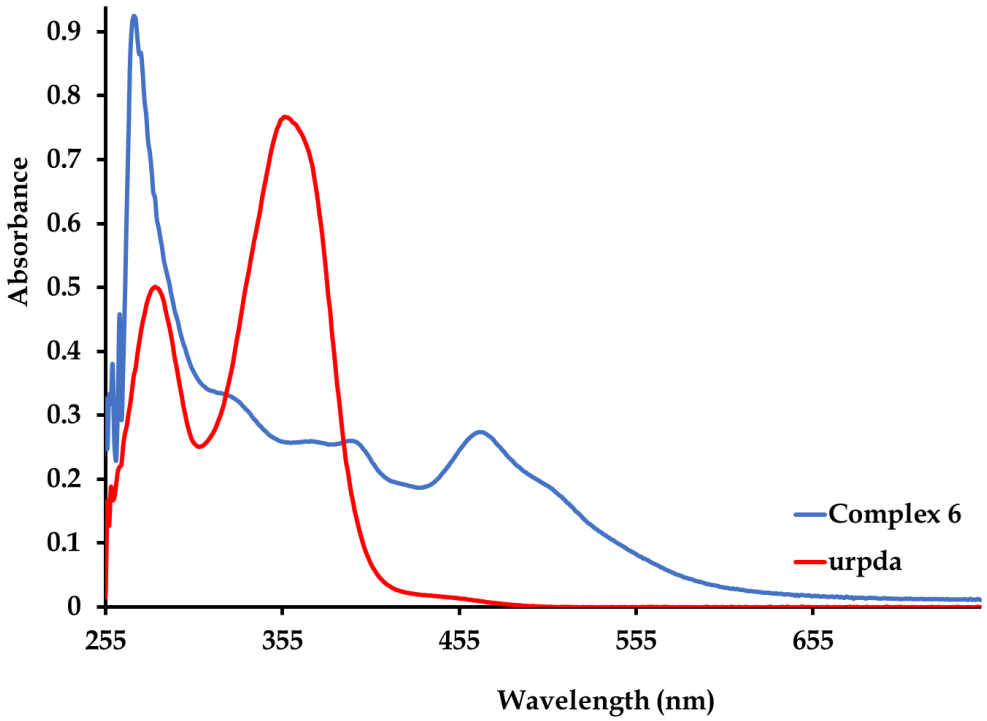

Figure 4. 25: *Overlay UV-vis spectra of* ***6*** *and its corresponding free-ligand, urpda.*

Substantiation of the experimental π-π* intraligand electronic transitions are supported by the electronic density shifting occurring within the respective Schiff base chelators of **1 – 6** when evaluating the differences between their relating frontier computed orbitals, refer to **Tables 4.3** and **4.4**. In addition, the pairing HOMO and LUMO surfaces of the para-cymene ruthenium(II) Schiff base complex cations where admixture nature of metal-to-ligand and ligand-to-metal charge transfer (viz. ML- and LMCT) for the experimental CT-bands can be established based on the variable electron densities of the chloride co-ligands and the metal centres for these respective metal complexes observed. In particular, the HOMO surface of the metal complex dication of **5** shows less electron density residing on its metal centre in comparison to that observed in LUMO surface which rationalize the ligand-to-metal charge transfer (LMCT) character of the real electronic transition at λ_{max} = 416 nm. In contrast, the stabilization of the ruthenium(II) centre by the dadp dianionic of **5** is clearly seen from the absence of electron density over dadp in the LUMO surface while electron delocalization occurs essentially across the whole molecule in its HOMO surface. A

similar effect is caused by the chloride co-ligands of **6** shifting electron density from its saturated p_{π}-orbitals into vacant d-orbitals orbitals of the metal centre.

Interestingly for **6**, there is hardly any contribution from its neutral urpda Schiff base chelator as seen in its HOMO surface. This is expected due to the variabilities in nucleophilicity that exists within the uracil Schiff base chelators of the metal complexes as well as their metal cores: cis-$[Ru(\eta^6\text{-cymene})]^{2+}$, cis-$[Ru(bipy)]^{2+}$ and trans-$[RuCl_2]$ and residual co-ligands as result of their differences in π-and σ-donating electron density, respectively. These electron density donations limit the effectiveness of the electrophilicity that exists on the positive charges of the individual ruthenium ions towards nucleophilic substitution. To corroborate these results, the global electrophilicity index (w) was used to determine the chemical reactivity of a system according to equations (I), (II) and (III) where η denotes the global chemical hardness and μ represents the electronic chemical potential which describes the charge transfer within a system in the ground state.[35]

$$w = \frac{\mu^2}{2\eta} \quad \textbf{(I)}$$

$$\eta = \frac{E_{LUMO} - E_{HOMO}}{2} \quad \textbf{(II)}$$

$$\mu = \frac{E_{LUMO} + E_{HOMO}}{2} \quad \textbf{(III)}$$

The chemical reactivity decreases in the opposite order of HOMO-LUMO band gap energies which shows that **4** and **5** are more reactive. The decreasing order of the LUMO energies of the respective metals are **6 > 3 > 1 > 2 > 5 > 4** and this trend correlates to the π-acceptor strength as well as the electrophilicity. Moreover, the stability of each metal depends on the width of the HOMO-LUMO band gap and it can be seen that band gap energies of **4** and **5** are the least among the respective metals which is contrary to the trend of the kinetic stability observed in the time-dependent spectral data where **4** and **5** were the least prone to fast hydrolysis.

Table 4. 3: *Summary of the computational data of* ***1*** *-* ***4****, and their energies expressed in electron volt (eV).*

Parameter	**1**	**2**	**3**	**4**
Electrophilicity index (w)	18.503	17.887	20.3776	7.4939
NPA charge of Ru atom	0.357	0.356	0.372	1.416
Band-gap energy (eV)	3.125	3.082	2.8547	0.7649
HOMO surface	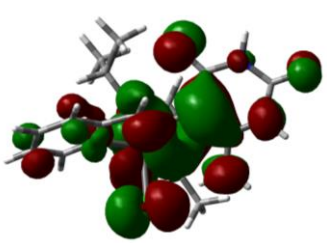	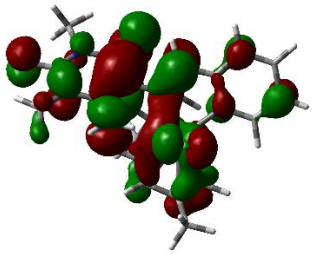	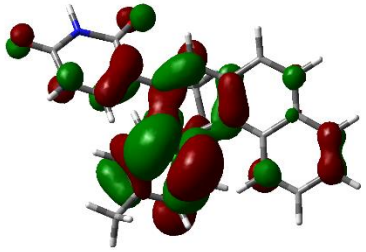	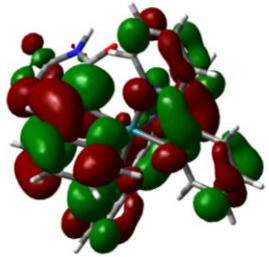
LUMO surface	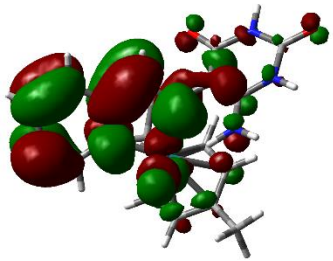	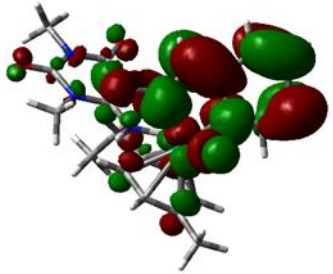	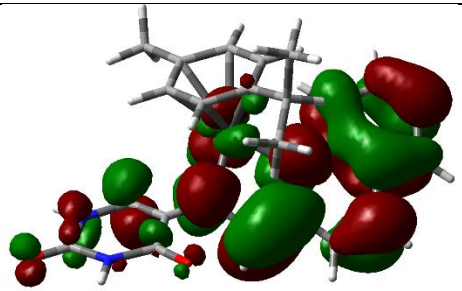	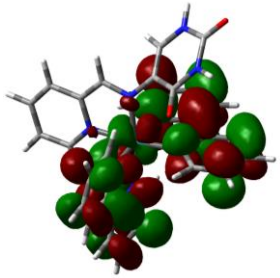

Table 4. 4: *Summary of the computational data of* **5** *and* **6**, *and their energies expressed in electron volt (eV).*

Parameter	**5**	**6**
Electrophilicity index (w)	7.4499	113.65
NPA charge of Ru atom	1.317	0.497
Band-gap energy (eV)	0.9943	1.091
HOMO surface	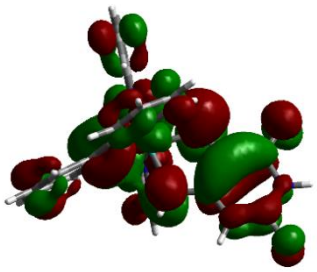	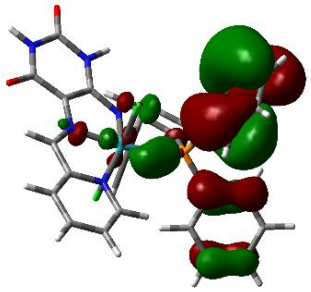
LUMO surface	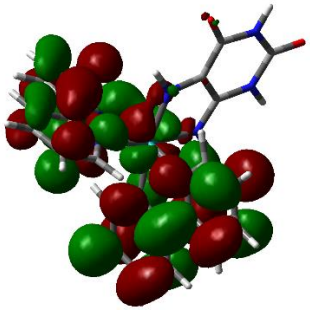	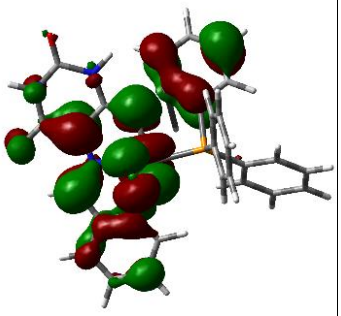

Evaluations of the solution behaviours for the prospective were performed in different solvents including analytical-grade dimethylsulphoxide (DMSO) or its aqueous mixture of 2% DMSO: 98% PBS UPW mixture where the former were used as the medium used for the planned in vitro anti-diabetic studies. Structural integrities of **1 – 6** were monitored using time-dependent UV-Vis spectrophotometry over 24 hrs where metal complexes which are inert will show no electronic spectral changes while those displaying physiochemical changes will manifested UV-Vis spectral alterations.[36]

Noticeable UV-Vis spectroscopic alterations in the electronic spectra of the majority of the metal complexes depicting hydrolysis and subsequent coordination of DMSO exchange except for **4** and **5** which can be rationalized by the fact that these metal compounds do not have any chloro co-ligands within their coordination spheres, see **Figures 4.26** and **4.27**. However, metal complex **5** showed comparatively minor changes in the 2% DMSO aqueous buffered solution. Although the nature of the keto-enol transformation could not be clearly delineated computationally and experimental by the electronic spectral alterations of **5** are reminiscent of metal complexes undergoing keto- and enol-conformer conversations.[37]

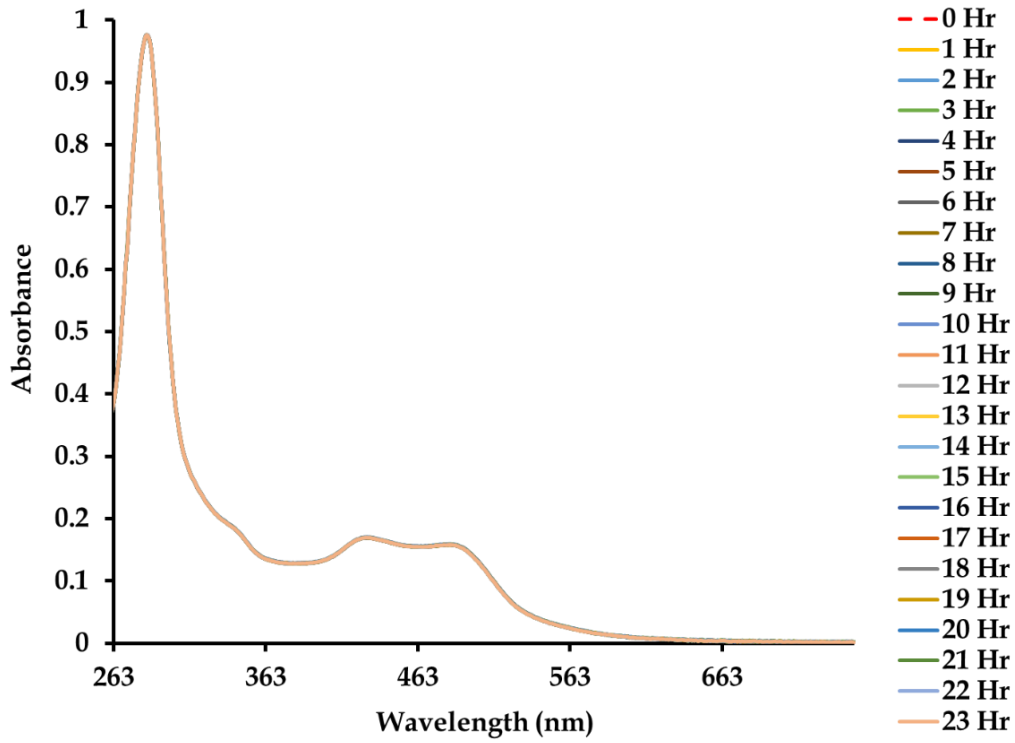

Figure 4. 26: *Time-dependent stability study conducted on* **4** *in a 2%: 98% (v:v) DMSO: PBS solution (250 µM, 298 K) monitored over a 24 hour period using UV-Vis spectrophotometry.*

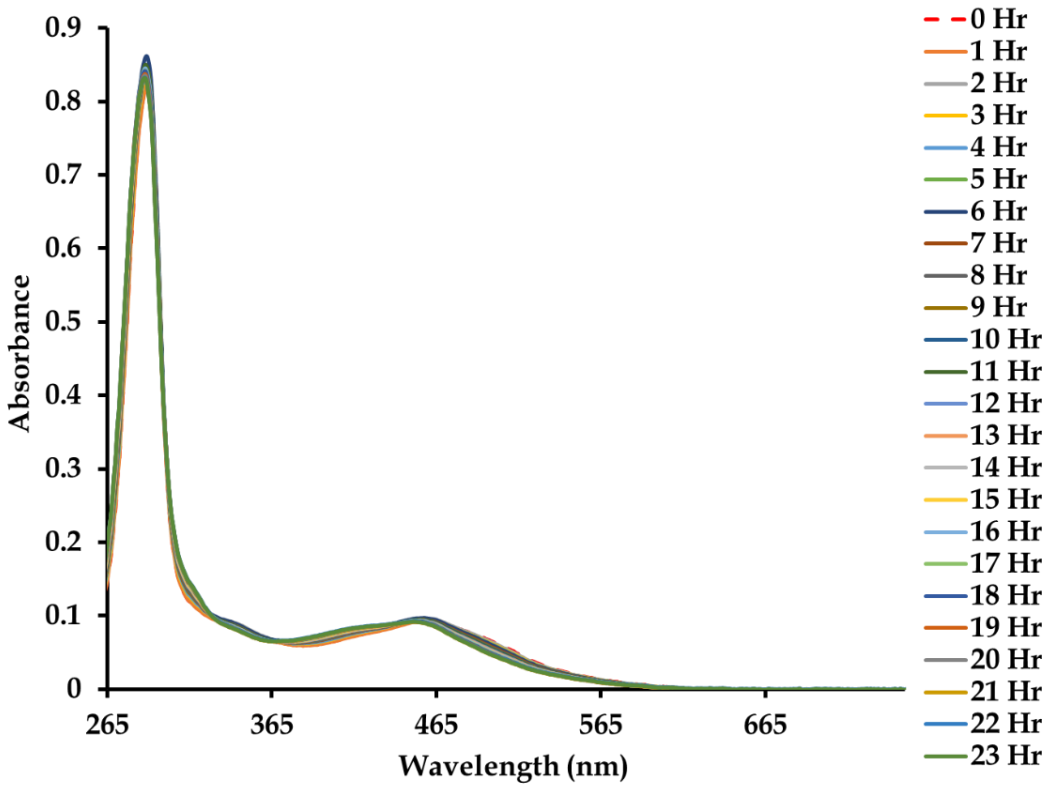

Figure 4. 27: *Time-dependent stability study conducted on* **5** *in a 2%: 98% (v:v) DMSO: PBS solution (250 µM, 298 K) monitored over a 24-hour period using UV-Vis spectrophotometry.*

In contrast, the chemical stabilities of **1 - 3** and **6** were evaluated in anhydrous DMSO since the labile chloro co-ligands are known to undergo ligand exchange with DMSO solvent molecules.[24] Electronic spectral data of **1 - 3** and **6** show noticeable alterations in their different electronic spectral profiles see, **Figures 4.28 – 4.31**. In particular, the individual charge transfer (CT) bands (415 nm for **1**, 423 nm for **2** and 324 nm for **3**) of the para-cymene ruthenium(II) Schiff base undergoes hypso- and hyperchromic effects leads two blue-shifted ligand-centred electronic transitions (343, 407 nm for **1**, 361, 409 nm for **2** and 382, 424 nm for **3**). Sequential collapses in the intraligand electronic transitions of **6** leading to the hypochromism of the existing CT-band at 354 nm while a new CT-band appears at 359 nm. In addition, well-defined isosbestic points were observed in the electronic spectral profiles of these metal complexes: 317 and 419 nm for **1**, 327, 427 and 523 nm for **2**, 327, 424, and 495 nm for **3** as well as 360 and 419 nm for **6**.

Consequently, a concurrent decreasing in the intensity of the MLCT band of respective compounds with an accompanying blue shift from 415 nm to 406 nm for **1.** Compound **2** showed a similar gradual decrease and new absorption bands that increase in intensity followed by the emergence of a new ligand-based electronic transition at 335 nm, and 385 nm comprising MLCT band at 575 nm. For **6** and **3** in DMSO solution, blue shifts of the peak maxima within the MLCT region were observed correspondingly at 459 nm to 466 nm, and 465 nm to 426 nm. Furthermore, the red-shifted CT-band for **6** only occurred at (400 nm to 418 nm).

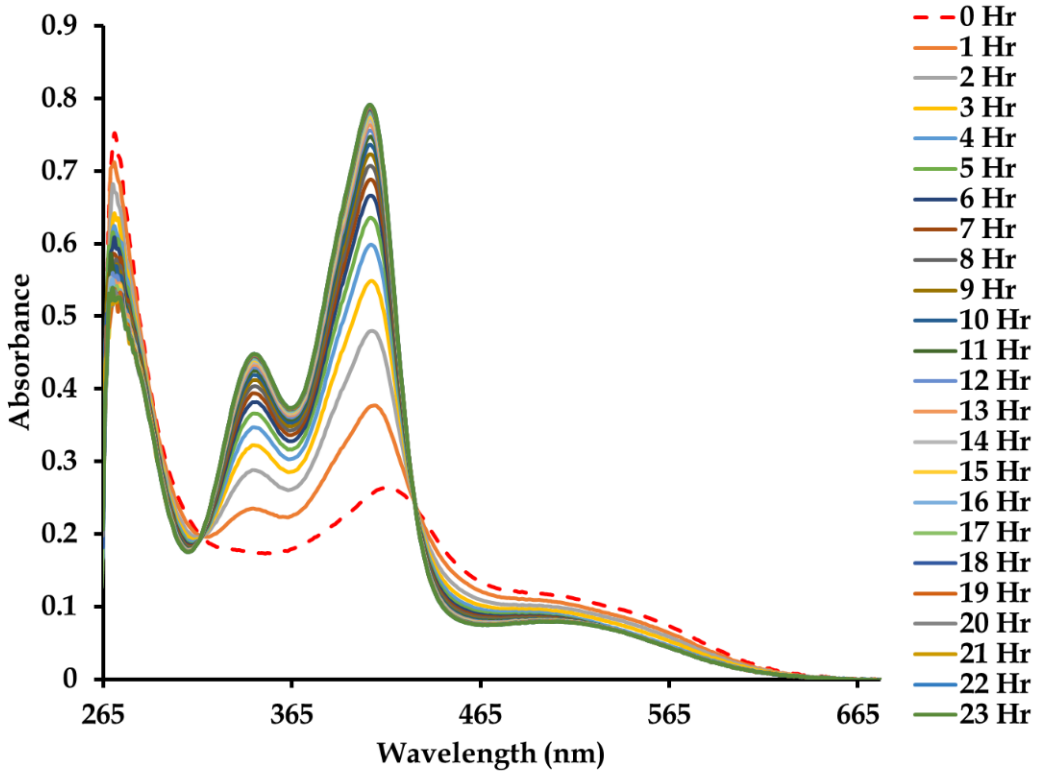

Figure 4. 28: *Time-dependent stability study of* ***1*** *executed in DMSO (10^{-5} M, 298 K, 24 Hr) monitored by UV-Vis spectrophotometry.*

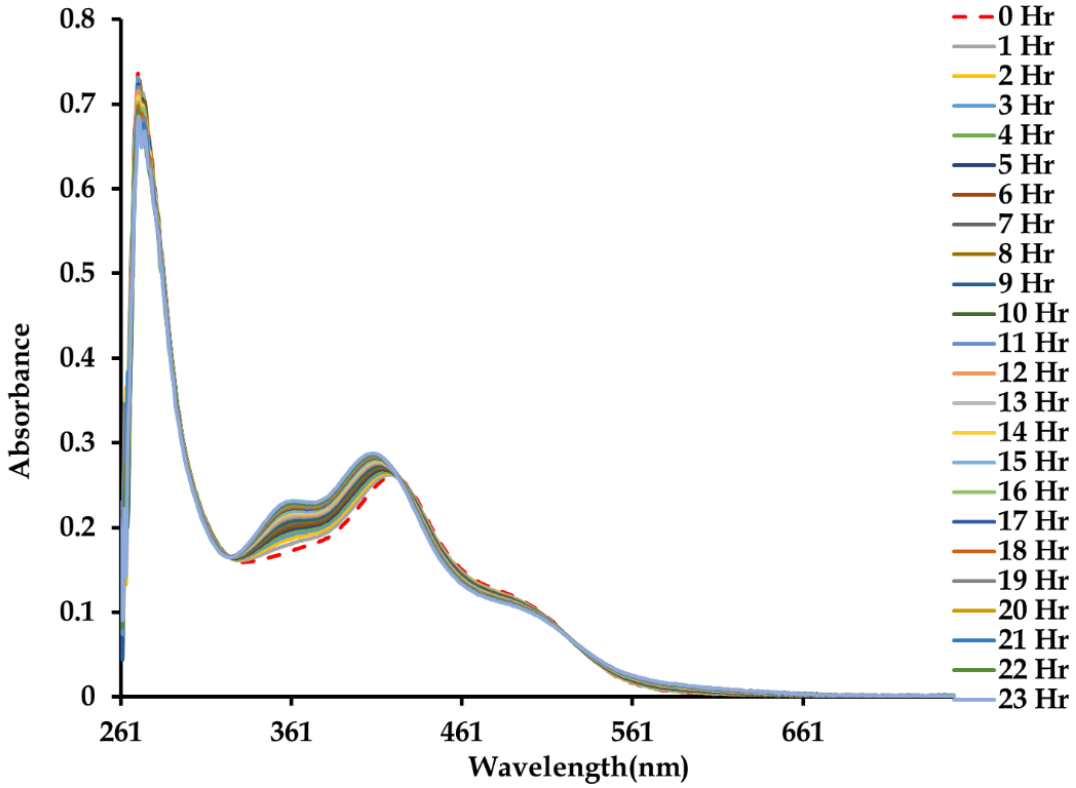

Figure 4. 29: *Time-dependent stability study of* **2** *executed in DMSO (10^{-5} M, 298 K, 24 Hr) monitored by UV-Vis spectrophotometry.*

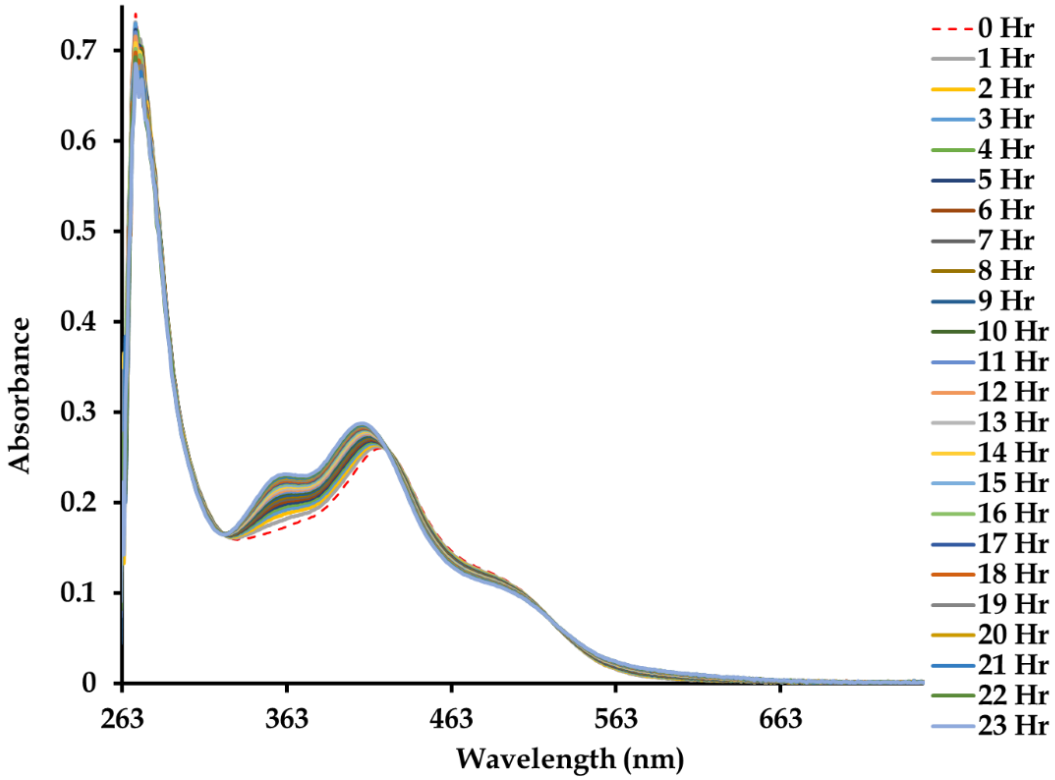

Figure 4. 30: *Time-dependent stability study of* **3** *executed in DMSO (10^{-5} M, 298 K, 24 Hr) monitored by UV-Vis spectrophotometry.*

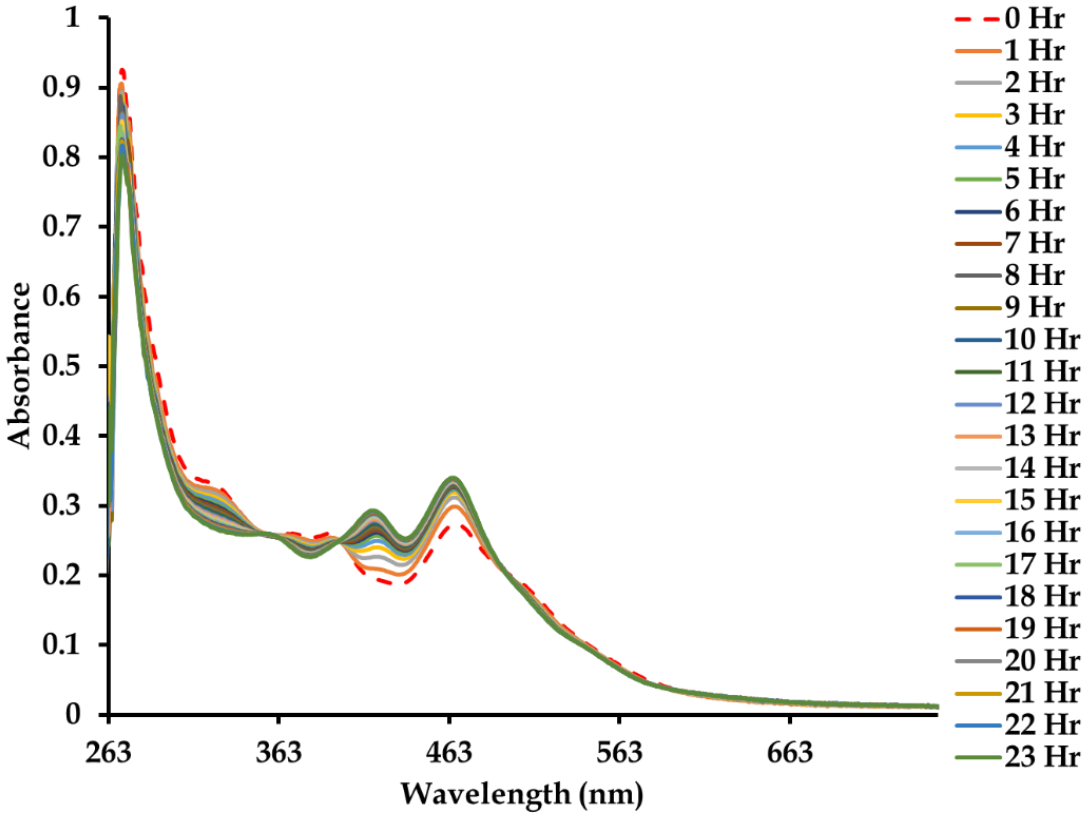

Figure 4. 31: *Time-dependent stability study of* ***6*** *executed in DMSO (10^{-5} M, 298 K, 24 Hr) monitored by UV-Vis spectrophotometry.*

For the chemically reactive metal complexes **1 – 3** in 2%: 98% of DMSO: PBS solvent mixture, distinctive electronic spectral changes synonymous with ligand displacement of their chloride co-ligands are observed see, **Figures 4.32 - 4.35**. The seamless stepwise conversions of the metal complexes to their relating DMSO analogues and then to their corresponding aqua derivatives are evident from diffusion isosbestic points at 281, 343, 364, 394, 400 nm for **1**, 332, 343, 523 nm for **2** and 324, 389, 466 nm for **3** which is indicative of ruthenium complexes undergoing multiple solvent-induced substitution processes. [24] Also, the isosbestic points of **1** and **2** are bridged by various dissipating CT-bands (417 nm for **1** and at 415 for **2**) and immerging intraligand-based electronic transitions (346 and 407 nm for **1**) and (361 and 411 nm) while the CT-band of **3** becomes more blue shifted from 427 nm to 419 nm. However, the time evolution spectral profile of **6** monitored in the buffered aqueous solution, showed an absence of isosbestic points but instead hypochromism

of all its electronic transitions see, **Figure 4.35**. This electronic spectral observation are accounted to the precipitation of the aqua derivative of **6** which was confirmed by the physical examination of the UV-Vis cuvette upon experimental completion, see **Figure 4.31**.[38]

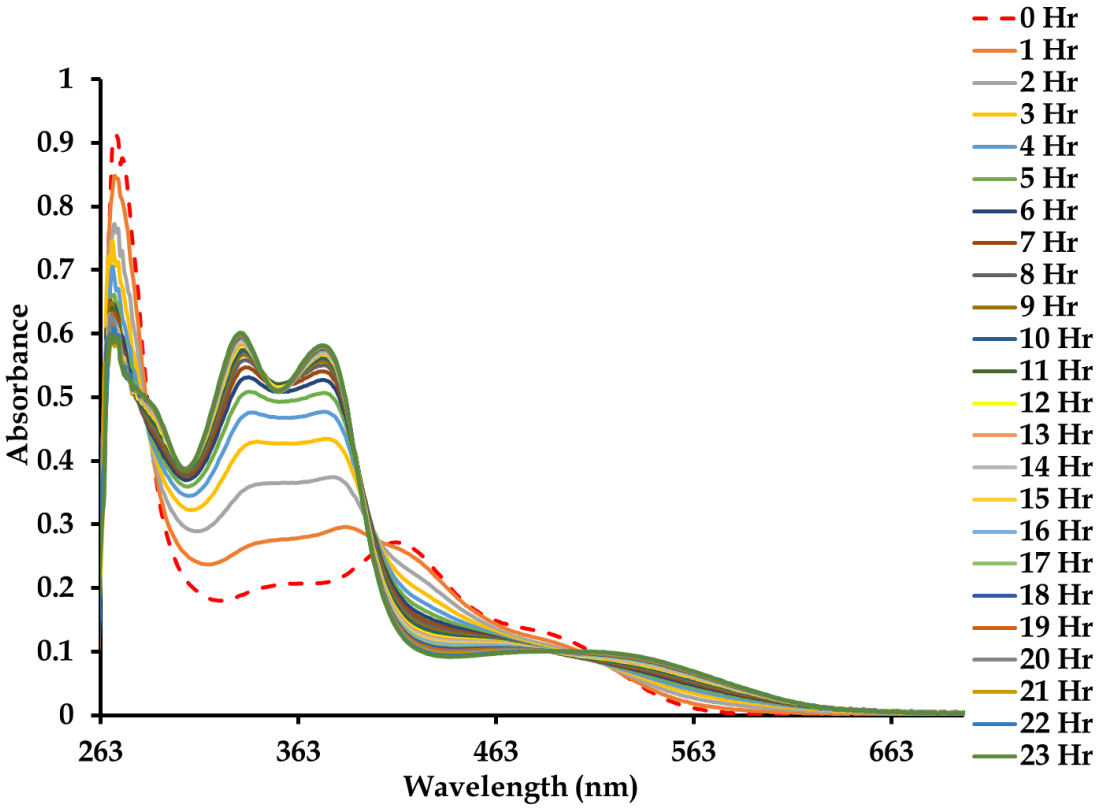

Figure 4. 32: *Time-dependent stability study of* ***1*** *in 2% (v:v) DMSO: PBS solution (250 µM, 298 K, 24 Hr) monitored by UV-Vis spectrophotometry.*

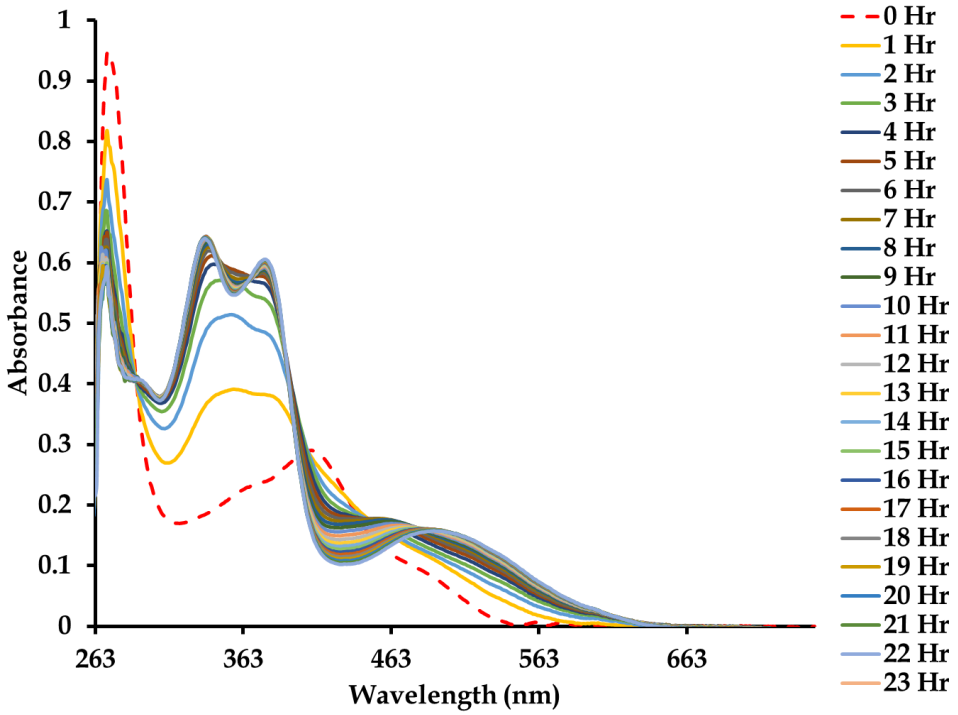

Figure 4. 33: *Time-dependent stability study conducted on* **2** *in a 2%: 98% (v:v) DMSO: PBS solution (250 µM, 298 K) monitored over 24 hour period using UV-Vis spectrophotometry.*

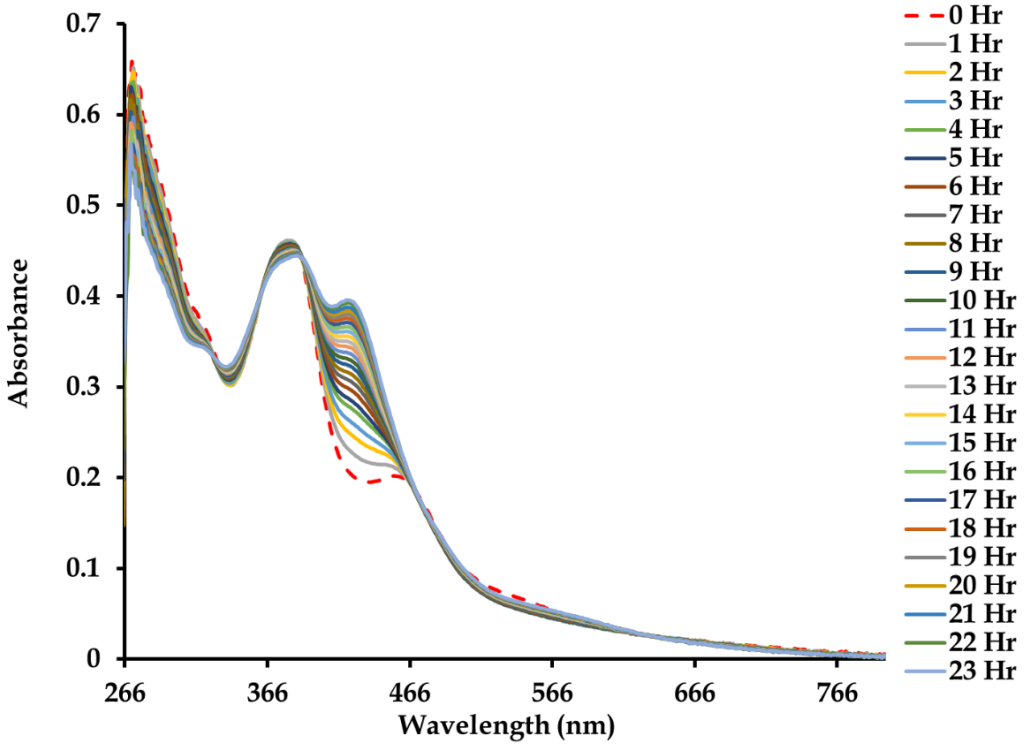

Figure 4. 34: *Time-dependent stability study conducted on* **3** *in a 2%: 98% (v:v) DMSO: PBS solution (250 µM, 298 K) monitored over 24 hour period using UV-Vis spectrophotometry.*

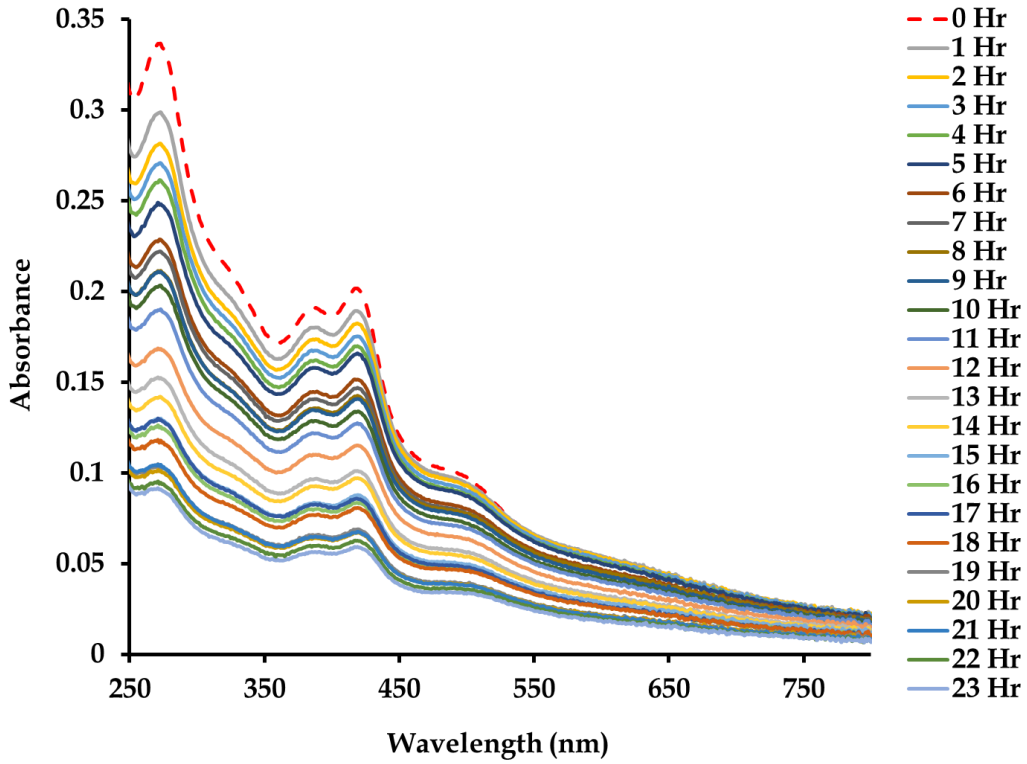

Figure 4. 35: *Time-dependent stability study conducted on* ***6*** *in a 2%: 98% (v:v) DMSO: PBS solution (250 µM, 298 K) monitored over a 24 hour period using UV-Vis spectrophotometry.*

To indirectly validate if chloride co-ligands do exchange with DMSO (vide supra), the electronic spectral data of the respective metal complexes **1** - **3** and **6** in analytical-grade DMSO were monitored in the presence of excess anhydrous LiCl for 24 h at hourly intervals, see **Figures 4.36. - 4.39**. UV-Vis spectral analysis of their kinetic stability profiles still indicated the chloride substitution from the metal complexes by DMSO molecules. However, the excess Cl^- ions retarded the displacement of the chloride co-ligand by DMSO due to the common ion effect. Consequently, these electronic spectrophotometric trends support the fact that metal complexes are reactive in the coordinative environment of DMSO and the resultant DMSO is susceptible to hydrolysis whereas the corresponding Ru(II) aqua species are kinetically stable in aqueous media simulative to the bloodstream, see **Scheme 3.1** in **Chapter 3**.

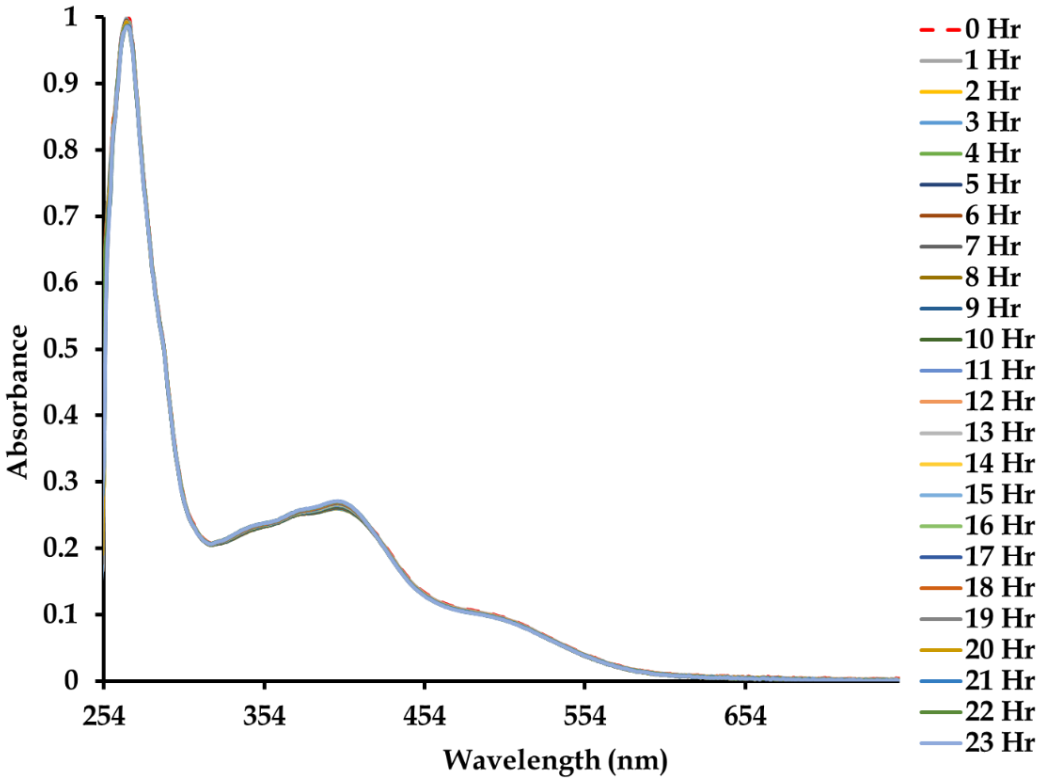

Figure 4. 36: *Time-dependent stability study of **1** in a solution of DMSO and saturated LiCl (10^{-5} M, 298 K, 24 Hr) monitored by UV-Vis.*

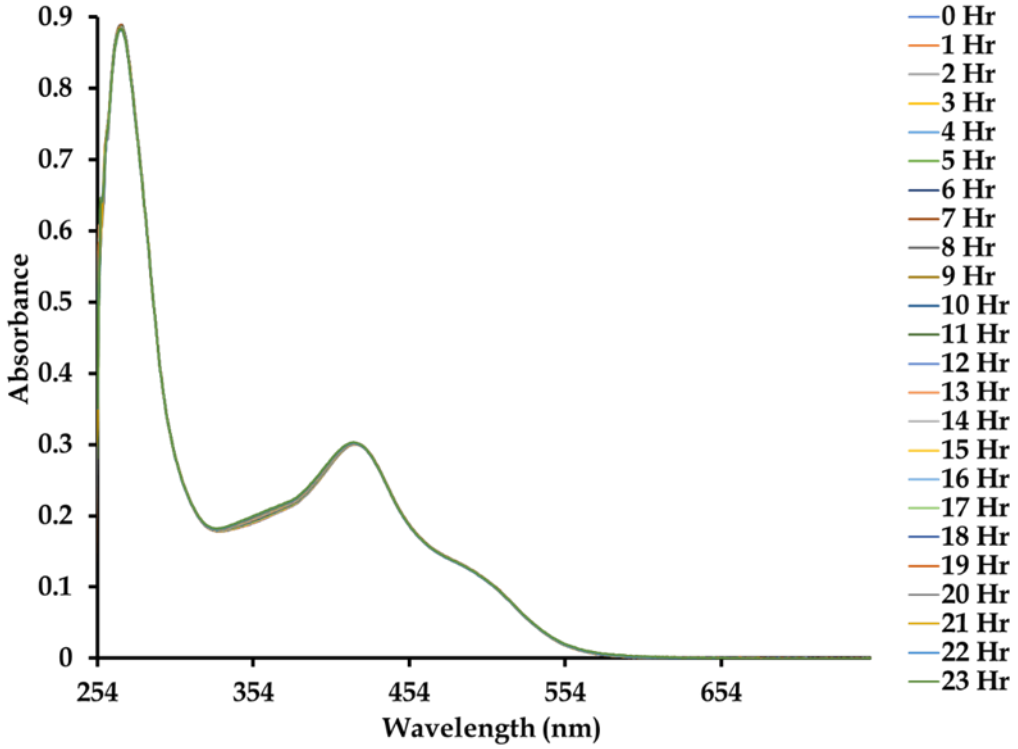

Figure 4. 37: *Time-dependent stability study of **2** in a solution of DMSO and saturated LiCl (10^{-5} M, 298 K, 24 Hr) monitored by UV-Vis spectrophotometry.*

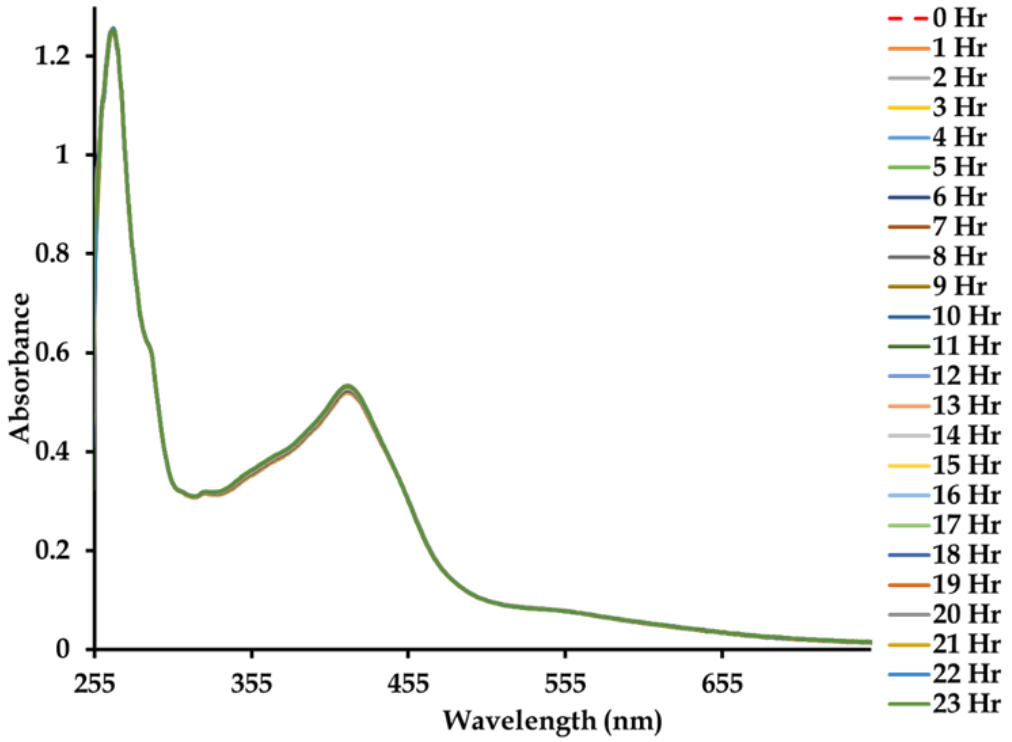

Figure 4. 38: *Time-dependent stability study of* ***3*** *in a solution of DMSO and saturated LiCl (10^{-5} M, 298 K, 24 Hr) monitored by UV-Vis.*

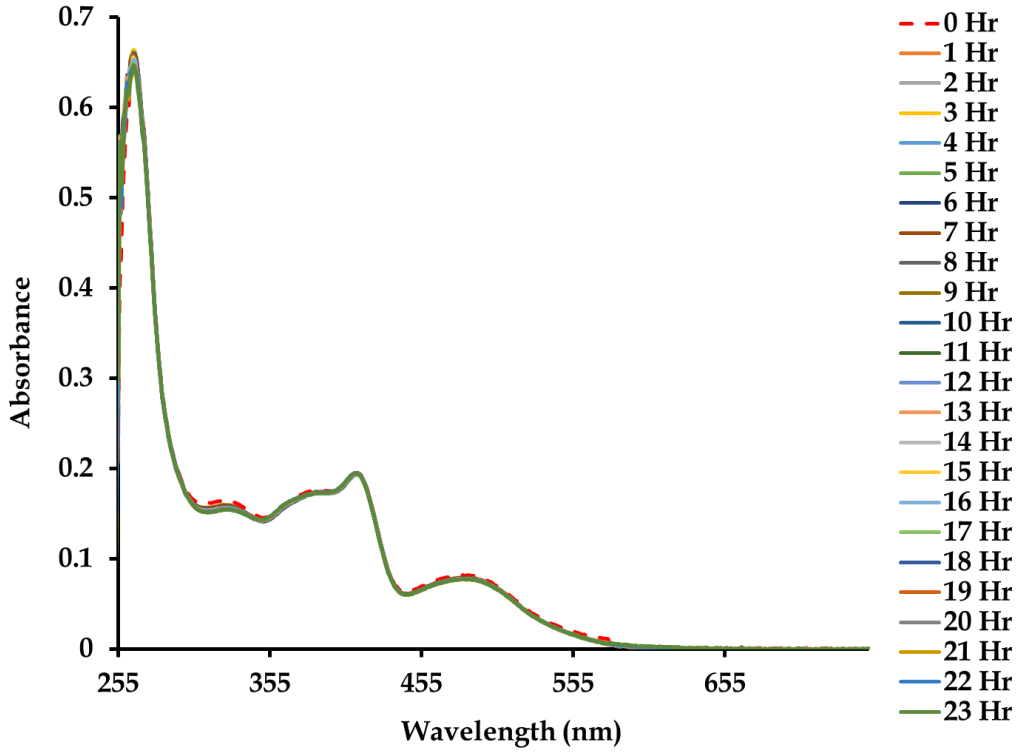

Figure 4. 39:*Time-dependent stability study of* ***6*** *in a solution of DMSO and saturated LiCl (10^{-5} M, 298 K, 24 Hr) monitored by UV-Vis.*

Ligand substitution studies of the aforementioned metal complexes were repeated in a non-coordinative environment of DCM. No redundancy in the electronic spectral trends were observed as those performed in the coordinative organic and simulated biological media, see **Figures 4.40 – 4.43.** This non-chemical reactivity in DCM is similar to other ruthenium complexes with liable chloro co-ligands such as [Ru(η^6-p-cymene)(NAP-HBT)Cl] (NAP-HBT = naphthyl-2-((2-(benzothiazol-2-yl)hydrazono)methylphenol)) and [Ru(η^6-p-cymene)(PPh_3)(T)Cl]PF_6 (T = N-(2-furoyl)-N′-(2-furfuryl)-thiourea).[39,29]

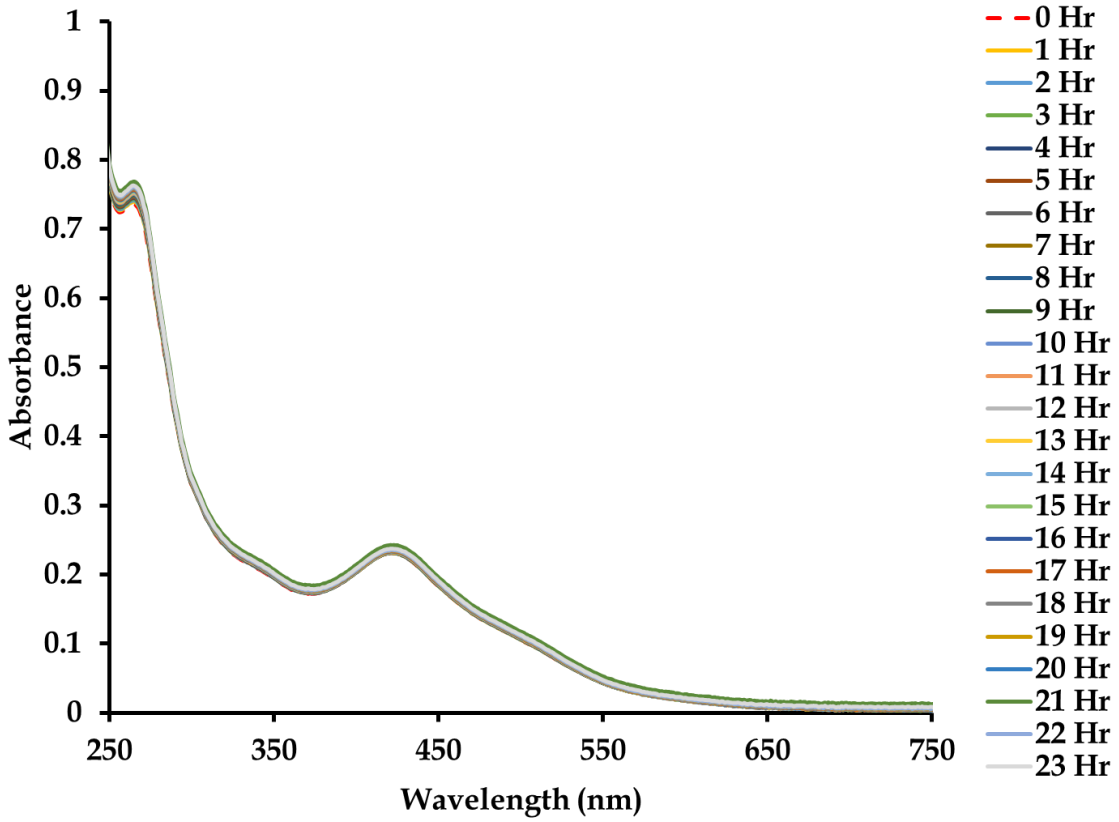

Figure 4. 40: *Time-dependent stability study of **1** in DCM (10^{-5} M, 298 K, 24 Hr) monitored by UV-Vis spectrophotometry.*

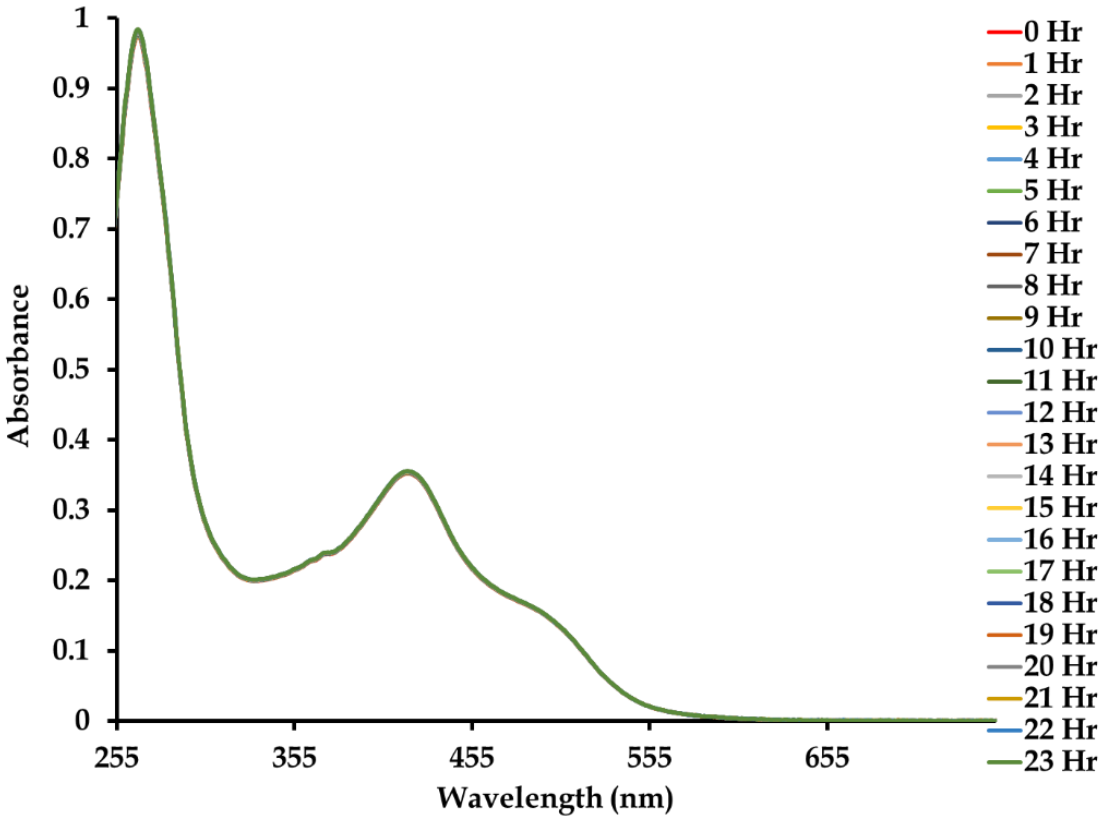

Figure 4. 41: *Time-dependent stability study of* **2** *in DCM (10^{-5} M, 298 K, 24 Hr) monitored by UV-Vis spectrophotometry.*

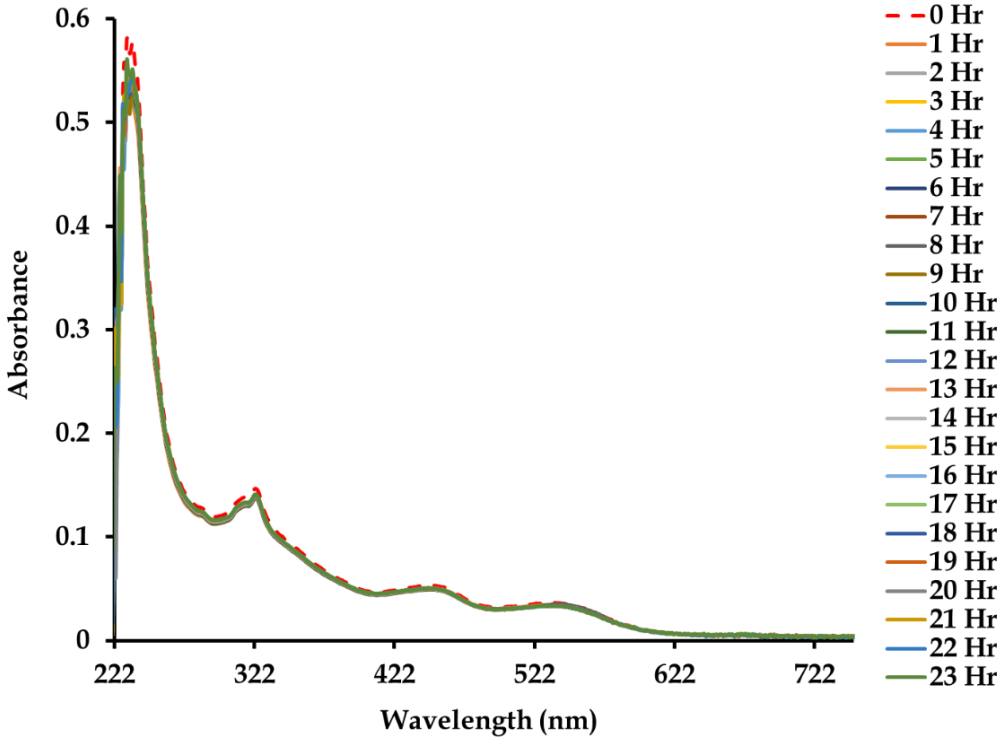

Figure 4. 42: *Time-dependent stability study of* **3** *in DCM (10^{-5} M, 298 K, 24 Hr) monitored by UV-Vis spectrophotometry.*

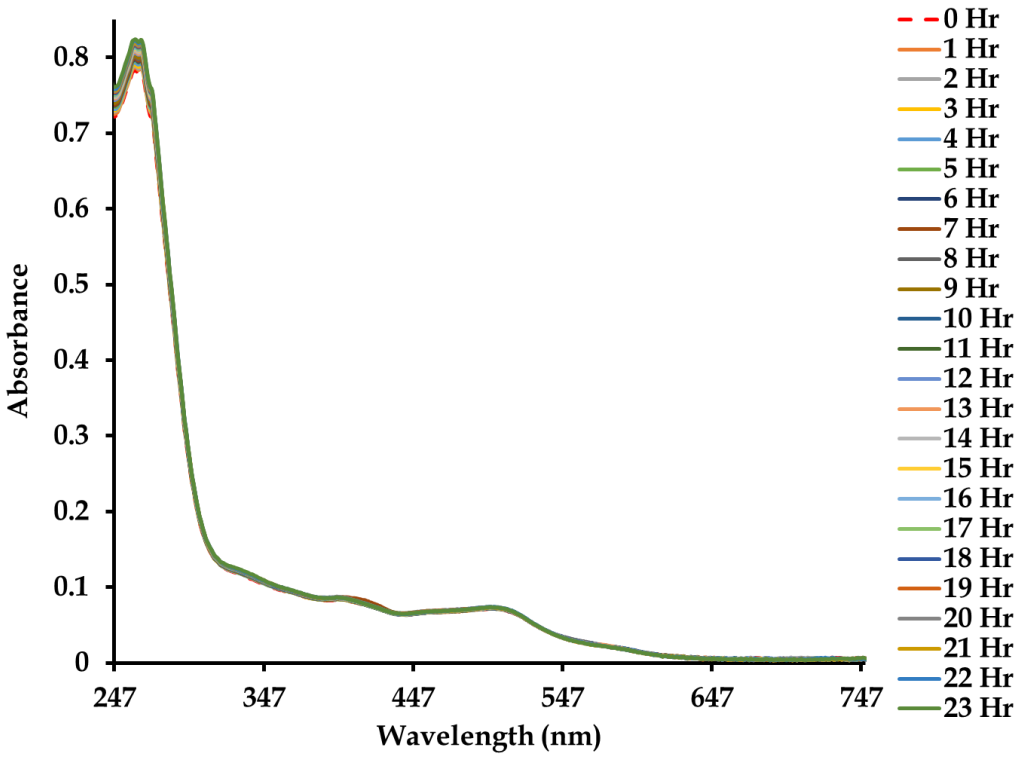

Figure 4. 43: *Time-dependent stability study of* ***6*** *in DCM (10^{-5} M, 298 K, 24 Hr) monitored by UV-Vis spectrophotometry.*

4.7.2 Crystallographic description.

Crystal systems of the respective metal compounds are monoclinic with space-groups of (C2/c (for **1** and **2**) and $P2_1/n$ (for **4**) whereas those of **3**, **5** and **6** are triclinic having a common P-1 space-group. **Figure 4.44** shows the intermolecular hydrogen-bonding network of opposing uracil groups of **1** interacting with one another forming dimers: O1 $_{\text{uracil-1}}$ •••H'-N3'/ O3 $_{\text{uracil-2}}$•••H-N3 = 1.928 Å. In addition, classical intramolecular hydrogen-bonding occur between the chloride co-ligands and one amino groups of the uracil moieties: Cl•••N-H3A$_{\text{py-1}}$= 2.378 Å while the other uracil amino proton reinforces the metal complex cation: anion adduct through P1-F1•••N3-H3B= 2.378 Å intermolecular bond. Altogether, these intrinsic close contacts allow the molecules of **1** to aligned to all the unit cell axes.

Similar stabilizing interactions of the crystal lattice for **2** were observed where the uracil amino protons undergo intra- and intermolecular hydrogen bonding with the chloride co-ligand (Cl1•••HA-N3 = 2.362 Å) and a F atom of the $[BF_4]^-$ anion (B-

F1•••HB-N3 = 2.104 Å), respectively. These set of close contacts leads to hydrogen-bonded dimers packing in columns in the directions of the [b]- and [c]-axes, see **Figure 4.45**. In the case of **3**, an intriguing hydrogen-bonded network where the molecules are directly linked through O3-H3B•••$O1_{uracil-1}$ =3.014 Å and O3-H3A•••$O1_{uracil-2}$ =3.014 Å bonds between adjacent molecules. In turn, the neighbouring dimers of **3** are interlinked by counterions and water molecules of recrystallization leadings to distinctive cavities within the molecular chains, see **Figure 4.46.**

Indicatively, molecules of **4** lies along the [a]- and [b]-axes which is facilitated by the intermolecular hydrogen-bonding pattern as observed, viz. uracil to uracil forming dimers through hydrogen bonding interactions given by [$O1_{uracil-1}$•••H'-N3'/ $O1_{uracil-2}$'•••H-N3= 2.101 Å], see **Figure 4.47**. In addition, the crystal lattice of **4** are enforced by the bridging water molecules of crystallization with a series of hydrogen-bonding interactions [N3-$H_{uracil-1}$•••$O_{water-1}$ = 1.929 Å, $(O-H)_{water-2}$ •••$O2_{uracil-1}$ = 1.899 Å, N3-$H_{uracil-2}$••$O_{water-3}$ = 1.929 Å, $(O-H)_{water-4}$ •••$O2_{uracil-3}$ = 1.899 Å, $(O-H)_{water-1}$ •••$(O-H)_{water-4}$ = 1.964 Å and $(O-H)_{water-2}$ •••$(O-H)_{water-3}$ = 1.964 Å].

On the contrary, and despite the presence of the uracil pharmacophore in the molecular structure of **5**, no classical hydrogen-bonding is observed but its molecule arrangements are dictated by weaker van der Waals close contacts, see **Figure 4.48**. For **6**, its crystal lattice is stabilized by a series intermolecular hydrogen-bonding interactions with bridging molecules of recrystallization occupying cavities between the molecular columns of **6**: $H4_{uracil-1}$•••$OH_{methanol-1}$= 2.027 Å, $OH_{methanol-1}$•••$OH_{methanol-2}$ = 1.817 Å, $OH_{methanol-2}$•••$OH_{methanol-3}$ = 1.818 Å, $O1_{uracil-2}$•••$OH_{methanol-3}$= 1.994 Å, $H4_{uracil-2}$•••$OH_{methanol-4}$= 2.027, $OH_{methanol-4}$•••$OH_{methanol-5}$ = 1.817, $OH_{methanol-5}$•••$OH_{methanol-6}$ = 1.818 Å, $O1_{uracil-1}$•••$OH_{methanol-6}$= 1.994 Å, $O6_{dioxygen-1}$•••ClA'/ $O6_{dioygen-1}$'•••ClB = 1.949 Å = 3.179 Å and $O1_{uracil-1}$•••H'-N5'/ $O1_{uracil-2}$'•••H-N5= 1.949 Å.

Secondary stabilization is induced by the formation of hydrogen-bonded network of dimers through interaction of opposing uracil molecules linking with one another as well as chloro groups of neighbouring molecules allowing molecules to align co-

planar with respect to the[c]-axis see, **Figures 4.48** and **4.50**. Furthermore, the non-chelated uracil moieties of the **1 – 4** affords wide dihedral angles with respect to the corresponding nitrogen donor coordinated groups (51.27° for **1**, 62.32° for **2**, 34.72° for **3** and 64.95° for **4**) while the strain in the coordinated uracilimino group of **6** are in the same plane relative to its metalated nitrogen donor coordinated moieties.

Table 4. 5: *Selected bond lengths (Å) and angles (º) for **1** - **3**.*

Bond lengths	**1**	**2**	**3**
Ru-Cl1	2.416(6)	2.407(9)	2.388(9)
Ru-N1	2.079(2)	2088(2)	2.116(4)
Ru-N2	2.099(2)	2.101(2)	2.089(4)
Ru-N3	**-**	-	-
Ru-Cl2	-	-	-
Ru-P	-	-	-
C6-N2	1.296(3)	1.291(3)	-
C29-N2	-	-	1.284(7)
C10-N2	-	-	-
Bond angles	-	**-**	**-**
N1- Ru-N2	77.12(6)	77.02(8)	76.60(1)
N1- Ru-Cl1	84.92(5)	82.33(6)	85.50(5)
N2- Ru-Cl1	87.02(5)	88.09(5)	88.80(5)
N3- Ru-N2	-	-	-
N1- Ru-Cl2	-	-	-
C6-C5-N2	117.5(2)	117.6(2)	-
C9-C10-N2			117.20(4)
P-Ru-Cl2	-	-	-
P-Ru-Cl1	-	-	-
P-Ru-N1	-	-	-
P-Ru-N3	-	-	-

Table 4.6:*Selected bond lengths (Å) and angles (º) for* ***4 - 6.***

Bond lengths	4	5	6
Ru-Cl1	-	-	2.348(2)
Ru-N1	2.065(3)	-	2.090(6)
Ru-N2	2.058(3)	-	2.042(6)
Ru-N3	-	2.001(2)	2.030(5)
Ru-Cl2	-	-	2.352(2)
Ru-P	-	-	2.350(2)
Ru-N4	-	2.054(3)	-
Ru-N5	2.058(3)	2059(2)	-
Ru-N6	2.058(4)	2.081(2)	-
Ru-N7	2.065(3)	2.054(3)	-
Ru-N8	2.060(3)	2.059(2)	-
C6-N2	1.286(5)	-	-
C29-N2	-	-	1.288(9)
Bond angles	-	**-**	
N1- Ru-N2	78.10(1)	-	78.80(2)
N1- Ru-Cl1	-	-	92.8(2)
N2- Ru-Cl1	-	-	88.30(2)
N3- Ru-N4	-	79.27(9)	-
N1- Ru-Cl2	-	-	80.90(2)
P-Ru-Cl2	-	-	95.51(7)
P-Ru-Cl1	-	-	88.27(6)
P-Ru-N1	-	-	102.00(2)
P-Ru-N3	-	-	98.40(2)
N2- Ru-N8	101.90(1)	-	-
N3- Ru-N5	-	98.86(9)	-
N3- Ru-N7	-	94.84(9)	-
N3- Ru-N8	-	91.53(9)	-
N5- Ru-N1	98.70(1)	-	-
N5- Ru-N2	85.00(1)	-	-
N5- Ru-N6	79.40(1)	78.36(9)	-
N5- Ru-N7	95.10(1)	93.97(9)	-
N6- Ru-N2	95.60(1)	-	-
N6- Ru-N7	89.00(1)	91.94(9)	-
N6- Ru-N8	93.20(1)	92.00(9)	-
N7-Ru-N8	78.70(1)	-	-
N8-Ru-N4	-	79.04(9)	-
C9-C10-N2	-	-	-
C6-C5-N2	117.20(4)	-	116.4(6)

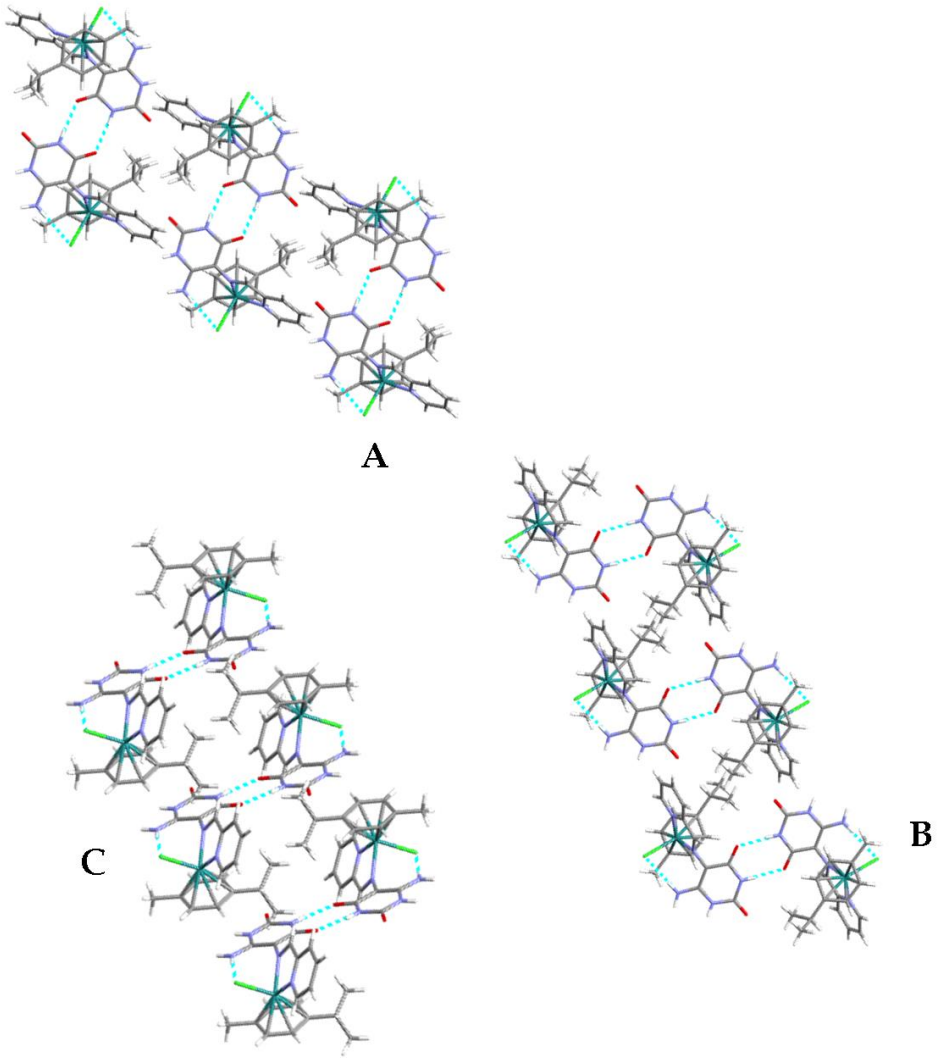

Figure 4. 44: *Perspective views of the intramolecular and intramolecular hydrogen-bonding network occurring within the crystal lattice of* ***1****: O1* $_{uracil\text{-}1}$ *•••H'-N3'/ O3* $_{uracil\text{-}2}$*'•••H-N3= 1.928 Å (Hydrogen-bonded dimerization), viewed down the a-axis(A), b-axis(B) and c-axis (C).*

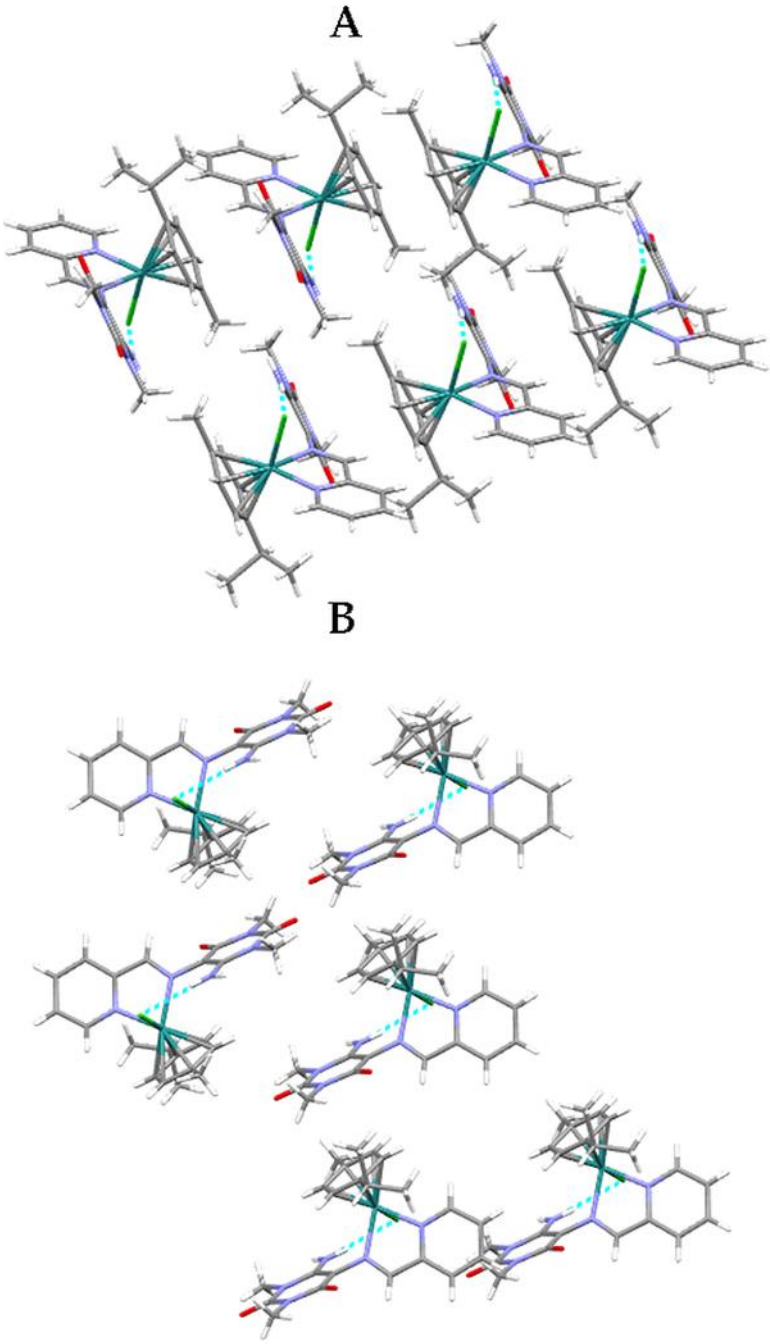

Figure 4. 45: *Perspective views of the crystal lattice for* **2** *illustrating the intramolecular hydrogen-bonding interactions between chloride cations and neighbouring molecules indicated as blue dashed lines viewed down the b-axis (**A**) and c-axis (**B**).*

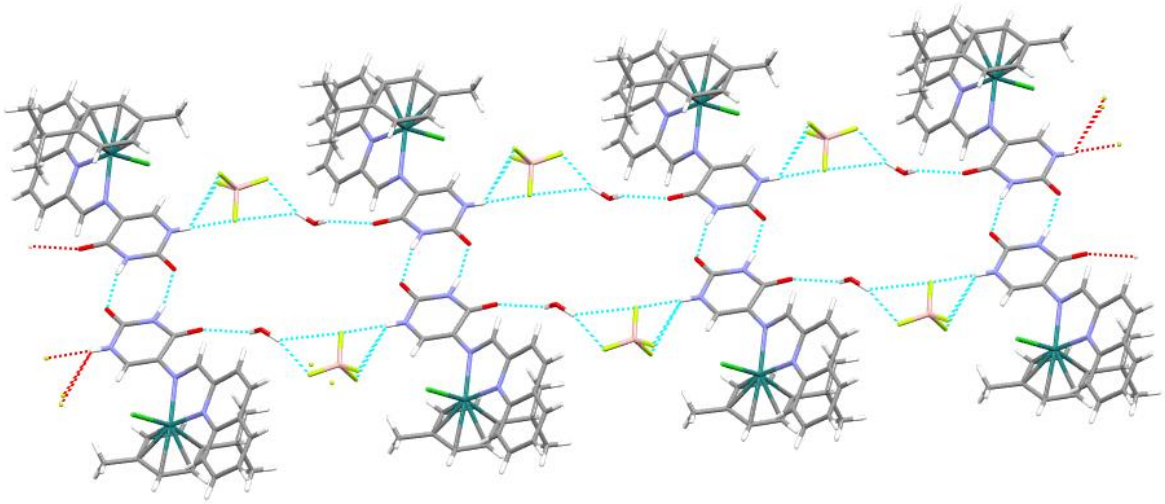

Figure 4. 46: *A perspective view of the hydrogen-bonding network occurring within the crystal lattice of* ***3****.*

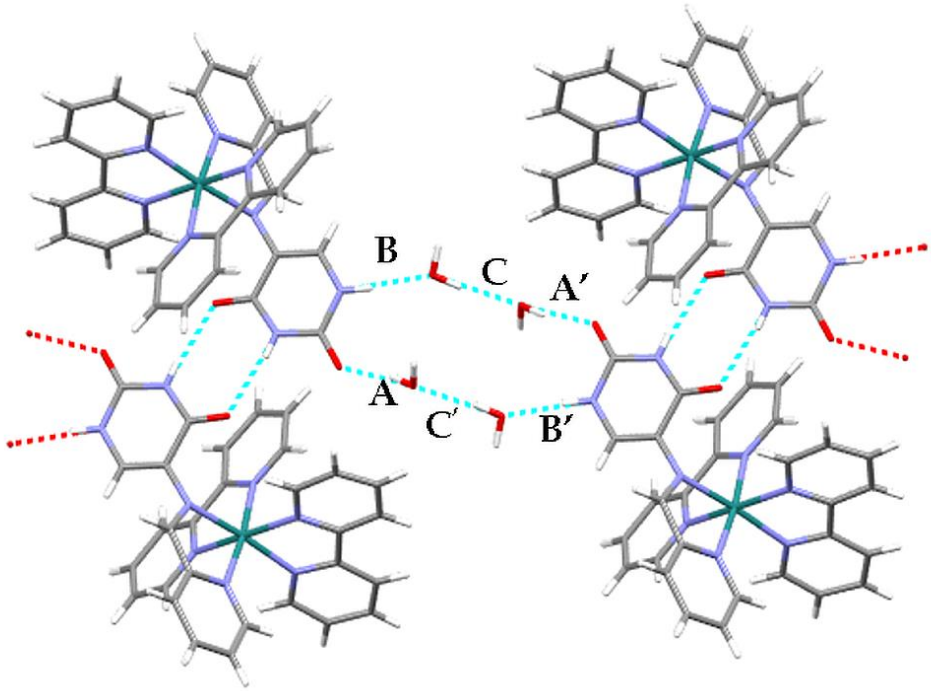

Figure 4. 47 : *A perspective view of four water molecules linking neighbouring molecules of* ***4****, which affords a network of hydrogen-bonded:* ***A****,* ***A′*** *2.018 Å;* ***B****,* ***B′*** *= 1.899 Å and* ***C****,* ***C′*** *= 1.964 Å.*

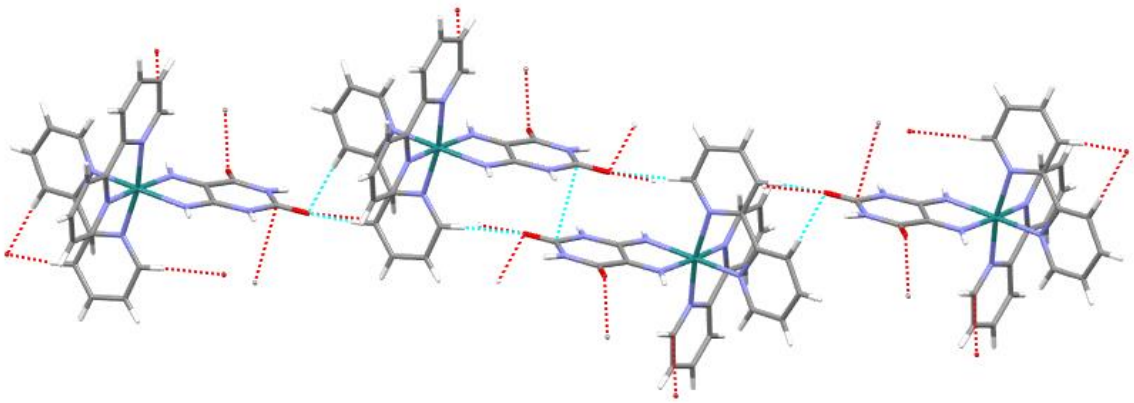

Figure 4.48: *An illustration of the non-classical hydrogen bonding interactions occurring in the crystal lattice of* ***5****.*

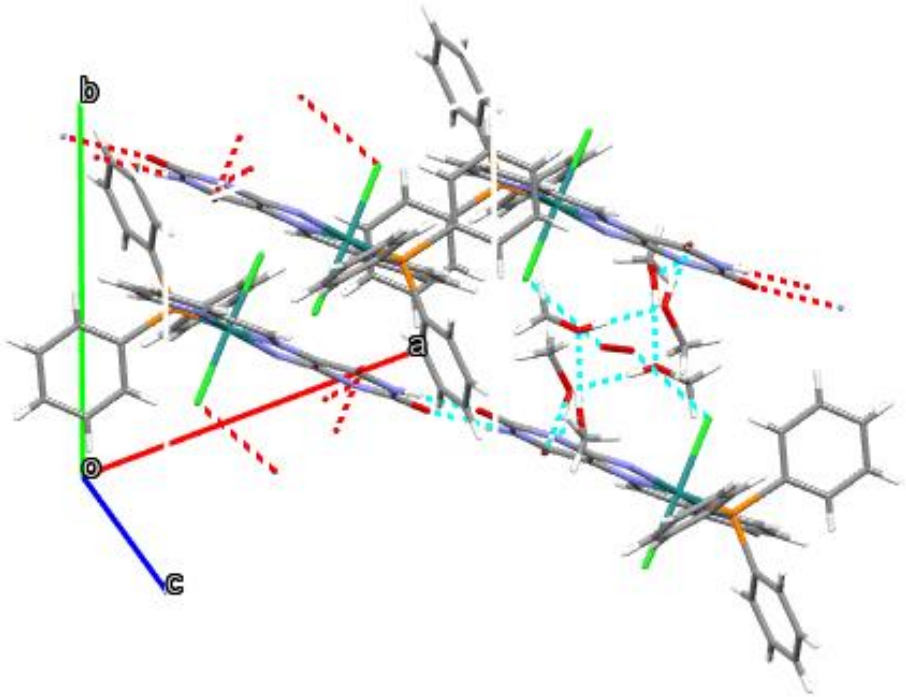

Figure 4. 48: *Triclinic unit cell of* ***6*** *showing the intermolecular hydrogen-bonding interactions within the dimer and molecules of recrystallization which are aligning in [c]-axis.*

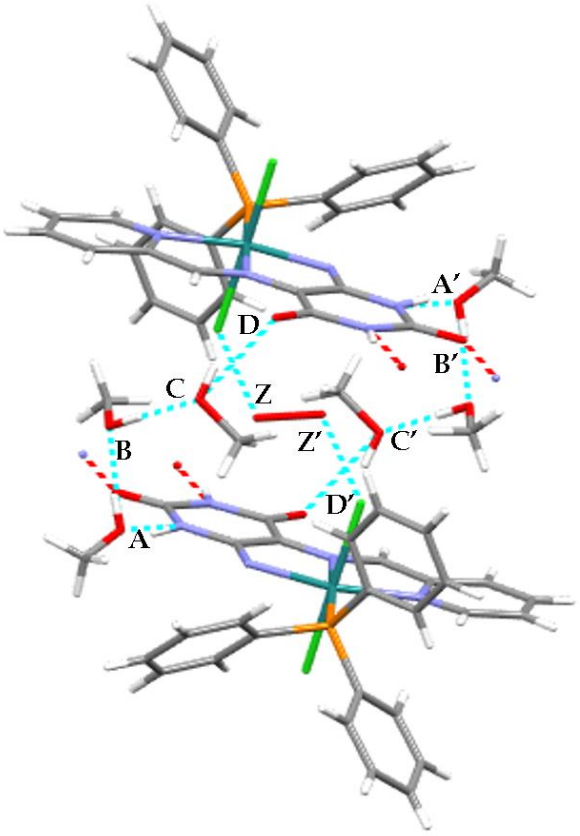

Figure 4. 49: *A perspective view of* ***6*** *where methanol molecules of recrystallization and oxygen linking neighbouring molecules of* ***6****, which affords a network of hydrogen-bonded supermolecule:* ***A****,* ***A′*** *= 2.027 Å;* ***B****,* ***B′*** *= 1.817 Å;* ***C****,* ***C′*** *= 1.818 Å.* ***D****,* ***D′*** *= 1.994 Å and* ***Z****,* ***Z′*** *= 3.179 Å.*

The metal centres are more pronounced in the 'piano stool' geometries of the para-cymene ruthenium(II) complexes **1** - **3**. The steric demands of the π-face coordinated benzoid ring of the para-cymene group imposes more constrain on the five-membered chelate rings at the respective Ru(II) centres; N1-Ru-N2 = 77.12(6)° for **1**, 77.02(8)° for **2**, 77.45(6)° for **3**, compared to the bite angles of **4** without the para-cymene moiety (N1-Ru-N2 =78.10(1)° for **4**, N4-Ru-N3 = 79.27(9)° for **5**) and 78.8(2)°) for **6** see, **Figures 4.51 - 4.56**. Consequently, the bond angles comprised ruthenium with opposing donor atoms all deviate from linearity: [N7-Ru-N2 = 175.3(1)°, N1-Ru-N6 = 173.6(1)°, N8-Ru-N5 = 170.5(1)° for **4**, and N8-Ru-N5 = 167.98(9)°, N6-Ru-N3 = 172.84(7)°, N7-Ru-N4 = 171.26(9)° for **5** and N1-Ru-N3 = 159.5(2)°, N2-Ru-P1 = 176.5(2)°] for **6**, see **Tables 4.5**

and **4.6**. Moreover, the angles of the aliphatic imino chains of the Schiff bases of **1 - 4**, and **6** are close to the idealized 120° at [C6-C5-N2 = 117.5(2)° for **1**, 117.6(2)° for **2**, 116.4(6)° for **6**, 117.20(4)° for **4**, and C9-C10-N2 = 117.20(4)° for **3**]. The similar coordination effects are also manifested in the imino bonds length [C10-N2 = 1.296(3) Å for **1** and 1.291(3) Å for **2**, C29-N2 = 1.288(9) Å for **6**, C6-N2 = 1.286(5) Å for **4** and C10-N2 = 1.284(7) Å for **3**] and compares well with other ruthenium Schiff base complexes reported in the literature.[24]

The ruthenium-to-halide bonds, [Ru-Cl1 = 2.416(6) Å for **1**, 2.407(9) Å for **2**, 2.388(9) Å for **3**, and Ru-Cl1 = 2.348(2) Å, Ru-Cl2 = 2.030(5), for **6**] differ since they are experiencing different trans-influences from the pyridyl nitrogen, triphenylphosphine phosphorous and p-cymene donor atoms, respectively. These Ru-Cl bond lengths of **1 - 3** and **6** and the Ru-N_{imino} bonds [Ru-N2 = 2.099(2) Å for **1**, 2.101(2) Å for **2**, 2.030(5) Å for **6,** 2.058(3) Å for **4**, Ru-N5 = 2.089(4) Å for **3**] of all metal compounds are comparable to those of the diamagnetic ruthenium(II) with a benzohydrazone-derived Schiff base ligand, e.g. [(η^6-p-cymene)Ru(L_1)Cl] (HL_1 = 3-methoxy-N'-((3-methylthiophen-2-yl)methylene)benzohydrazide) with Ru-Cl and Ru-N_{imino} bonds of 2.4238(7) Å and 2.058(3) Å, respectively.[40]

The Ru-$N_{pyridyl(Schiff\ base)}$ bonds are 2.079(2) Å for **1**, 2.088(2) Å for **2**, 2.090(5) Å for **6**, 2.058(3) Å for **4**, and 2.116(4) Å for **3** and the difference between them is accounted by the higher electronegativity of Cl1 donor atom oppose in the latter compared to the $N_{pyridyl}$ donor atom in the former. However, Ru-$N_{pyridyl}$ bonds ranging from 2.050(2) - 2.077(2) Å of the respective compounds compare well with each other and that of other Ru(II) complex salts.[41] In addition, the N_{amido} bond distances of **5,** [Ru-N3 = 2.001(2) and Ru–N4 = 2.054(3) Å] are comparable with cis-Cl, trans-P-[$RuCl_2(PPh_3)_2$(ddd)](ddd=5,6-diamino-1,3-dimethyl uracil) at [Ru-N1 = 2.017(3) and Ru–N2 = 1.969(3) Å] as reported.[26]

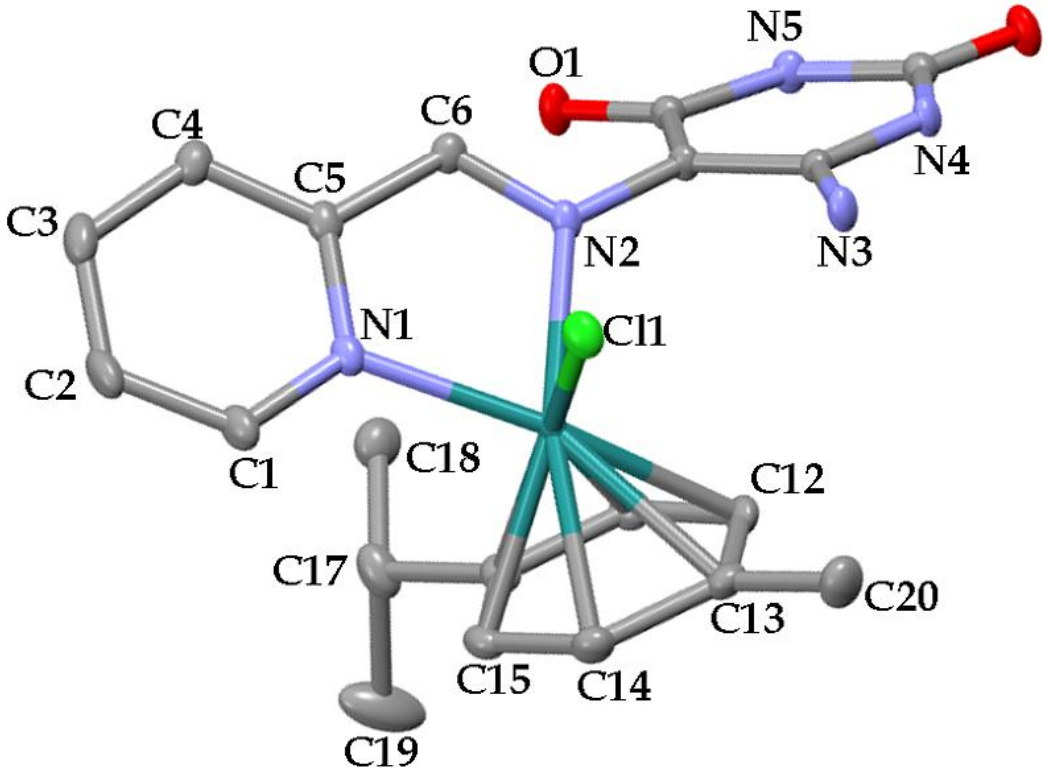

Figure 4. 50: *Molecular structure of **1**, shown with 50% probability displacement ellipsoids and the selected atom-numbering scheme. The solvent molecule of recrystallization, protons and the counterion have been omitted to improve clarity.*

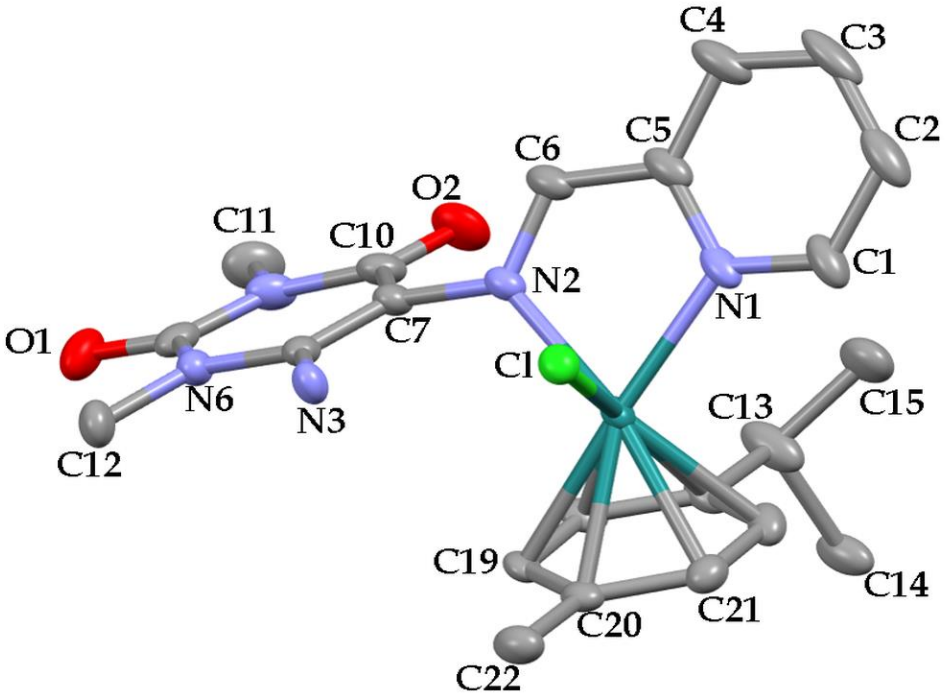

Figure 4. 51: *Molecular structure of* **2**, *shown with 50% probability displacement ellipsoids and the selected atom-numbering scheme. The solvent molecule of recrystallization, protons and the counterion have been omitted to improve clarity.*

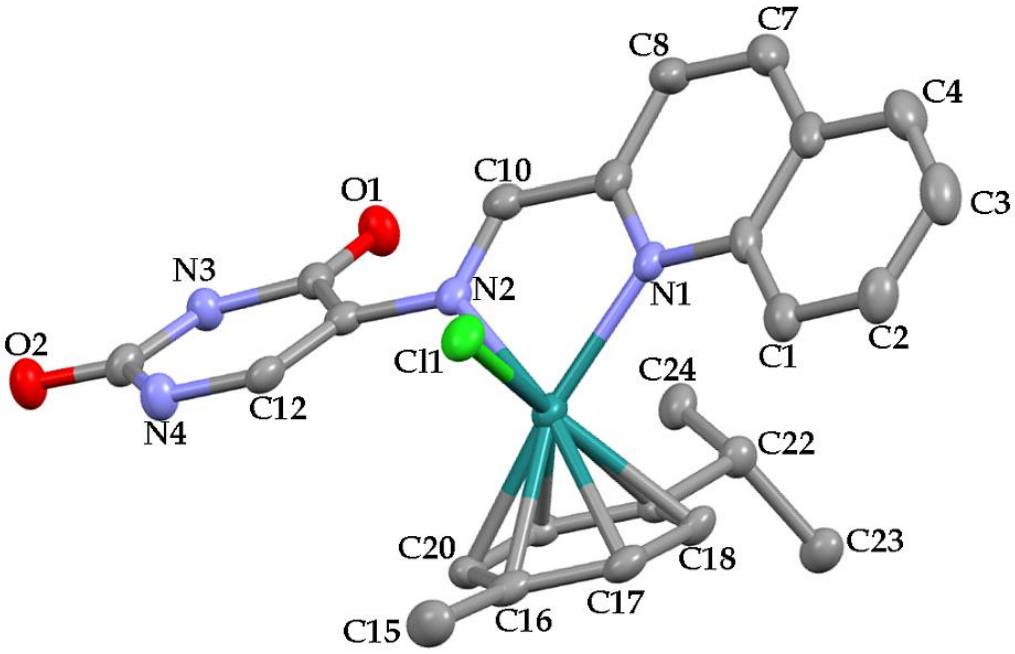

Figure 4. 52: *Molecular structure of* **3**, *shown with 50% probability displacement ellipsoids and the selected atom-numbering scheme. The solvent molecule of recrystallization, protons and the counterion have been omitted to improve clarity.*

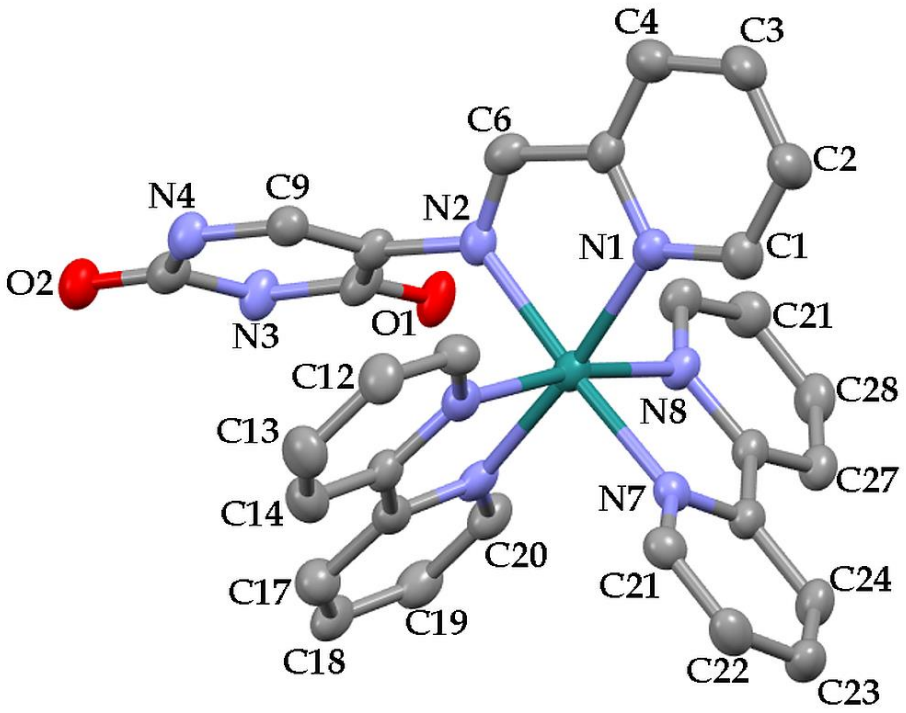

Figure 4. 53: *Molecular structure of* ***4****, shown with 50% probability displacement ellipsoids and the selected atom-numbering scheme. The solvent molecule of recrystallization, protons and the counterion have been omitted to improve clarity.*

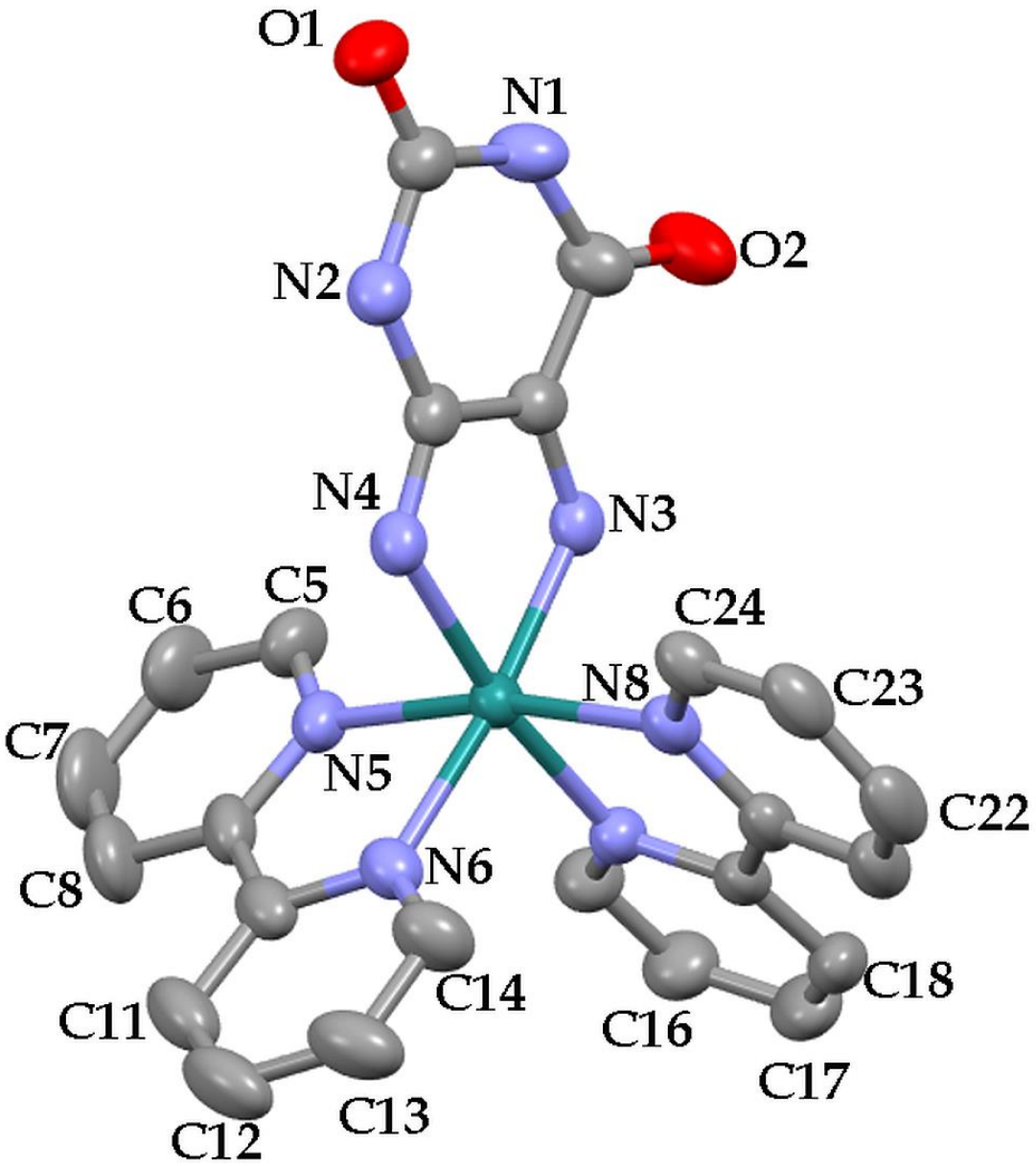

Figure 4. 54: *Molecular structure of* **5**, *shown with 50% probability displacement ellipsoids and the selected atom-numbering scheme. Their solvent molecule of recrystallization, protons and the counterion have been omitted to improve clarity.*

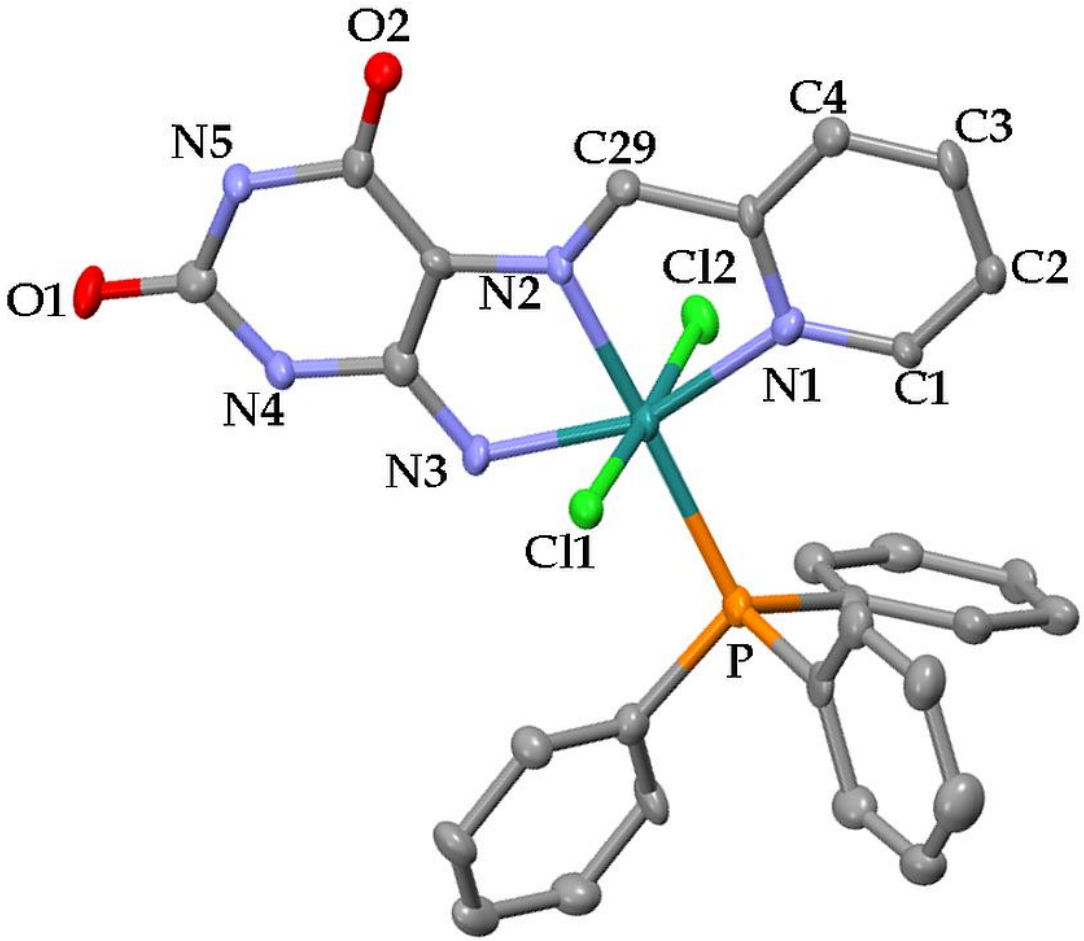

Figure 4. 55: *Molecular structure of* ***6****, shown with 50% probability displacement ellipsoids and the selected atom-numbering scheme. The solvent molecule of recrystallization, protons and the counterion have been omitted to improve clarity.*

4.3.3 BSA interaction studies

Efficient uptake of pharmaceuticals into the bloodstream by the albumins and transferrin is critical to their in vivo biodistribution to target tissues for therapeutic purposes.[42] More specifically, BSA is a protein prototype to Human Serum Albumin (HSA) due to their structural similarities. Consequently, BSA is generally experimentally used for preliminary assessment of the potential drug transportability. Metal complexes typically bind non-coordinatively into the subdomains (**A** and **B**) of the active site BSA domains **I – III**. BSA-metal complex adduct formation is typically governed by the stereo-electronic properties of the metal complex. In addition, serum albumins do not alter their structural integrity while transporting metallo-pharmaceuticals and maintaining many physiological processes at the same time.[43]

Biomolecular titrations between the in vivo drug carrier BSA and metal complexes **1 - 6** were monitored by fluorescence spectrophotometry. Mutually, the fluorescence spectral profiles show gradual quenching of the BSA peak maximum upon the additions of the respective metal complexes. These emission spectral trends are indicative of non-covalent interactions between BSA and the separate metal complexes.[44] Shifts in peak maxima which are seen from each graph (**Figures 4.57 - 4.64**) are proportional to the linear correlation coefficients graphs (**Figures 4.57 - 4.64**) of respective compounds. The anti-coagulant agent, Warfarin is known to bind to Sudlow site I of BSA and HSA whereas ibuprofen is also known to bind in site **II** of BSA and HSA molecule. Consequently, upon additions of respective metals in the presence of a constant equimolar (1:1) mixture of BSA and subdomain site markers (warfarin or ibuprofen), there was a gradual decrease in initial emission intensity see **Figures 4.57 - 4.64**. The BSA binding constants values of the respective metals **1 – 6** (with and without site-markers) were calculated using equation [**3**], and are presented in **Table 4.7.** Compounds **1 - 6** displayed varying binding constants of BSA in the presence of site markers during displacement studies.

Table 4. 7: *Non-covalent interaction parameters, calculated from the BSA fluorescence spectroscopic titrations with the metal complexes **1 - 6**.*

Compound	No site marker			Binding site(s)	Ibuprofen			Warfarin		
	K_{sv} (M^{-1})	k_q (M^{-1} s^{-1})	K_b (M^{-1})	n	K_{sv} (M^{-1})	k_q (M^{-1} s^{-1})	K_b (M^{-1})	K_{sv} (M^{-1})	k_q (M^{-1} s^{-1})	K_b (M^{-1})
1	3.65×10^{5}	3.65×10^{12}	2.03×10^{7}	1.3514	3.68×10^{5}	3.68×10^{12}	1.91×10^{8}	4.39×10^{5}	4.39×10^{12}	2.01×10^{7}
2	6.26×10^{5}	6.26×10^{12}	6.59×10^{7}	1.3967	4.09×10^{5}	4.09×10^{12}	1.55×10^{8}	4.26×10^{6}	4.26×10^{12}	3.82×10^{7}
3	2.89×10^{5}	2.89×10^{12}	4.35×10^{7}	1.4347	3.25×10^{5}	3.25×10^{12}	1.15×10^{8}	3.66×10^{5}	3.66×10^{12}	1.29×10^{6}
4	2.89×10^{5}	2.89×10^{12}	2.21×10^{6}	1.1445	3.52×10^{5}	3.52×10^{12}	3.35×10^{7}	2.76×10^{5}	2.76×10^{12}	6.78×10^{7}
5	4.65×10^{5}	465×10^{12}	5.20×10^{6}	1.2195	3.03×10^{5}	3.03×10^{12}	5.91×10^{6}	2.83×10^{5}	2.83×10^{12}	4.97×10^{5}
6	6.23×10^{5}	6.23×10^{12}	8.74×10^{5}	1.142	2.31×10^{5}	2.31×10^{12}	3.18×10^{6}	3.19×10^{5}	3.19×10^{12}	3.74×10^{5}

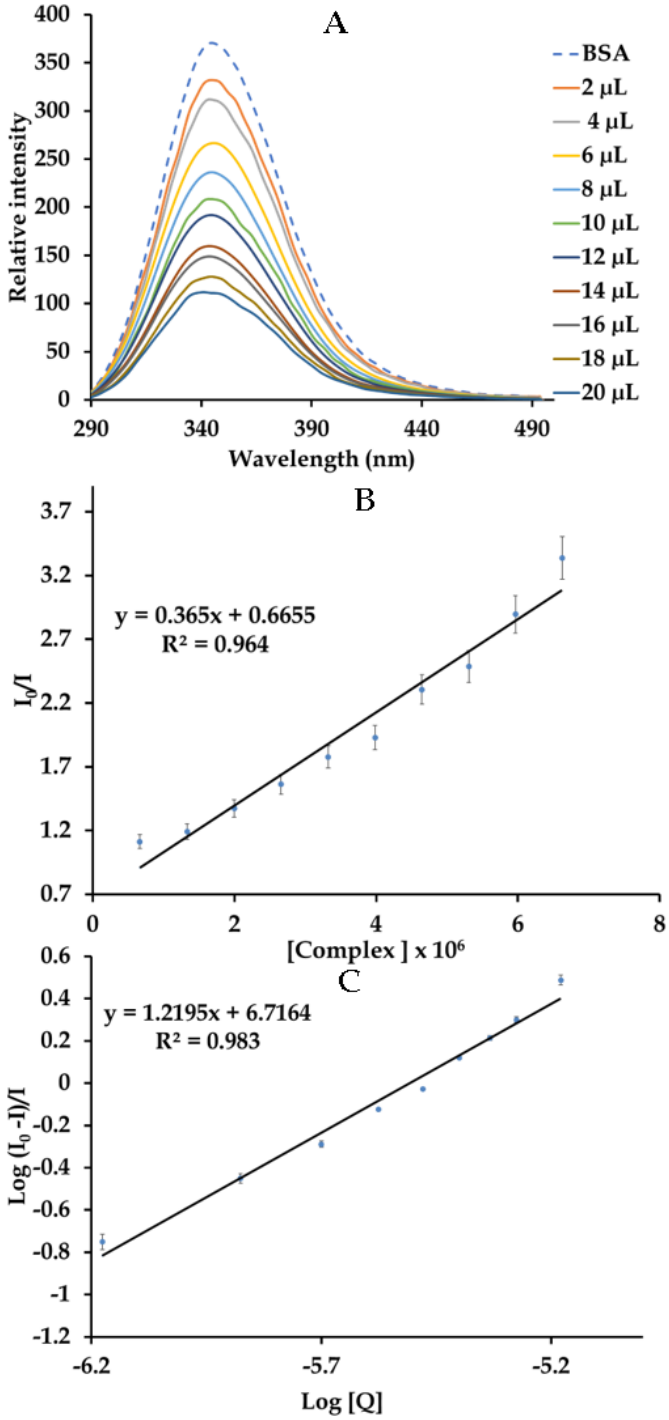

Figure 4. 56: *(**A**) Fluorometric titration of BSA with complex **1** (excitation wavelength = 280 nm). (**B**) Stern-Volmer plot and the linear regression plot (**C**) of Log(I_0-I/I) vs Log[Q]. The relative standard addition of each data point (n = 3) was below 5%.*

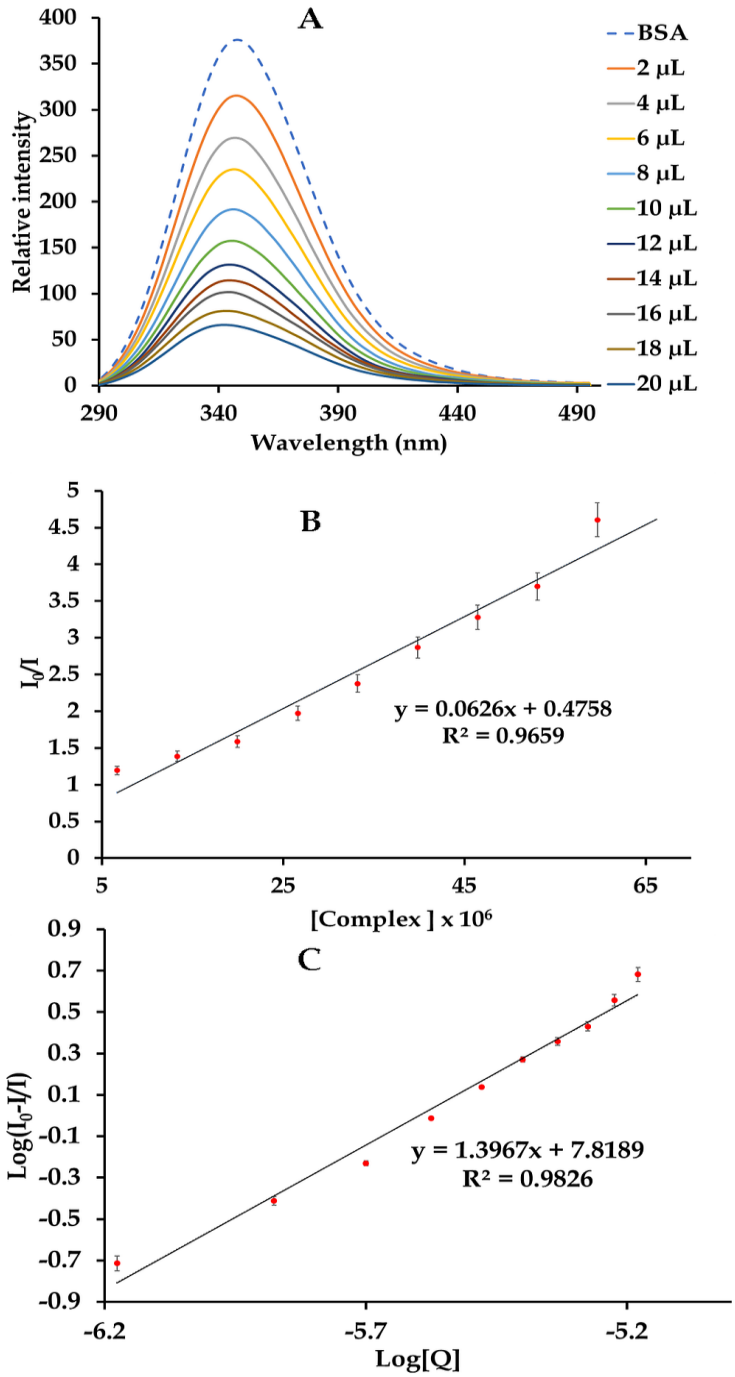

Figure 4. 57: *(**A**) Fluorometric titration of BSA with complex **2** (excitation wavelength = 280 nm). (**B**) Stern-Volmer plot and the linear regression plot (**C**) of Log(I₀-I/I) vs Log[Q]. The relative standard addition of each data point (n = 3) was below 5%.*

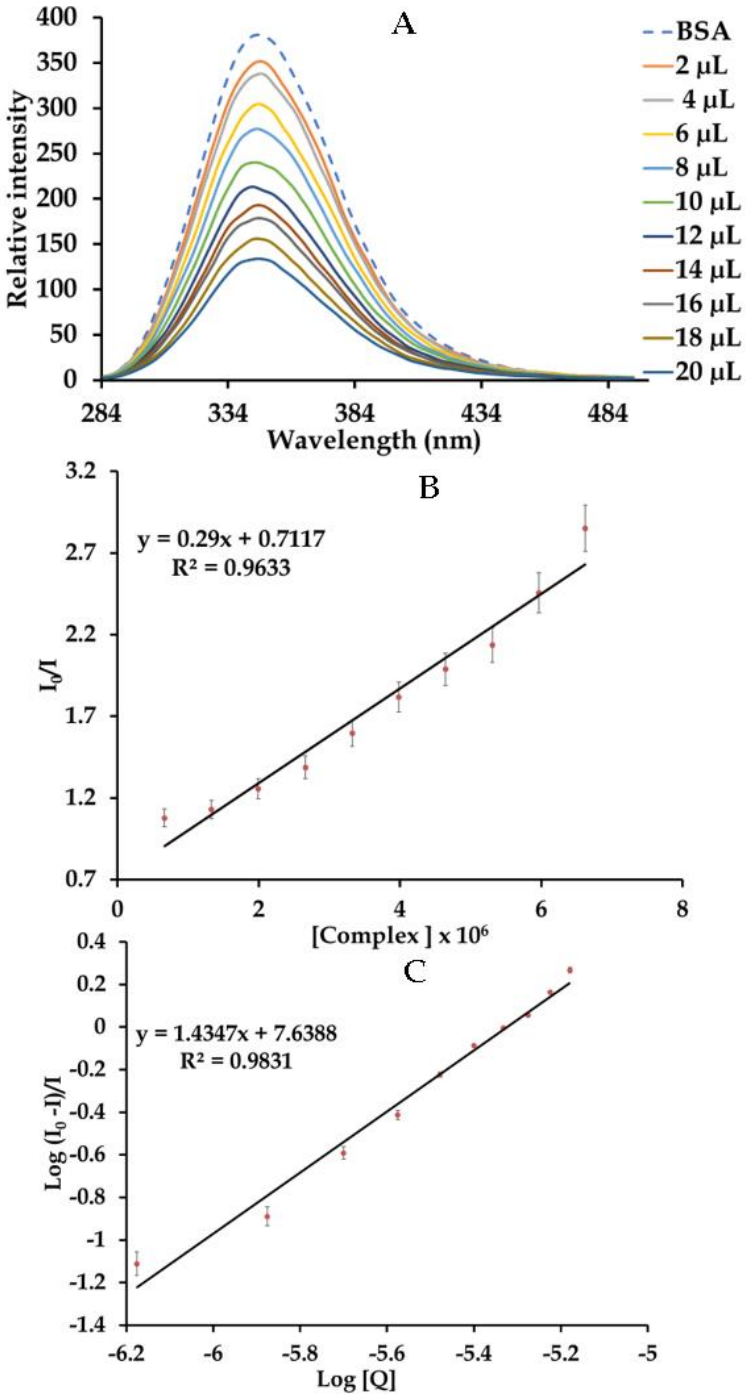

Figure 4. 58: *(**A**) Fluorometric titration of BSA with complex **3** (excitation wavelength = 280 nm). (**B**) Stern-Volmer plot and the linear regression plot (**C**) of Log(I_0-I/I) vs Log[Q]. The relative standard addition of each data point (n = 3) was below 5%.*

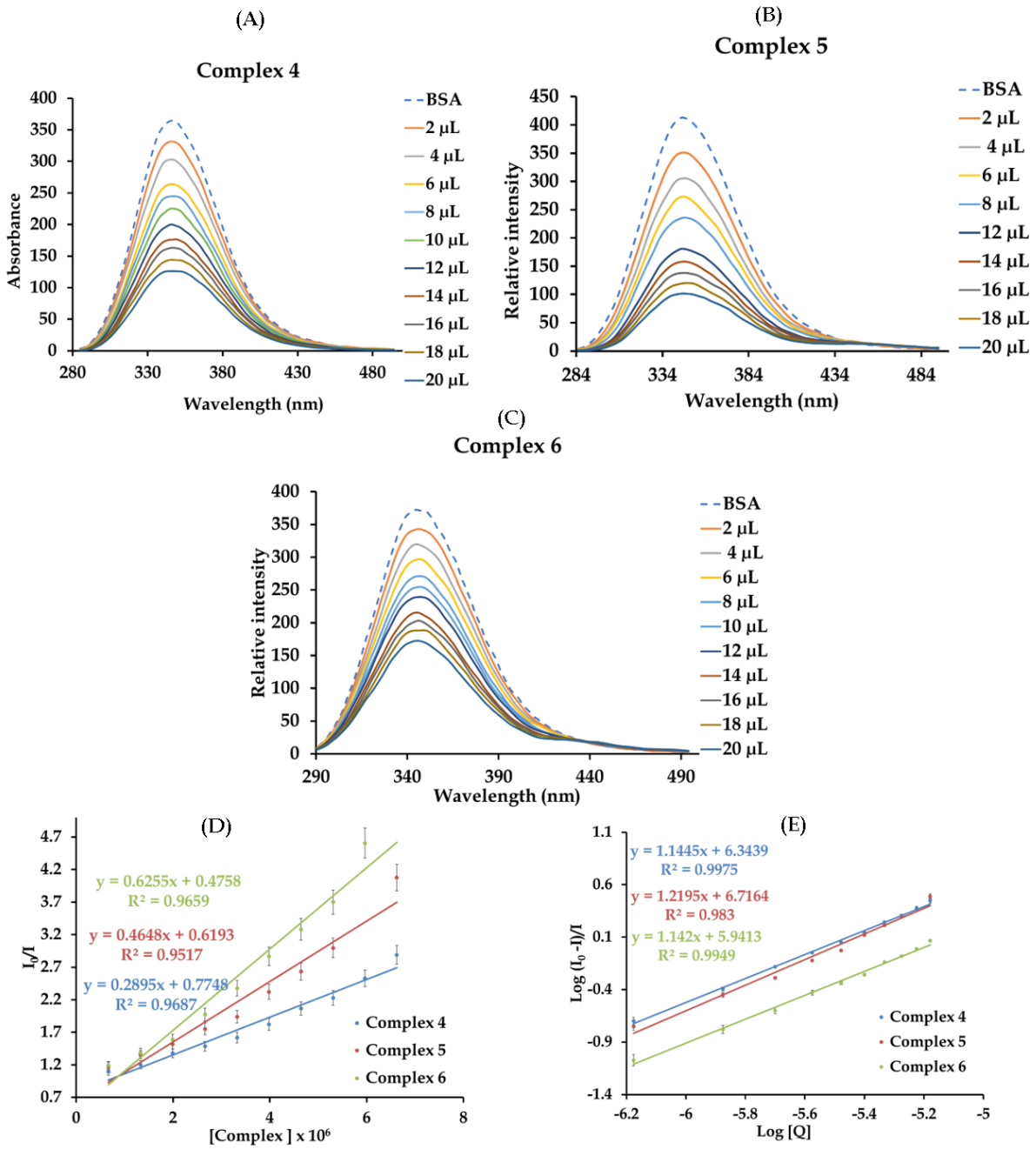

Figure 4. 59: *Fluorescence emission spectral profiles of BSA with equimolar amounts of (A-C) and their Stern-Volmer plots and the linear regression plot (D) between Log(I_0-I/I) vs Log[complex] (C). The relative standard deviation of each data points (n = 3) where all below 5%.*

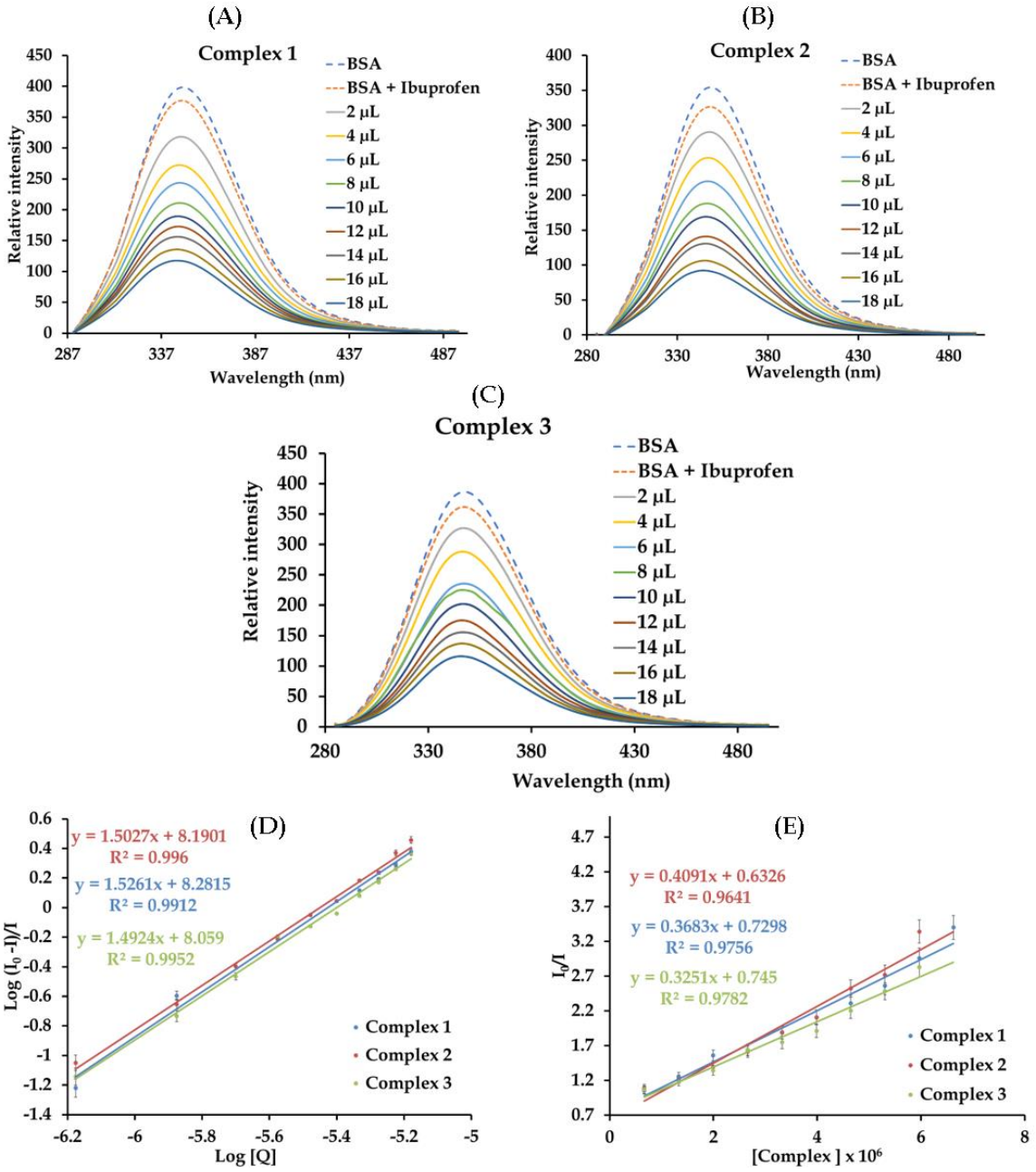

Figure 4. 60: *Fluorescence emission spectral profiles of BSA with equimolar amounts of (A-C) Ibuprofen upon the addition of* ***1-3*** *and their Stern-Volmer plots and the linear regression plot (D) between Log(I₀-I/I) vs Log[complex] (E). The relative standard deviation of each data points (n = 3) where all below 5%.*

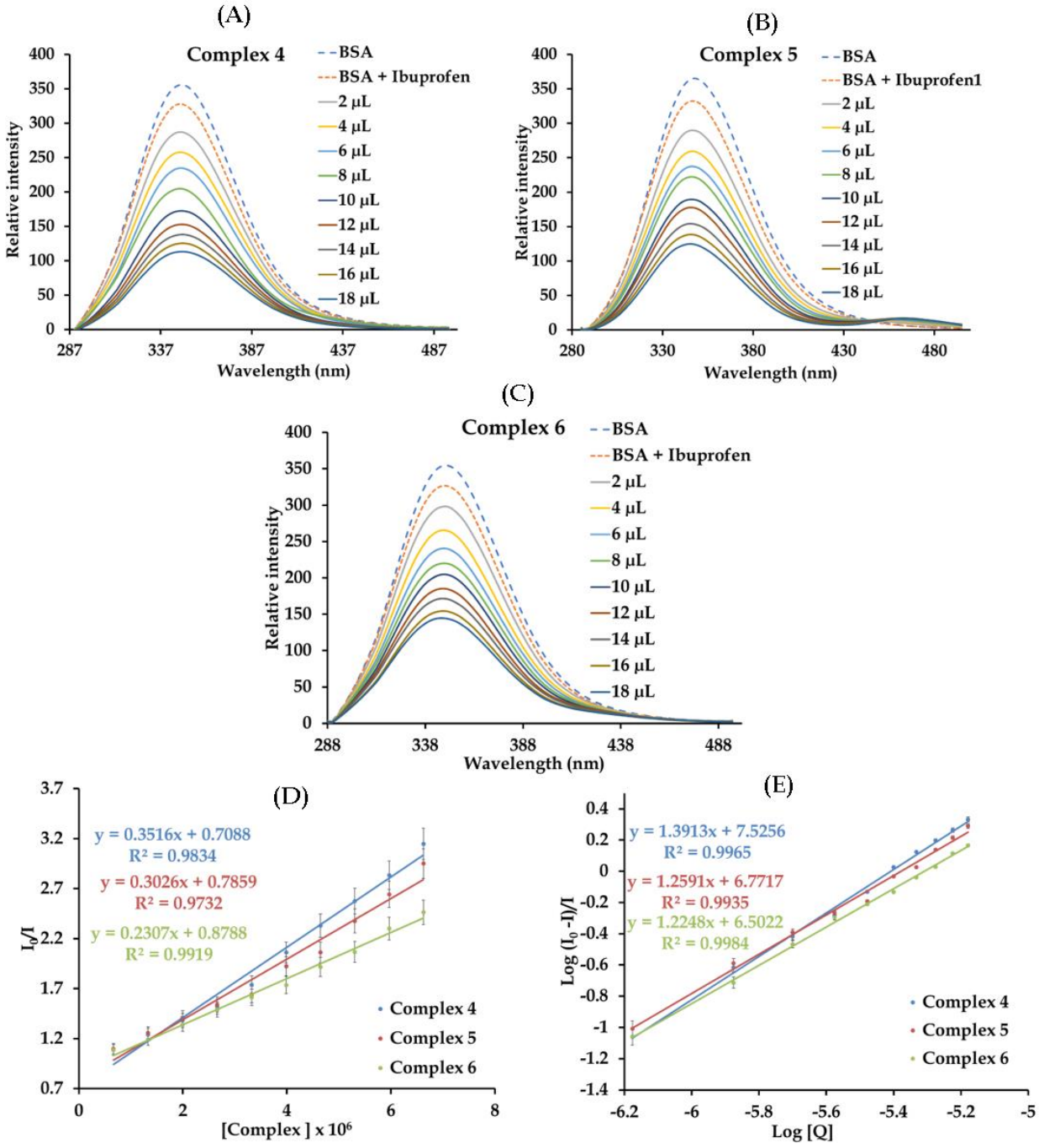

Figure 4. 61: *Fluorescence emission spectral profiles of BSA with equimolar amounts of (A-C) Ibuprofen upon the addition of* ***4 - 6*** *and their Stern-Volmer plots and the linear regression plot (D) between Log(I_0-I/I) vs Log[complex] (E). The relative standard deviation of each data points (n = 3) where all below 5%.*

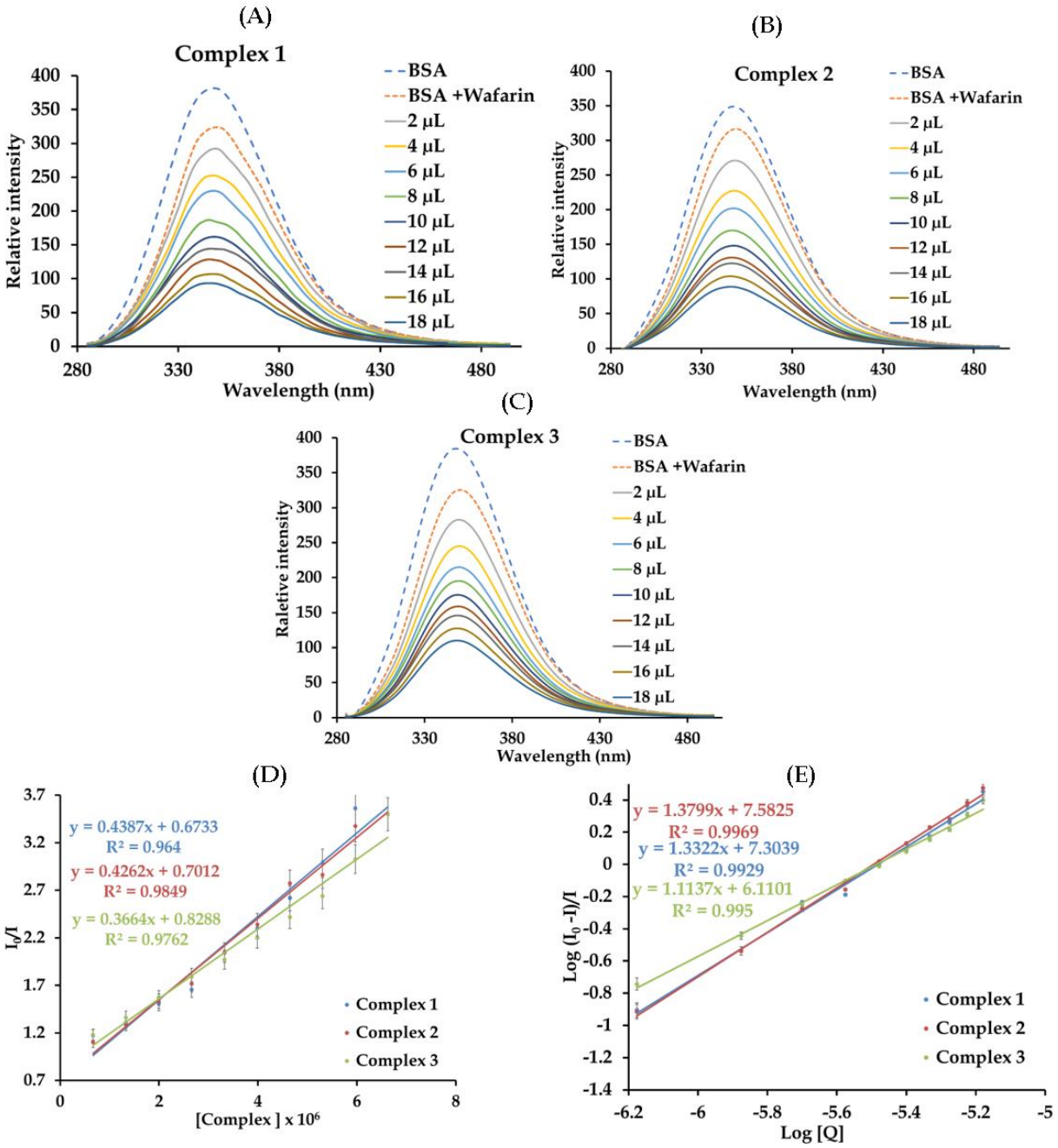

Figure 4. 62: *Fluorescence emission spectral profiles of BSA with equimolar amounts of (A-C) Warfarin upon the addition of* ***1 - 3*** *and their Stern-Volmer plots and the linear regression plot (D) between Log(I₀-I/I) vs Log[complex] (E). The relative standard deviation of each data points (n = 3) where all below 5%.*

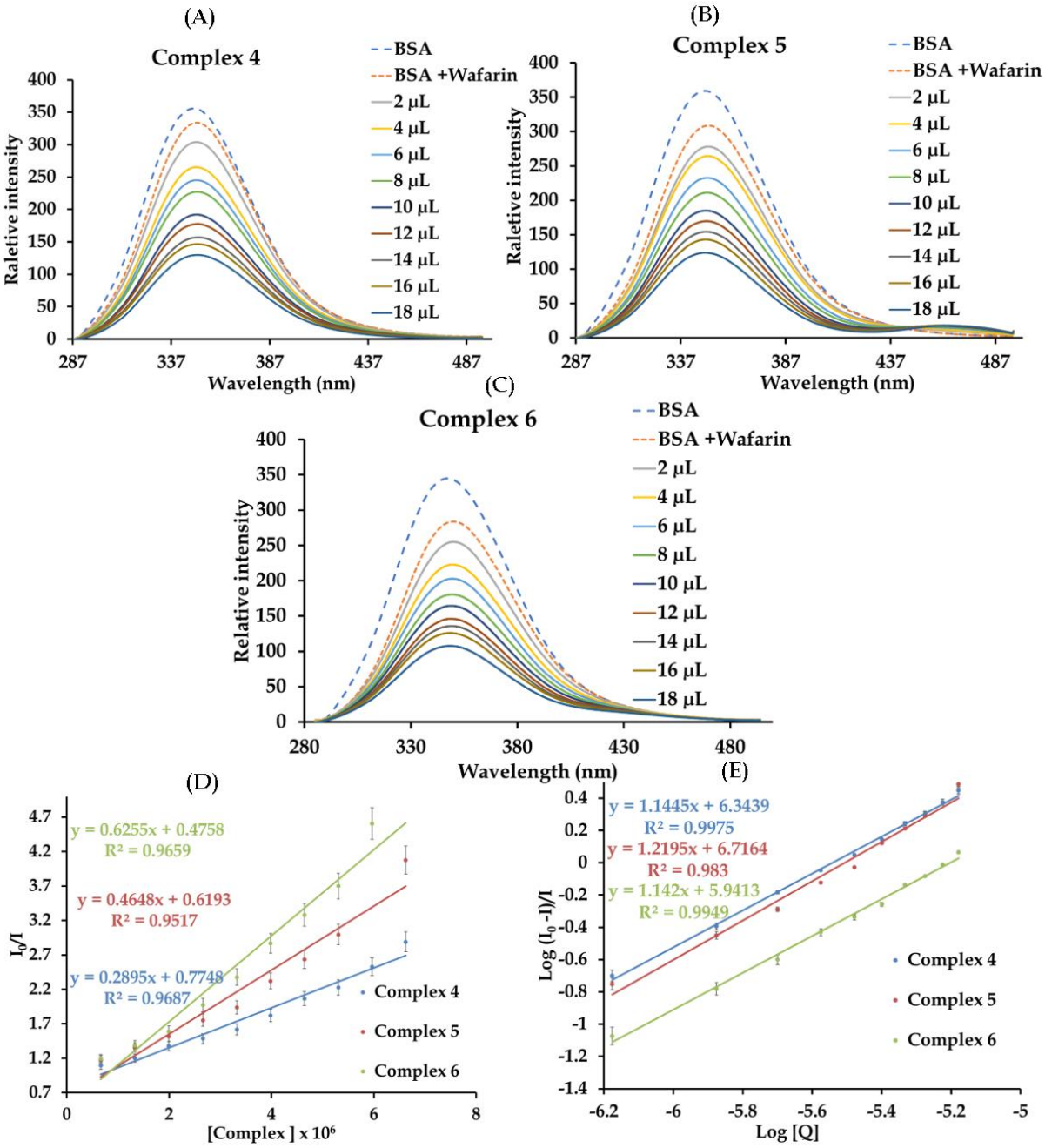

Figure 4. 63: *Fluorescence emission spectral profiles of BSA with equimolar amounts of (A-C) Warfarin upon the addition of* ***4 - 6*** *and their Stern-Volmer plots and the linear regression plot (D) between Log(I₀-I/I) vs Log[complex] (E). The relative standard deviation of each data points (n = 3) where all below 5%.*

The values of the quenching constant (K_{sv}) and Stern–Volmer equation (k_q) as determined from the slope of the linear plots given in **Table 4.7**, were invariant. The fluorescence quenching data for **1 – 6** obtained from the Stern–Volmer equation (k_{sv}) and quenching constant (K_q) were found in the ranges of 2.31×10^5 to 6.23×10^5 M^{-1} and 2.31×10^{12} to 6.23×10^{12} $M^{-1}.S^{-1}$ which suggests a static quenching mechanism, respectively.[44] The K_b values for the affinity of **1 - 5** for BSA decreased in the presence of ibuprofen as well as in **3** and **5** in the presence of Warfarin. The decreases in binding constants of the respective metal compounds observed in the presence of warfarin and ibuprofen may be attributed to significant loss in the tertiary structure of the BSA molecule at higher concentrations of respective compounds which is in fact indicative of displacement of site markers by respective compounds.

On the other hand, the binding constant K_b values of **5** (in the presence of ibuprofen), while **6** in the presence of Warfarin) were invariant and thus, show no preference between the BSA sub-domains. Furthermore, site marker displacement studies suggest that complexes **1-5** preferentially occupy site I while complex **3** and **5** occupies site II of the microenvironment of BSA domains. However, in the case of **4** in site I with warfarin and **1-4** and **6** in site II with ibuprofen the increase in binding constants in the presence of site markers is indicative of cooperative binding of the respective metal complex with the site markers is due to the allosteric mechanism.[45] As evidenced by trends in the literature, HSA has actually demonstrated target specificity towards pancreatic islet cells.[46] For instance, HSA has been found to exhibit early mediation for cell apoptosis by lowering elevated levels of caspase 3, beta-mercapto-ethanol as well as towards fibrillization of islet amyloid polypeptide (IAPP) and αS. Therefore, these findings suggest the synergy of respective metal complexes with HSA can provide multifaceted antidiabetic mechanism.

4.7.4 Anti-oxidant properties

Elevated free radical concentration in the body is linked to the physiological degradation of the pancreatic β-cells. Therefore, it is important to evaluate the potential of the metal-based anticancer and anti-diabetic drug can scavenge these reactive oxygenated species (ROS) in the bloodstream.[47] In fact, Schiff base complexes of ruthenium have portrayed optimal activities against ROS through redox-mediated electron transfer, proton donation originating from the Schiff base chelator, or direct binding of radicals to the metal complexes.[24] Generally, the free radicals can be neutralized by anti-oxidants through the donation of an electron. On the other hand, a previous study showed that the parent Ru(II) Schiff base complex, **1** neutralised the formation of radicals in elevated amounts that triggered the genesis of oxidative stress of Streptozotocin (STZ)-diabetic rats.[48]

Scavenging of the model oxidative radicals (viz. $DPPH^{\bullet}$ and $NO^{\bullet}$) by **1 - 6** were better than that of ascorbic acid (as positive control) based on the noticeable lower IC_{50} values of the metal complexes, refer to **Table 4.8**. In particular, these metal compounds show preferential neutralizing tendencies towards the bulky organic $DPPH^{\bullet}$ radical. However, ascorbic acid displayed the low radical scavenging capabilities for the $DPPH^{\bullet}$ and $NO^{\bullet}$ radicals compared to respective compounds. Compared to ascorbic acid (positive control), **3** and **8** of the investigated metal complexes showed a higher radical scavenging activity. The results of the other ruthenium(II) complexes were consistent with the parent compound **7** and the novel complexes **1 - 6** and **8 - 10** according to the literature trends for antioxidants.[24,49]

Table 4. 8: *Antioxidant activities of vitamin C, **1**-**6**, and **8**-**10** against the DPPH$^{\bullet}$ and NO$^{\bullet}$ radicals.*

Compound	DPPH$^{\bullet}$ Radical	NO$^{\bullet}$ Radical
	IC_{50} (µM)	IC_{50} (µM)
1	47	33
2	65	42
3	29	34
4	52	33
5	43	60
6	28	24
8	27	41
9	26	24
10	32	31
Vitamin C	249	136

4.7.5 Amyloid fibril interaction studies

Aggregation of amyloid to form fibrils can be induced by thermal agitation at temperatures above 55 °C.[50] To probe the potentials of the metal complexes **1** - **6** as fibril disaggregation agents, the microstructure of the thermally-agitated BSA amyloid fibrils (in pH 7.4 PBS) was probed by Transmission electron microscopy (TEM) in the absence and presence of 50 µM of the different metal complexes and formvar (negative control) after their 24 h incubation at neo physiological conditions, see **Figure 4.64**. TEM analysis revealed that the amyloid fibrils fragmented strands in the form of smaller and dispersed particles. The exposure of BSA-fibrils to respective metal complex dismantled the amyloid fibril aggregates (see micrograph **B**) into smaller spherical nanoparticles with an average diameter in increasing order of 21.90 nm for **3** < 29.22 nm for **4** < 34.2 nm for **1** <

nm < 38.6 for **6** < 59.0 nm for **2** < 66.3 nm for **5**. Based on the TEM analysis, it is evident that the disaggregation activities of **3** and **4** were better than their congener counterparts. Subsequently, the nature of the interactions between the metallodrugs and BSA fibrils were investigated by fluorescence titrations of the individual metal complexes against the BSA fibrils to corroborate the microscopic visual trends observed via TEM. To monitor the amyloid fibrillation and the subsequent disaggregation, a fixed concentration of Thioflavin T (ThT) was excited at 440 nm and its fluorescence (ThT) peak at 510 nm in the presence of incremental amounts of the different metal complexes **1 - 6**. The fluorescence emission spectral profiles show that peak maxima were quenched while **4** also initially underwent hypochromism but at metal complex higher concentrations, hyperchromism was observed. The latter electronic spectral observations suggest that this metal complex initially underwent non-directional bonding with BSA aggregates followed by direct covalent bonding to the latter.[51]

In contrast, as per literature trends other metal complexes portraying the classical fluorescence quenching of ThT-amyloid fibrils adheres well to the metal complexes which induces non-covalent interactions such as hydrogen-bonding or ion-dipole interactions with the ThT-fibril conjugates.[52] The metal complexes **1 - 6** contain uracil moieties, which are characterized by free electronegative N-H and C=O groups. These groups can form strong intermolecular hydrogen bonds with similar groups in the BSA structure, forming stable adducts in the process. The inhibition of amyloid fibrillation may be achieved by the folding of BSA-fibril residues and keeping the tryptophan hidden inside its hydrophobic pocket. The range of fluorescence quenching from **1 - 6** at higher concentrations is 95.5% to 99.8% as depicted in **Figure 4.65**. Furthermore, in the fluorescence spectroscopic titrations carried out with respective compounds, suggests that the hydrolysis susceptibility of labile chloro-containing metal complexes **1 - 3** and **6** can result in the concurrent ligand-exchange of the aqua co-ligands leading to direct binding of the corresponding metal complexes with BSA-fibrils. [53] The distinct covalently bound fibril (BSA)-fibril–metal complex adducts of **1 - 6** are supported by the overlap in

the electronic spectra of these various metal complexes upon addition of respective metals. Due to the fluorescence intensity profiles of the adducts of **1 – 6** with BSA fibrils are also noteworthy because they resemble those of BSA and quench with the addition of each of the respective compounds. As well as, in fact, when interacting with other similar cross-β-sheet structures, the biomolecular interaction capabilities of **1 – 6** are comparable to earlier studies conducted with NAMI-A, its derivatives and ruthenium bipyridyl compounds.[54-55]

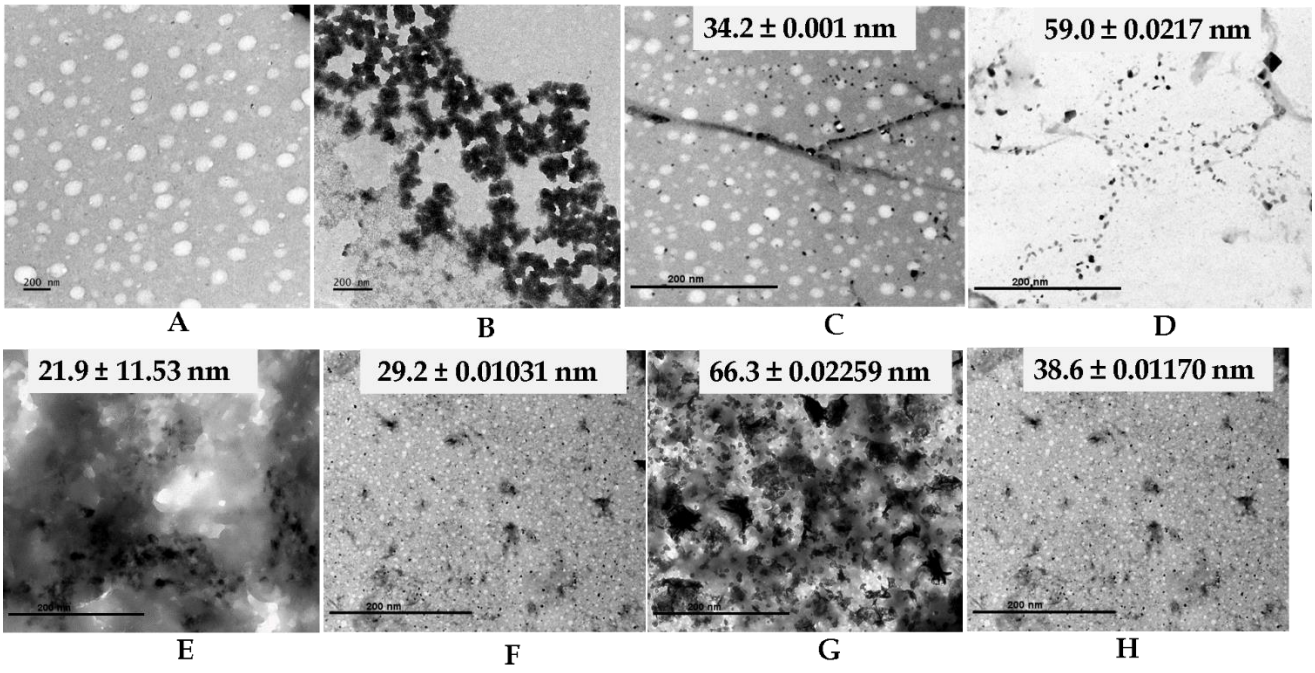

Figure 4. 64: *TEM micrographs of thermally agitated and aggregated BSA amyloid fibrils at (50 μM in pH 7.4 PBS) with (**A**) formvar (negative stain control), (**B**) no complex (absence) and (**C-H**) presence of complexes **1-6** (at 75 μM) after incubation for 24 h at physiological temperature. The length of the scale bars is 200 nm.*

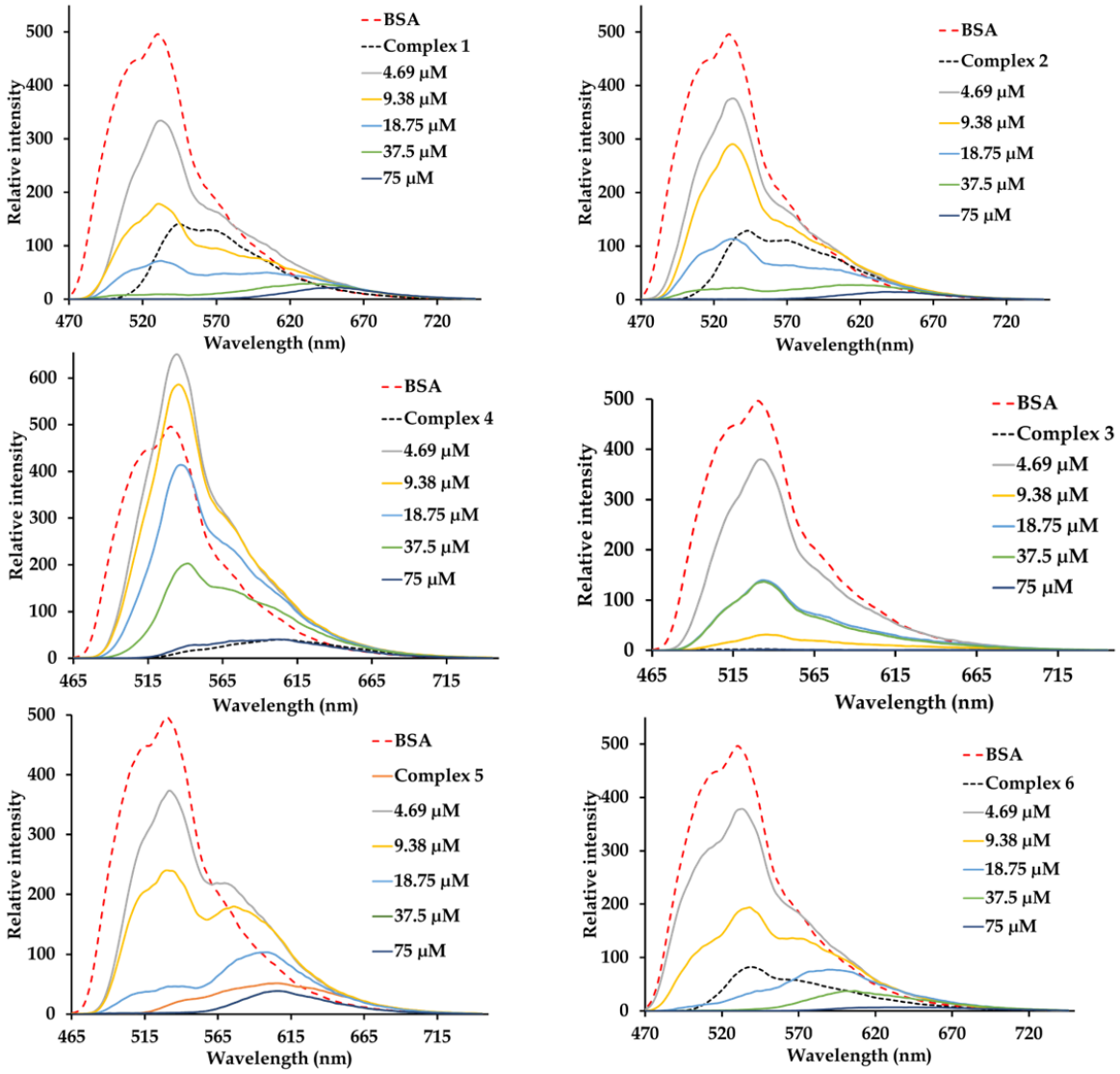

Figure 4. 65: *Quenching titrations between the fluorescent conjugate of 50 µM BSA-amyloid 20 µM THT and the respective metal complexes* ***1- 6*** *(excitation and emission wavelengths = 440 and 510 nm, respectively).*

4.4. References

(1) Newsholme, P.; Keane, K. N.; Carlessi, R.; Cruzat, V. Oxidative stress pathways in pancreatic β-cells and insulin-sensitive cells and tissues: importance to cell metabolism, function, and dysfunction. Am J Physiol Cell Physiol **2019**, 317 (3), C420-c433
(2) Ashraf, G. M.; Greig, N. H.; Khan, T. A.; Hassan, I.; Tabrez, S.; Shakil, S.; Sheikh, I. A.; Zaidi, S. K.; Akram, M.; Jabir, N. R.; et al. Protein misfolding and aggregation in Alzheimer's disease and type 2 diabetes mellitus. CNS Neurol Disord Drug Targets **2014**, 13 (7), 1280-129.
(3) Almeida, Z. L.; Brito, R. M. M. Structure and Aggregation Mechanisms in Amyloids. Molecules **2020**, 25 (5). Jeong, H. R.; An, S. S. Causative factors for formation of toxic islet amyloid polypeptide oligomer in type 2 diabetes mellitus. Clin Interv Aging **2015**, 10, 1873-1879.
(4) Bortoletto, A. S.; Graham, W. V.; Trout, G.; Bonito-Oliva, A.; Kazmi, M. A.; Gong, J.; Weyburne, E.; Houser, B. L.; Sakmar, T. P.; Parchem, R. J. Human Islet Amyloid Polypeptide (hIAPP) Protofibril-Specific Antibodies for Detection and Treatment of Type 2 Diabetes. Adv Sci (Weinh) **2022**, 9 (34), 1-12.
(5) Fawzi, N. L.; Kohlstedt, K. L.; Okabe, Y.; Head-Gordon, T. Protofibril Assemblies of the Arctic, Dutch, and Flemish Mutants of the Alzheimer's Aβ1–40 Peptide. Biophysical Journal **2008**, 94 (6), 2007-2016.
(6) Selivanova, O. M.; Suvorina, M. Y.; Dovidchenko, N. V.; Eliseeva, I. A.; Surin, A. K.; Finkelstein, A. V.; Schmatchenko, V. V.; Galzitskaya, O. V. How to Determine the Size of Folding Nuclei of Protofibrils from the Concentration Dependence of the Rate and Lag-Time of Aggregation. II. Experimental Application for Insulin and LysPro Insulin: Aggregation Morphology, Kinetics, and Sizes of Nuclei. The Journal of Physical Chemistry B **2014**, 118 (5), 1198-1206.
(7) Mulaj, M.; Foley, J.; Muschol, M. Amyloid Oligomers and Protofibrils, but Not Filaments, Self-Replicate from Native Lysozyme. Journal of the American Chemical Society **2014**, 136 (25), 8947-8956.
(8) von Euler Chelpin, M.; Söderberg, L.; Fälting, J.; Möller, C.; Giorgetti, M.; Constantinescu, R.; Blennow, K.; Zetterberg, H.; Höglund, K. Alpha-Synuclein Protofibrils in Cerebrospinal Fluid: A Potential Biomarker for Parkinson's Disease. J Parkinsons Dis **2020**, 10 (4), 1429-1442.
(9) Vetri, V.; D'Amico, M.; Foderà, V.; Leone, M.; Ponzoni, A.; Sberveglieri, G.; Militello, V. Bovine Serum Albumin protofibril-like aggregates formation: Solo but not simple mechanism. Archives of Biochemistry and Biophysics **2011**, 508 (1), 13-24.
(10) Szymaszek, P.; Fiedor, P.; Chachaj-Brekiesz, A.; Tyszka-Czochara, M.; Świergosz, T.; Ortyl, J. Molecular interactions of bovine serum albumin (BSA) with pyridine derivatives as candidates for non-covalent protein probes: aspectroscopic investigation. Journal of Molecular Liquids **2022**, 347, 118262, 1-36.
(11) Siddiqui, S.; Ameen, F.; ur Rehman, S.; Sarwar, T.; Tabish, M. Studying the interaction of drug/ligand with serum albumin. Journal of Molecular Liquids **2021**, 336, 116200.
(12) Kundu, S.; Banerjee, C.; Sarkar, N. Inhibiting the Fibrillation of Serum Albumin Proteins in the Presence of Surface Active Ionic Liquids (SAILs) at Low pH:

Spectroscopic and Microscopic Study. The Journal of Physical Chemistry B **2017**, 121 (32), 7550-7560.
(13) Mukhopadhyay, A.; Stoev, I. D.; King, D. A.; Sharma, K. P.; Eiser, E. Amyloid-Like Aggregation in Native Protein and its Suppression in the Bio-Conjugated Counterpart. Frontiers in Physics **2022**, 10, 924864, 1-12.
(14) Sedov, I.; Khaibrakhmanova, D. Molecular Mechanisms of Inhibition of Protein Amyloid Fibril Formation: Evidence and Perspectives Based on Kinetic Models. International Journal of Molecular Sciences **2022**, 23 (21), 13428.
(15) Alam, D.; Naaz, F.; Islam, A.; Sardar, M.; Ahmad, T. Role of sugar osmolytes and their nano-counterparts as inhibitors in protein fibrillation. Journal of Molecular Liquids **2023**, 386, 122479, 1-11.
(16) Nguyen, Y. T.; Kim, N.; Lee, H. J. Metal Complexes as Promising Matrix Metalloproteinases Regulators. International Journal of Molecular Sciences **2023**, 24 (2), 1258, 1-16.
(17) Păunescu, E.; Boubaker, G.; Desiatkina, O.; Anghel, N.; Amdouni, Y.; Hemphill, A.; Furrer, J. The quest of the best – A SAR study of trithiolato-bridged dinuclear Ruthenium(II)-Arene compounds presenting antiparasitic properties. European Journal of Medicinal Chemistry **2021**, 222, 113610, 1-36.
(18) Ngoepe, M.; Clayton, H. Metal Complexes as DNA Synthesis and/or Repair Inhibitors: Anticancer and Antimicrobial Agents. Pharmaceutical Fronts **2021**, 03, e164-e182.
(19) Banerjee, P.; Mukherjee, D.; Maiti, T. K.; Sarkar, N. Unveiling the Self-Assembling Behavior of 5-Fluorouracil and its N,N′-Dimethyl Derivative: A Spectroscopic and Microscopic Approach. Langmuir **2017**, 33 (41), 10978-10988.
(20) Stella, V. Pro-drugs: An Overview and Definition. In Pro-drugs as Novel Drug Delivery Systems, ACS Symposium Series, Vol. 14; AMERICAN CHEMICAL SOCIETY, 1975; pp 1-115.
(21) Burgos-Morón, E.; Abad-Jiménez, Z.; Marañón, A. M.; Iannantuoni, F.; Escribano-López, I.; López-Domènech, S.; Salom, C.; Jover, A.; Mora, V.; Roldan, I.; Solá, E.; Rocha, M.; Víctor, V.M. Relationship Between Oxidative Stress, ER Stress, and Inflammation in Type 2 Diabetes: The Battle Continues. J Clin Med **2019**, 8 (9), 1-22.
(22) Yang, Y.; Weaver, M. N.; Merz, K. M., Jr. Assessment of the "6-31+G** + LANL2DZ" mixed basis set coupled with density functional theory methods and the effective core potential: prediction of heats of formation and ionization potentials for first-row-transition-metal complexes. J Phys Chem A **2009**, 113 (36), 9843-9851.
(23) Maikoo, S.; Booysen, I. N.; Xulu, B.; Rhyman, L.; Ramasami, P. Stabilization of the ruthenium (II) and -(III) centres by chelating N-donor ligands: Synthesis, characterization, biomolecular affinities and computational studies. Journal of Molecular Structure **2021**, 1244, 130986, 1-14.
(24) Maikoo, S.; Xulu, B.; Mambanda, A.; Mkhwanazi, N.; Davison, C.; de la Mare, J. A.; Booysen, I. N. Biomolecular interactions of cytotoxic ruthenium compounds with thiosemicarbazone or benzothiazole Schiff base chelates. ChemMedChem **2022**, 17 (20),1-15.
(25) Schneider, C. A.; Rasband, W. S.; Eliceiri, K. W. NIH Image to ImageJ: 25 years of image analysis. Nature Methods **2012**, 9 (7), 671-675.

(26) Booysen, I. N.; Maikoo, S.; Piers Akerman, M.; Xulu, B.; Munro, O. Ruthenium(II/IV) complexes with potentially tridentate Schiff base chelates containing the uracil moiety. Journal of Coordination Chemistry **2013**, 66 (20), 3673-3685.
(27) Ismail, M. B.; Booysen, I. N.; Akerman, M. P.; Grimmer, C. Rhenium(I) complexes with bidentate carbohydrazide Schiff bases: Synthesis, characterization, computational and DNA interaction studies. Journal of Organometallic Chemistry **2017**, 833, 18-27.
(28) Yousif, Y.; Al-Rawi, J. High-resolution 1H NMR spectra of bis(2,2′-bipyridine)(4,4′-dialkyl-2,2′-bipyridine) ruthenium(II) salts. Polyhedron **1992**, 11, 1411–1418.
(29) Vijayapritha, S.; Viswanathamurthi, P. New half-sandwich (η6-p-cymene)ruthenium(II) complexes with benzothiazole hydrazone Schiff base ligand: Synthesis, structural characterization and catalysis in transamidation of carboxamide with primary amines. Journal of Organometallic Chemistry **2020**, 929, 121555.
(30) Koz, G.; Özdemir, N.; Astley, D.; Dinçer, M.; Astley, S. T. Synthesis, spectroscopic and structural characterization of cobalt(II) complex with uracil-containing 2,6-diformylpyridine ligand: Theoretical studies on the ligand and pentagonal-bipyramidal [Co(L)(H2O)2]2+ and [Zn(L)(H2O)2]2+ cations. Journal of Molecular Structure **2010**, 966 (1), 39-47.
(31) Nolin, B.; Jones, R. N. The Infrared Absorption Spectra of Diethyl Ketone and its Deuterium Substitution Products. Journal of the American Chemical Society **1953**, 75 (22), 5626-5628
(32) Mehrani, S.; Tayyari, S. F.; Heravi, M.; Morsali, A. Vibrational spectra, normal coordinate analysis, and structure of keto form of acetylacetone. A DFT approach. Egyptian Journal of Chemistry **2019**.1868. Mines, G. W.; Thompson, H. Infrared and Photoelectron Spectra, and Keto-Enol Tautomerism of Acetylacetones and Acetoacetic Esters. Proceedings of the Royal Society of London Series A **1975**, 342, 327-339.
(33) Liu, B.; Jabed, M. A.; Kilina, S.; Sun, W. Synthesis, Photophysics, and Reverse Saturable Absorption of trans-Bis-cyclometalated Iridium(III) Complexes (C^N^C)Ir(R-tpy)+ (tpy = 2,2′:6′,2″-Terpyridine) with Broadband Excited-State Absorption. Inorganic Chemistry **2020**, 59 (12), 8532-8542.
(34) Maikoo, S.; Chakraborty, A.; Vukea, N.; Dingle, L. M. K.; Samson, W. J.; de la Mare, J.-A.; Edkins, A. L.; Booysen, I. N. Ruthenium complexes with mono- or bis-heterocyclic chelates: DNA/BSA binding, antioxidant and anticancer studies. Journal of Biomolecular Structure and Dynamics **2021**, 39 (11), 4077-4088.
(35) Miar, M.; Shiroudi, A.; Pourshamsian, K.; Oliaey, A.; Hatamjafari, F. Theoretical investigations on the HOMO–LUMO gap and global reactivity descriptor studies, natural bond orbital, and nucleus-independent chemical shifts analyses of 3-phenylbenzo[d]thiazole-2(3 H)-imine and its para -substituted derivatives: Solvent and substituent effects. Journal of Chemical Research **2020**, 45, 174751982093209.
(36) Homocianu, M.; Airinei, A.; Dorohoi, D. O.; Olariu, I.; Fifere, N. Solvatochromic effects in the UV/vis absorption spectra of some pyridazinium ylides. Spectrochimica Acta Part A: Molecular and Biomolecular Spectroscopy **2011**, 82 (1), 355-359.
(37) Singh, V.; Fedeles, B. I.; Essigmann, J. M. Role of tautomerism in RNA biochemistry. Rna **2015**, 21 (1), 1-13.

(38) San Tan, S.; Yanagisawa, S.; Inagaki, K.; Morikawa, Y.; Kassim, M. B. Augmented pH-sensitivity absorbance of a ruthenium(ii) bis(bipyridine) complex with elongation of the conjugated ligands: an experimental and theoretical investigation. Physical Chemistry Chemical Physics **2017**, 19 (37), 25734-25745.
(39) Hanif, M.; Nazarov, A.; Hartinger, C. Synthesis of [Ru-II(eta(6)-p-cymene)(PPh3)(L)Cl]PF6 complexes with carbohydrate-derived phosphites, imidazole or indazole co-ligands. Inorganica Chimica Acta - INORG CHIM ACTA **2012**, 380, 211-215.
(40) Soh, C.; Kollipara, M. R.; Banothu, V.; Diengdoh, D. F.; Kaminsky, W.; Rymmai, E. K. Synthesis and molecular structure of arene ruthenium(II) complexes containing benzhydrazone derivative ligands with antibacterial and antioxidant properties. Journal of Molecular Structure **2022**, 1269, 133775.
(41) Kumari, M.; Bera, S. K.; Lahiri, G. K. Noninnocence of the deprotonated 1,2-bis((1H-pyrrol-2-yl)methylene)hydrazine bridge in diruthenium frameworks – a function of co-ligands. Dalton Transactions **2021**, 50 (28), 9891-9903.
(42) Ascone, I.; Messori, L.; Casini, A.; Gabbiani, C.; Balerna, A.; Dell'Unto, F.; Congiu, A. Exploiting Soft and Hard X-Ray Absorption Spectroscopy to Characterize Metallodrug/Protein Interactions: the Binding of [trans -RuCl 4 (Im)(dimethylsulfoxide)][ImH] (Im = imidazole) to Bovine Serum Albumin. Inorganic Chemistry - INORG CHEM **2008**, 47, 8629-8634.
(43) Garg, P.; Kaur, G.; Chaudhary, G. R.; Kaur, S.; Gawali, S. L.; Hassan, P. A. Investigating the structural integrity of Bovine serum albumin in presence of newly synthesized metallosurfactants. Colloids Surf B Biointerfaces **2018**, 164, 116-124.
(44) Topală, T.; Bodoki, A.; Oprean, L.; Oprean, R. Bovine Serum Albumin Interactions with Metal Complexes. Clujul Med **2014**, 87 (4), 215-219.
(45) Ali, M. S.; Muthukumaran, J.; Jain, M.; Tariq, M.; Al-Lohedan, H. A.; Al-Sanea, A. S. S. Detailed Experimental and In Silico Investigation of Indomethacin Binding with Human Serum Albumin Considering Primary and Secondary Binding Sites. Molecules **2023**, 28 (7), 2979, 1-19.
(46) Barbaro, B.; Kuechle, J.; Salehi, P.; Rodriguez, L.; Qi, M.; Gangemi, A.; Benedetti, E.; Oberholzer, J. Increased albumin concentration reduces apoptosis and improves functionality of human islets. Artif Cells Blood Substit Immobil Biotechnol **2008**, 36 (1), 74-81. Zoellner, H.; Hou, J. Y.; Lovery, M.; Kingham, J.; Srivastava, M.; Bielek, E.; Vanyek, E.; Binder, B. R. Inhibition of microvascular endothelial apoptosis in tissue explants by serum albumin. Microvasc Res **1999**, 57 (2), 162-173. Kakinen, A.; Javed, I.; Faridi, A.; Davis, T. P.; Ke, P. C. Serum albumin impedes the amyloid aggregation and hemolysis of human islet amyloid polypeptide and alpha synuclein. Biochimica et Biophysica Acta (BBA) - Biomembranes **2018**, 1860 (9), 1803-1809.
(47) Bhatti, J. S.; Sehrawat, A.; Mishra, J.; Sidhu, I. S.; Navik, U.; Khullar, N.; Kumar, S.; Bhatti, G. K.; Reddy, P. H. Oxidative stress in the pathophysiology of type 2 diabetes and related complications: Current therapeutics strategies and future perspectives. Free Radical Biology and Medicine **2022**, 184, 114-134.
(48) Mabuza, L. P.; Gamede, M. W.; Maikoo, S.; Booysen, I. N.; Ngubane, P. S.; Khathi, A. Amelioration of risk factors associated with diabetic nephropathy in diet-induced pre-diabetic rats by an uracil-derived diimine ruthenium(II) compound. Biomedicine & Pharmacotherapy **2020**, 129, 110483, 1-7.

(49) Ramachandran, R.; Viswanathamurthi, P. Ruthenium(II) carbonyl complexes containing pyridine carboxamide ligands and PPh3/AsPh3/Py coligands: Synthesis, spectral characterization, catalytic and antioxidant studies. Spectrochimica acta. Part A, Molecular and biomolecular spectroscopy **2012**, 103C, 53-61.
(50) Sharma, L. G.; Pandey, L. M. Thermomechanical process induces unfolding and fibrillation of bovine serum albumin. Food Hydrocolloids **2021**, 112, 106294.
(51) Chan, T. G.; Ruehl, C. L.; Morse, S. V.; Simon, M.; Rakers, V.; Watts, H.; Aprile, F. A.; Choi, J. J.; Vilar, R. Modulation of amyloid-β aggregation by metal complexes with a dual binding mode and their delivery across the blood-brain barrier using focused ultrasound. Chem Sci **2021**, 12 (27), 9485-9493.
(52) Maikoo, S.; Makayane, D.; Booysen, I. N.; Ngubane, P.; Khathi, A. Ruthenium compounds as potential therapeutic agents for type 2 diabetes mellitus. European Journal of Medical Chemistry **2021**, 213, 113064.
(53) Alberti, E.; Zampakou, M.; Donghi, D. Covalent and non-covalent binding of metal complexes to RNA. J Inorg Biochem **2016**, 163, 278-291.
(54) Ma, L.; Fu, Y.; Yu, L.; Li, X.; Zheng, W.; Chen, T. Ruthenium complexes as inhibitors of human islet amyloid polypeptide aggregation, an effect that prevents beta cell apoptosis. RSC Advances **2015**, 5 (23), 17405-17412. Bacac, M.; Hotze, A. C. G.; Schilden, K. v. d.; Haasnoot, J. G.; Pacor, S.; Alessio, E.; Sava, G.; Reedijk, J. The hydrolysis of the anti-cancer ruthenium complex NAMI-A affects its DNA binding and antimetastatic activity: an NMR evaluation. Journal of Inorganic Biochemistry **2004**, 98 (2), 402-412.He, L.; Wang, X.; Zhao, C.; Wang, H.; Du, W. Ruthenium complexes as novel inhibitors of human islet amyloid polypeptide fibril formation. Metallomics : integrated biometal science **2013**, 5(12), 1599-603.

Chapter 5

Encapsulation of anti-diabetic ruthenium(II) uracil compounds into chitosan (CS)-polyvinyl alcohol (PVA) electrospun nanofibers: Nanofabrication, characterization and desorption kinetics

5.1 Introduction

Insulin injection is the mainstream therapy for diabetes management but patients often develop insulin resistance after prolonged use of this hormone.[1] Plausible alternative medicines are orally-administered anti-diabetic drugs such as metformin which has a unique mechanism of action that enhances insulin for effective glucose metabolism. However, prolonged use of this drug generally leads to gastrointestinal discomfort.[2] Prior studies have shown that the hormone or orally administered drugs can be embedded into transdermal patches or biocompatible bulk drug delivery platforms.[3, 4]

Most medicinal treatments, especially for chronic diseases, require miniaturized drug delivery systems (DDS) that are biocompatible, ameliorate toxicity, encourage oral drug administration and at the same time enhance drug efficacy through target and controlled release of the shuttled drug at the site of action.[5] One way of achieving high drug payload DDSs is to convert bulk polymer preloaded with the drugs into electrospun nanofibers (drug embedded-ENFs) with the main aim of enhancing drug bioavailability at a controlled rate. These ENF DDSs have numerous functional advantages including, tuneable aqueous solubility, high surface-to-volume ratios, adjustable porosities and the ability to encapsulate a wide range of drugs. In addition, these nanocomposites are designed to possess the ability to release the drug at the target site and on-demand as well with accompanying low toxicity due to the biodegradable polymers.[6] In addition, the desorption kinetics of the embedded drugs from the ENFs can potentially be manipulated through alteration of their polymeric consituents.[7]

More specifically, ENFs comprising polyvinyl alcohol (PVA) and chitosan (CS) polymer blends have served as attractive DDS for pharmaceuticals such as antibiotics, chemotherapeutic, and anti-diabetic agents.[8] The preference of these polymers over others as DDS constituents is attributed to their lower cost and superior drug absorption capacity, biocompatibility as well as gradual physiological biodegradability. [9] Blended PVA-CS ENFs (comprising both PVA and CS) have been prepared using various techniques, such as melt-blowing and solvent casting. With the aid of electrospinning, it is anticipated that higher yields of PVA-CS ENFs and fine-tuneability in their properties are more readily achieved. However, prior to pursuing the in vitro and in vivo studies of drug-embedded ENFs as DDSs, it is imperative that a thorough investigation of their physical, and chemical properties and drug-release kinetics be done to gain a complete understanding of how they can influence the targeted delivery and related pharmaceutical applications.[10]

In this chapter, the lead metal complex, [RuCl(PPh$_3$)(H$_3$ucp)] (**1**) (H$_4$ucp = 2,6-bis-((6-amino-3,4-dimethyluracilimino)methylene)pyridine) and bis-uracil derivatives: cis-[Ru(bipy)$_2$(urdp)]Cl2 (**2**) (urdp = 2,6-bis-((uracilimino)methylene)pyridine), trans-[RuCl$_2$(PPh$_3$)(urdp)] (**3**), and cis-[Ru(bpy)2(H4ucp)](PF6)^2 (**4**) as well as its mono-uracil analogues: [(η^6-p-cymene)Ru^{II}(L)Cl] (L = urpda = 5-((pyridin-2-yl)methyleneamino)-6-aminouracil) for **5** urdpy = 6-amino-1,3-dimethyl-5-((pyridin-2-ylmethylene)amino)uracil) for **6**, trans-[RuII(L)(PPh$_3$)Cl$_2$] (L = urpda for **7**), cis-[RuII(L)(bipy)2] (L = urpy = 5-((pyridin-2-yl)methyleneamino)uracil) for **8** and H2dadp = 5,6-diaminouracil for **9**), and [(η6-p-cymene)RuII(L)Cl] (L= urqd = 5-((quinolin-2-yl)methyleneamino)-6-aminouracil) for **10**), were embedded into PVA-CS ENFs via electrospinning. The resultant Ru-CS-PVA ENFs nanocomposites were characterized by Scanning Electron Microscopy - X-ray Photon Energy Dispersive (SEM-EDX), powder X-ray diffraction (PXRD), and Fourier transform infrared spectroscopy (FTIR) techniques. The rate of drug release as well as the release efficiency was evaluated by UV-Vis absorption spectrophotometry.

5.2 Experimental

5.2.1 Fabrication of Ru-CS-PVA ENFs

A solution of 1% weight-to-volume (w/v) CS was made by dissolving 0.20 g of CS in 20.00 mL of acetic acid (90%, v/v) and the mixture was left to stir overnight at 60 °C. Similarly, 6.0 g of PVA was homogenized in 50.00 mL (12 w/v %) deionized water by stirring it for 4 h. The composition of CS and PVA for optimum electrospinning was pre-determined by electrospinning trial mixtures comprising 90:10, 80:20, and 70:30 volume ratios of the 1% CS/12%PVA solution. The best aspect ratios for the trial ENF mats was for the 70:30 1%CS/12%PVA mixture, and this mixture was applied to the electrospinning of Ru(**1-10**)-embedded CS-PVA ENFs as described ahead.

For the nanofabrication of the ENFs of **1-10**, approximately 10 mg of the respective complexes **1 - 10** was first dispersed into 10.00 mL of the 1% CS solution. It was then added to 10.00 mL of the (70:30) 1% CS/12% PVA and the resultant solution was stirred for 12 h to yield a **1 - 10** loading of 0.1%(w/v). An aliquot (10 mL) of **1 - 10** in the CS-PVA bulk polymer solution was placed in a syringe that was secured to a pump of the Inovenso NE300 electrospinning instrument. Then, the bulk polymer solution of **1 - 10** was pumped at a rate of 1.2 mL/h into the spinneret which was set at an emitting voltage of 35 kV voltage relative to the ground. During the electrospinning process, the distance between the collector unit and the spinneret was maintained fixed and within 9 – 12 cm. The individual Ru-CS-PVA - electrospun nanofiber (Ru-CS-PVA ENFs) of **1 - 10** were collected on an aluminum foil that was electrically grounded to a stationary flat collector unit. Residual solvent was removed by drying the Ru-CS-PVA ENFs of **1 - 10** under vacuum for 24 h at 60° C.[20]

5.2.2 Hydration and swelling capacity of Ru-CS-PVA ENFs of **1 - 10**

A mass of 0.042 ± 0.001 g of the individual pre-dried Ru-CS-PVA ENFs was added to separate 10.00 mL aqueous solutions of PBS buffers of pH values of 1.5 and 7.4, respectively, and left to equilibrate for one day. The hydrated Ru-CS-PVA ENFs were vacuum-dried thoroughly and reweighed. The capacity of the Ru-CS-PVA ENFs was calculated according to Equation (A), where, m_i is the initial mass before dispersion and m_f is the dried and reweighed mass of hydrated Ru-CS-PVA ENF.[21]

$$\text{Swelling capacity} = \frac{m_f}{m_i} - 1 \qquad (\mathbf{A})$$

5.2.3 Release rates and efficiency of **1-10** from respective Ru-CS-PVA ENFs

To determine the rate of release of the encapsulated ruthenium(II) complexes, **1 - 10** from the Ru-CS-PVA ENFs, the temporal (real time) concentration of **1 – 10** in a 2% (v:v) DMSO: PBS solution, adjusted to pHs of 1.5 and 7.4 were estimated from their respective overlay UV-visible absorption spectra (MLCT band) recorded over 1 h (at pH 1.5 at 5 min intervals) and 24 h (at pH 7.4 at one-hour intervals), respectively. The 2% DMSO component was included to enhance aqueous of **1 – 10**. The real-time equilibrium concentration of **1 - 10** at each pH, and absorbances at t = 0 and 24 h were substituted in the predetermined calibration equation made at λ_{max} of the MLCT absorption band of the respective complexes, **1 - 10** from the Ru-CS-PVA ENFs. The releasing rate (RR) and % releasing efficiency (RE) of complexes **1 – 10**, were calculated from equations **2** and **3.**

$$\text{RR} = \frac{c_t - c_O}{t} \qquad (\mathbf{B})$$

$$\text{RE} = \frac{c_{24h} - c_O}{c_{thrt.}} \text{x } 100\% \qquad (\mathbf{C})$$

where c_O, c_t and $c_{thrt.}$ are the equilibrium concentrations, [**1 - 10**] at the onset, and after t

h incubation (determined from respective calibration equations and theoretical concentration at full release, respectively.[22]

5.3 Results and discussion

5.3.1 Nanofabrication and characterization.

Nanoconjugates of Ru(**1 – 10**)-CS-PVA ENFs designed to serve as DDSs for **1 – 10** were fabricated. Under the optimum electrospinning instrumental parameters (viz. polymer flowrate, voltage supply, and distance between collector unit and spinneret) and polymer solution parameters (attained from the varying volume ratios of the 1% CS and 12% PVA), the PVA-CS ENFs were fabricated. In particular, the optimal instrumental parameters were a voltage of 35 kV, a polymer flowrate of 0.5 mL/h, and a distance between the collector unit and the spinneret of 9 cm, in **Figure 5.1** optimal distance is 9 cm. A 70:30 volume-to-volume ratio of 1% CS and 12% PVA (as the bulk polymer blend for electrospinning) presented the best aspect ratios (the smallest average diameter (116 nm ± 232) and non-beaded-woven ENFs) as shown in the micrograph of **Figure 5.1**.

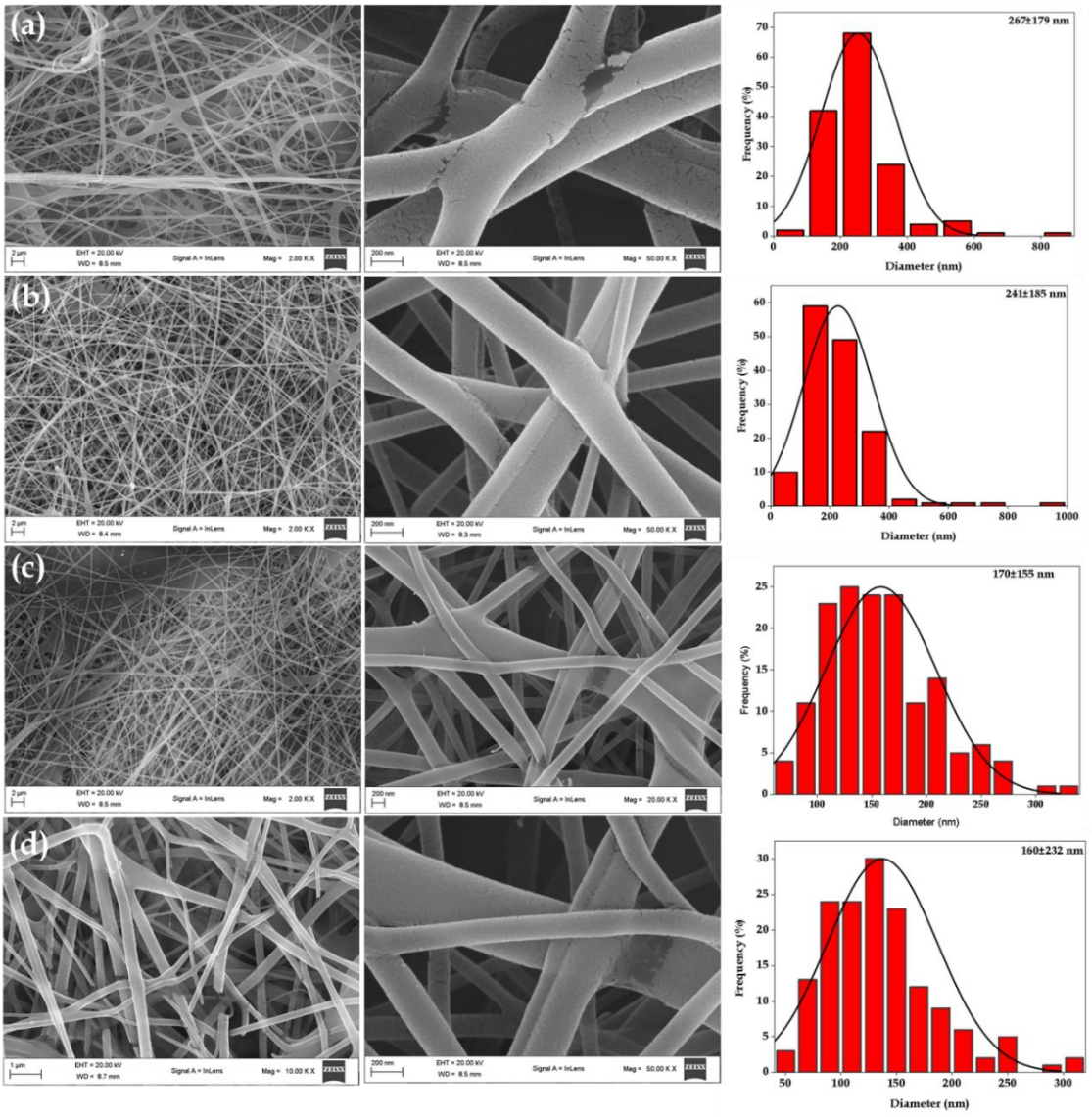

Figure 5. 1: *SEM images for hollow (without the Ru complex) PVA-CS ENFs and respective diameter distribution graphs fabricated from polymer blends of variable volume ratios (12%PVA: 1% CS): (a) 100: 0, (b) 90: 10, (c) 80: 20 and (d) 70: 30 at a high voltage of 35 kV and a 9 cm spinneret-to-collector unit distance.*

Although the SEM characterization data cannot concretely delineate the interactions between **1 – 10** and the other constituents of ENFs, it is presumed that the kinetically inert metal complexes **2**, **4**, **8** and **9** predominately interact constituents of the polymer blend

through their respective polar uracil functional groups and pi-conjugated systems with those complementary polymeric features of the CS-PVA ENFs. Based on the fact that the ruthenium complexes **1**, **2**, **5 - 7** and **10** are susceptible to ligand substitution, it can be deduced that these metal complexes can exhibit the same intermolecular interactions as the chemically inert metal complexes[11]; in addition weak covalent bonding is possible, whereby the labile ligands of these metal complexes are substituted by the nucleophilic donor atoms of the PVA and CS constituents of the nanocomposite forming hemilabile intermediates within the DDSs.[12] It is important to recognize bonding strength of both the inorganic and the polymer constituents will predominately dictate the dissolution rates of the prospective anti-diabetic drugs (**1 – 10**) from the nanocomposites.[13]

It is evident in **Figure 5.1**, that as the composition of CS within the PVA-CS ENFs increases, there is a progressive decrease in the hollow (without the Ru complex)-ENF diameter. Given that CS contains a great proportion of polarized amino and amine groups, in an acetic acid solution, a proportional increase will lead to the gradual lowering of the critical charge density of the bulk polymer blends which leads to faster ejection of the polymer streams and hence narrower diameters.[14] Comparative visual inspections of the micrographs with those comprising only of PVA, reveals that the latter have visible cracks within the ENFs indicative of brittleness and poor polymer elasticity. Thus, the ENFs made from the CS-PVA blend are likely to have better mechanical strength. Furthermore, all subsequent studies were done with the PVA-CS ENFs affording the thinnest diameters and it was hypothesized that these holo-ENFs with the narrowest diameter and hence highest surface area would afford the superior drug-loading capacity.[15]

Introduction of **1 – 10** within the PVA-CS bulk solution affected the polarity as well as viscosity of the respective solutions and their hence electrospinnability. For example, the best aspect ratios for all was at spinneret-to-collector unit distance of 12 cm compares to 9 cm for the holo-ENFs. Also, the morphological features (see **Figure 5.2**) of the nanocomposites differed from that of the PVA-CS ENFs. The inclusion of metal complexes in the PVA-CS blends enhanced conductivity, which led to coalescing of the ENF strands into beads for some nanoconjugates. Since the PVA and CS polymer concentrations have been pre-optimized in the nanofabrication of their ENFs (see micrographs of **Figure 5.2** - **5.3**, the presence of beads within some of the fabricated ENFs can be solely accounted for the embedded metal compound dopants. Furthermore, the expanded bead formations observed within micrographs of nanoconjugates **1**, **7**, and **9** (all bearing labile ligands) suggest the formation of coordinative adducts between their hydrolyzed derivatives and the polymer constituents.

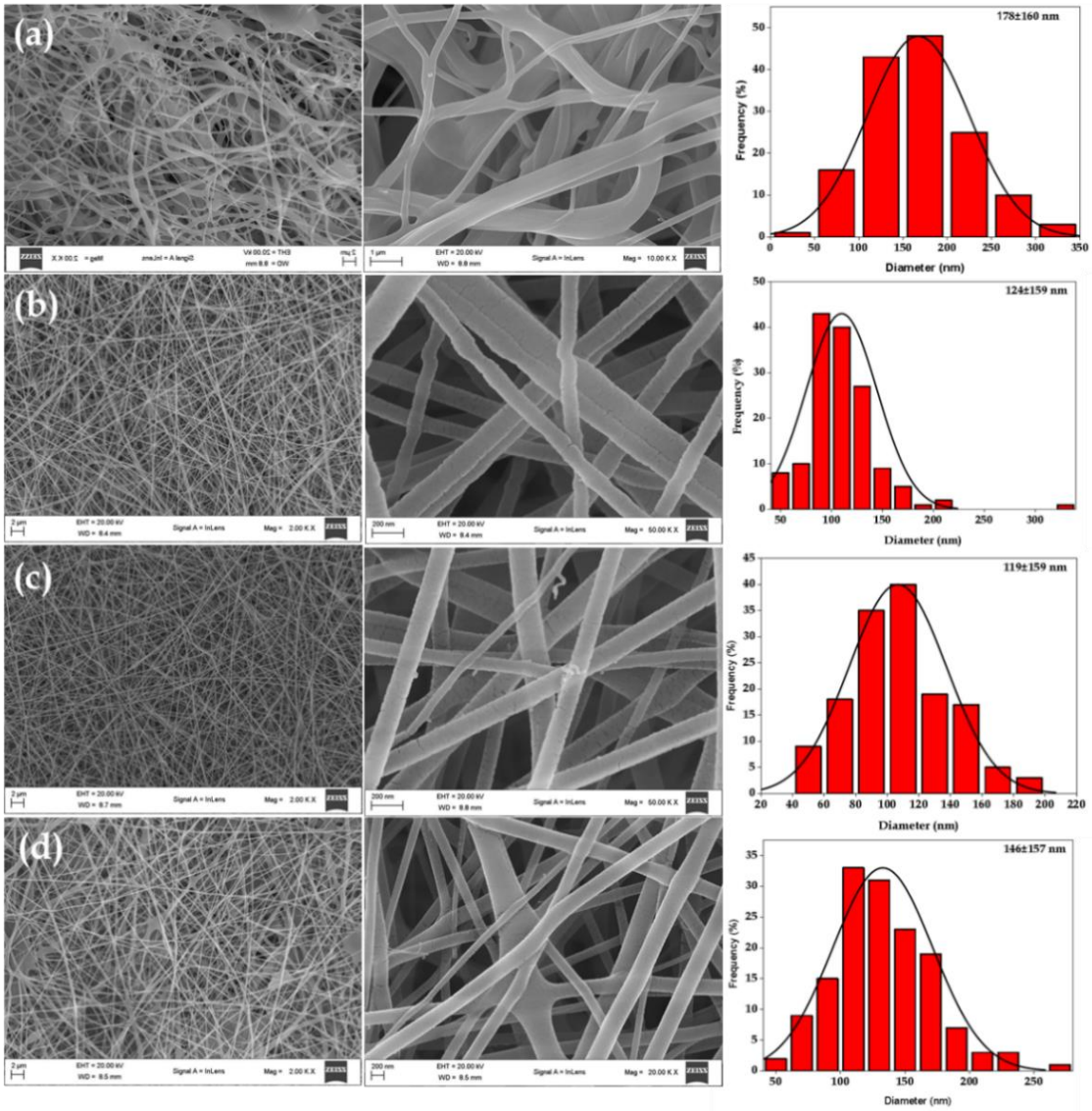

Figure 5. 2: *The SEM images of Ru-CS-PVA ENFs of (a)* ***1****, (b)* ***2****, (c)* ***3****, (d)* ***4*** *and their correlating diameter distribution graphs obtained at spinneret-to-collector a distance of 12 cm and 35 kV.*

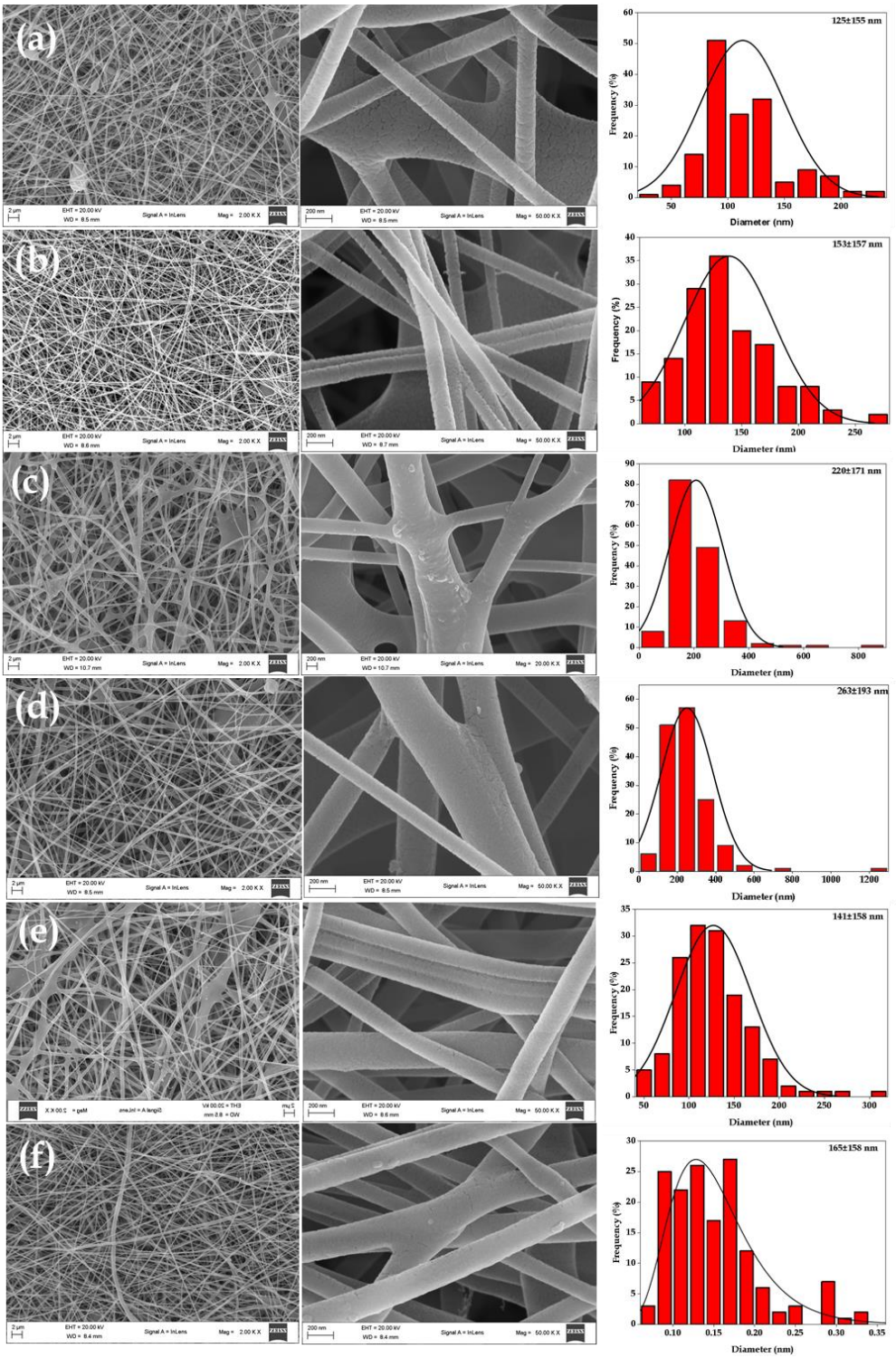

Figure 5. 3: *The SEM micrographs of Ru-CS-PVA-ENFs of (a)* ***5****, (b)* ***6****, (c)* ***7****, (d)* ***8****, (e)* ***9****, (f)* ***10*** *and their corresponding diameter distribution graphs obtained at spinneret-to-collector a distance of 12 cm at 35 kV.*

Overlaid FT-IR spectra of PVA, CS, the individual metal complexes **1 - 10**, and their corresponding nanoconjugates are displayed in **Figures 5.4 – 5.6**. Firstly, the characteristic signals of CH bonds were linked to distinct vibrational bands occurring in the proximity of 2950 cm^{-1} which were common for all materials.[16] Characteristically, the cyclic ether bonds of the CS polymer, CS-PVA ENFs, and their inorganic nanocomposites appear as a broad and intense vibration in the range of 610 -755 cm^{-1}.[17] As the hydroxyl groups are mutual to the CS and PVA polymeric constituents, wide IR stretching bands are found in their FTIR spectra. While the aforementioned analogous signals along with the $\nu(N\text{-}H)_{CS}$ signals appeared in the solid-state infrared spectra, the polymer hydroxyl signals were absent in the FTIR spectra of the metal complexes as expected.[18] Contrastingly, the dominating frequency bands for the solid-state infrared spectra of the metal complexes are the C=O vibrations of the uracil groups. However, these appear as substantially lower intensity signals in the ENFs, which suggests their encapsulation of **1 - 10** and thus suppressed vibrations by the polymer blend constituents. Similarly, the ruthenium-to-nitrogen infrared stretches of the different metal complexes are essentially not observed in the IR spectra of the metal complex nanohybrids. [19]

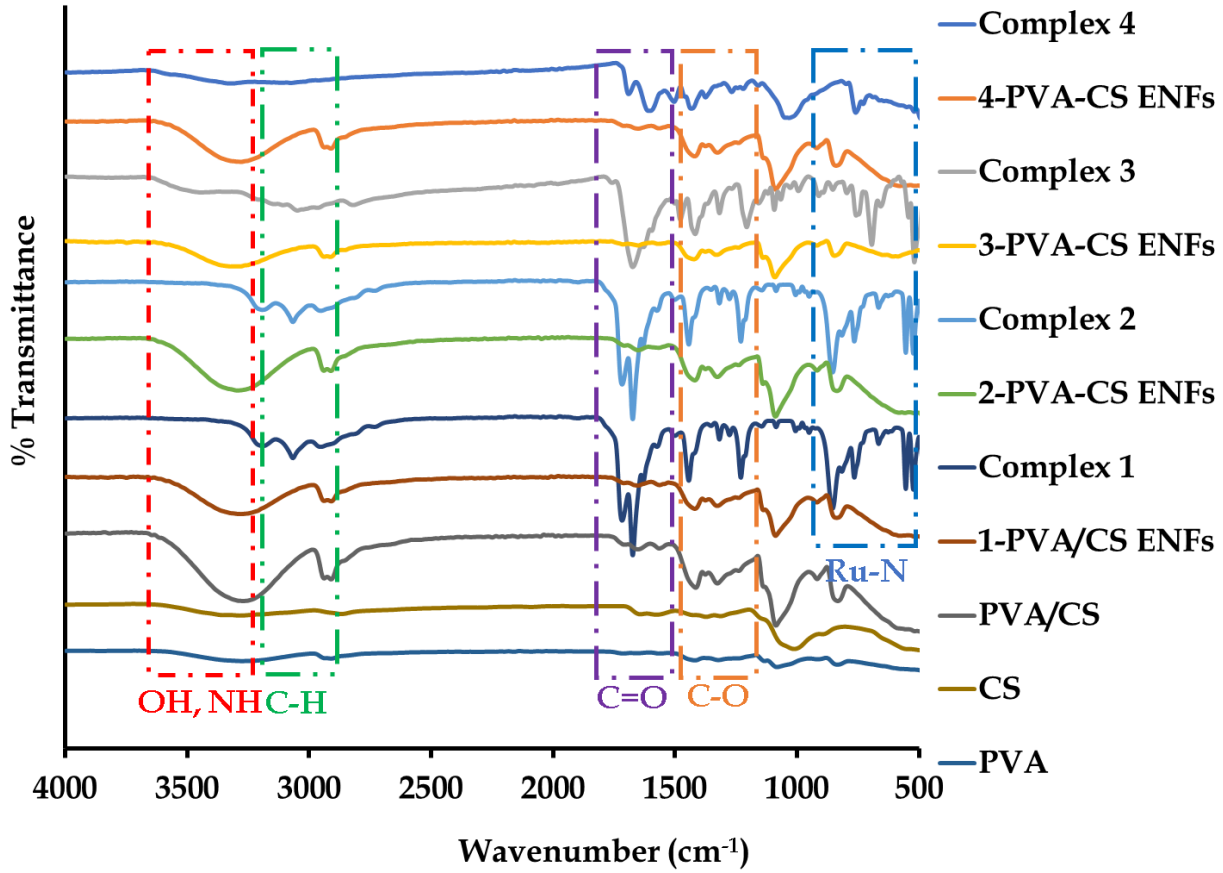

Figure 5. 4: *Overlaid FTIR spectra of PVA, CS, PVA-CS ENFs and Ru-CS-PVA ENFs of* ***1*** *-* ***4*** *electrospun from a (70:30) CS/PVA blend with a (w/v)% Ru loading of 0.1.*

The blending of PVA resulted in a shift in wavenumbers of most vibrational peaks, see **Figures 5.4 – 5.6**. The shift in peaks for the CS-PVA demonstrates the physical transformation of the free components of the blend as well as in the fibrous microstructure of the Ru-CS-PVA NFs of **1 - 10**. For example, blending with PVA leads to a remarkable decrease in the $\nu(NH)_{uracil}$ and $\nu(C=O)_{uracil}$ and intensities of Ru-CS-PVA NFs of **1-10**. This suggests that covalent or hydrogen bonding functional groups of **1 - 10** and polyvinyl acetate groups of PVA and NH groups of CS have occurred. While ν(O-H) for the PVA changed to a higher number, the ν(O-H) of the ENFs was contracted with that of the CS, indicative of the presence of the hydroxyl groups in the ENFs. The O-H peak's intensity for the ENFs also suggested that some hydroxyl groups were partially

hydrogen bonded while others were free, which permitted drug release in a kinetically controlled manner. Moreover, the intensity of the CH group increased noticeably to approximately 2924 cm^{-1}.

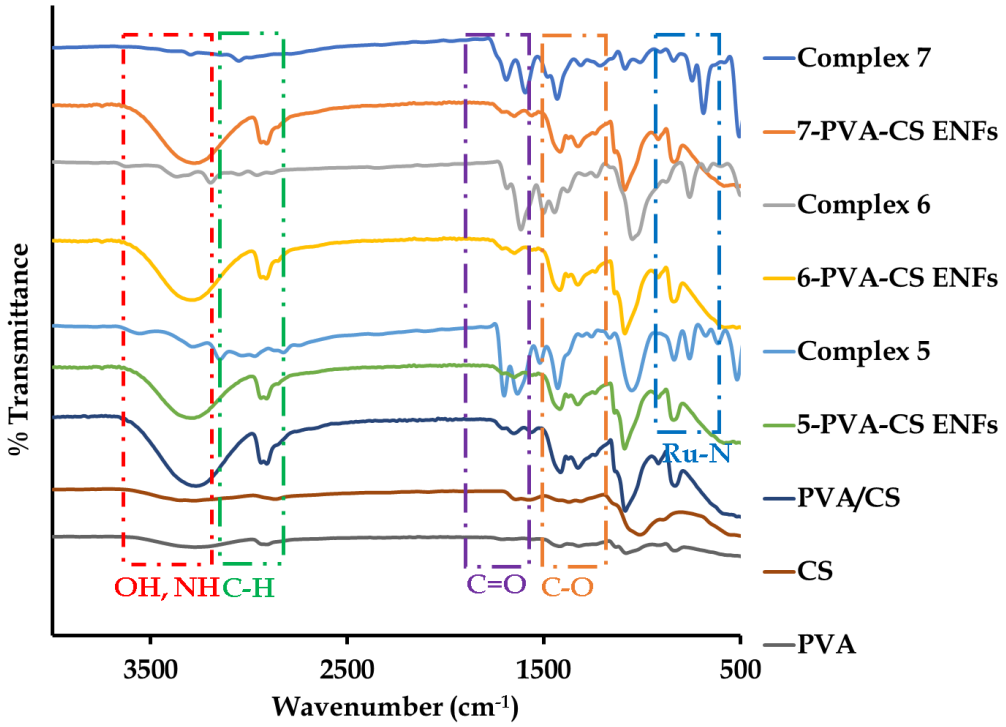

Figure 5. 5: *Overlaid FTIR spectra of PVA, CS, PVA-CS, and Ru-CS-PVA NFs of* **5-7** *electrospun from a (70:30) CS/PVA blend with a (w/v)% Ru loading of 0.1.*

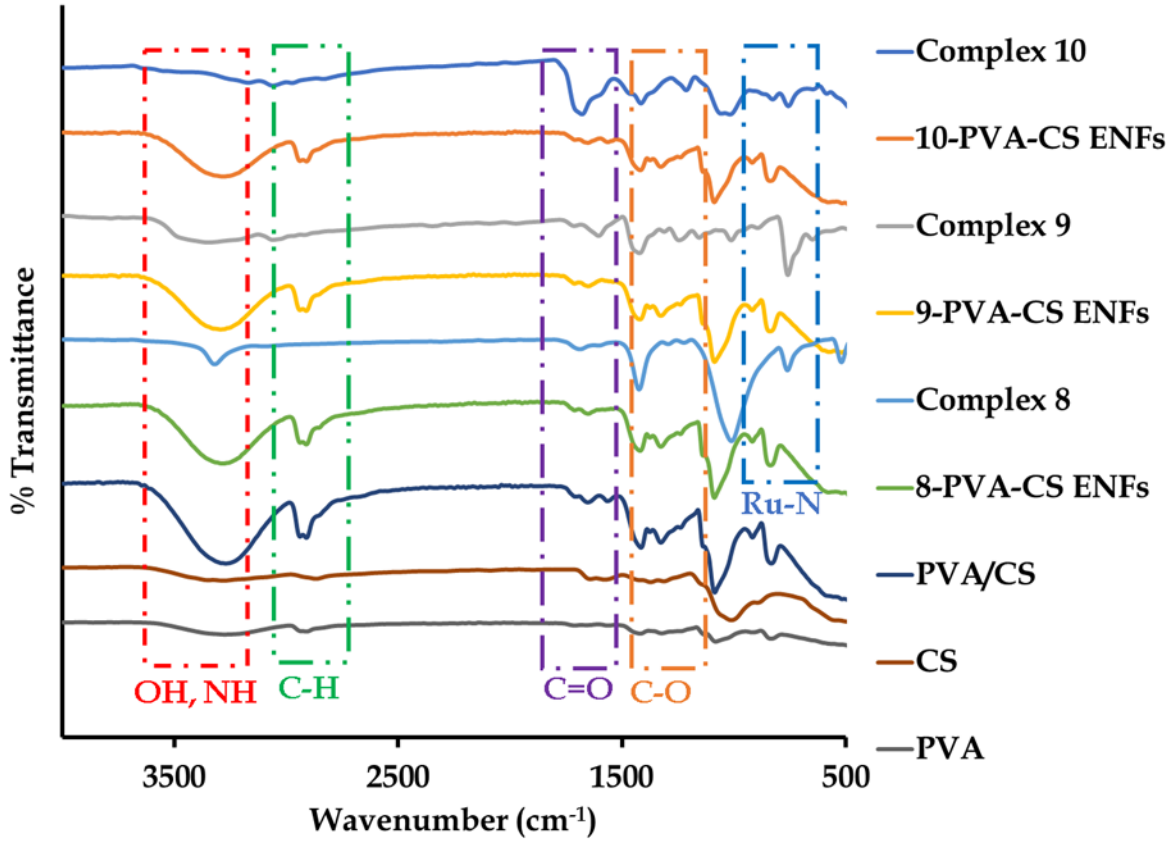

Figure 5. 6: *Overlaid FTIR spectra of PVA, CS, PVA-CS and Ru-CS-PVA NFs of* ***8-10*** *electrospun from a (70:30) CS/PVA blend with a (w/v)% Ru loading of 0.1.*

The peak intensities of the amides and polyvinyl acetates in Ru-CS-PVA ENFs nanomaterials decreased compared to the corresponding functional groups to **1-10**, shifting from 1666 cm^{-1} to 1720 cm^{-1}, following the loading of **1–10** into the polymer blends. This might be attributed to covalent hydrogen bonding. The common peak around 755 cm^{-1} in the spectra of **1–10** (unencapsulated) is characteristic of v(N-Ru-N) vibrational bands of Ru(II) complexes.[20] However, as a result of encapsulation the characteristic spectral bands diminished which is indicative of successful deep entrapment of metal complexes in ENFs matix.

Crystalline materials of **1 - 10** and their ENF blends were analysed using powder X-ray diffraction. Powder XRD diffractograms (PXRDs) of **1 - 10** showed sharp peaks at 2θ values given in **Table 5.1** which depicts typical diffraction patterns of crystalline Ru complexes, see **Figure 5.7**. Furthermore, common 2θ-peaks between 10 - 30° are broader and are thus characteristic of amorphous materials.[21] For instance, a peak appearing within PXRDs at 19.02° (for PVA-CS only) is slightly shifted in the Ru-CS-PVA ENFs to 20.02° for (**1**), 19.54° for (**2**), 19.37° for **3**, 19.36° for **4**, 19.54° for **5**, 19.37° for **6**, 19.42° for **7**, 19.56° for **8**, 19.06° for **9**, and 19.33° for **10** see **Figure 5.8**. The PVA-CS ENFs peaks decreased in intensities in the Ru-CS-PVA ENFs of **1 - 10**, indicating the formation of intra- and intermolecular hydrogen bonds between the functional group of the polymer blend and the ligands of the complexes **1 - 10** during the electrospinning process.[14] The absence of any distinctive peaks associated with the metal complexes in Ru-CS-PVA ENFs is indicative of the encapsulation of the metal complexes in the polymer matrix of the ENFs. The PXRD data confirm the amorphous nature of the Ru-CS-PVA ENFs in which the inorganic complexes are randomly distributed within the CS-PVA ENFs matrix.[22]

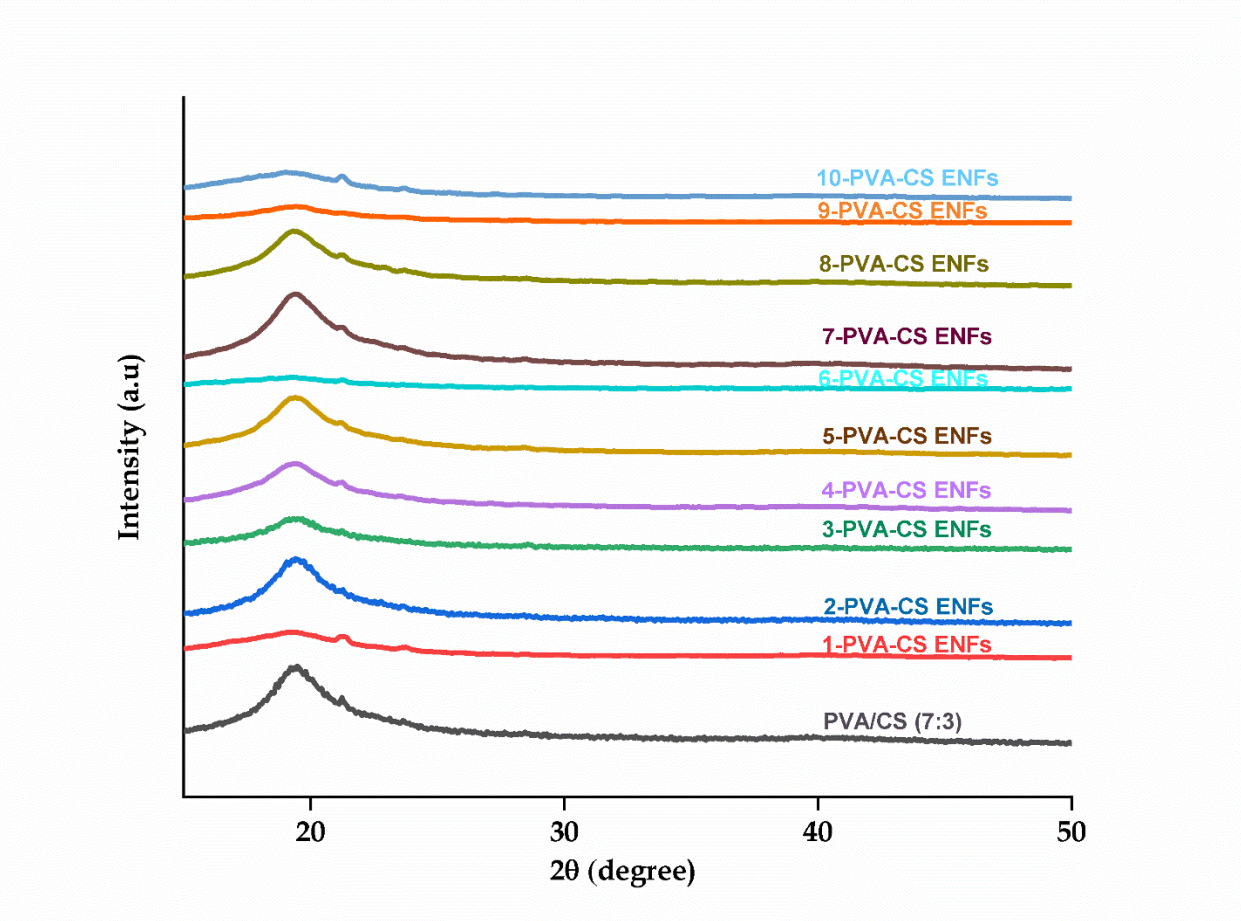

Figure 5. 7: *X-ray diffraction pattern of Ru-CS-PVA ENFs of* ***1-10****, electrospun from a (70:30) CS/PVA blend with a (w/v)% Ru loading of 0.1%.*

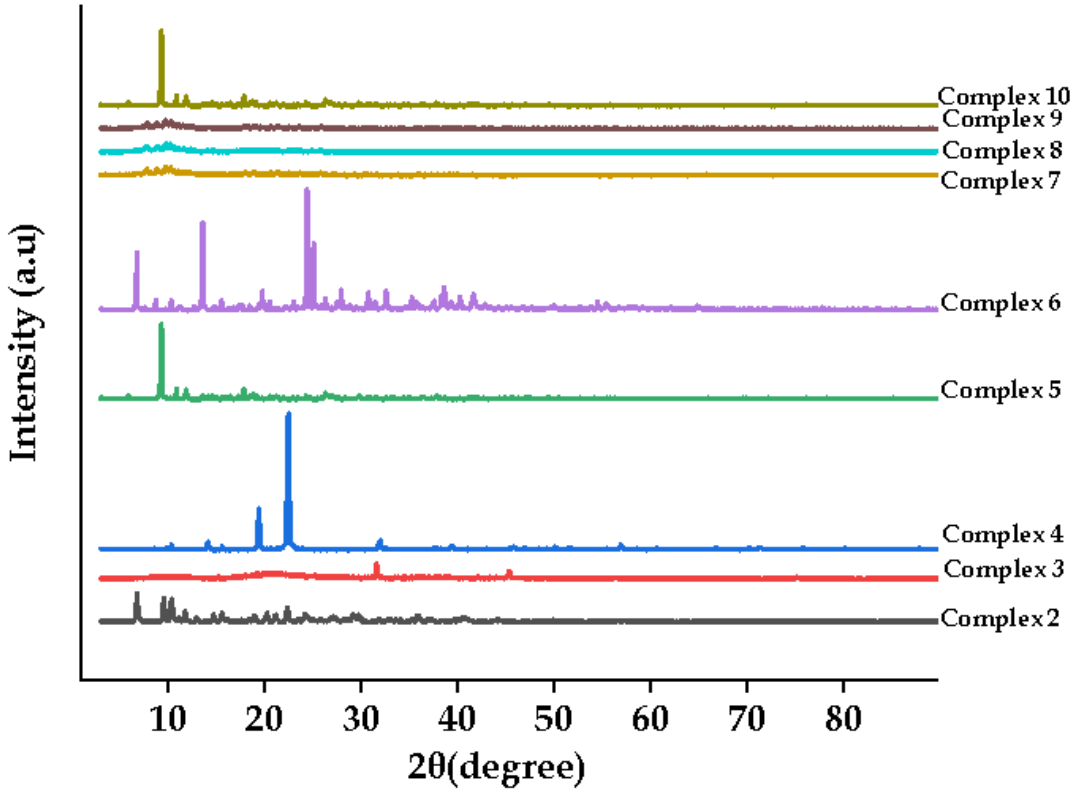

Figure 5. 8: *PXRDs of* ***2*** *-* ***10****.*

Table 5. 1: *The corresponding (2θ °) diffraction peaks of* ***2*** *-* ***10****.*

2	**3**	**4**	**5**	**6**	**7**	**8**	**9**	**10**
6.87	14.37	14.11	9.61	9.18	7.65	8.69	7.98	8.85
9.43	19.11	19.77	11.01	10.93	8.86	9.11	9.47	11.18
10.72	22.14	23.62	12.53	11.97	10.08	10.26	10.67	12.17
12.19	32.17	32.32	13.18	17.81	19.90	13.96	14.86	14.06
14.84	38.56	39.41	17.80	19.15	29.11	19.12	17.95	19.02
15.39	37.77	50.56	18.90	21.03	31.75	25.04	20.28	21.32
18.39	45.65	57.22	21.37	26.62	40.68	39.51	25.78	27.36
22.15	56.36		26.63	30.03			40.43	30.13
24.33	79.37		30.11	38.32				36.79
27.30			37.18	41.77				38.93
29.68								42.22
36.58								
40.38								

5.3.3 Hydration behaviors of the Ru-CS/PVA ENFs nanocomposites:

To understand the kinetics of release of the encapsulated Ru complexes **1-10** from the Ru-CS-PVA ENF DDSs we first studied the hydration equilibria in PBS at pH 1.5 (for **1** h only) and 7.4 (for 24 h). The pH conditions and timing were chosen to mimic absorption conditions of the acidic conditions of the stomach and the near-neutral conditions of the small intestines after their oral administration. The masses of the Ru-CS-PVA ENF (pre-dried) and after equilibrating them for time, t, were measured and the percentage hydration (aqueous absorption) capacity of the CS-PVA and Ru-CS-PVA ENFs mats of **1-10** was determined using **Equation A.** The pre-activation data of the ENFs obtained at the two pHs is depicted as bar graphs in **Figure 5.9.** After 24 h of hydration at pH 7.4, the metal-free PVA-CS ENFs swelled about 3 times more than in the acidic pH (1.5 compared to the data measured after 1 h). This emphasizes the pre-activation by hydration of the Ru(**1 - 10**)-embedded ENFs as driven by an inherent osmotic pressure between the bulk solution and the hydrophilic groups (acetates, hydroxy, & amino) in the core of the CS-PVA polymer blend.

At a low pH (1.5), this osmotic gradient that drives the absorption of water molecules is virtually absent. The protons catalyze the acid hydrolysis or participate in the protonation of the groups within the constituents of the ENFs. The swelling and hydration ratios for all the Ru-CS-PVA ENFs at each pH are more or less the same, showing that the inclusion of **1-10** has little to no effect on this pre-activation for the release of drug by these ENFs. It is anticipated that the hydration and formation of the semi-fiber gel by the ENFs is a critical step towards the controlled release of the metal complex drugs. Thus, the activation of the Ru-CS-PVA ENFs to release their payload (**1 - 10**) would be enhanced under neutral pH absorption conditions than under acidic conditions such as those of the GI tract. This can be advantageous since the drug-pre-loaded ENFs will be activated and conditioned better for the controlled release (only a small amount) only after most of it had reached the small intestines (where most absorption occurs and pH is near neutral)

for 24 h after administration. The time and amount of CS present were reported to be proportional to the percentage of swelling of NFs, while acidic pHs do not affect the pre-activation and thus controlled release of the Ru-CS-PVA ENFs.[22]

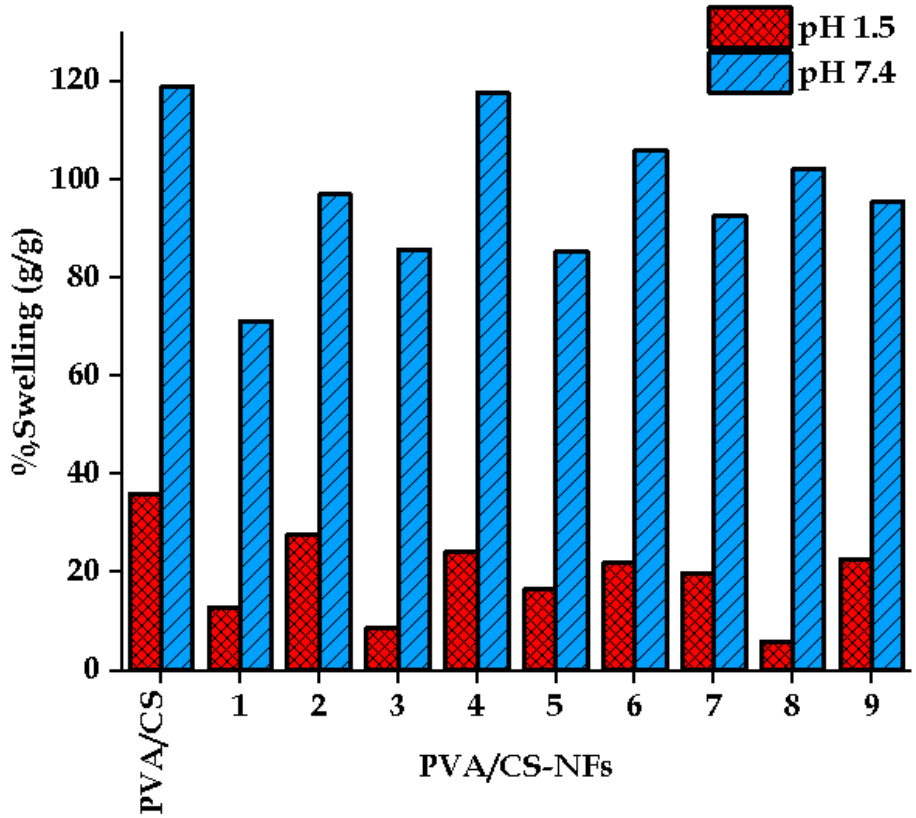

Figure 5. 9: *Hydration capacity ratios (%) of PVA-CS and Ru-CS-PVA ENF mats electrospun from a (70:30) CS/PVA blend with a (w/v)% Ru loading of 0.1.*

5.4 Release rate and efficiency release of **1-10** from Ru-CS-PVA ENFs

To estimate the real-time concentration of each of the leased complexes (**1- 6**, **8 – 10**) in 2% (v/v) DMSO: PBS solution, an absorption spectrometer was calibrated to measure the temporal absorbance of each complex at its charge transfer band using standard solutions of **1- 6**, **8 – 10**. The calibration plots are as depicted in **Figures 5.10 - 5.18**. The release rate and efficiency of complexes **1 - 10** molecules from Ru-CS-PVA ENFs into pH 1.5 and pH 7.4 buffer solutions were estimated from the initial and final spectral data as illustrated

in the respective UV-Visible absorption overlay data (**Figures 5.19 - 5.28**), The calculated data (refer to equations (**3** & **4**) is given in **Table 5.2**. The release rate at a pH of 1.5 is much higher (μM^{-1} min^{-1}) than at a pH of 7.4. However, the release efficiency is higher at neutral pHs. It is noteworthy that at a pH of 1.5 and after 1 h after incubation, complexes **1 - 10** are released from Ru-CS/PVA ENFs at releasing rates (RR) of 0.0146 to 2 μM min^{-1} with an estimated efficiency ranging from 5.69 to 37.6 %. Contrastingly, at pH 7.4 and after an incubation time of 24 h, it ranged from 0.0104 - 3.90 μM h^{-1} with an estimated efficiency range of 19.1 – 87.3 %.

As already demonstrated and discussed for the hydration activation step for release, the ENFs release the complexes at a slower and controllable rate but higher efficiency at pH 7.4 than they do at pH 1.5 as shown in **Table 5.2** except for complex **7** which is prone to undergone concomitant ligand exchange (at least according to overlay absorption data) during the activation for drug release timeframe as illustrated in **Scheme 3.2** in **Chapter 3**. At a pH of 1.5, there is an estimated release of **7** from Ru-CS-PVA ENFs of about 40%. At a pH of 7.4, the same complex is roughly 50% released into the solution.

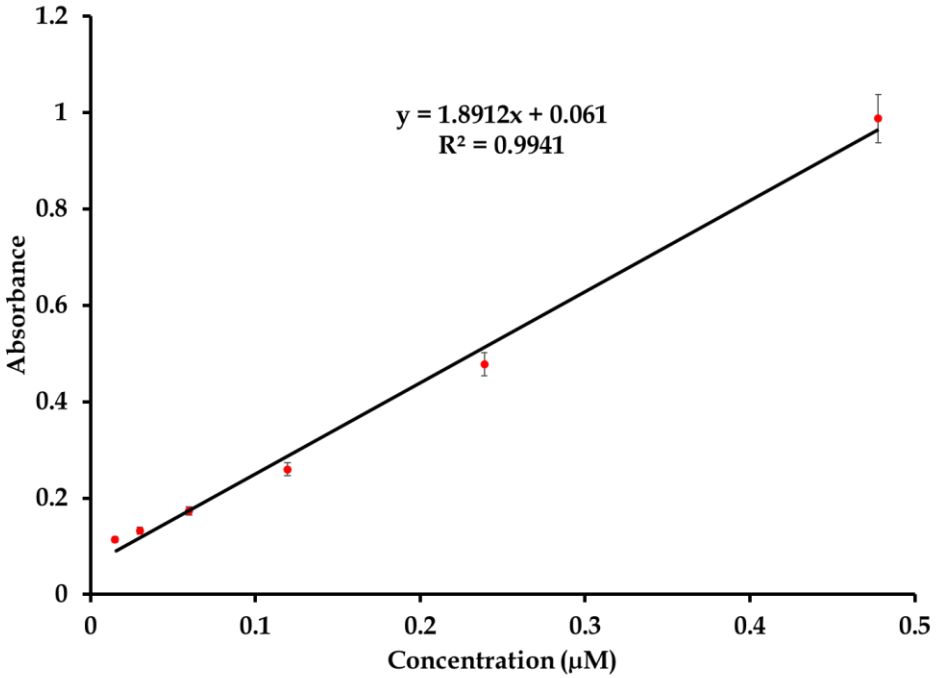

Figure 5. 10: *Linear calibration curve of **1** at 365 nm.*

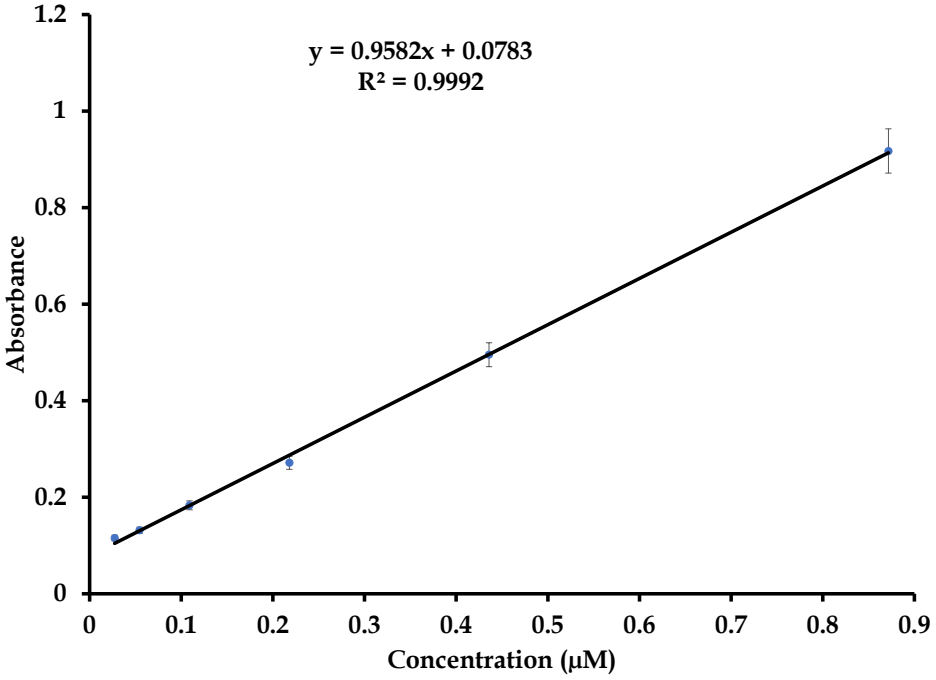

Figure 5. 11: *Calibration curve of **2** at 365 nm.*

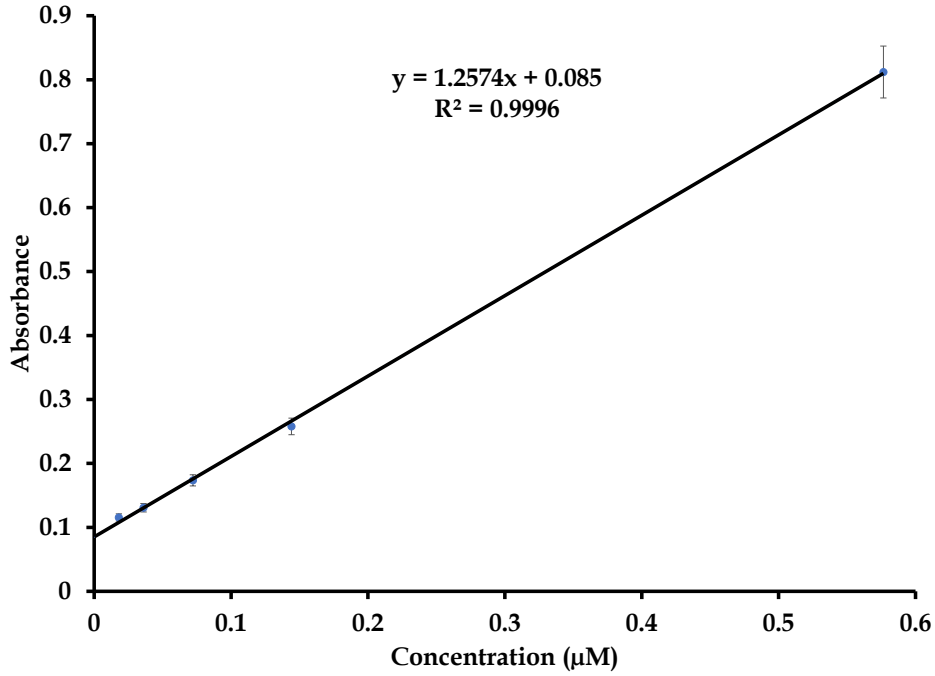

Figure 5. 12: *Calibration curve of **3** at 368 nm.*

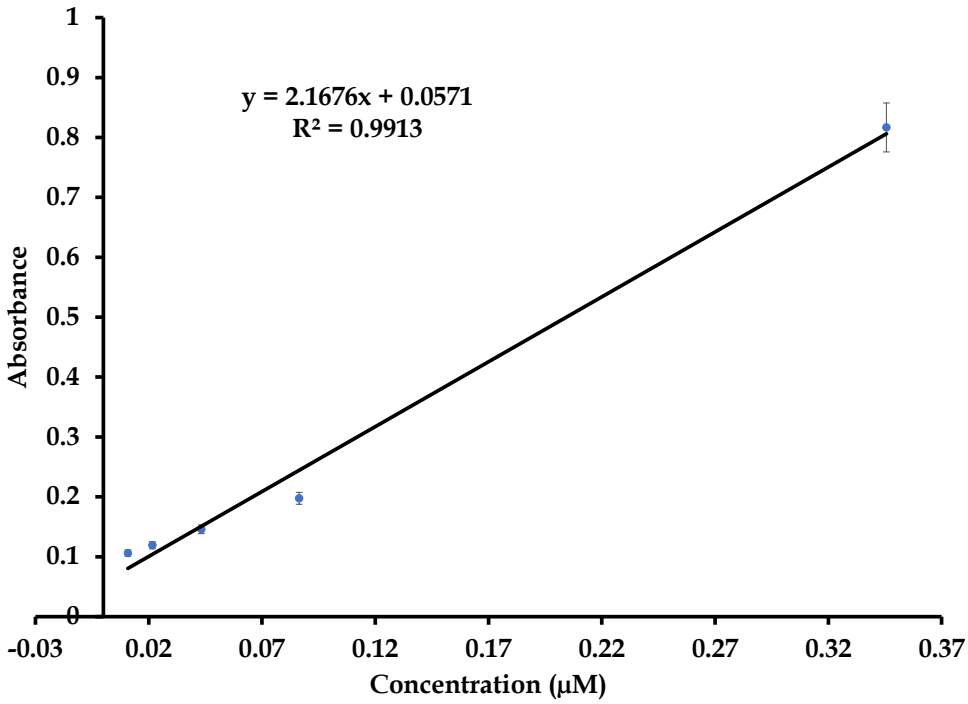

Figure 5. 13: *Calibration curve of **4** at 368 nm.*

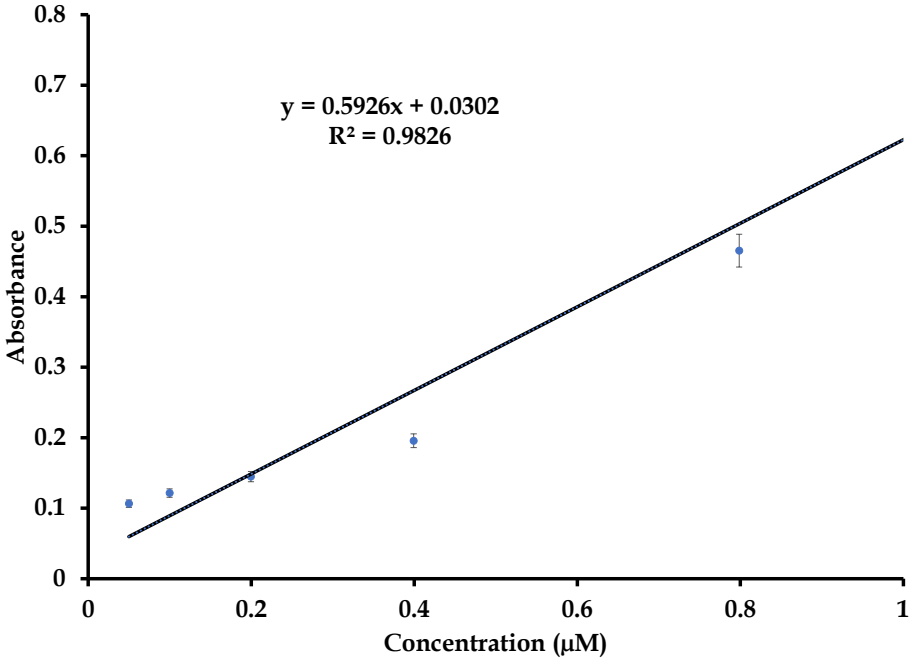

Figure 5. 14: *Calibration curve of* ***5*** *at 337 nm.*

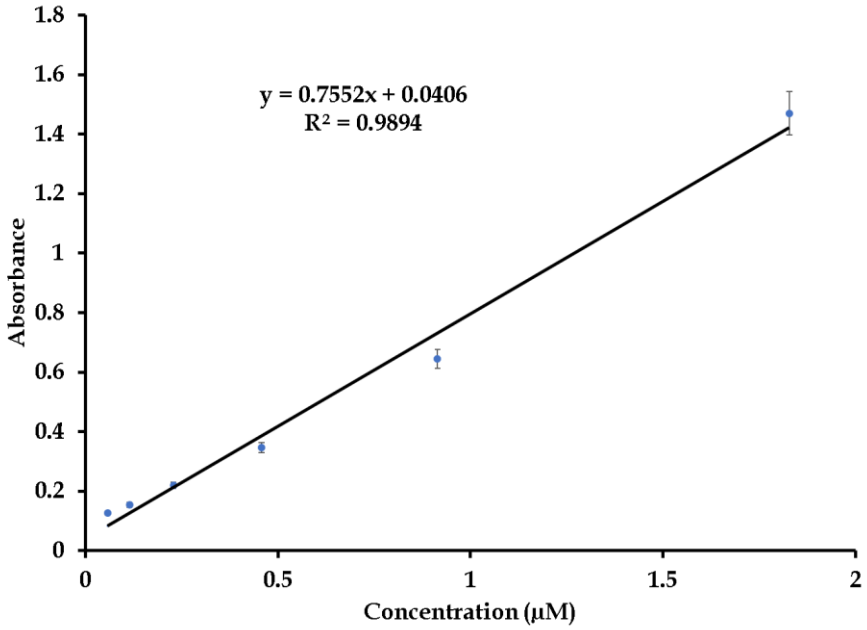

Figure 5. 15: *Calibration curve of* ***6*** *at 337 nm.*

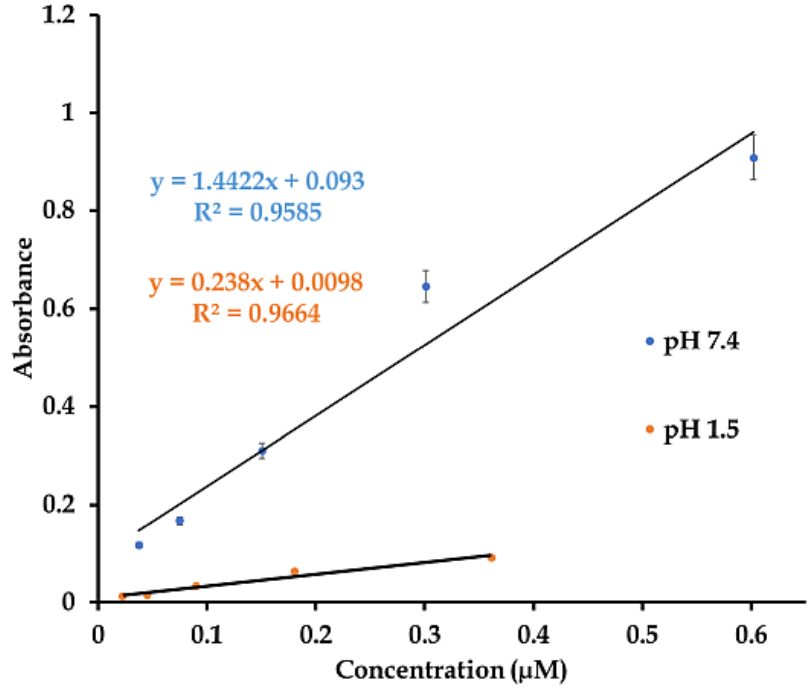

Figure 5. 16: *Calibration curve of* ***7*** *at 329 nm at (A) pH 1.5 and (B) at 439 nm for pH 7.4 nm.*

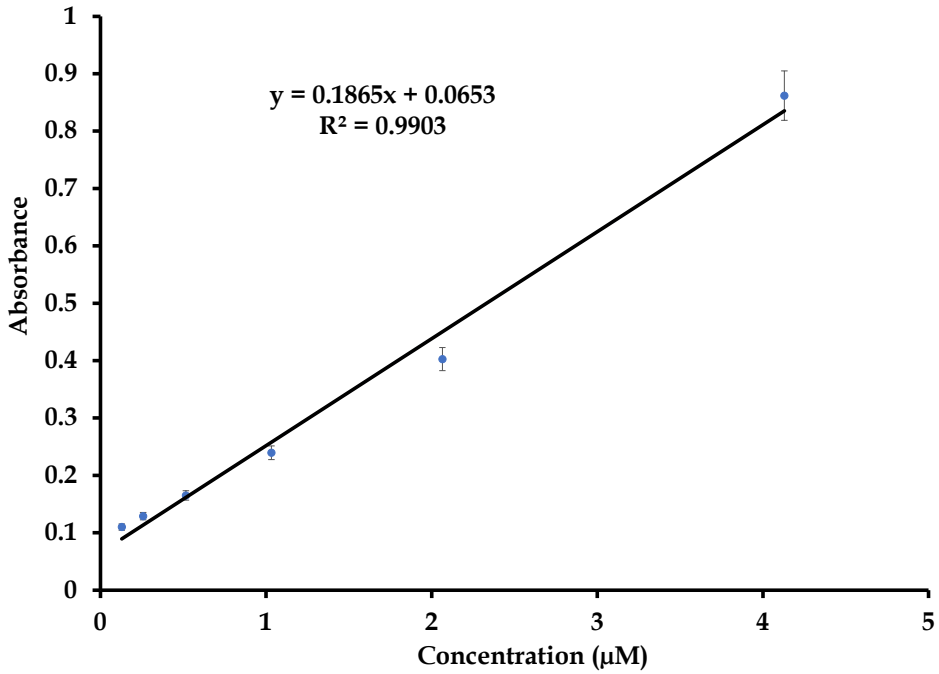

Figure 5. 17: *Calibration curve of 8 at 429 nm.*

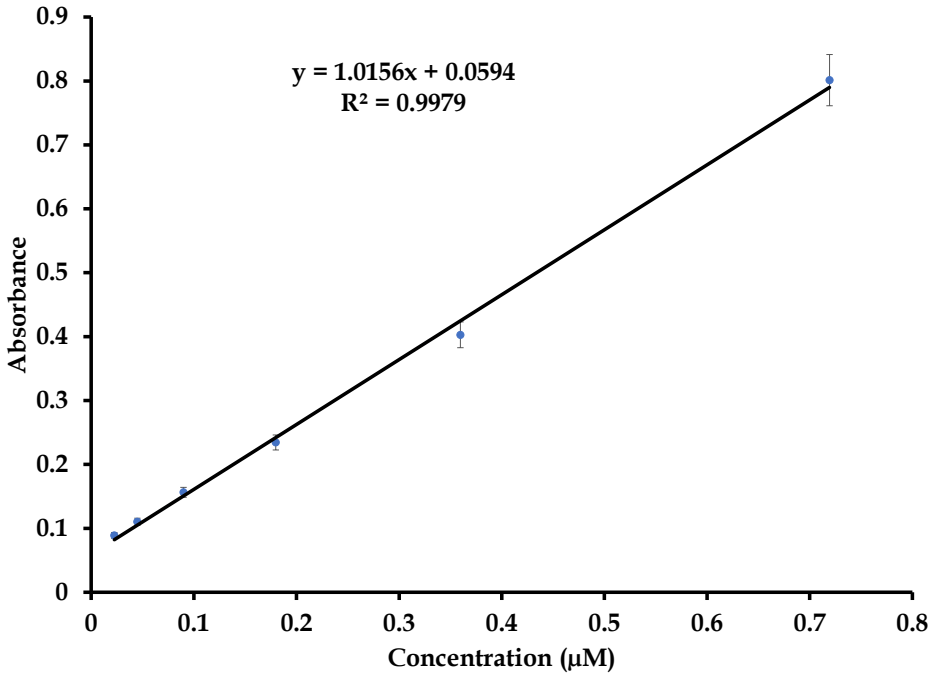

Figure 5. 18: *Calibration curve of **9** at 533 nm.*

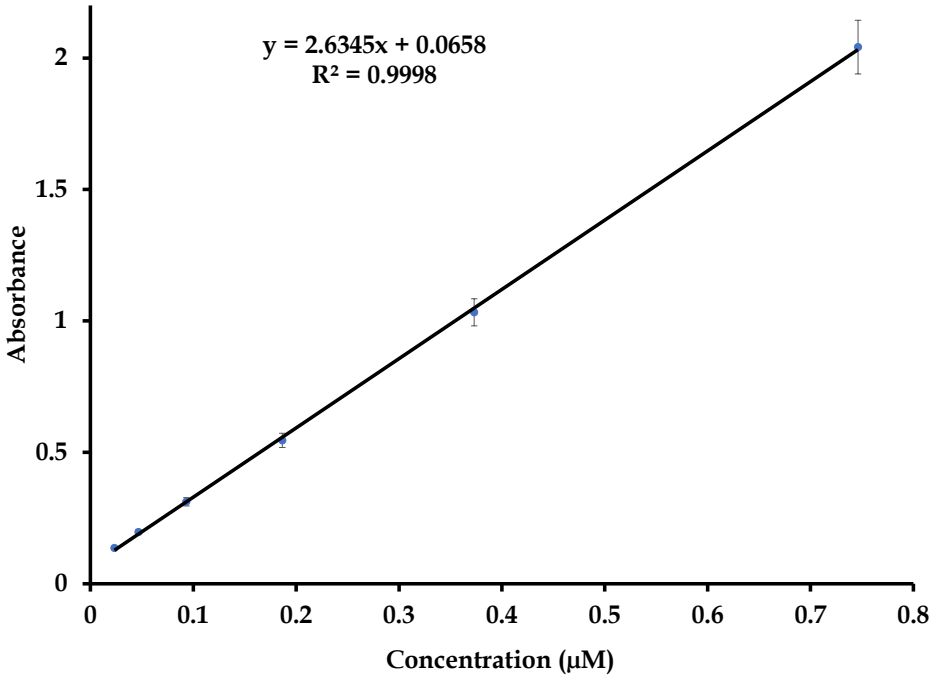

Figure 5. 19: *Calibration curve of **10** at 402 nm.*

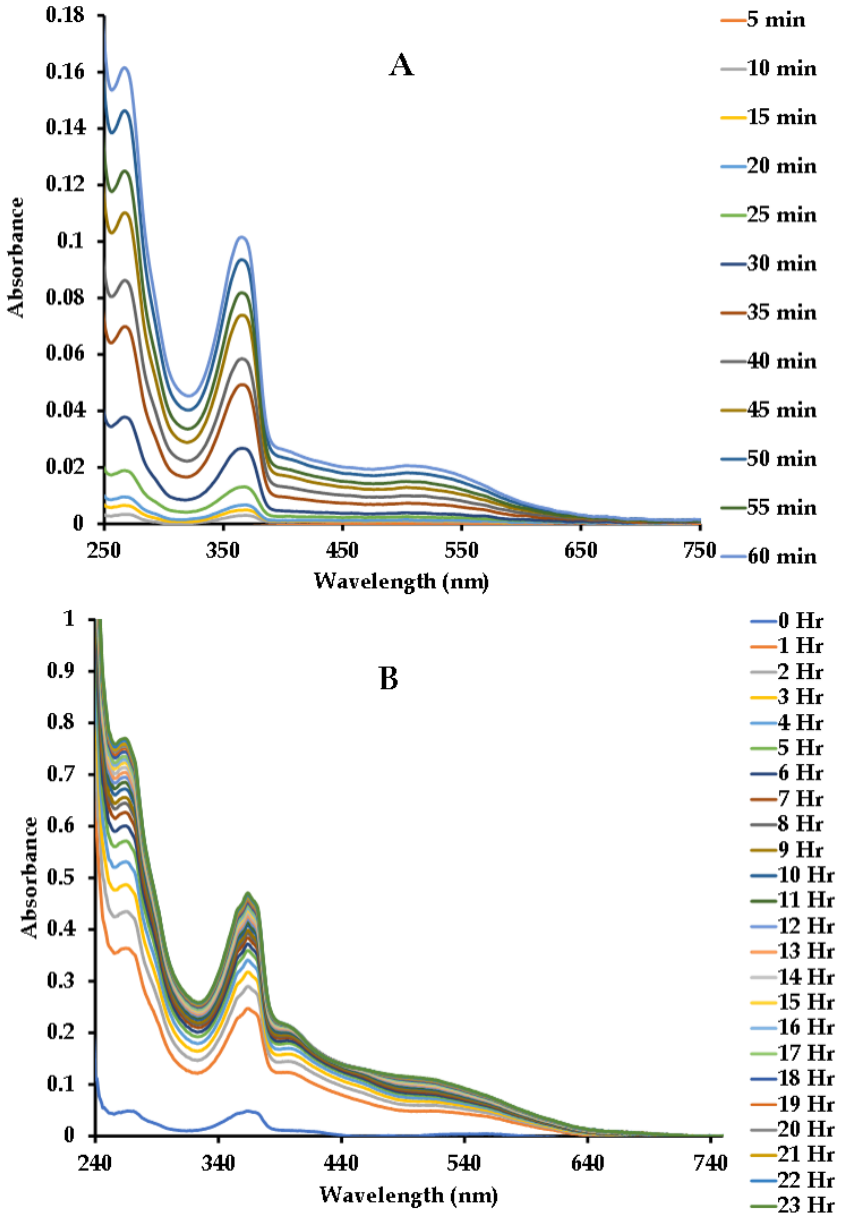

Figure 5. 20: *UV/Visible absorption spectral profile of* ***1*** *encapsulated in PVA-CS ENFs electrospun from a (70:30) CS/PVA blend with a (w/v)%Ru loading of 0.1, illustrating kinetic drug release at 365 nm at (A) a pH 1.5 and (B) pH 7.4 PBS solution.*

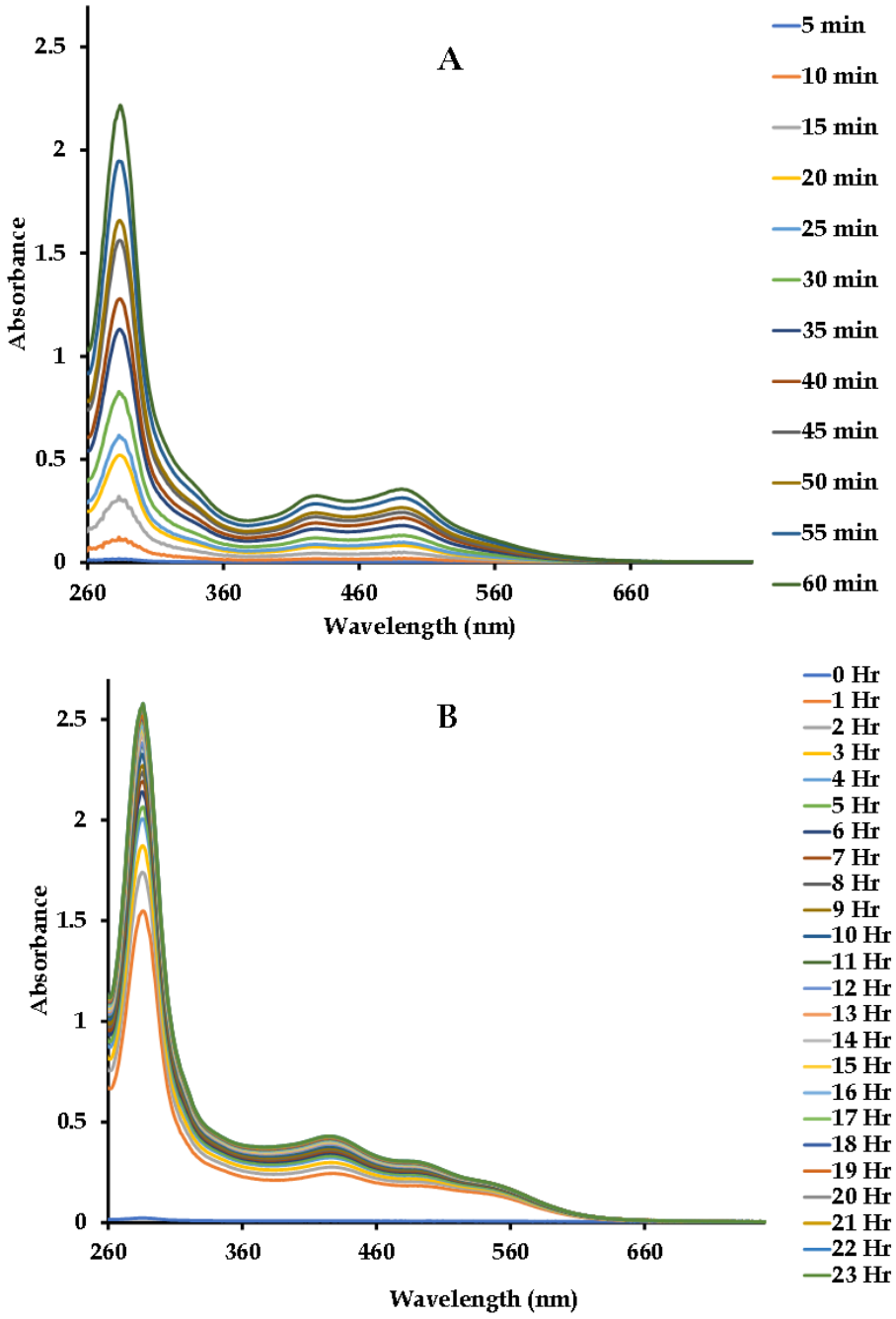

Figure 5. 21: *UV/Visible absorption spectral profile of 2 encapsulated in PVA-CS ENFs electrospun from a (70:30) CS/PVA blend with a (w/v)%Ru loading of 0.1, illustrating kinetic drug release at 365 nm at (A) pH 1.5 and (B) pH 7.4 PBS solution.*

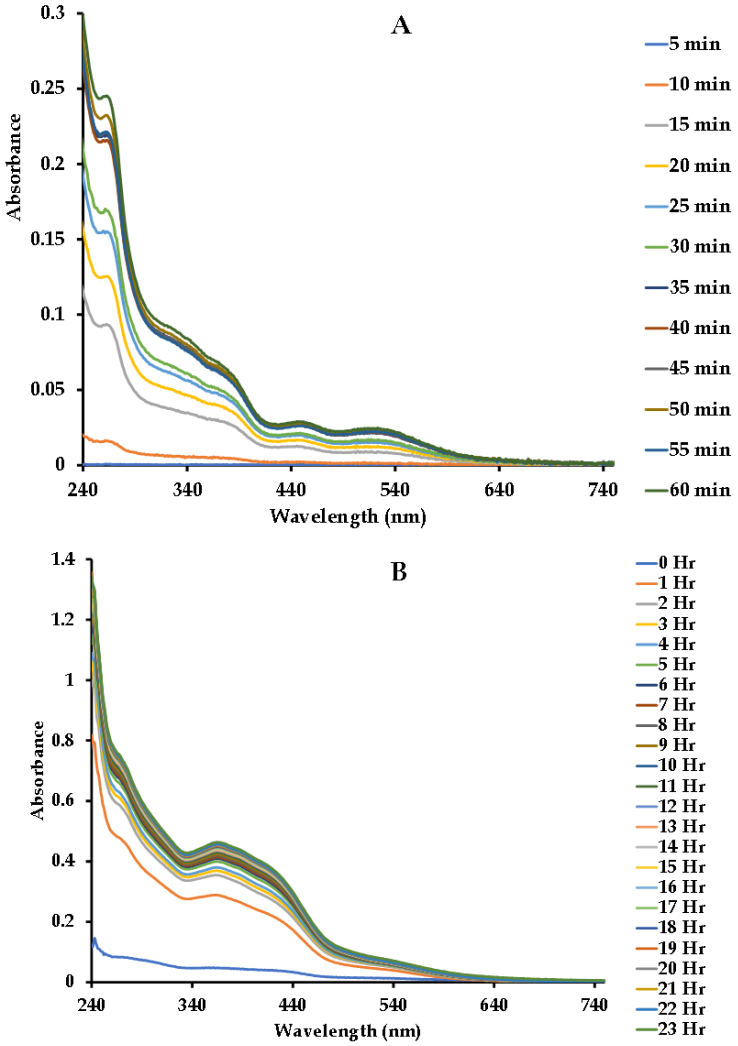

Figure 5. 22: *UV/Visible absorption spectral profile of* ***3*** *encapsulated in PVA-CS ENFs electrospun from a (70:30) CS-PVA blend with a (w/v)% Ru loading of 0.1, illustrating kinetic drug release at 368 nm at (A) pH 1.5 and (B) a pH 7.4 PBS solution.*

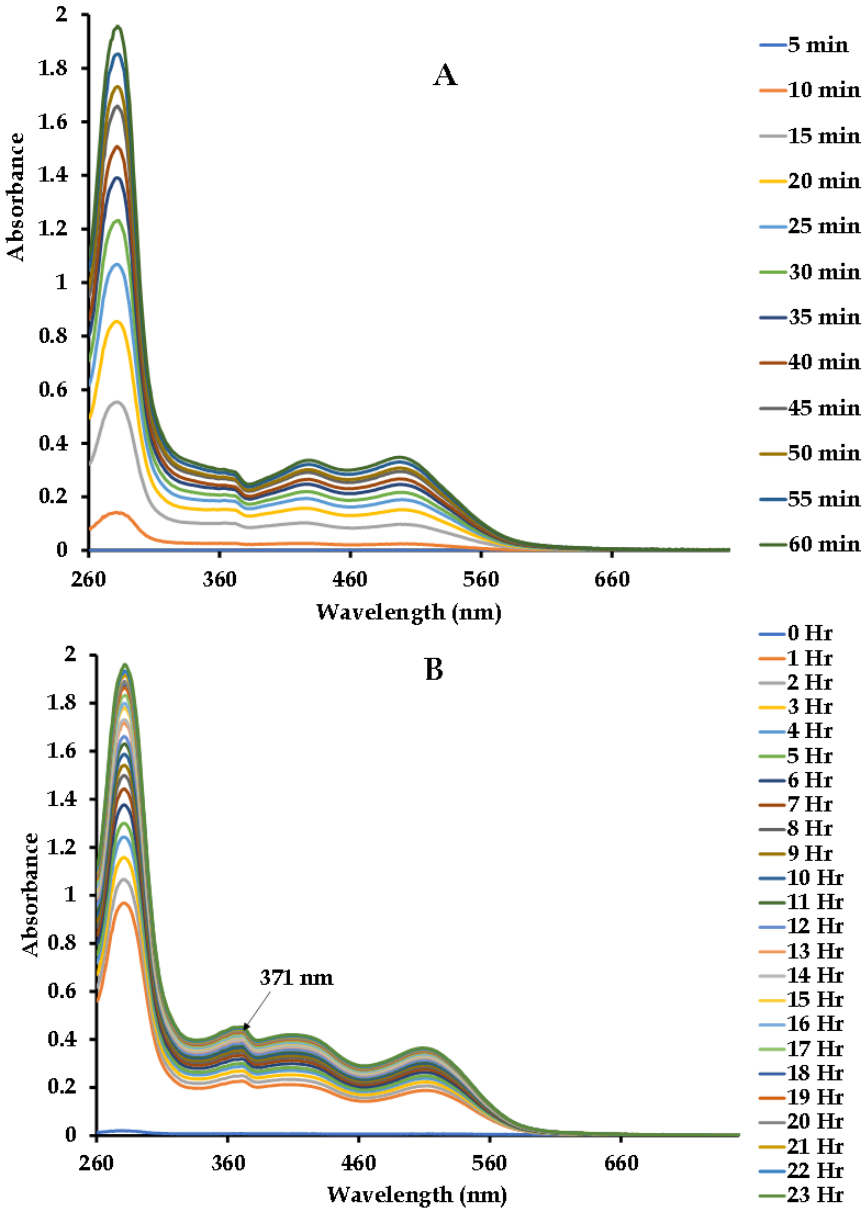

Figure 5. 23: *UV/Visible absorption spectral profile of* ***4*** *encapsulated in PVA-CS ENFs electrospun from a (70:30) CS-PVA blend with a (w/v)% Ru loading of 0.1, illustrating kinetic drug release at 368 nm at (A) a pH 1.5 and (B) pH 7.4 PBS solution.*

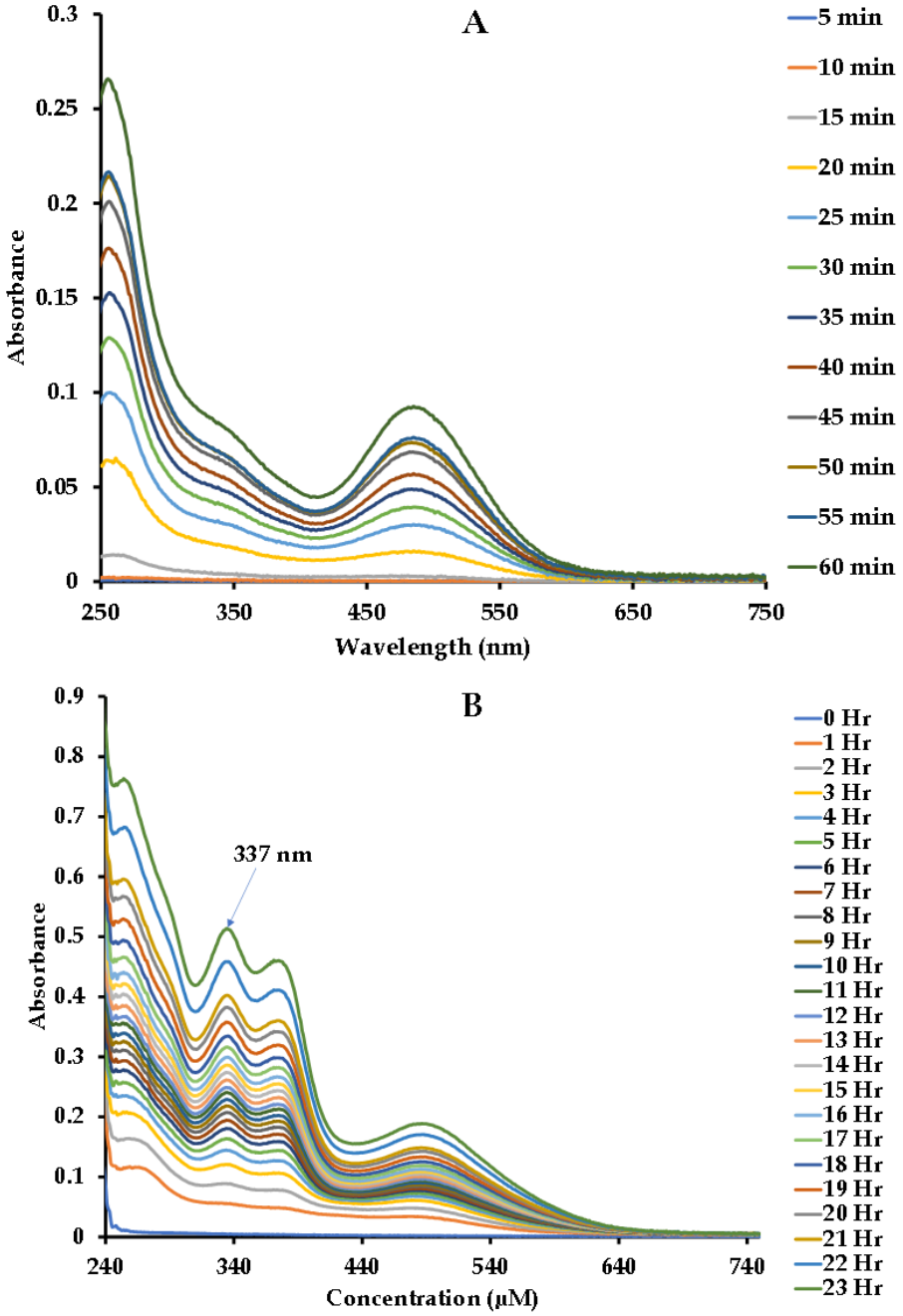

Figure 5. 24: *UV/Visible absorption spectral profile of* **5** *encapsulated in PVA-CS ENFs electrospun from a (70:30) CS-PVA blend with a (w/v)%Ru loading of 0.1, illustrating kinetic drug release at 337 nm at (A) a pH 1.5 and (B) pH 7.4 PBS solution.*

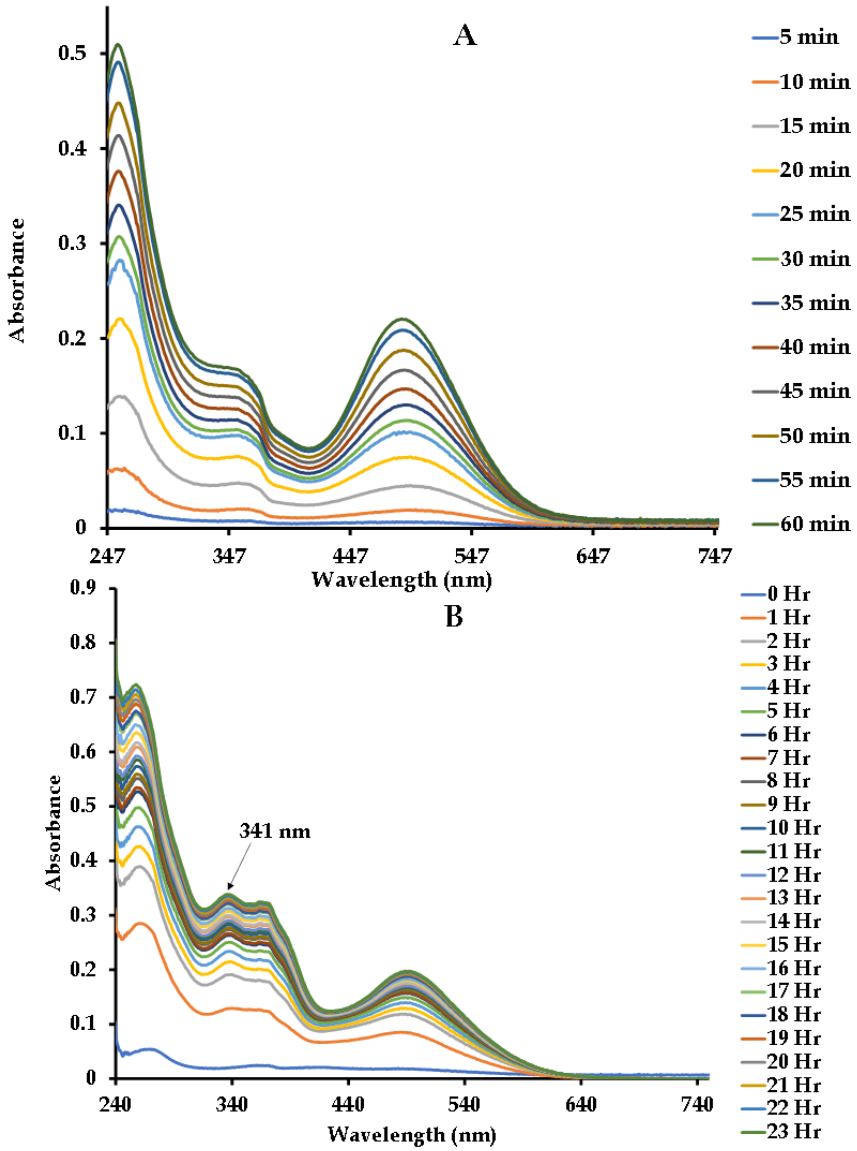

Figure 5. 25: *UV/Visible absorption spectral profile of* ***6*** *encapsulated in PVA-CS ENFs electrospun from a (70:30) CS/PVA blend with a (w/v)%Ru loading of 0.1, illustrating kinetic drug release at 341 nm at (A) pH 1.5 and (B) a pH 7.4 PBS solution.*

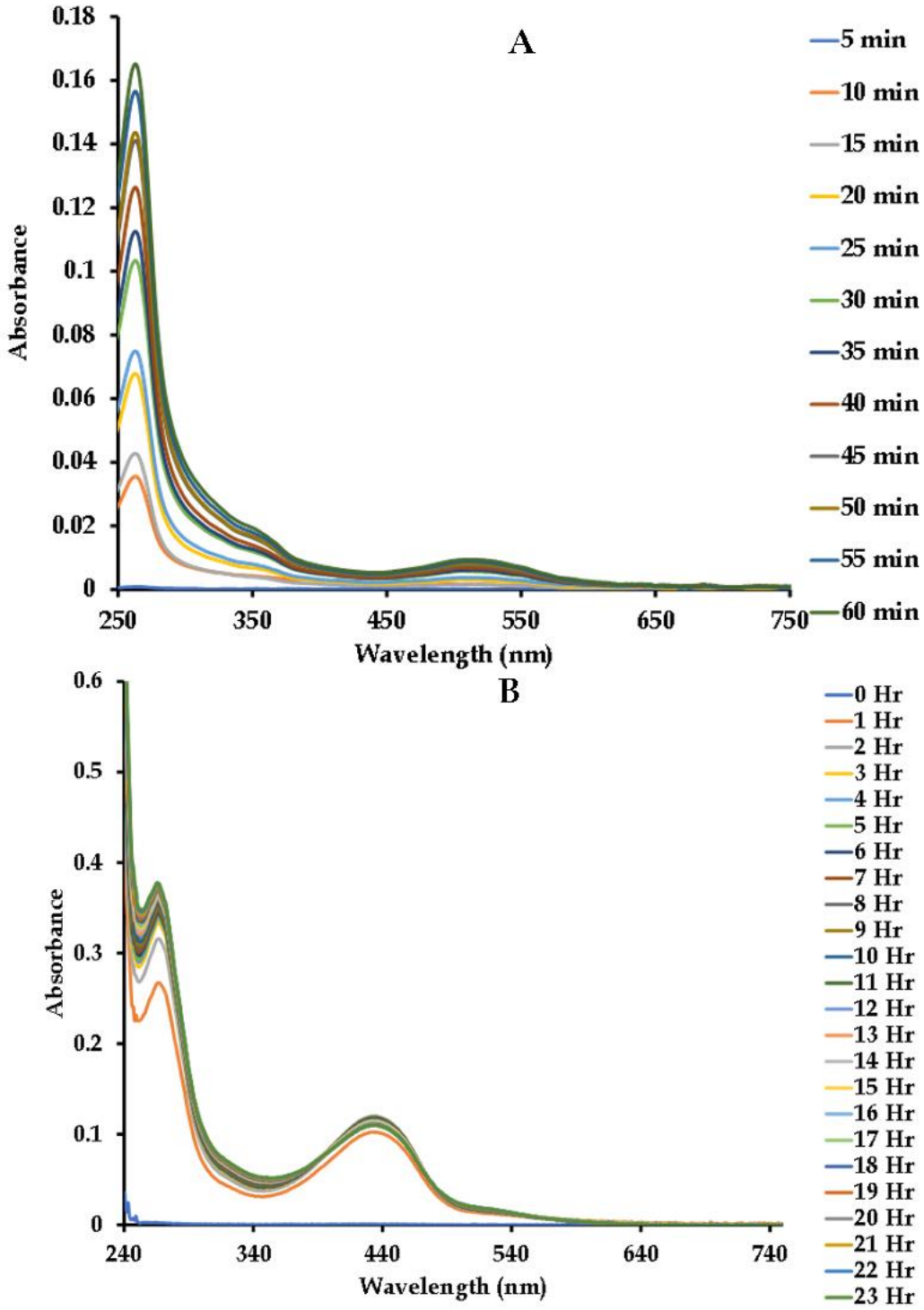

Figure 5. 26: *UV/Visible absorption spectral profile of* **7** *encapsulated in PVA-Cs ENFs electrospun from a (70:30) CS/PVA blend with a (w/v)%Ru loading of 0.1, illustrating kinetic drug release at 329 nm at (A) pH 1.5 and (B) at 439 nm for a pH 7.4 PBS solution.*

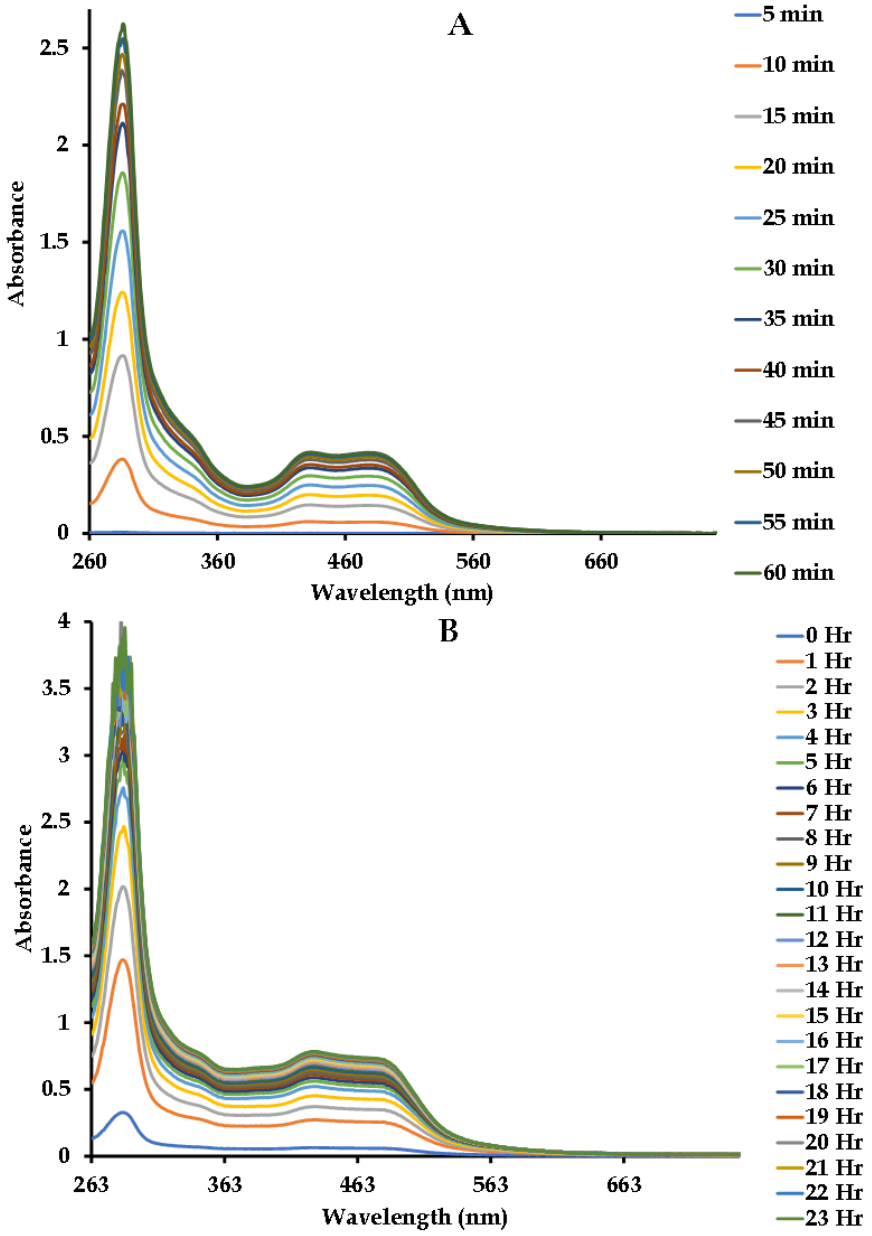

Figure 5. 27: *UV/Visible absorption spectral profile of* ***8*** *encapsulated in PVA/Cs-ENFs electrospun from a (70:30) CS/PVA blend with a (w/v) % Ru loading of 0.1, illustrating kinetic drug release at 429 nm at (A) pH 1.5 and (B) at 439 nm for pH 7.4 PBS solution.*

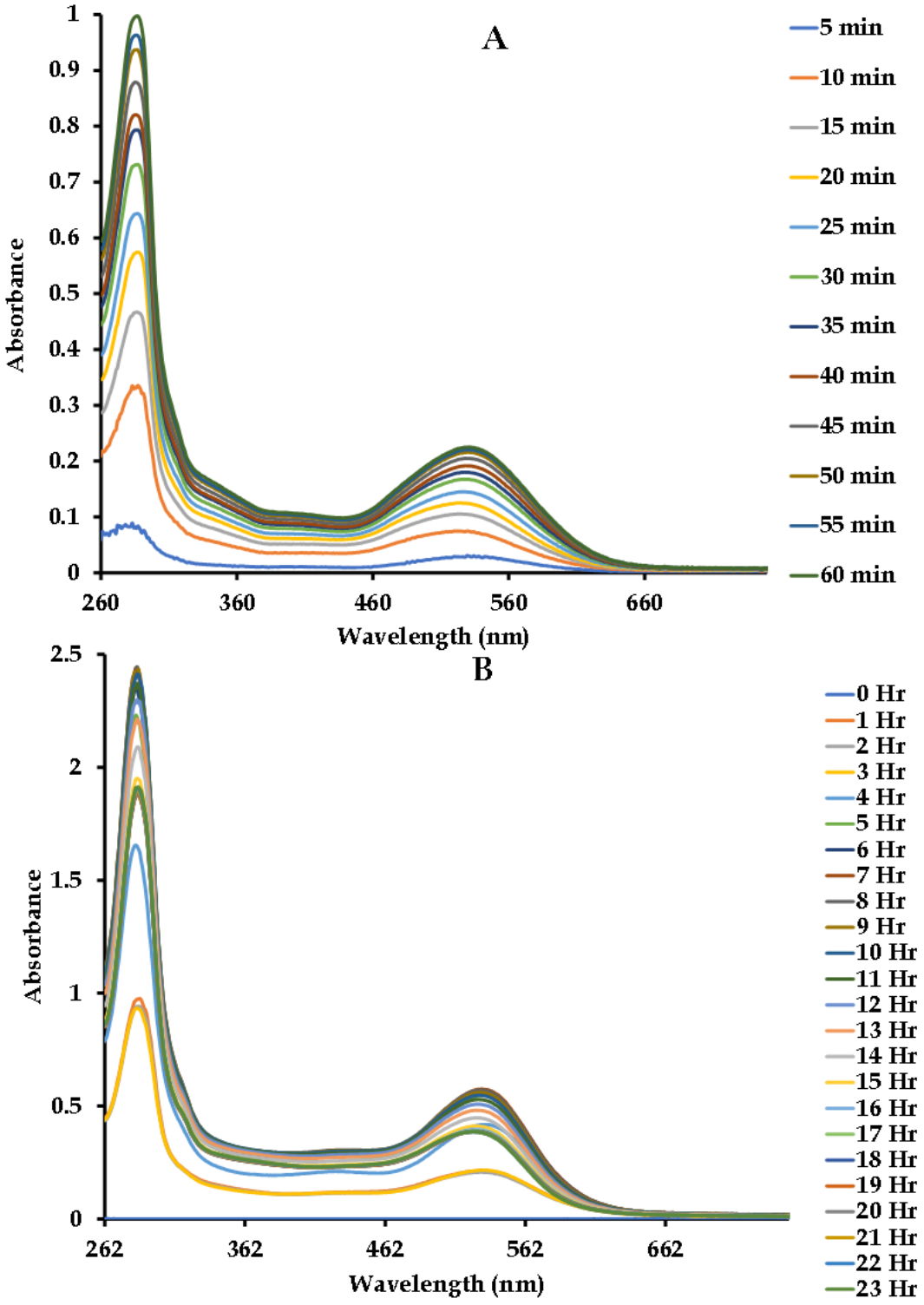

Figure 5. 28: *UV/Visible absorption spectral profile of* ***9*** *encapsulated in PVA/Cs-ENFs electrospun from a (70:30) CS/PVA blend with a (w/v)% Ru loading of 0.1, illustrating kinetic drug release at 533 nm at (A) pH 1.5 and (B) at 439 nm for a pH 7.4 PBS solution.*

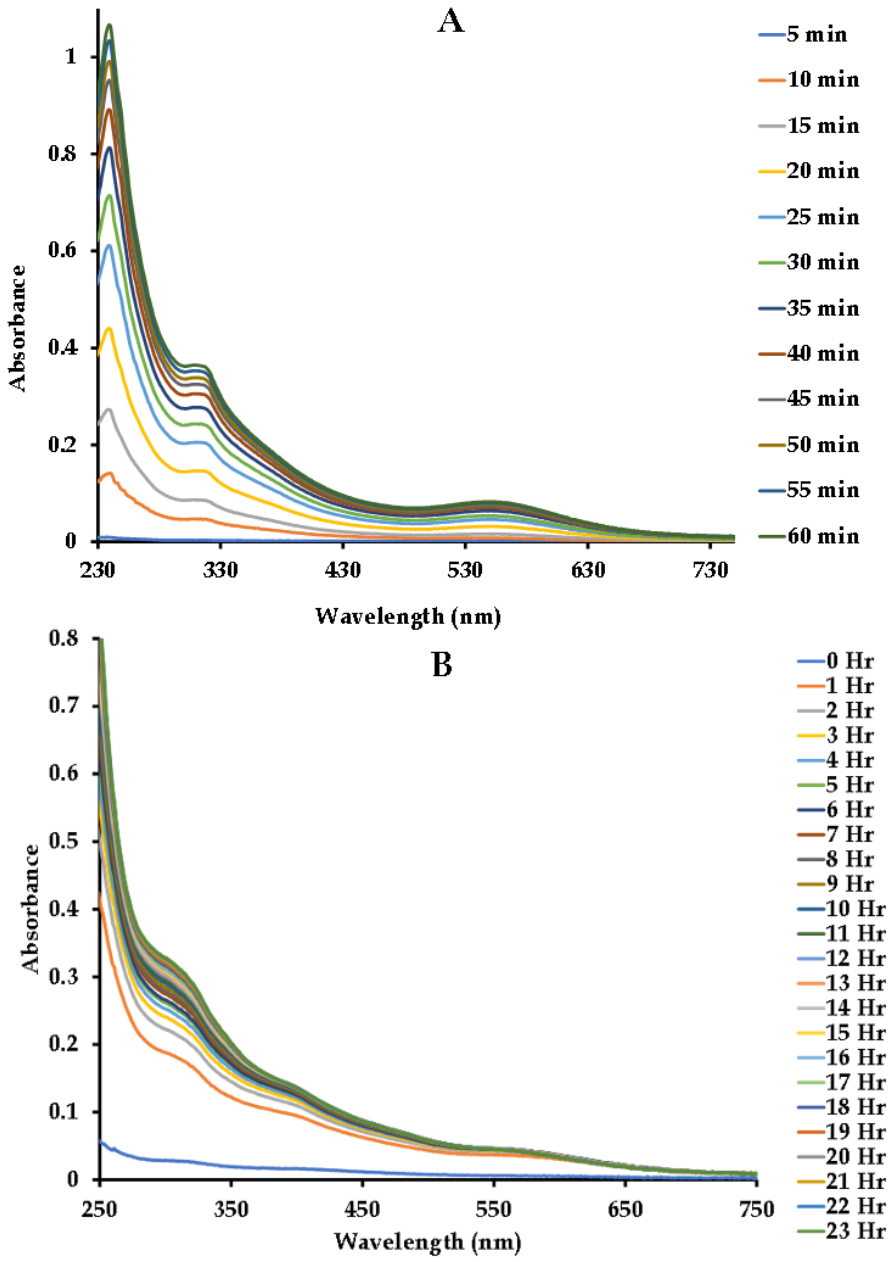

Figure 5. 29: *UV/Visible absorption spectral profile of* ***10*** *encapsulated in PVA/Cs-ENFs electrospun from a (70:30) CS/PVA blend with a (w/v)% Ru loading of 0.1, illustrating kinetic drug release at 533 nm at (A) pH 1.5 and (B) at 439 nm for a pH 7.4 PBS solution.*

Table 5. 2: *Drug release rates (RR) and the percentage drug release efficiencies (RE) of Ru-CS-PVA ENFs nanocomposites of* ***1*** *-* ***10*** *monitored for 1 h (5 min intervals) at pH 1.5 and 24 h (1 h intervals) at pH 7.4.*

Compound	RR at pH 1.5 ($\mu M\ min^{-1}$)	RR at pH 7.4 ($\mu M\ h^{-1}$)	(%)RE at pH 1.5	(%)[a] RE at pH 7.4
1	0.01462	0.01037	22.58	87.32
2	0.02449	0.03243	37.56	50.31
3	0.05464	0.05253	5.686	34.41
4	0.08913	0.1621	15.47	28.14
5	0.08742	0.0161	6.587	60.78
6	0.1294	0.03674	27.27	63.69
7	-	-	-	-
8	2.744	3.89	34.558	48.98
9	0.08149	0.0183	13.6	66.56
10	0.05172	0.0238	41.6	19.14

At pH 1.5, the Ru-CS/PVA-ENFs are rapidly acid-leached, leading to a more rapid release of **1-6**, **8-10**. However, the overall release efficiency is lower that at neutral (pH 7.4) and over a longer period of time (24 h). This makes conditioning and per activation of the ENFs a priority for ensuring controlled release of the metal complexes at a higher temporal release efficiency. At higher pHs (pH 7.4), the basic/anionic groups of CS/PVA within the ENFs make them negatively charged and, thus more hydrophilic. Consequently, slowly undergo hydrolysis with water molecules, leading to a gradual water uptake and higher swelling capacity as was experimentally verified in the trends of the hydration capacity data of the ENFs. Their functional groups also form favorable hydrogen bonds between the solvent molecules, establishing a steady-state equilibrium that leads to the gradual but more efficient release of the complexes **1 – 10** from the Ru-CS-PVA ENFs at a controllable manner, as evident from in the trends of the data at the two pHs. Furthermore, at physiological pH, the similar charged groups repel each other electrostatically.[23] As a result, the polymer network may swell, and accelerate the rate of release. Thus, conditioning/pre-activation for drug release from the ENFs is an important factor in the design of efficient and tuneable fiber-based DDSs. Consequently, there the swelling capacity of the ENFs under neutral conditions increased as the surface pore sizes of the matrix structure also increased. This establishes a partitioning equilibrium for the complexes to be released from the solid phase of the ENFs into the solution but in a kinetically controlled manner. It is expected that the embedded drugs **1 - 10** would be rapidly released out of the ENF mats at pH 1.5 as found in the acidic conditions of the GI track. This means that these novel DDSs should be co-administered as an admixture of the ENFs coated with an acid protective gel/shell, for them to reach the small intestines where absorption of most drugs occurs. If that precaution is not taken, the data points out to a risk of rapid release (1 h after administration) and loss of the Ru complexes in the GI tract and may be excreted along with faeces. By establishing a conditioning pre-equilibrium for the ENFs at higher pHs, electrostatic interactions within the polymer chains are activated, leading to other favourable changes (the acid-base interactions) between the solvent molecules, the complexes

(**1 – 10**) and other constituents of the polymer. This establishes an equilibrium for the controlled release of the complexes. Noteworthy is how the condition (pH, temperature, ionic balance) at the point of drug release (as in small intestines, pH 7.4) such as the overall charge reorganization affects some of the critical properties of the ENFs (polymer pre-swelling - conditioning/activation, wettability, solubility and absorptivity). All these factors are affecting the efficiency of the DDSs. Since the diffusion of free molecules within the polymer matrix can be tailored to the application, allowing different kinetics for the diffusion of entrapped drugs, swelling is particularly interesting in biomedical sciences.[24,25] These results imply that at neutral pHs there are stronger interactions between the complexes (**1 – 10**) and the other constituents of the ENFs matrix network given the ubiquitous presence of residual amino, amides, and acetate groups all of which form strong hydrogen bonds and increase the hydrophilicity and hence controlled release at an established portioning equilibrium. That is why, at higher pH levels, the amide/acetates group of the constituents of the ENFs can establish stronger bonds with the functional groups of the complexes.[12] At lower pH, the acid medium rapidly digests/dissolves the matrix, which may result in the release of the complexes from the ENFs at a faster rate lower releasing efficiency.

5.4 References

(1) Kolb, H.; Kempf, K.; Röhling, M.; Martin, S. Insulin: too much of a good thing is bad. BMC Medicine **2020**, 18 (1), 224, 1-12.
(2) Baker, C.; Retzik-Stahr, C.; Singh, V.; Plomondon, R.; Anderson, V.; Rasouli, N. Ther Adv Endocrinol Metab **2021**, 12, 1-13.
(3) Ng, L.; Gupta, M. Transdermal Drug Delivery Systems in Diabetes Management: A Review. Asian Journal of Pharmaceutical Sciences **2019**, (1):13-25.
(4) Abdel Moneim, A.; Ramadan, H. Novel strategies to oral delivery of insulin: Current progress of nanocarriers for diabetes management. Drug Development Research **2021**, 83, (2):301-316.
(5) Li, C.; Wang, J.; Wang, Y.; Gao, H.; Wei, G.; Huang, Y.; Yu, H.; Gan, Y.; Wang, Y.; Mei, L.; et al. Recent progress in drug delivery. Acta Pharm Sin B **2019**, 9 (6), 1145-1162.
(6) Hawthorne, D.; Pannala, A.; Sandeman, S.; Lloyd, A. Sustained and targeted delivery of hydrophilic drug compounds: A review of existing and novel technologies from bench to bedside. Journal of Drug Delivery Science and Technology **2022**, 78, 103936,1-27.
(7) Ghaderpour, A.; Hoseinkhani, Z.; Yarani, R.; Mohammadiani, S.; Amiri, F.; Mansouri, K. Altering the characterization of nanofibers by changing the electrospinning parameters and their application in tissue engineering, drug delivery, and gene delivery systems. Polymers for Advanced Technologies **2021**, 32, 1-27. (8) Zahra, F. T.; Quick, Q.; Mu, R. Electrospun PVA Fibers for Drug Delivery: A Review. Polymers (Basel) **2023**, 15 (18), 1-36.
(9) Harugade, A.; Sherje, A. P.; Pethe, A. Chitosan: A review on properties, biological activities and recent progress in biomedical applications. Reactive and Functional Polymers **2023**, 191, 105634, 1-27.
(10) Ali, I. H.; Khalil, I. A.; El-Sherbiny, I. M. Design, development, in-vitro and in-vivo evaluation of polylactic acid-based multifunctional nanofibrous patches for efficient healing of diabetic wounds. Sci Rep **2023**, 13 (1), 3215, 1-17.
(11) Munteanu, A. C.; Uivarosi, V. Ruthenium Complexes in the Fight against Pathogenic Microorganisms. An Extensive Review. Pharmaceutics **2021**, 13 (6), 1-51.
(12) Eberhardt, E. S.; Raines, R. T. Amide-Amide and Amide-Water Hydrogen Bonds: Implications for Protein Folding and Stability. J Am Chem Soc **1994**, 116 (5), 2149-2150.
(13) Abadi, P. G. S.; Irani, M. Electrospun metal-organic frameworks-loaded nanofibrous carriers for drug delivery systems. Chemical Engineering Journal **2023**, 474, 145840, 1-44.
(14) Liu, Q.; Ouyang, W.-C.; Zhou, X.-H.; Jin, T.; Wu, Z.-W. Antibacterial Activity and Drug Loading of Moxifloxacin-Loaded Poly(Vinyl Alcohol)/Chitosan Electrospun Nanofibers. Frontiers in Materials **2021**, 8, 643428, 1-9.
(15) Pant, B.; Park, M.; Park, S. J. Drug Delivery Applications of Core-Sheath Nanofibers Prepared by Coaxial Electrospinning: A Review. Pharmaceutics **2019**, 11 (7), 1-21.
(16) Farazin, A.; Mohammadimehr, M.; Ghasemi, A. H.; Naeimi, H. Design, preparation, and characterization of CS/PVA/SA hydrogels modified with mesoporous Ag(2)O/SiO(2) and curcumin nanoparticles for green, biocompatible, and antibacterial biopolymer film. RSC Adv **2021**, 11 (52), 32775-32791.

(17) Santiago-Castillo, K.; Del Angel-López, D.; Torres-Huerta, A. M.; Domínguez-Crespo, M. A.; Palma-Ramírez, D.; Willcock, H.; Brachetti-Sibaja, S. B. Effect on the processability, structure and mechanical properties of highly dispersed in situ ZnO:CS nanoparticles into PVA electrospun fibers. Journal of Materials Research and Technology **2021**, 11, 929-945.
(18) Abbas, W.; Sharafeldin, I.; Omar, M.; Allam, N. Novel mineralized electrospun chitosan/PVA/TiO 2 nanofibrous composites for potential biomedical applications: computational and experimental insights. Nanoscale Advances **2020**, 2, 1-11.
(19) Laurence, M.; Budlayan, M. L.; Phyre, J.; Oracion, J. P.; De, L.; Rosa, L.; Joy, M.; Rodriguez, D.; Patricio, J.; Perez, S. J. L.; et al. Preparation of Spin-Coated Poly(vinyl alcohol)/ chitosan/ Gold Nanoparticles Composite and Its Potential for Colorimetric Detection of Cyanide in Water. Polish Journal of Environmental Studies **2022**, 31, 1-8.
(20) Munshi, M. U.; Martens, J.; Berden, G.; Oomens, J. Vibrational Spectra of the Ruthenium-Tris-Bipyridine Dication and Its Reduced Form in Vacuo. J Phys Chem A **2020**, 124 (12), 2449-2459.
(21) Karthikeyan, P.; Banu, T.; Meenakshi, S. Synthesis and characterization of metal loaded chitosan-alginate biopolymeric hybrid beads for the efficient removal of phosphate and nitrate ions from aqueous solution. International Journal of Biological Macromolecules **2019**, 1(130), 407-418.
Rahma, A.; Munir, M. M.; Rachmawati, H.; Khairurrijal, K. Correlation between Structures and Antioxidant Activities of Polyvinylpyrrolidone/ Garcinia mangostana L. Extract Composite Nanofiber Mats Prepared Using Electrospinnin. Journal of Nanomaterials **2017**, 2017, 1-10.
(23) Zhou, H. X.; Pang, X. Electrostatic Interactions in Protein Structure, Folding, Binding, and Condensation. Chem Rev **2018**, 118 (4), 1691-1741. Schoeller, J.; Itel, F.; Wuertz-Kozak, K.; Fortunato, G.; Rossi, R. M. pH-Responsive Electrospun Nanofibers and Their Applications. Polymer Reviews **2022**, 62 (2), 351-399.
(24) Scranton, A. B.; Rangarajan, B.; Klier, J. Biomedical applications of polyelectrolytes. In Biopolymers II, Berlin, Heidelberg, 1995//, 1995; Peppas, N. A., Langer, R. S., Eds.; Springer Berlin Heidelberg: pp 1-54. Tripathy, S.; Kumar, J.; Nalwa, H. S. Handbook of Polyelectrolytes and Their Applications, 3-Volume Set; 2002.
(25) Nafo, W. Hydrogel Biomaterials for Drug Delivery: Mechanisms, Design, and Drugs. 2022, 1-21.

Chapter 6

Conclusion and recommendation for further studies

6.1 Conclusions

In first experimental chapter, structural analogues of 2,6-*bis*-((6-amino-1,3-dimethyluracilimino)methylene)pyridine (H_4ucp) afforded different coordination modes to the *cis*-$[Ru(bipy)_2]^{2+}$ (in **2** and **4**) and *cis*-$[RuCl_2(PPh_3]$ (**3**) cores in comparison to the coordination behavior of the monoanionic ucp tetradentate diimine chelator in **1**. Insight was also obtained in the variable real solution stabilities between the metal complex cations and the chloro-containing metal complexes using the simulated data. Metal complexes **2 – 4** are deemed strong BSA binders based on the intrinsic binding (K_b) constants, while the Stern-Volmer (K_{SV}) constants show that these metal complexes have high affinities for drug carrier protein in solution. Amylin fluorescence spectroscopic titrations suggest that **1** and **3** can be classified as pro-drugs that undergo hydrolysis before directly binding to this polypeptide. In contrast, the metal complex cations **2** and **4** bind with amylin *via* hydrogen bonding and electrostatic attractions. Ruthenium complexes **2 – 4** enhanced glucose metabolism, as can be observed by the increased glucose utilization and glycogen synthesis in liver Chang cell lines. The ability of ruthenium complexes to independently promote glucose metabolism in the liver cells may be beneficial in managing diabetes. Metal complex **3** was the most effective in reducing media glucose concentrations in the liver cells, and the induced glucose concentrations were lower than that of the insulin-treated cells at all three dosages suggesting insulin-mimetic effects. However, *in vivo* studies are still required to determine the exact mechanism behind the potential anti-diabetic activity.

In Chapter 4, the uracil Schiff bases displayed various classical coordination modes towards the $[(\eta^6\text{-}p\text{-cymene})Ru]^{2+}$, *trans*-$[Ru(PPh_3)_2]^{2+}$ and *cis*-$[Ru(bpy)_2]^{2+}$ cores whereas the crystal structure of (dapda) showed that the Schiff base underwent

hydrolysis. Time-dependent stability studies showed that in the presence of a nucleophilic solution such as DMSO, the labile chloride co-ligands of **1-3** and **6** are readily prone to substitution by the former. In contrast, the excess chloride ions in solution caused substitution suppression due to Le Chatelier's effect. However, these metal complexes are stable in a non-coordinative solvent, DCM or in aqueous buffered solution (pH 7.4). DFT computed data show that the nature of the leaving group affects the effective charge, electrophilicity, and hence the reactivity of the complex. Despite the structural differences of the *mono*- and diimine uracil metal complexes, their radical activities IC_{50} values for the neutralization of the DPPH and NO radicals were far superior than the natural antioxidant, vitamin C. Their interactions with BSA, studied by spectrophotometric titrations illustrated non-coordinative interactions with the biomolecules. These metal complexes showed comparable disaggregation capabilities for the BSA (ThT) amyloidal plaques which was established from the visual inspections of the TEM micrographs. Interestingly, the majority of the metal complexes bind in a non-coordinative manner to BSA-ThT oligomers while the fluorescence spectral trends show that the binding of **1-3** and **6** was initiated by non-covalent binding followed by directional bonding.

Chapter 5 reports on the nanofabrication of Ru-CS-PVA ENFs of **1 - 10** from a bulk (*v: v* = 70: 30) CS: PVA polymer blend doped with a (*w: v*)% with respect to metal complex loading of 0.1% *via* electrospinning. These ruthenium complex-ENF nanoconjugates were designed to serve as oral-administered DDSs for Diabetes Mellitus. The stepwise optimization of the polymer solution parameters showed that the CS proportion within the CS-PVA ENFs inversely varied the ENF diameter and hence the effective surface area for metal embedment. It can be hypothesized that the main stabilizing factors of the nanoconjugates include complementary hydrogen bonding and π-π stacking between the polymeric constituents and the metal complexes while the chemical lability of ruthenium compounds containing chloride co-ligands can undergo coordinative bonding with the appropriate functional groups of the PVA and CS polymers. SEM-EDX provided visual confirmation that the metal complexes were included in the nano-confined polymeric fibers while powder X-ray diffraction

suggests the individual inorganic complex molecules are randomly distributed within the constituents of the ENFs. Comparative FTIR analysis showed characteristic vibrational bands due to the functional groups of the components for all Ru-SC-PVA-ENFs with no distinctive shifts in the peak frequencies.

The ENFs are more activated by hydration of the metal complex release in neutral pH conditions than under acidic. The release rate under acidic pH (1.5) was significantly higher, which suggested instant decomposition of the ENFs to cause a rapid release (within 1 h after incubation) of the metal complexes **1 – 10**, while it was slower (with estimated release rate in the range of 0.0104 - 3.89 μM h^{-1} with a higher estimated % release efficiency ranging between 19.1 – 87.3 %. The trends in the release data that the fabricated Ru-CS-PVA-ENFs are pH responsive since their hydrophobic/hydrophilic group variably influence the conditioning/pre-activation process and hence the ENFs desorption rates. The behavioral drug release profiles of the nanofabricated ENFs indicate that they are well suited for oral DDS *in vivo* application.

6.2 Future work:

As aforementioned, Significant strides have been made towards achieving the planned research aims. However, several key research questions remain to be answered which includes:

(1) How does the *in vitro* anti-diabetic activities of the *mono*-imine uracil ruthenium compounds compare with the diimine *bis*-uracil ruthenium compounds?

(2) Will incorporation of the respective metal complexes into the PVA-CS ENFs promote stability of the metal complexes in the GI tract during the *in vivo* anti-diabetic studies?

(3) Can comparable *in vivo* anti-diabetic activities be attained when orally administering the Ru-CS-PVA ENFs nanoconjugates to STZ-diabetic rats with respect to intravenously injecting the lead metal complexes?

(4) Will the Ru-CS-PVA ENFs nanoconjugates provide a controlled release of the metal-based drugs under *in vivo* conditions?

Furthermore, the inherent hydrolytic instability of Schiff base; especially under the acidic conditions of the GI tract[1] can be addressed by isolating ruthenium compounds with uracil amide and benzimidazole ligands, see **Figures 6.1** and **6.2**.

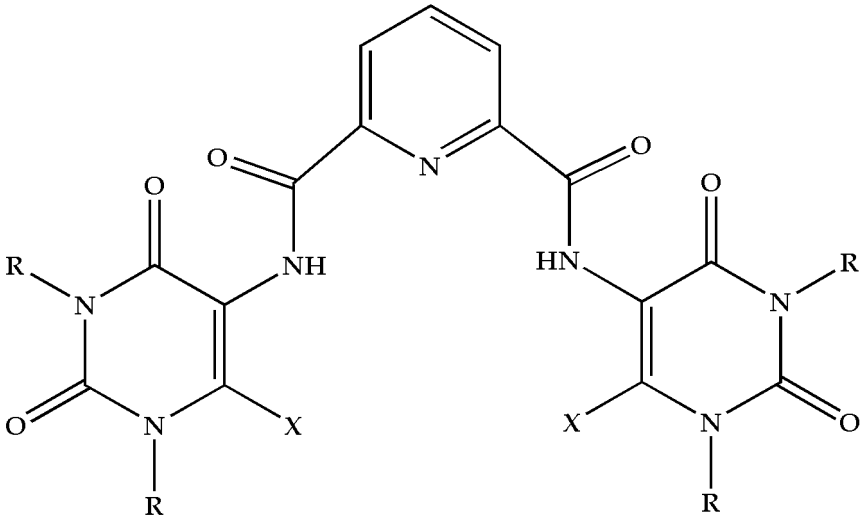

Figure 6. 1: *Generic structure of bis-uracil and -amide free-ligands with a bridging pyridyl moiety.*

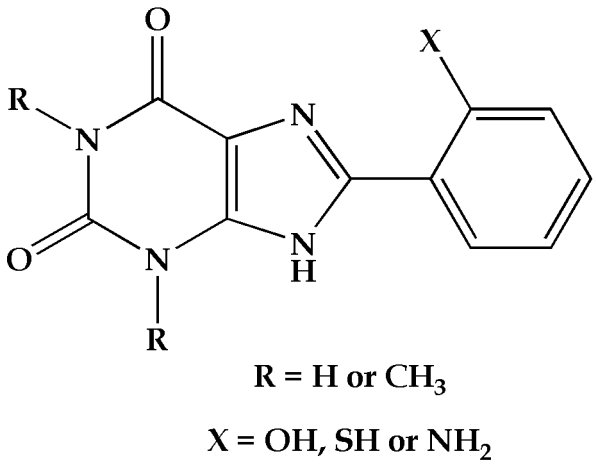

Figure 6. 2: *Generic structure of the mono-benzimidazole uracils which can act as N_{uracil}, X = O, N or S donors.*

6.3 References

(1) Shabsoug, B. Synthesis, Characterization and Hydrolysis Study of the Imine and the Hydrazone of p- nitro benzaldehyde, under Simulated Physiological Conditions. **2023**, *12*, 2913-2924.